THESE

DE DOCTORAT DE L'INSTITUT PHYSIQUE DU GLOBE DE PARIS

Spécialité : Géophysique interne

présentée par **Alessio PIATANESI**

Pour obtenir le grade de

DOCTEUR DE L'INSTITUT PHYSIQUE DU GLOBE DE PARIS

Sujet de la thèse :

Caractérisation des sources sismiques par étude des tsunamis

Soutenue le 25 Octobre 1999 devant le jury composé de :

Armando CISTERNAS	Rapporteur
Emile A. OKAL	Rapporteur
Jean-Philippe AVOUAC	Directeur de thèse
Philippe HEINRICH	Examinateur
Stefano TINTI	Examinateur
Jean-Pierre VILOTTE	Examinateur

Remerciements

Je remercie Stefano Tinti, Professeur au Département de Physique de l'Université de Bologne, qui est à l'origine de mes premières armes dans le monde de la recherche.

La plus grande partie de cette thèse a été préparée au Laboratoire de Détection et de Géophysique (LDG), au sein du Département Analyse, Surveillance, Environnement (DASE) du CEA de Bruyères-le-Châtel. Je tiens à remercier Yves Caristan et Jean-François Sornein chefs de Département successifs et Jacques Bouchez, directeur du LDG, pour m'avoir chaleureusement accueilli.

Je suis reconnaissant à Bernard Massinon qui, tout au long de ma thèse, m'a montré son intérêt pour mon travail.

Je remercie Jean-Pierre Issartel, pour m'avoir accueilli dans le laboratoire de Simulation des Effets dans la Géosphère et mis à ma disposition des moyens techniques de haut niveau.

Je suis reconnaissant à Jean-Philippe Avouac d'avoir accepté de diriger cette thèse: tout en me laissant une grande liberté pour mener à bien ce projet, il s'est montré toujours disponibles vis à vis de mes problèmes ou de mes questions.

Je souhaite adresser des remerciements particuliers à Philippe Heinrich, pour son travail d'encadrement de tous les jours et pour la patience vis à vis des nombreux petits problèmes logistiques qui m'ont concerné.

Je remercie Emile Okal pour m'avoir fait participer à son enthousiasme de scientifique pendant le travail sur la détection des tsunamis par satellite et pour les nombreuses discussions sur le tsunami de Papouasie Nouvelle-Guinée.

Je suis également reconnaissant à Armando Cisternas d'avoir accepté d'être un de mes rapporteurs et à Jean-Pierre Vilotte d'avoir fait partie de mon jury de thèse.

Je remercie l'équipe du laboratoire de Simulation des Effets dans la Géosphère et, particulièrement, Jean-Marc Guerin et Roger Roche pour leur disponibilité.

Je souhaite faire part de ma sympathie à tous les thésards et stagiaires du LDG dont la bonne humeur a contribué à instaurer une atmosphère toujours agréable.

La plupart de mon travail de thèse a été financé par la Communauté Européenne, grâce à une bourse « Marie Curie » du programme « Training and Mobility of Research » (contrat ENV4-CT96-5044).

Je ne terminerais pas cette page sans avoir une pensée pour ma femme Barbara qui a partagé avec moi tous les moments.

Table des matières

PARTIE I

LES TSUNAMIS ET LEUR MODELISATION

Chapitre 1

Introduction

Le terme ″tsunami″, d'origine japonaise, signifie ″grande vague dans le port″ et est universellement utilisé par les scientifiques pour désigner une oscillation gravitationnelle de l'océan, souvent appelée « raz-de-marée », terme incorrect puisque ces phénomènes ne sont pas liés à l'attraction de la Terre par les astres.
Les tsunamis sont des ondes de gravité qui se propagent à la surface des océans: ils sont caractérisés par des longueurs d'onde qui peuvent varier de 10 à plusieurs centaines de kilomètres et par des périodes de 5 à 45 minutes. Les tsunamis représentent un danger pour les populations résidant le long des côtes, en particulier celles de l'océan Pacifique et dans une moindre mesure celles de l'Océan Indien, de l'Océan Atlantique et de la Méditerranée. Du point de vue du risque naturel, les tsunamis ont des caractéristiques qui les distinguent nettement des tremblements de terre: ces derniers sont des événements locaux, qui concentrent les dégâts autour de la source dans un rayon de l'ordre de la centaine de kilomètres; un tsunami a la capacité de produire des dégâts importants soit dans la région de la source, soit en champ lointain à plusieurs milliers de kilomètres de distance. En effet, une onde de tsunami peut se propager sur de très longues distances avec une faible atténuation. L'amplitude typique d'une onde de tsunami qui se propage en plein océan est de l'ordre de 5-20 cm (jusqu'à 1 m dans des cas exceptionnels): à cause de la faible amplitude et de la grande longueur d'onde, les tsunamis ne sont jamais ressentis par les marins à bord des bateaux. Mais lorsque l'onde se rapproche de la côte, en se propageant sur le plateau continental, elle diminue de longueur d'onde tout en augmentant en amplitude: cet effet (en anglais dit de *shoaling*), dont l'importance

dépend beaucoup de la bathymétrie du plateau, et auquel s'ajoutent des effets locaux, permet aux tsunamis d'atteindre des amplitudes de plusieurs mètres, voire de quelques dizaines de mètres. Ces vagues sont d'une puissance extraordinaire : en déferlant sur la côte, elles sont capables de détruire complètement des bâtiments, tandis que les courants générés par l'écoulement de l'eau, de l'ordre de 10-20 m/s, peuvent facilement transporter des blocs de béton de plusieurs tonnes, éroder les fondations des ponts et des bâtiments. Si en général l'inondation ne pénètre pas plus de quelques centaines de mètres à l'intérieur des terres, en revanche elle peut s'étaler le long de plusieurs centaines de kilomètres de côte.

1.1 Distribution géographique des tsunamis

Les côtes de l'Océan Pacifique sont les plus fréquemment touchées par les tsunamis. Au cours du dernier siècle, la carte des tsunamis observés sur les côtes du Pacifique (voir Figure 1) montre que, de la même façon que les séismes, les tsunamis sont concentrés les long des régions tectoniquement les plus actives, c'est à dire les zones de subduction. Effectivement, comme on le verra plus en détail dans la section suivante, les grands tsunamis sont générés, dans la plupart des cas, par des séismes qui produisent un déplacement vertical important du fond océanique. Il est donc naturel que les zones de subduction soient les régions les plus affectées par les tsunamis. Néanmoins, les côtes du pacifique ne sont pas toutes touchées avec la même importance et ce n'est pas par hasard que le terme « tsunami » est d'origine japonaise: les tsunamis ont souvent provoqué au Japon de véritables catastrophes, soit en terme de nombre de victimes soit par les dégâts causés aux bâtiments. Le dernier tsunami important, ayant touché le Japon date de 1993. Le séisme de magnitude 7.7, situé en mer du Japon, a généré un tsunami qui a causé la mort de 330 personnes et des dégâts matériels pour 1.5 milliards de dollars. C'est encore au Japon qu'en 1896, un tsunami particulièrement puissant a causé plus de 25000 victimes.

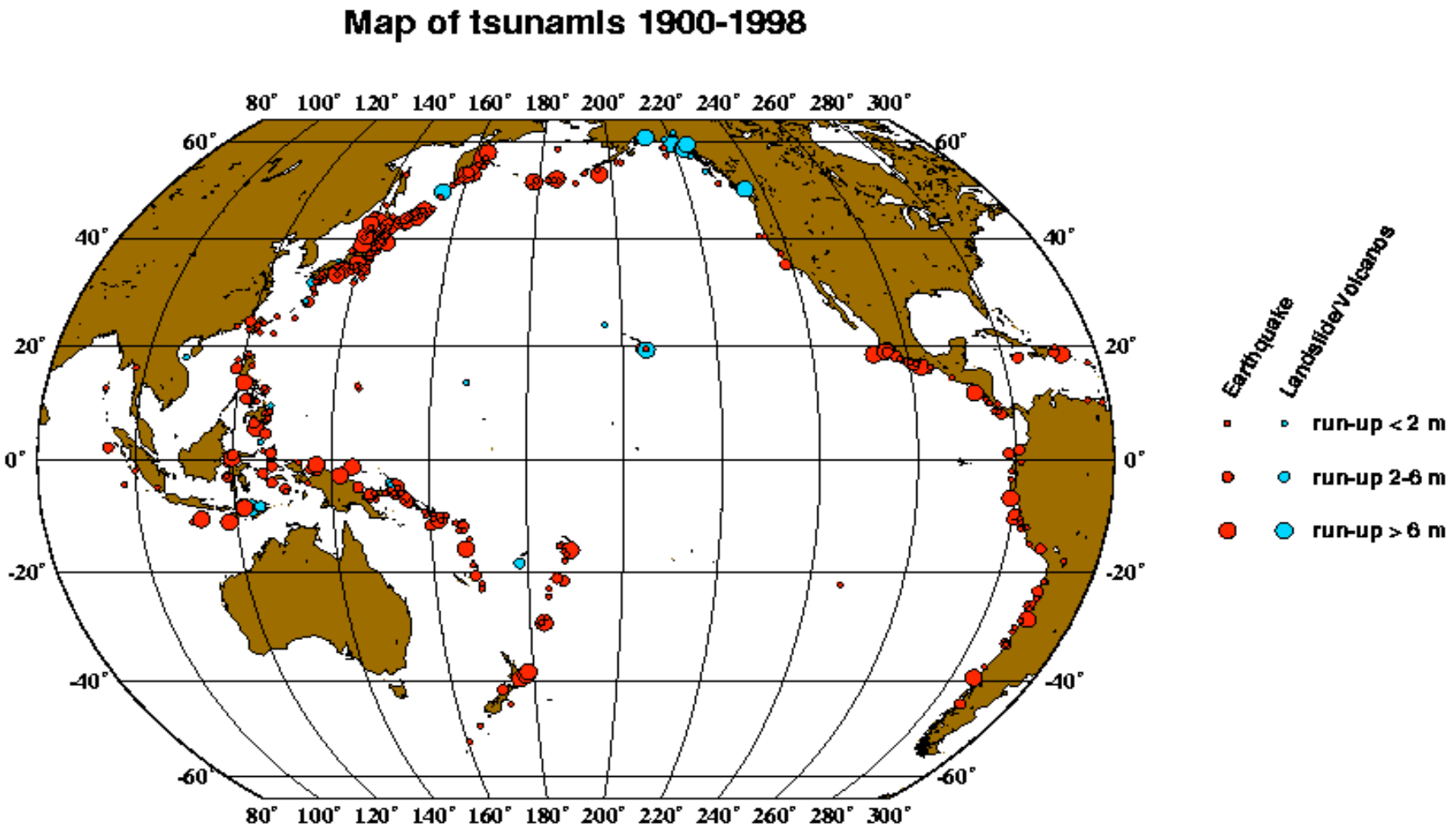

Figure 1. Distribution des tsunamis dans l'océan pacifique depuis 1900. Les symboles représentent l'épicentre de l'événement, et non pas nécessairement le lieu des dégâts les plus importants.

L'une des caractéristiques des tsunamis est celle de pouvoir causer des dégâts importants, même à des milliers de kilomètres de la source: c'est par exemple le cas des tsunamis de 1946 et 1960 qui ont causé aux îles Hawaï la mort de 173 et 61 personnes respectivement. Ces tsunamis ont été générés par des séismes dont les épicentres étaient localisés respectivement aux Iles Aléoutiennes (à 4000 km de distance) et au Chili (à 8000 km de distance).

Même s'ils ne représentent qu'un très faible pourcentage de l'ensemble des tsunamis, les tsunamis générés par les explosions volcaniques sont en général plus meurtriers. C'est le cas de l'explosion du volcan Krakatoa qui, en 1883, a généré un gigantesque tsunami, avec des vagues de plus de 30 mètres de hauteur, et ayant causé plus de 36000 victimes le long des côtes du détroit de la Sonde. Récemment, en 1997, un petit tsunami local, généré par une avalanche de débris déclenchée par une éruption volcanique à Montserrat (Petites Antilles), a alerté la communité scientifique sur les risques tout à fait réels des tsunamis d'origine volcanique (*Heinrich et al.,* 1998a; *Heinrich et al.*, 1998b; *Heinrich et al.*, 1999).

Le dernier tsunami important, qui s'est révélé être le plus meurtrier des 60 dernières années, s'est produit le 17 juillet 1998 en Papouasie Nouvelle-Guinée. Sur quelques dizaines de kilomètres de côte seulement, le tsunami a balayé et détruit entièrement plusieurs villages en causant la mort de plus de 2200 personnes. Il sera traité plus en détails dans le chapitre 7.

De façon plus occasionnelle que dans l'Océan Pacifique, les côtes européennes sont aussi touchées par les tsunamis. Pour donner seulement quelques exemples, on peut rappeler le tsunami de Lisbonne en 1755 qui provoqua la mort de quelque 5000 personnes et celui de Messine en 1908, dans le sud de l'Italie, qui causa environ 1000 victimes. Plus récemment en Grèce (1956) un tsunami local a apporté des dégâts dans l'île d'Amorgos (archipel des Cyclades). En 1969, le long des côtes du Portugal et du Maroc les marégraphes ont enregistré des oscillations de quelques dizaines de cm., dues à un tsunami généré au large du Portugal. Dans la méditerranée le risque de tsunamis d'origine volcanique est aussi important, par exemple dans l'archipel des

îles Eolienne (Italie du Sud) (*Tinti et al.,*1999b) et dans celui des Cyclades (mer Egée), où l'explosion du volcan Santorin aurait anéanti la civilisation crétoise.

1.2 Cadre tectonique des zone tsunamigéniques

Comme on l'a vu dans la section 1.1, la distribution géographique des sources tsunamigéniques est fortement corrélée à celle de la sismicité, qui marque d'ailleurs les zones tectoniquement les plus actives de la Terre, c. à d. les zones de subduction: le cadre tectonique est ici suffisamment clair et les événements assez nombreux, pour tenter une classification des séismes tsunamigéniques. Sur la base de la localisation de la source, *Satake and Tanioka* (1999) suggèrent une classification en trois types: séismes interplaques « typiques », séismes intraplaques et « tsunami earthquakes » (Fig. 2).

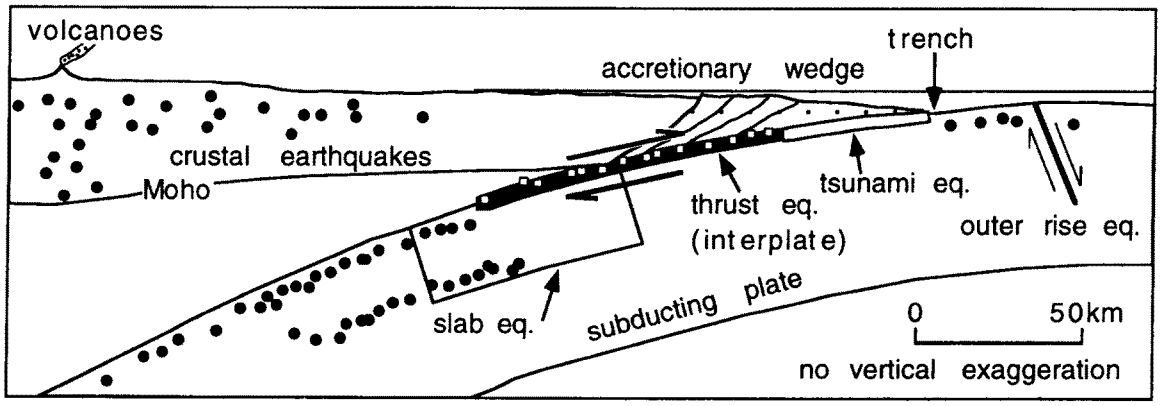

Figure 2. Classification des différents types de tsunamis qui se produisent dans les zones de subduction (d'après *Satake and Tanioka*, 1999)

Les séismes interplaques typiques sont générés à l'interface (« megathrust ») entre la plaque océanique en subduction et celle continentale située au-dessus. Parmi les séismes intraplaques, ceux localisés au dehors de l'axe du fossé, sont appelés événements « outer-rise », ceux localisés dans la plaque en subduction sont des « slab earthquakes ». Ces derniers comprennent aussi les séismes profonds, même si les séismes situés à une profondeur supérieure à ≈70 km, sont rarement tsunamigéniques

sauf, peut-être celui de Tonga en 1977 qui avait une faille se propageant verticalement de ≈60 km à 150 km (*Lundgren and Okal*, 1988). Enfin les séismes intraplaques qui cassent la plaque continentale au dessus de celle océanique en subduction peuvent être tsunamigéniques, si la source se trouve sous l'eau (bassin de arrière-arc). Selon un des modèles existants, les « tsunami earthquakes » ont une origine dans la partie la plus superficielle de la zone sismogénique interplaque, typiquement en dessous du prisme d'accrétion (Fig. 3).

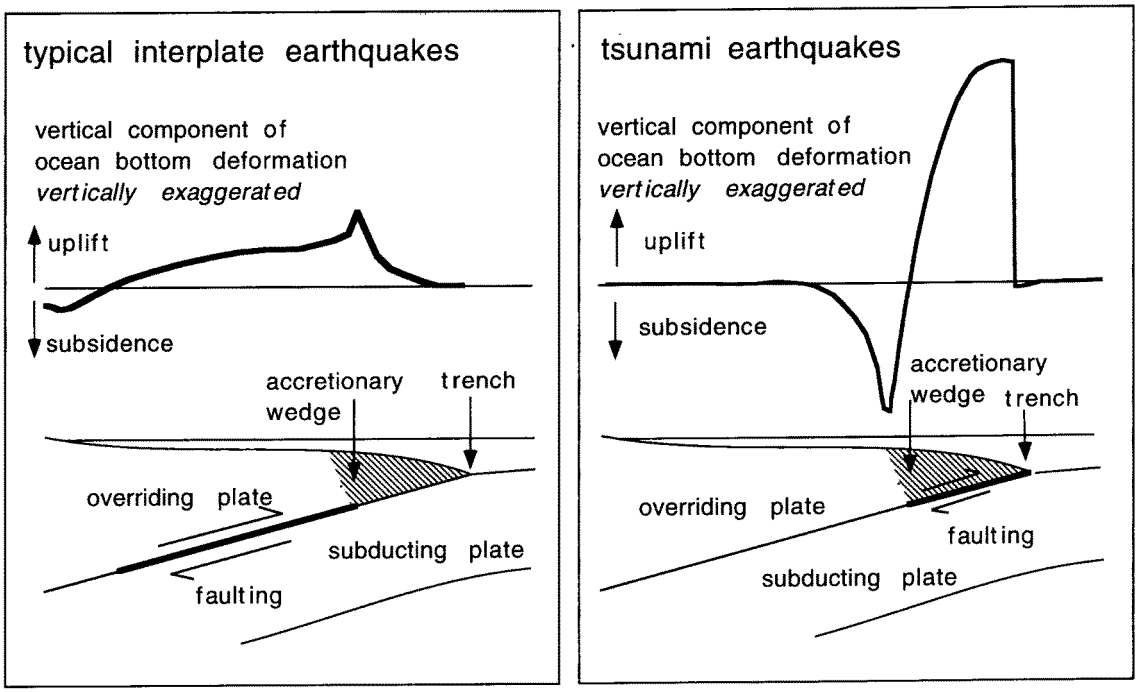

Figure 3. Représentation schématique du cadre tectonique pour un des modèles existants de « tsunami earthquakes » (d'après *Satake and Tanioka*, 1999).

Les tsunami earthquakes restent un problème ouvert en sismologie (l'un d'entre eux est traité à la section 5.1) et nécessitent une présentation plus précise des modèles existant.

1.2.1 Les « tsunami earthquakes »

Une classe d'événements tsunamigéniques particulièrement dangereux – et encore très mal compris – sont les « tsunami earthquakes », définis par *Kanamori* (1972) comme des séismes dont les tsunamis sont d'une amplitude démesurée par rapport à celle de leurs ondes sismiques. Les exemples les plus classiques en sont les séismes de Sanriku (Japon) en 1896, des Iles Aléoutiennes (1946), du Nicaragua (1992) et de Java (1994). L'étude systématique de ces événements depuis bientôt 30 ans a permis de dégager plusieurs scénarios possibles de génération des « tsunamis earthquakes ».

- Une rupture de faille lente résultant en une sous-estimation systématique de la relâche du moment sismique à très longue période lors de la mesure des ondes sismiques, de périodes nécessairement plus basses. Cet effet est bien sûr aggravé si la taille du séisme est estimée à partir d'une magnitude classique telle que M_S, mesurée à la période relativement courte de 20 secondes. Certains « tsunami earthquakes » restent cependant anormaux même en vue de leur moment sismique. C'est probablement le cas du séisme des Aléoutiennes de 1946. C'est aussi celui du tsunami catastrophique de Papouasie Nouvelle-Guinée en 1998. La lenteur de rupture de faille est en général interprétée comme mettant en cause un milieu de propriétés médiocres souvent décrit comme « sédimentaire ». Cette remarque donne lieu à son tour à deux cas de figure possibles: une rupture se propageant à l'intérieur d'une structure sédimentaire telle qu'un prisme d'accrétion. Ce scénario (Figure 3) pourrait s'appliquer au cas des séismes des Kouriles de 1963 (*Fukao*, 1979). *Okal* (1988) a notamment montré, sur la base de la théorie des modes normaux, qu'une source en double-couple (dans une géométrie de faille en rejet) dans une couche sédimentaire engendre des tsunamis d'amplitude supérieure aux Rayleigh, relativement au cas d'une structure de propriétés mécaniques classiques. Le deuxième cas de figure serait celui d'une lubrification de la faille interplaque en présence d'une couche sédimentaire entraînant au cours de la subduction. *Kikuchi and Kanamori* (1993) ont notamment proposé ce mécanisme pour le séisme du Nicaragua du 2 septembre 1992. Une rupture lente dans un milieu sédimentaire pourrait entraîner une violation des

relations de similitude sismique et en particulier la saturation de M_S mesurée à 20 s dès M_S=7.3 (au lieu de 8.2 pour des roches «dures»), ce qui, d'après *Pelayo and Wiens* (1992) pourrait contribuer au déficit des amplitudes sismiques mesurées à relativement courtes périodes.

Dans tous le cas de figures, *Newman and Okal* (1998) ont montré que des séismes lents peuvent être aisément reconnus en comparant leur moment sismique M_0 (mesuré typiquement sur les ondes de surface à 100-200 s) à l'énergie sismique (mesurée typiquement sur les ondes *P* à 1 s) (voir Fig. 4).

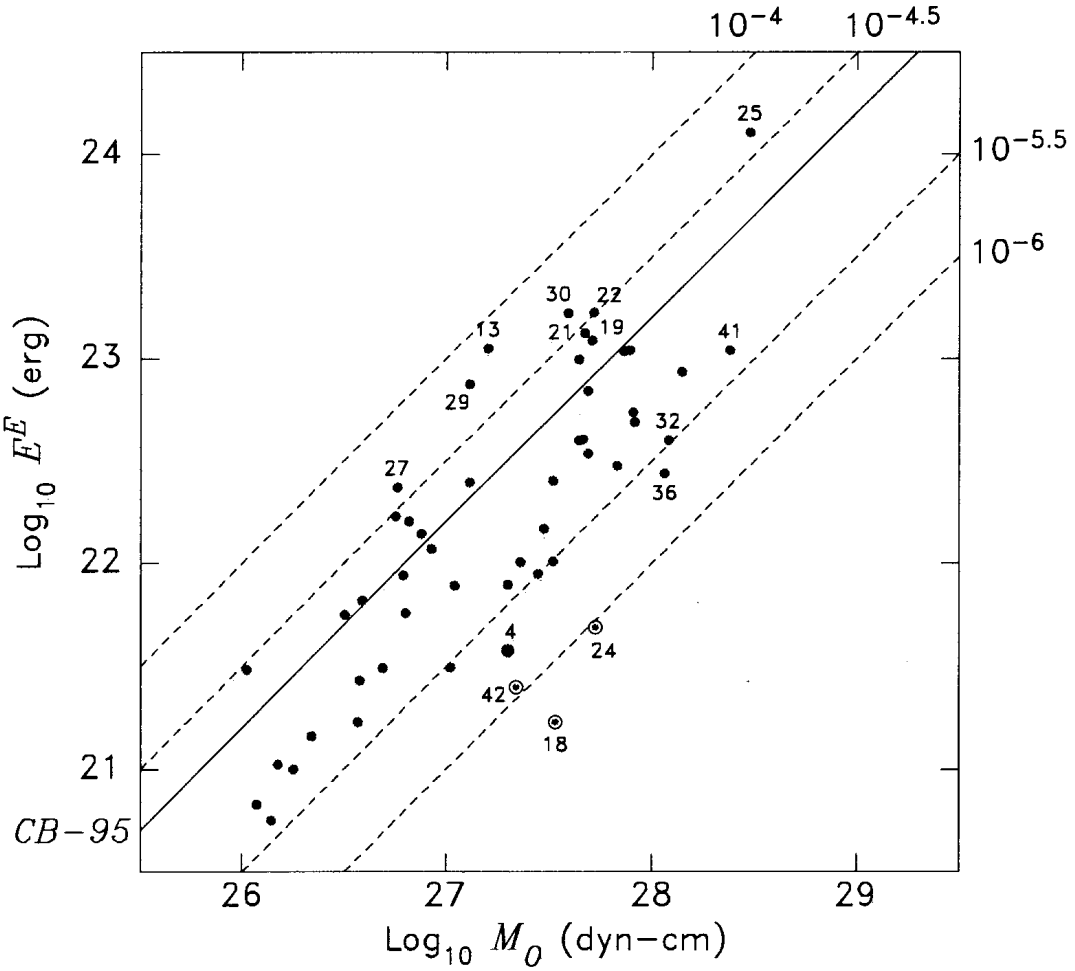

Figure 4. Energie sismique estimée E^E versus le moment sismique M_0. Le lignes diagonales correspondent à des valeurs constants du rapport E^E/M_0. Les tsunami earthquakes, représentés avec le symbole point-cercle, sont caractérisés par un rapport $E^E/M_0<10^{-5.8}$ (d'après *Newmann and Okal*, 1998).

- Une rupture mettant en cause un glissement de terrain sous-marin. Mis à part les cas d'éboulements documentés à l'échelle locale (Nice, 1979 [*Rzadkiewicz and Heinrich*, 1999]; Skagway, 1994 [*Kowalik*, 1997]) ou régionale (Grands Bancs de Terre Neuve, 1929 [*Lander and Lockridge*, 1989]), ce scénario s'applique sans doute aux séismes de Kalapana, Hawai en 1975 (*Ma et al.*, 1999) et des Iles Aléoutiennes en 1946, ainsi que, localement, aux amplitudes exceptionnelles enregistrées dans la partie nord-est de l'île de Flores lors du tsunami de Flores en 1992 (*Hidayat et al.,* 1995; *Imamura et al.*, 1995; *Tsuji et al.*, 1995). Au vu de l'absence de lenteur caractérisée dans le spectre sismique du tsunami de Papouasie Nouvelle-Guinée de 1998, le chapitre 7 sera consacré à un effort de modélisation de ce séisme.

1.3 Position du problème

Dans cette section nous parcourons, d'une façon très synthétique, les problèmes posés et les réponses données dans cette thèse.
La question fondamentale est de savoir si la modélisation et l'observation des tsunamis peuvent apporter des informations sur la source.

Cette question, très générale, soulève alors des questions plus spécifiques, auxquelles nous tenterons de répondre dans cette thèse:

1) Quelles sont les données expérimentales disponibles et leur précision ?
2) De quels outils faut-il disposer pour pouvoir exploiter ces données ?
3) Quels sont les paramètres de la source qui peuvent être contraints, et à l'aide de quelles données ?
4) Les données sont-elles suffisamment précises pour estimer les paramètres de la source ?

Le point 1) est abordé dans le deuxième chapitre. Nous présentons les principales données expérimentales qui permettent d'étudier un tsunami: les marégrammes, les données des capteurs de pression océaniques, les hauteurs de run-up et les mesures par altimétrie satellitaire du niveau de la mer.

Dans le chapitre 3 nous présentons les outils qui permettent de modéliser la génération, la propagation et l'impact d'un tsunami sur la côte. Ces outils permettent de calculer des données « simulées », qui seront comparées avec les données expérimentales.

Les outils numériques développés dans le Chap. 3 nous permettront d'aborder les points 3) et 4).

Dans le chapitre 4, l'étude des plusieurs cas réels, montre que les données de run-up et les polarités des premières vagues observées permettent de contraindre l'épicentre et l'orientation du plan de faille. Nous montrons également que des données qualitatives, telles que les dégâts causés par le tsunami, peuvent apporter des contraintes importantes sur la source

Dans le chapitre 5 nous présentons une méthode d'inversion des données de run-up, qui permet de déterminer la distribution du glissement co-sismique le long d'une faille. L'application de cette méthode au tsunami du Nicaragua 1992 montre que la distribution du glissement le long de la faille source est très hétérogène. La même méthode appliquée au tsunami de Messine (Italie du Sud) 1908 montre que la distribution des hauteurs de run-up, calculée pour une source avec un glissement hétérogène, conduit à des résultats plus proches des observations.

Le problème concernant la limite de résolution des modélisation de tsunamis est abordé dans le chapitre 6, à l'aide d'un exemple, le tsunami des Iles Kourile 1994, pour lequel de nombreux marégrammes de bonne qualité sont disponibles. Dans ce cas très particulier le problème est de discriminer deux modèles de source qui donnent des déformations en surface très proches. Les résultats numériques montrent que, compte tenue des erreurs dans les données bathymétriques, la modélisation du tsunami n'a pas une sensibilité suffisante pour apporter une réponse.

Enfin, dans le chapitre 7 nous étudions le tsunami catastrophique du 17 juillet 1998 en Papouasie Nouvelle Guinée. Pour étudier ce tsunami, très meurtrier et très local à la fois, nous disposons seulement des données de run-up, mesurées pendent une campagne d'inspection post-événement. Les outils mis en place au cour de cette thèse permettent de préciser certains caractères de la source.

Les études menées au cours de cette thèse ont fait l'objet de différentes publications dans des journaux scientifiques: ils seront proposés dans leur texte intégral, ordonnés et groupés dans des chapitres différents, en fonction des informations apportées sur la source.

Chapitre 2

Les données expérimentales

Le tsunami est composé d'une ou plusieurs ondes de gravité qui se propageant à la surface de la mer; on pourra donc le caractériser en mesurant sa longueur d'onde, son amplitude et sa période. Pour cela on dispose aujourd'hui de plusieurs outils et techniques qui nous permettent d'étudier les caractéristiques d'un tsunami pendant les différentes phases de sa propagation.

2.1 Les marégrammes

Le marégramme est la donnée la plus répandue et la plus utilisée: elle est obtenue par un capteur, habituellement placé dans un port, qui mesure les variations du niveau de la mer. La figure 5 montre un exemple de marégramme, sur lequel on voit le signal associé au tsunami, généré à la suite d'un séisme au large des Iles Kouriles en octobre 1994. A ce signal est superposé le signal longue période de la marée, dont le filtrage permet d'obtenir la véritable forme d'onde associée au tsunami, caractérisé par une période de 15-20 minutes et par une amplitude de la première oscillation de 1.2 mètres. Le principal avantage de ce type de donnée est sans doute la bonne couverture spatiale des capteurs: en effet ils sont installés un peu partout le long des côtes et, dans certaines régions particulièrement touchées par les tsunamis comme le Japon, il existe de véritables réseaux marégraphiques qui assurent une couverture exceptionnelle. Ces derniers ne sont pas cependant toujours facilement exploitables. D'abord, il y a un problème de non-homogénéité de la technologie utilisée. Les

appareils récents sont peu nombreux, ce sont des marégraphes digitaux avec un pas d'échantillonnage d'une minute ou de 30 secondes, spécifiquement conçus pour la détection des tsunamis (comme la plupart des capteurs du réseau japonais). La plupart des appareils sont des marégraphes analogiques enregistrant sur papier ou des marégraphes digitaux qui échantillonnent le signal tous les 5-10 minutes: ils ont été conçus pour enregistrer les périodes typiques des marées (de l'ordre de quelques heures) et ont une mauvaise réponse aux périodes des tsunamis (de l'ordre de la dizaine de minutes); le pas d'échantillonnage est insuffisant pour représenter correctement la forme d'onde d'un tsunami.

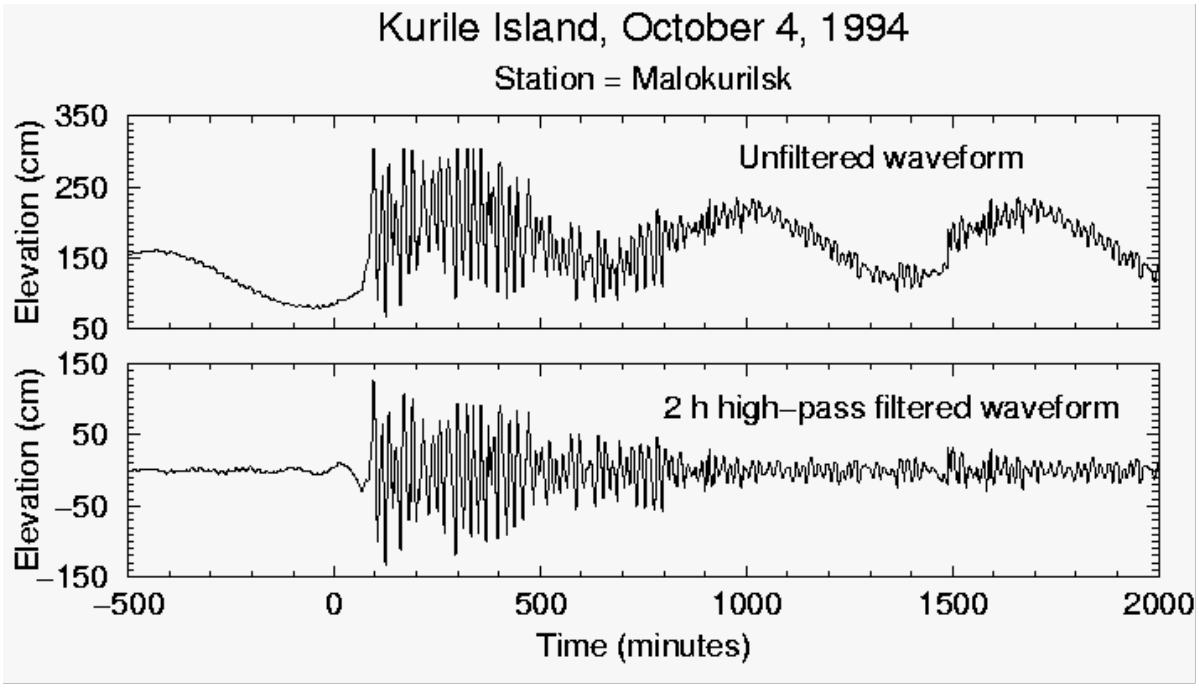

Figure 5. Marégramme enregistré à Malokurilsk (Shikotan, Iles Kouriles) lors du tsunami de Shikotan en 1994. En haut la forme d'onde originale; en bas la forme d'onde après filtrage.

Le deuxième problème est lié à l'emplacement des capteurs qui sont, dans la plupart des cas, situés dans les ports ou dans des petites baies. La bathymétrie locale autour du capteur agit alors comme une fonction de transfert finale sur le signal du tsunami, en modifiant à la fois les périodes et les amplitudes de la forme d'onde initiale. Dans

certains cas, il est difficile de séparer les effets dus à ces phénomènes locaux et leur modélisation s'avère souvent compliquée (*Rabinovich*, 1997). Un exemple est montré sur la Figure 6, qui présente le signal enregistré dans une baie japonaise à la suite d'un tsunami survenu en Papouasie Nouvelle-Guinée en juillet 1998.

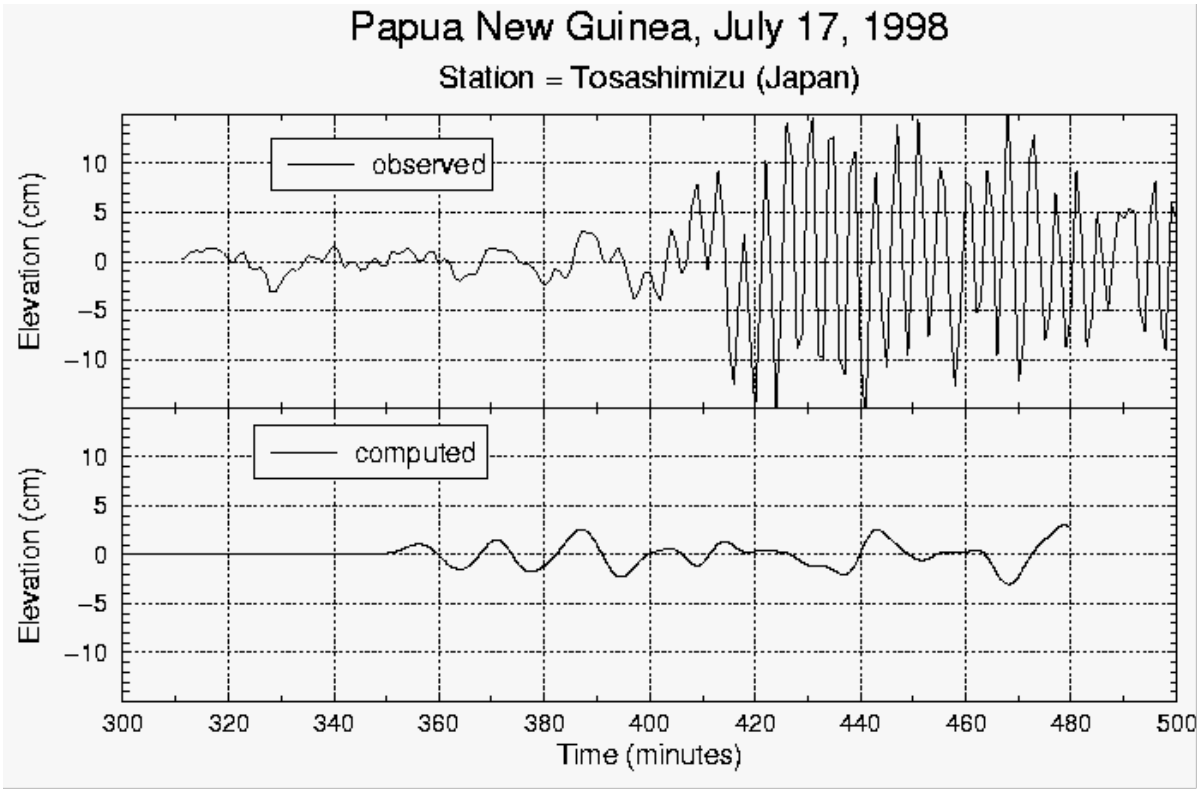

Figure 6. En haut: marégramme enregistré à Tosashimizu (Japon) lors du tsunami de Papouasie Nouvelle Guinée en 1998. Les périodes de 2-3 minutes et les amplitudes de 20 cm sont générées par des effets de résonance de la baie, à l'intérieur de laquelle le capteur est placé. En bas: marégramme synthetique, calculé en utilisant une bathymetrie trop grossière pour tenir en compte des effets de la baie.

Dans ce cas les périodes de 2-3 minutes ainsi que les amplitudes de 20 cm sont générées par les résonances de la baie à l'intérieur de laquelle le capteur est placé. Malgré l'ensemble de ces limitations, les marégrammes représentent la donnée la plus exploitée pour étudier les tsunamis.

2.2 Les capteurs de pression océaniques

Il s'agit de capteurs de pression ancrés au fond de l'océan, à des profondeurs qui peuvent varier entre 1000 et 6000 mètres. Le principe de fonctionnement est simple: une variation de l'élévation de la surface de la mer, due à l'onde de tsunami qui se propage, est enregistrée comme une variation de pression au fond de l'océan. La couche d'eau océanique agit comme un filtre, qui atténue l'amplitude du signal au fond de l'océan selon une loi ~exp(-*kh*), où *k* est le nombre d'onde et *h* la profondeur de l'océan (*Webb et al.*, 1991). Ainsi, les ondes générées par le vent, caractérisées par une longueur d'onde de la centaine de mètres et par une fréquence d'environ 10^{-1} Hz, signaux des tsunamis (10^{-3} Hz).

A la différence des formes d'onde enregistrées par les capteurs placés dans les ports ou dans les baies, celles acquises par les capteurs de pression océaniques ne sont pas perturbées par les effets locaux (reflexion sur les côtes et amplifications locales) et permettent d'avoir accès aux véritables périodes et amplitudes des tsunamis se propageant en plein océan: la Figure 7 montre un exemple de ce type d'enregistrement. Ce qui empêche l'utilisation routiniere de ce type de données est le très faible nombre de capteurs operationnels aujourd'hui, inférieur à 10 (*Gonzalez et al.*, 1991; *Gonzalez and Kulikov*, 1993). Ces capteurs fournissent de données de très haute qualité, ils ont eté par exemple utilisés avec succès pour l'inversion des paramètres de deux séismes tsunamigéniques dans le golf d'Alaska en 1987 et 1988 (*Ritsema et al.*, 1995).

Capteur de pression océanique

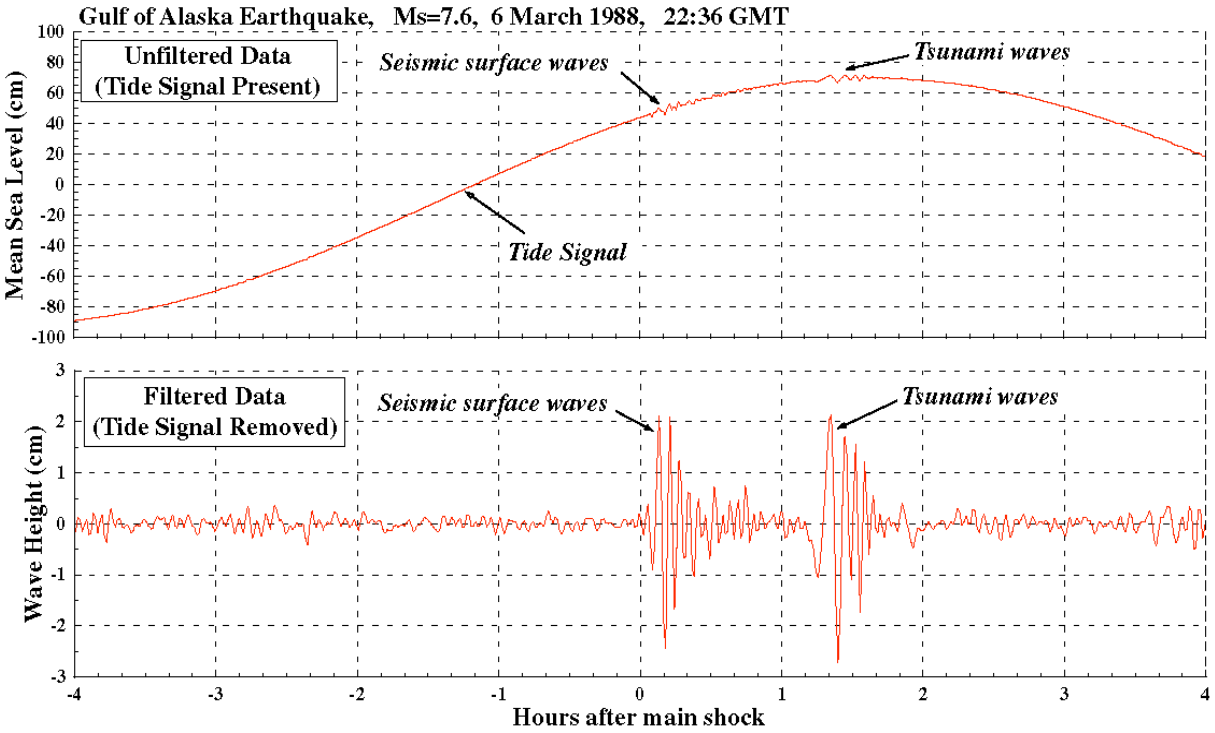

Figure 7. Exemple de forme d'onde enregistrée par un capteur de pression océanique. En haut la forme d'onde originale, dans laquelle on voit la signal de la marée, auquel se superposent les signaux des ondes de Rayleigh et du tsunami. En bas la forme d'onde filtré.

2.3 Les hauteurs de « run-ups »

La dernière phase de la propagation d'un tsunami est l'inondation de la côte. Depuis 10 ans environ, des campagnes d'inspection post-événement sont systématiquement organisées dans les jours ou semaines qui suivent les tsunamis majeurs. Pendant cette campagne on collecte plusieurs types de données, dont les mesures de « run-ups »:

ces données représentent les hauteurs maximales atteintes par les vagues le long du trait de côte touché par le tsunami; la figure 8 montre le principe de la mesure et la Figure 9 la représentation habituelle de ces données.

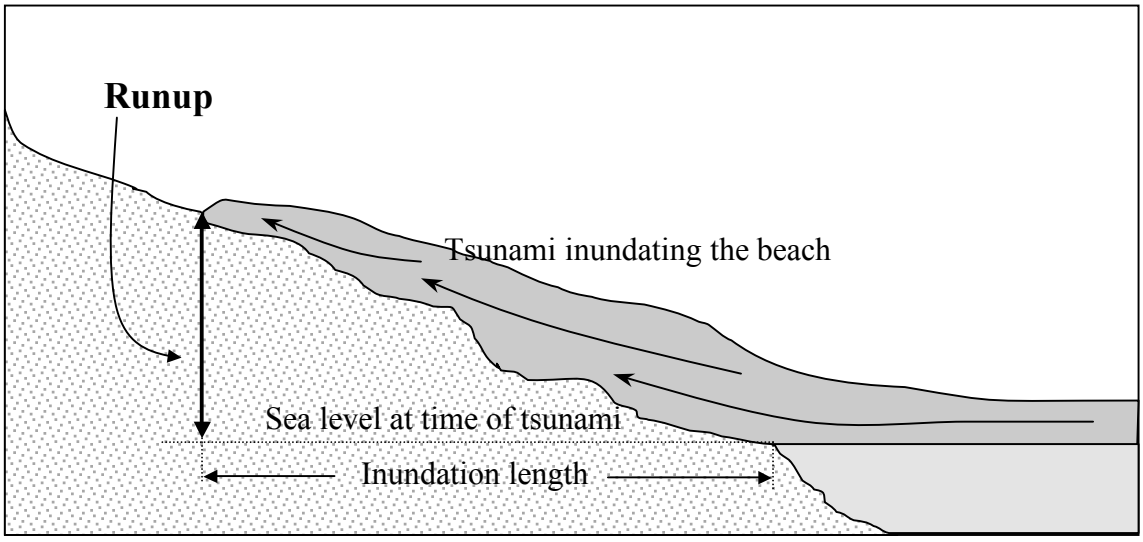

Figure 8. Représentation schématique du run-up.

La hauteur de « run-up » est une donnée de terrain qui est fortement corrélée à l'importance des dégâts provoqués par le tsunami sur le lieu de mesure: il s'agit donc d'une donnée comparable à l'intensité macrosismique, qui elle aussi dépend beaucoup des effets de site. En raison de ces effets, la modélisation des distributions des hauteurs de « run-up » est complexe et nécessite des données bathymétriques et topographiques suffisamment précises. Néanmoins, les « run-ups » sont des données fondamentales, et en absence de marégrammes sont souvent les seules disponibles pour étudier le mécanisme d'un tsunami (*Piatanesi et al., 1996*). C'est aussi la donnée la plus pertinente en terme de risque. De ce point de vue c'est la plus importante.

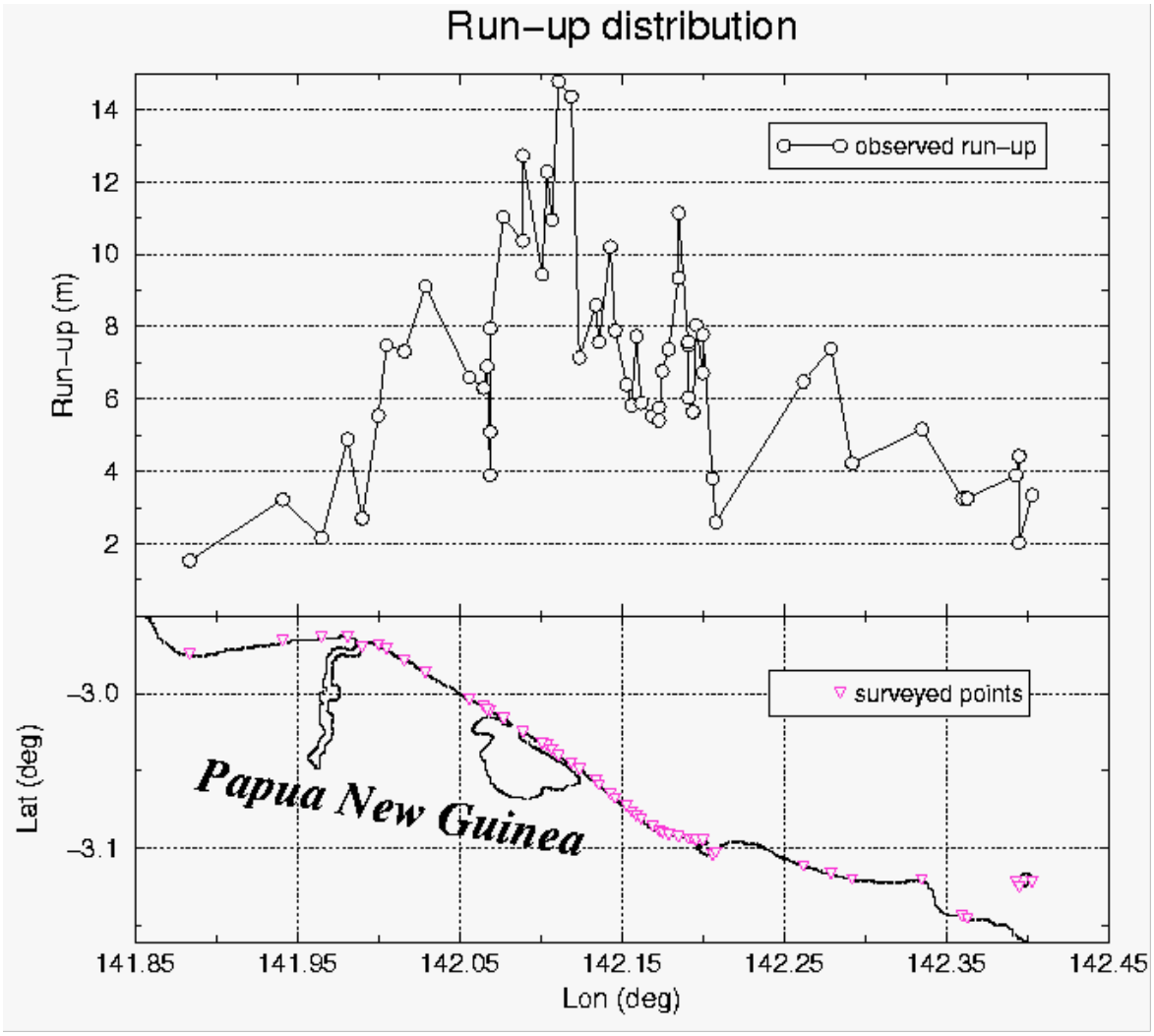

Figure 9. Distribution des hauteurs de run-up mesurées pendent la campagne d'inspection post-événement lors du tsunami de Papouasie Nouvelle Guinée 1998.

2.4 Les données altimetriques satellitaires

Dans ces dernières années, les missions TOPEX/POSEIDON, ERS-1 et ERS-2, permettent de disposer d'une nouvelle technique pour mesurer l'élévation de la surface de la mer: l'altimétrie radar satellitaire. Ces satellites, explorent la surface de la Terre le long de trajets fixés, parcourus avec une périodicité de 35 jours pour ERS-1 et de 9.916 jours pour TOPEX-POSEIDON. Ces satellites ont été conçus pour mesurer des variations du niveau de la mer caractérisées par des amplitudes de la

dizaine de centimètres, des longueurs d'onde de quelques centaines à des milliers de kilomètres et des périodes de quelques jours à plusieurs années. Les tsunamis se situant à la limite des ces bornes, il est théoriquement possible de détecter un train d'onde associé à un tsunami se propageant en plein océan. En pratique, le niveau du bruit du fond de ces mesures est très élevé et empêche la détection des tsunamis. Seules des techniques sophistiquées de discrimination ont permis de détecter le tsunami du Nicaragua 1992 et, peut etre, celui du Chili (Antofagasta) 1995 (*Okal et al.* 1999). De même que les capteurs de pression, ces données ont l'avantage de permettre l'étude des tsunamis se propageant en plein océan, à l'abri des phénomènes locaux d'amplification et de résonance.

Chapitre 3

La modélisation des tsunamis

La vie d'un tsunami est constituée de 3 phases:

- la génération d'une instabilité gravitaire à la surface de l'océan
- la propagation au large
- l'interaction des ondes avec le plateau continental et l'inondation de la côte.

Le modèle physique idéal qui prendrait en compte le phénomène dans sa globalité, avec des hypothèses raisonnables, n'a pas encore été développé. Il existe aujourd'hui principalement deux théories qui décrivent l'excitation et la propagation d'un tsunami: la théorie des ondes de gravité et celle des modes normaux. Chacune de ces théories présente des avantages et des limitations que l'on discutera dans les paragraphes suivants. La théorie des modes normaux, n'étant pas utilisée dans cette thèse, sa description est plus succinte.

3.1 Modes normaux

Du point de vue de la sismologie globale, les ondes de tsunami apparaissent d'une façon naturelle dans cette théorie, qui utilise un modèle de Terre réaliste et qui prend en compte le couplage entre les océans, couvrant 70% de la planète, et la couche solide située juste en dessous (lithosphère océanique). Comme le soulignent récemment *Dahlen and Tromp* (1998), les tsunamis représentent les véritables modes fondamentaux d'un modèle de Terre avec une couche fluide à sa surface. La théorie

des modes normaux, utilisée à l'origine par *Ward* (1980), considère les tsunamis comme des oscillations libres d'une Terre sphérique non-rotationnelle élastique et isotrope (SNREI): dans cette représentation, où les oscillations libres de la Terre sont réparties en modes sphéroïdaux et toroïdaux, on considère les tsunamis comme des modes sphéroïdaux gravitationnels. Les avantages principaux de cette approche sont 1) la possibilité d'utiliser un modèle réaliste de la structure de la Terre, qui inclut, en particulier, la description des couches sédimentaires superficielles et 2) un couplage eau-roche parfaitement intégré dans le modèle, et donc une description remarquable du mécanisme de génération. Les travaux basés sur cette approche (*Ward*, 1980, 1981, 1982; *Okal*, 1982, 1988) ont mis en évidence des relations entre les paramètres des sources sismiques et les tsunamis en champ lointain. Ces études ont montré ainsi que le paramètre majeur dans l'excitation d'un tsunami est le moment sismique M_0 du séisme. Celui-ci est directement proportionnel à l'amplitude des ondes de tsunami en champ lointain et son estimation en temps quasi-réel est à la base des systèmes modernes d'alerte « tsunamis » (*Okal and Talandier*, 1987; *Talandier et al.*, 1987, *Okal and Talandier,* 1989, 1991, *Talandier and Okal,* 1989, *Newman and Okal*, 1998; *Reymond et al.,* 1991, *Schindele et al.*, 1995).

Néanmoins l'approche des modes normaux souffre d'un défaut important, celui de ne pas tenir compte de l'épaisseur variable de la couche d'eau océanique. La vitesse de propagation des tsunamis dépendant de la profondeur de l'océan, la propagation d'un tsunami s'avère être anisotrope, avec des fronts d'onde affectés par des phénomènes de réfraction. Les effets de bathymétrie sont importants pour la propagation du tsunami au large, ils deviennent majeurs lorsque le tsunami atteint les côtes. Ici, les variations de la bathymétrie et de la topographie à l'échelle de la centaine de mètres (voire de la dizaine de mètres) peuvent engendrer des différences sur les amplitudes des ondes jusqu'à un ordre de grandeur.

Dans le chapitre 2, on vu que les données de tsunami les plus utilisées sont les marégrammes et les hauteurs de « run-up », toutes les deux étant affectées par des variations bathymétriques et topographiques de l'ordre de la centaine et de la dizaine de mètres respectivement. Une modélisation fiable de ces données, ne peut donc pas

s'appuyer sur la théorie des modes normaux, il est nécessaire de développer un autre modèle.

3.2 Ondes superficielles de gravité

Du point de vue hydrodynamique, les tsunamis sont des ondes de gravité qui se propagent à la surface de l'océan, ce dernier étant considéré comme un fluide homogène, incompressible et non visqueux.

La longueur d'onde typique des tsunamis est de plusieurs dizaines de km, tandis que la profondeur moyenne des océans est de seulement 4-5 km: l'approximation « shallow-water » ou « couche mince » des équations de Navier-Stokes est donc très bien adaptée pour décrire la propagation des ondes de tsunami.

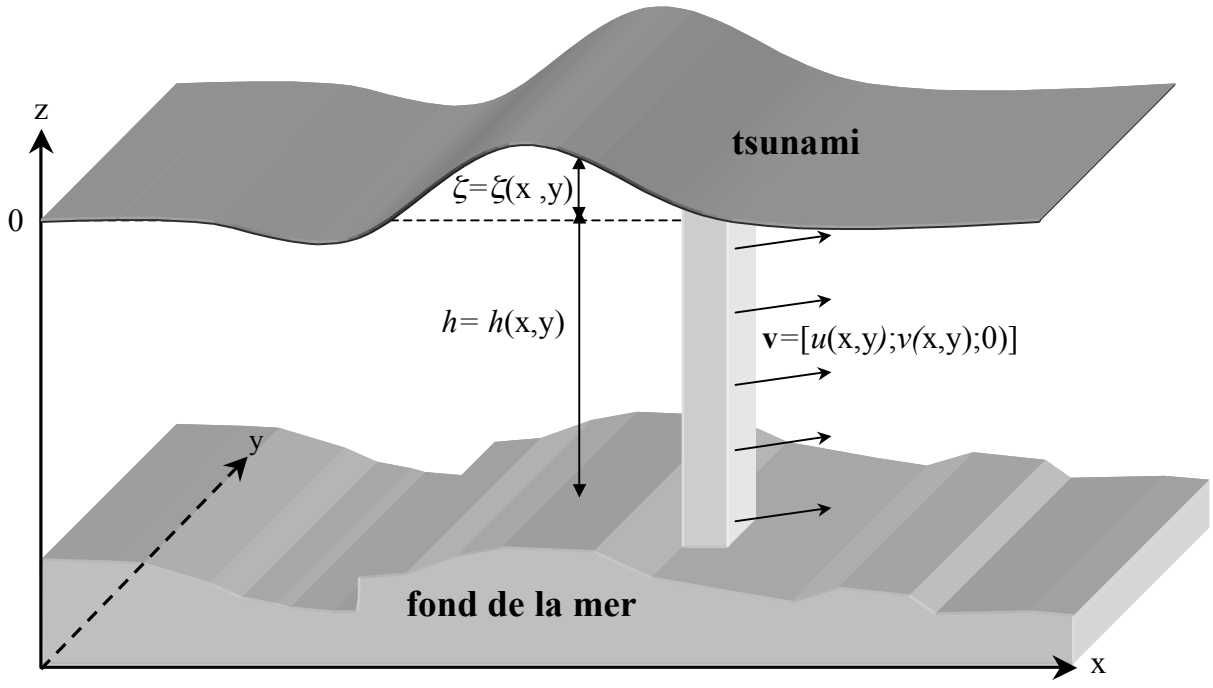

Figure 10. Schéma de la propagation d'un tsunami.

Sur la figure 10, on a schématisé la géométrie du problème de propagation. Au fond de la mer, la condition limite, habituellement imposée dans les problèmes d'hydrodynamique, qui est d'annuler la vitesse à l'interface liquide-solide, n'est pas retenue. En effet, on considère à la fois que la vitesse verticale des particules est négligeable (v_z=0) et que le vecteur vitesse horizontal est constant dans toute la colonne d'eau. La condition de « no-slip » au fond de la mer n'est donc pas verifiée; dans la réalité les effets de la viscosité de l'eau sont concentrés dans une couche d'eau très mince, d'épaisseur ε, située au dessus du fond de la mer (boundary layer), dans laquelle la vitesse horizontale des particules chute à zéro (voir Figure 11).

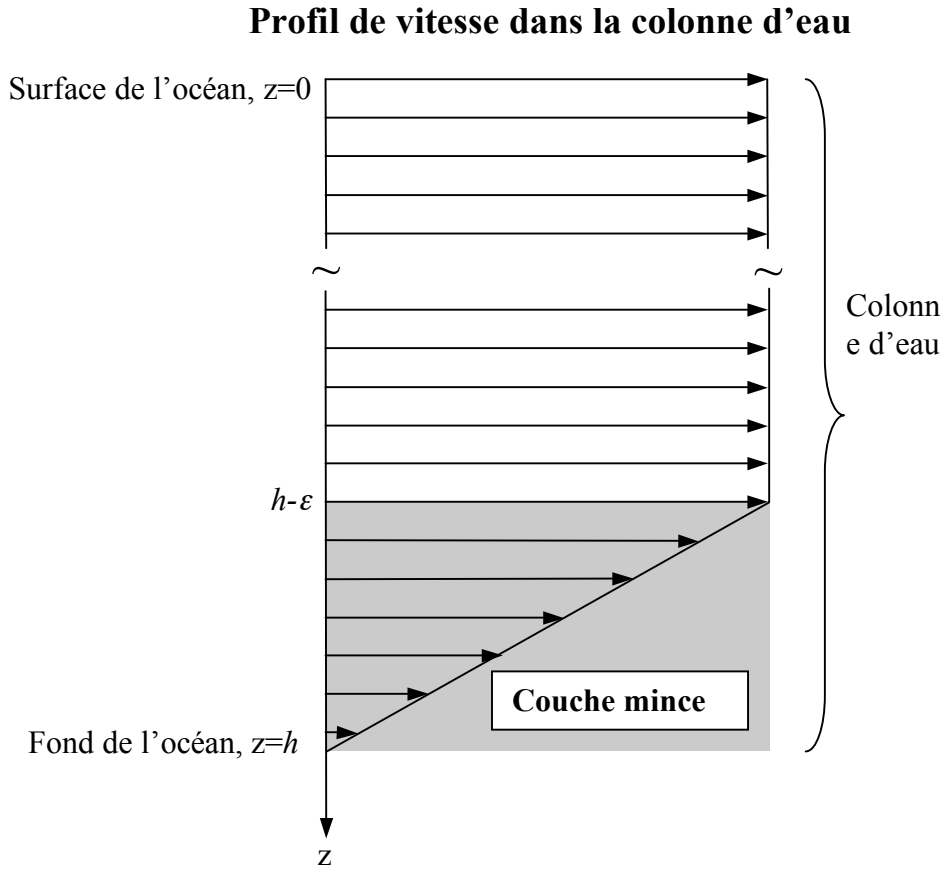

Figure 11. Schéma de la « couche mince ».

Avec ces hypothèses, le problème initialement 3D devient 2D et, mathématiquement, notre modèle peut s'écrire de la façon suivante:

$$\begin{cases} \partial_t \zeta = -\partial_x (Du) - \partial_y (Dv) \\ \partial_t u = -g\partial_x \zeta - u\partial_x u - v\partial_y u - C_f \dfrac{u(u^2+v^2)^{1/2}}{D} + fv \\ \partial_t v = -g\partial_y \zeta - u\partial_x v - v\partial_y v - C_f \dfrac{v(u^2+v^2)^{1/2}}{D} - fu \end{cases} \tag{1}$$

Dans les équations (1), en se rapportant à la Figure 10, $D=h+\zeta$, $h=h(x,y)$ représente la profondeur de l'océan, $\zeta=\zeta(x,y;t)$ est l'élévation du niveau de la mer, $u(x,y,t)$ et $v(x,y,t)$ sont les composantes, respectivement dans les directions x et y, du vecteur vitesse (horizontale), g l'accélération de la pesanteur, C_f est un coefficient de frottement et $f=2\omega\sin\phi$ est le paramètre de Coriolis, ϕ étant la latitude et ω la vitesse angulaire de rotation de la Terre. D'un point de vue physique, la première des eqs. (1) représente la conservation de la masse; la deuxième la conservation de la quantité de mouvement. Pour modéliser la propagation d'un tsunami en plein océan, on utilise souvent une version linearisée de l'équation (1), dans laquelle on considère que $h+\zeta \cong h$ (l'amplitude des ondes est négligeable par rapport à la profondeur de l'océan). De plus on néglige dans (2) le terme d'advection $\mathbf{v}\cdot\nabla\mathbf{v}$ et le terme de dissipation dûe au frottement sur le fond:

$$\begin{cases} \partial_t \zeta = -\partial_x (hu) - \partial_y (hv) \\ \partial_t u = -g\partial_x \zeta + fv \\ \partial_t v = -g\partial_y \zeta - fu \end{cases} \tag{2}$$

Les équations (2) modèlisent une propagation purement hydrostatique et sont souvent une approximation tout à fait raisonnable. Les eqs. (1) ou (2) sont à compléter par des conditions limites qui sont, généralement, d'absorption complète en plein océan

(condition ouverte) et de réflexion pure le long des côtes (condition de mur), réalisées par les équations suivantes:

$$\mathbf{v} \cdot \mathbf{n} = 2(c_1 - c_0) \qquad \text{en condition ouverte} \qquad (3)$$

$$\mathbf{v} \cdot \mathbf{n} = 0 \qquad \text{en condition de mur} \qquad (4)$$

où $\mathbf{v}=[u,v]$ est le vecteur vitesse horizontale, $c_0=(gh)^{1/2}$ est la vitesse de phase de l'onde linéaire, $c_1=[g(h+\zeta)]^{1/2}$ est la vitesse de phase locale et **n** est le vecteur unitaire normal au bord du domaine.

Généralement la condition initiale est définie par l'élévation initiale de la surface de l'eau $\zeta(x,y,t_0)= \zeta_0(x,y)$, en supposant que le champ de vitesse initial est nul, à savoir $u(x,y,t_0)=v(x,y,t_0)=0$. Ces hypothèses sont appropriées lorsque le processus de génération peut être considéré comme instantané, c'est à dire quand l'échelle de temps est beaucoup plus petite que la période du tsunami. C'est le cas des tsunamis générés par des séismes sous-marins, pour lesquels la déformation co-sismique du fond de la mer est relâchée dans un intervalle de temps <100 s, tandis que la période caractéristique d'un tsunami est de l'ordre de 1000 s. Le champ de déplacement vertical du fond de la mer est habituellement calculé sur la base d'un modèle de dislocation tel que celui développé par Okada (*Okada,* 1985). De nombreux exemples de séismes en domaine continental, documentés par des mésures géodésiques, montrent que ce type de modèle rend correctement compte des déplacements co-sismique du sol (e.g. *Meyer et al*., 1996; *Michel et al*., 1999). Ce modèle fait l'hypothèse d'un milieu élastique isotrope et homogène dans lequel une faille rectangulaire casse avec un glissement uniforme (voir Figure 12). Le champ de déplacement peut être ainsi calculé à partir de 9 paramètres géométriques qui déterminent de façon univoque la géométrie de la faille, (latitude, longitude, profondeur, longueur, largeur, angles de strike, dip, rake et slip) et de 2 paramètres

mécaniques qui définissent les propriétés élastiques du milieu (constantes de Lamé λ et μ).

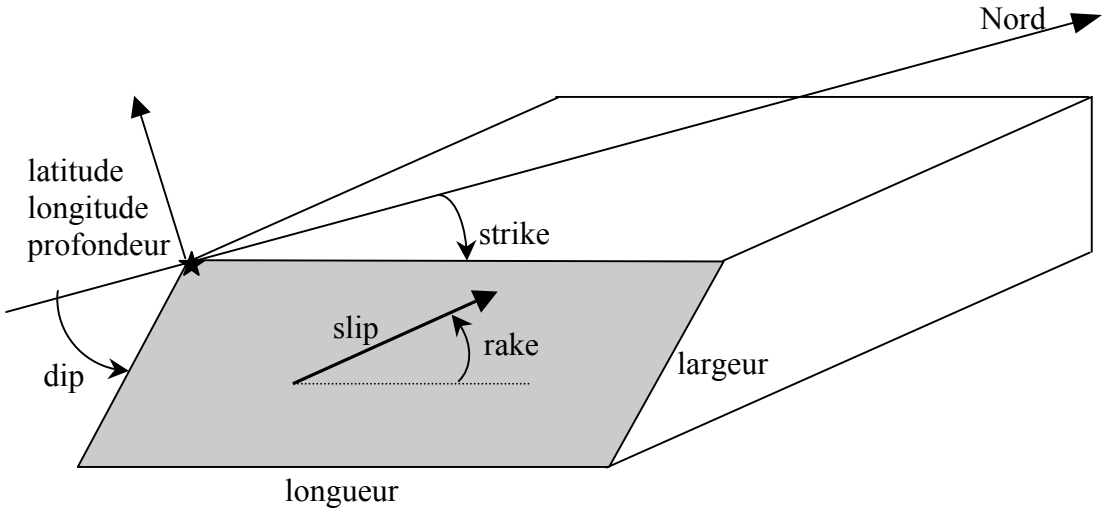

Figure 12. Définition des paramètres de faille. L'étoile représente l'origine du repère d'Okada, donné en latitude, longitude et profondeur.

Les longueurs d'ondes des tsunamis sont grandes devant la profondeur et la vitesse de rupture de la faille est supérieure à 10 fois la vitesse de propagation des tsunamis. Cela permet de supposer que la déformation du fond de la mer est transmise instantanément à la surface de l'océan et sans aucune modification. De façon plus précise, la couche d'eau océanique agit comme un filtre qui atténue fortement les hautes fréquences selon une loi proportionnelle à 1/cosh(*kh*) (*Kajura*, 1963; 1981). On peut considérer que la déformation du fond de l'océan est identique à celle de la surface lorsque le contenu en hautes fréquences est faible: cela est vrai si le bord supérieur de la faille est en dessous de la surface de la croûte terrestre, à une profondeur supérieure à 2-3 kilomètres. Dans les cas de failles très superficielles, il est nécessaire d'appliquer le filtre 1/cosh(*kh*), afin de ne pas introduire dans le problème de propagation des hautes fréquences, qui ne sont pas physiques.

Les solutions analytiques des équations (1), ou de leur version linéarisée (2), existent seulement pour des cas très simplifiés dans lesquels on considère des domaines rectangulaires ou à symétrie cylindrique, et des bathymétries linéaires ou linéaires par morceaux (e.g. *Tinti and Vannini*, 1995). Mais la réalité est toujours plus complexe: les côtes ne sont pas rectilignes et sont découpées en baies, fjords et promontoires, de même la bathymétrie de l'océan n'est pas une fonction analytique simple de la latitude ou de la longitude. Ainsi, la modèlisation d'un cas réel nécessite des méthodes numériques, parmi lesquelles les méthodes aux éléments finis et aux différences finies sont les plus utilisées. Le choix de la méthode (éléments ou différences finies) dépend du problème étudié. Dans les paragraphes suivants, on présentera le modèle aux éléments finis développé au Département de physique de l'Université de Bologne (Italie) et celui aux différences finies développé au Laboratoire de Détection et de Géophysique (CEA, Bruyères-le-Châtel), qui ont été utilisés dans cette thèse.

3.3 Méthode aux éléments finis

La méthode aux éléments finis est une approche intégrale, dont le but est de développer un équivalent discrétisé des équations d'origine. Les équations de conservation (1) ou (2), qu'on peut écrire d'une façon générale $L(f)=0$, sont multipliées par une fonction poids w_i puis intégrées sur le domaine étudié (méthode des résidus pondérés). La relation intégrale qui en suit $\int L(f)w_i ds=0$ est utilisée comme base de départ pour résoudre le problème: la méthode procède en supposant une forme analytique de la solution, contenant les constantes inconnues, qui est ensuite substituée dans l'équation intégrale. Cette procédure conduit à un système d'équations différentielles ordinaires en temps. La méthode utilisée pour la discrétisation des équations est présentée plus en détail dans ce paragraphe. Le système d'équations (1), gouvernant la propagation du tsunami, est résolu dans un

domaine fini Ω, subdivisé en un nombre M d'éléments polygonaux Ω_k disjoints, la grille obtenue étant constituée de N nœuds (voir Figure 13).

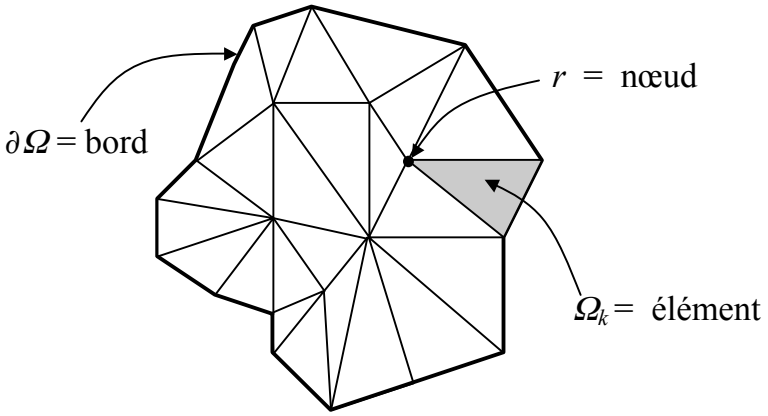

Figure 13. Exemple de grille aux éléments finis constituée d'éléments triangulaires.

L'idée fondamentale de cette approche est de supposer que pour chaque élément Ω_k toute fonction régulière $f(x,y,t)$ peut être approchée par les fonctions $f_r^k(t)$ définies au nœud r appartenant à l'élément k, à l'aide d'une superposition linéaire de fonctions géométriques $S_r^k(x,y)$ vérifiant $S_r^k(x,y)=1$ sur le nœud r de Ω_k et $S_r^k(x,y)=0$ sur les autres nœuds de cet élément:

$$f(x,y,t) \cong f^k(x,y,t) = \sum_r S_r^k(x,y) f_r^k(t) \qquad \text{dans } \Omega_k \tag{5}$$

Au noeud r, on montre aisément que $f(x,y,t)=f^k(x,y,t)=f_r^k(t)$. Les solutions $\zeta(x,y,t)$, $u(x,y,t)$ et $v(x,y,t)$ sont ainsi approchées de la même façon par l'expression (5). Les nouvelles inconnues du problème deviennent les valeurs aux nœuds des ces fonctions, à savoir $\zeta_q(t)$, $u_q(t)$ et $v_q(t)$ où q=1,…N est le numéro du nœud. Transformons maintenant les équations aux dérivées partielles (1) en équations intégrales, à l'aide du raisonnement suivant. Si ζ, u et v satisfont les équations (1), ils doivent aussi satisfaire, après multiplication par ζ^*, u^* et v^*, la forme intégrale suivante:

$$\begin{cases} \int_\Omega \zeta^* \partial_t \zeta d\Omega = & -\int_\Omega \zeta^* u \partial_x D d\Omega & -\int_\Omega \zeta^* D \partial_x u d\Omega - & -\int_\Omega \zeta^* v \partial_y D d\Omega \\ & -\int_\Omega \zeta^* D \partial_y v d\Omega & & \\ \int_\Omega u^* \partial_t u d\Omega = & -g\int_\Omega u^* \partial_x \zeta d\Omega & -\int_\Omega u^* u \partial_x u d\Omega - & -\int_\Omega u^* v \partial_y u d\Omega \\ & -\int_\Omega u^* C_f \frac{u(u^2+v^2)^{1/2}}{D} d\Omega & -\int_\Omega f u^* v d\Omega & \\ \int_\Omega v^* \partial_t v d\Omega = & -g\int_\Omega v^* \partial_y \zeta d\Omega & -\int_\Omega v^* u \partial_x v d\Omega - & -\int_\Omega v^* v \partial_y v d\Omega \\ & -\int_\Omega v^* C_f \frac{u(u^2+v^2)^{1/2}}{D} d\Omega & -\int_\Omega f v^* u d\Omega & \end{cases} \tag{6}$$

où ζ^*, u^* et v^* sont des fonctions arbitraires définies dans le domaine Ω. Considérons maintenant un ensemble de fonctions de Green indépendantes $G_i(x,y)$ i=1,…,N, telles que $G_i(x,y)$=1 sur le nœud i et $G_i(x,y)$=0 sur tous les autres nœuds. Si on pose $\zeta^* = u^* = v^* = G_i(x,y)$ dans le système intégral (6) et en utilisant l'approximation (5), on obtient 3N conditions pour les 3N inconnues $\zeta_q(t)$, $u_q(t)$ et $v_q(t)$. Par exemple, considérons le membre de gauche dans la première équation du système (6):

$$\int_\Omega \zeta^*(x,y)\partial_t \zeta(x,y,t) d\Omega \cong \sum_k \int_{\Omega_k} G_i^k(x,y)\partial_t \zeta^k(x,y,t) d\Omega_k \tag{7}$$

qui, en utilisant les fonctions de forme $S_r^k(x,y)$, devient:

$$\int_\Omega \zeta^*(x,y)\partial_t \zeta(x,y,t) d\Omega \cong \sum_k \int_{\Omega_k} \sum_{r,s} S_r^k(x,y)\delta_{ri}^k S_s^k(x,y)\dot{\zeta}_s(t) d\Omega_k \tag{8}$$

où δ_{ri}^k est la fonction delta de Kronecker et la somme double sur r et s s'étendent sur tous les nœuds appartenant à Ω_k. Ici, le symbole $\dot{\zeta}_s(t)$ est utilisé pour désigner la

dérivée temporelle de la fonction $\zeta_s(t)$. Comme les fonctions de forme sont connues, les intégrales sur chaque élément Ω_k peuvent être calculées séparément et l'équation (8) peut s'écrire de la façon suivante:

$$\int_{\Omega} \zeta^*(x,y)\partial_t \zeta(x,y,t)d\Omega \cong \sum_q K_{iq}\dot{\zeta}_q(t) \tag{9}$$

Les coefficients K_{iq} ci-dessus s'écrivent dans ce cas:

$$K_{iq} = \sum_k \int_{\Omega_k} S_i^k(x,y) S_q^k(x,y) d\Omega_k \tag{10}$$

et définissent un opérateur linéaire symétrique **K** dans l'espace R^N agissant sur le vecteur $\tilde{\zeta}(t)$ de composantes $\zeta_q(t)$. On procéde, de la même façon, pour discrétiser dans l'espace toutes les autres intégrales du système (6), qui deviendra ainsi un système d'équations différentielles où les inconnues $\tilde{\zeta}(t)$, $\tilde{u}(t)$ et $\tilde{v}(t)$ dépendent uniquement du temps *t*:

$$\begin{cases} \mathbf{K}\dot{\tilde{\zeta}} = -\mathbf{Ø}_x(\tilde{u})\tilde{\zeta} - \mathbf{Ø}_x(\tilde{D})\tilde{u} - \mathbf{Ø}_y(\tilde{v})\tilde{\zeta} - \mathbf{Ø}_y(\tilde{D})\tilde{v} - \overline{\mathbf{Ø}}_x(\tilde{h})\tilde{u} - \overline{\mathbf{Ø}}_y(\tilde{h})\tilde{v} \\ \mathbf{K}\dot{\tilde{u}} = -g\mathbf{P}_x\tilde{\zeta} - \mathbf{Ø}_x(\tilde{u})\tilde{u} - \mathbf{Ø}_y(\tilde{v})\tilde{u} - \ddot{\mathbf{O}}(\tilde{u},\tilde{v},\tilde{D})\tilde{u} \\ \mathbf{K}\dot{\tilde{v}} = -g\mathbf{P}_y\tilde{\zeta} - \mathbf{Ø}_x(\tilde{u})\tilde{v} - \mathbf{Ø}_y(\tilde{v})\tilde{v} - \ddot{\mathbf{O}}(\tilde{u},\tilde{v},\tilde{D})\tilde{v} \end{cases} \tag{11}$$

Les opérateurs sont ici désignés en gras majuscule, tandis que les vecteurs sont indiqués par un tilde. Les indices *x* et *y* sont utilisés pour indiquer que les opérateurs proviennent d'une dérivation spatiale. L'opérateur $\mathbf{Ø}_x(\tilde{u})$ n'est pas constant, et dépend du vecteur inconnu $\tilde{u}(t)$: des opérateurs similaires sont obtenus dans les 3 équations du système (11), ils sont l'expression de la non-linéarité des équations d'origine (1). Le système (11) peut également s'écrire sous une forme compacte:

$$\mathbf{A}\dot{\tilde{\alpha}}(t) = \mathbf{B}(\tilde{\alpha})\tilde{\alpha}(t) \tag{12}$$

où $\tilde{\alpha}(t)$ est un vecteur à 3N composantes défini par:

$$\tilde{\alpha} = \begin{pmatrix} \tilde{\xi} \\ \tilde{u} \\ \tilde{v} \end{pmatrix} \tag{13}$$

et **A** et **B** les opérateurs agissant dans l'espace R^N définis par:

$$\mathbf{A} = \begin{pmatrix} \mathbf{K} & 0 & 0 \\ 0 & \mathbf{K} & 0 \\ 0 & 0 & \mathbf{K} \end{pmatrix} \tag{13}$$

$$\mathbf{B} = \begin{pmatrix} -\mathbf{Ø}_x(\tilde{u}) - \mathbf{Ø}_y(\tilde{v}) & -\mathbf{Ø}_x(\tilde{D}) - \mathbf{Ø}_x(\tilde{h}) & -\mathbf{Ø}_y(\tilde{D}) - \mathbf{Ø}_y(\tilde{h}) \\ -g\mathbf{P}_x & -\mathbf{Ø}_x(\tilde{u}) - \mathbf{Ø}_y(\tilde{v}) - \mathbf{Ö}(\tilde{u},\tilde{v},\tilde{D}) & \mathbf{K}f \\ -g\mathbf{P}_y & -\mathbf{K}f & -\mathbf{Ø}_x(\tilde{u}) - \mathbf{Ø}_y(\tilde{v}) - \mathbf{Ö}(\tilde{u},\tilde{v},\tilde{D}) \end{pmatrix} \tag{14}$$

Le problème est maintenant réduit à la résolution de (12): il s'agit d'un système de 3N équations différentielles du premier ordre en temps, dont les inconnues sont les valeurs de l'élévation $\zeta_i(t)$ et les vitesses $u_i(t)$ et $v_i(t)$ sur les i nœuds, i=1,…,3N. Pour la discrétisation temporelle, on utilise un schéma d'intégration à deux demi-pas de temps, précis au deuxième ordre en temps Δt:

$$
\left.\begin{aligned}
&\tilde{\alpha}_{n+1/2} = \tilde{\alpha}_n + \frac{\Delta t}{2}\mathbf{A}^{-1}\tilde{\chi}_n \\
&\Downarrow \\
&\tilde{\alpha}^C_{n+1/2} = \mathbf{C}\tilde{\alpha}_{n+1/2}
\end{aligned}\right\} 1^{er}\ pas
$$

$$
\Downarrow
$$

$$
\tilde{\chi}_{n+1/2} = \mathbf{B}(\tilde{\alpha}^C_{n+1/2})\tilde{\alpha}^C_{n+1/2} \qquad (15)
$$

$$
\Downarrow
$$

$$
\left.\begin{aligned}
&\tilde{\alpha}_{n+1} = \tilde{\alpha}_n + \Delta t\mathbf{A}^{-1}\tilde{\chi}_{n+1/2} \\
&\Downarrow \\
&\tilde{\alpha}^C_{n+1} = \mathbf{C}\tilde{\alpha}_{n+1}
\end{aligned}\right\} 2^{eme}\ pas
$$

Dans le système (15), $\tilde{\alpha}_n$ est la solution au temps $t_0+n\Delta t$ et $\tilde{\chi}_n = \mathbf{B}(\tilde{\alpha}_n)\tilde{\alpha}_n$ représente le membre de droite de l'équation (12), calculé au même temps. Aux deuxième et dernière ligne du système (15), on impose les conditions limites (3) et (4) du problème, en appliquant au vecteur « libre » $\tilde{\alpha}_n$, qui ne satisfait pas les conditions limites, un opérateur **C**, que l'on appelle « opérateur des contraintes ». Le vecteur $\tilde{\alpha}^C_n$ qui en résulte, satisfait les conditions limites: il est identique au vecteur $\tilde{\alpha}_n$ sur tous les nœuds, sauf sur ceux sur lequels les conditions limites s'appliquent, à savoir sur les nœuds qui appartiennent au bord du domaine. Le chemin présenté dans (15) représente le principe de la discrétisation dans le temps; en réalité la version implémentée dans le code aux éléments finis utilisé est plus complexe, incluant en particulier des routines de filtrage et de lissage, qui réduisent les oscillations numériques générées par le code. Pour une description plus complète de cette méthode et des tests de validation, on peut se référer à *Tinti et al.* (1994), *Tinti and Piatanesi* (1995) et *Tinti and Gavagni* (1995).

3.4 Méthode aux différences finies

Dans la méthode aux différences finies utilisée dans cette thèse, les équations sont discrétisées sur une grille constituée de mailles de type C: l'élévation de l'eau ζ et la profondeur h sont calculées au centre des mailles et les vitesses u et v aux centres des côtés des mailles (Figure 14).

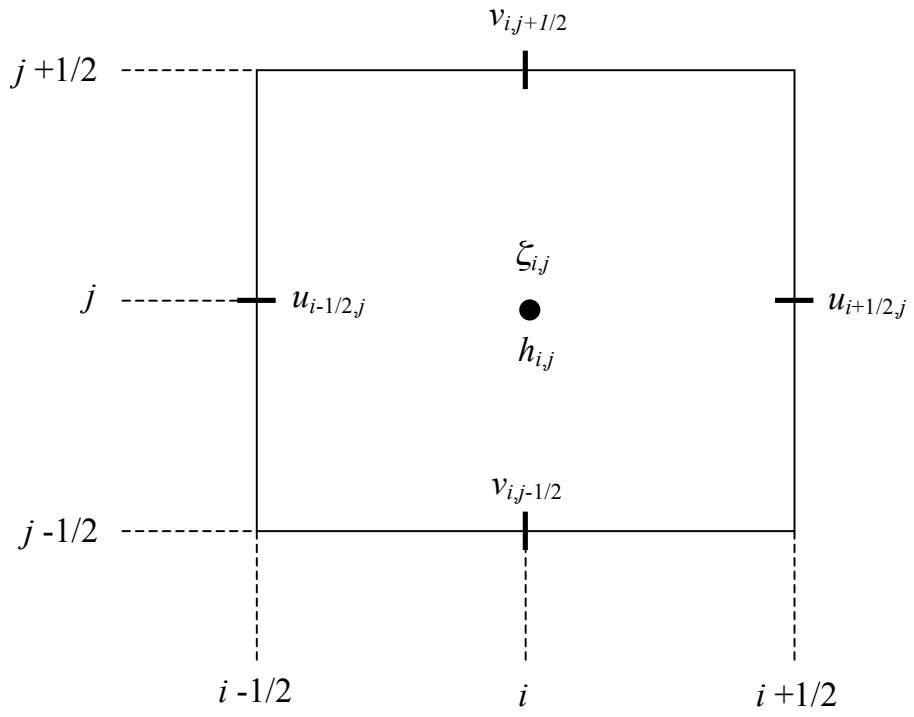

Figure 14. Maille de type C, utilisée dans la méthode aux différences finies: l'élévation de l'eau ζ et la profondeur h sont calculées au centre des mailles et les vitesses u et v aux centres des côtés des mailles.

Le schéma numérique, centré en temps et décentré en espace, est implicite de type Crank-Nicolson (voir par exemple *Peyret and Taylor*, 1983), précis au deuxième ordre dans le temps. Les équations qui suivent représentent la version discrétisée,

selon ce schéma, du système d'équations (1), dans lesquelles on a supprimé le terme dû au frottement, pour des raisons de clarté d'écriture:

$$\begin{aligned}\zeta_{i,j}^{n+1} = \quad & \zeta_{i,j}^{n} - \Delta t \cdot \vartheta_c \left\{ \frac{1}{\Delta x}\left[u_{i+\frac{1}{2},j}^{n+1} TD1 - u_{i-\frac{1}{2},j}^{n+1} TD \right] + \frac{1}{\Delta y}\left[v_{i,j+\frac{1}{2}}^{n+1} TV1 - v_{i,j-\frac{1}{2}}^{n+1} TV \right] \right\} - \\ & - \Delta t(1-\vartheta_c) \left\{ \frac{1}{\Delta x}\left[u_{i+\frac{1}{2},j}^{n} TD1N - u_{i-\frac{1}{2},j}^{n} TDN \right] + \frac{1}{\Delta y}\left[v_{i,j+\frac{1}{2}}^{n} TV1N - v_{i,j-\frac{1}{2}}^{n} TVN \right] \right\}\end{aligned} \tag{16}$$

les quantités *TD, TDN* etc. étant définies ci-dessous (eq. (17)-(20)):

$$TD = h_{i,j} + \zeta_{i,j}^{n+1} \qquad TDN = h_{i,j} + \zeta_{i,j}^{n} \qquad (u_{i-\frac{1}{2},j}^{n} < 0) \tag{17a}$$

$$TD = h_{i-1,j} + \zeta_{i-1,j}^{n+1} \qquad TDN = h_{i-1,j} + \zeta_{i-1,j}^{n} \qquad (u_{i-\frac{1}{2},j}^{n} > 0) \tag{17b}$$

$$TD1 = h_{i+1,j} + \zeta_{i+1,j}^{n+1} \qquad TD1N = h_{i+1,j} + \zeta_{i+1,j}^{n} \qquad (u_{i+\frac{1}{2},j}^{n} < 0) \tag{18a}$$

$$TD1 = h_{i,j} + \zeta_{i,j}^{n+1} \qquad TD1N = h_{i,j} + \zeta_{i,j}^{n} \qquad (u_{i+\frac{1}{2},j}^{n} > 0) \tag{18b}$$

$$TV = h_{i,j} + \zeta_{i,j}^{n+1} \qquad TVN = h_{i,j} + \zeta_{i,j}^{n} \qquad (v_{i,j-\frac{1}{2}}^{n} < 0) \tag{19a}$$

$$TV = h_{i,j-1} + \zeta_{i,j-1}^{n+1} \qquad TVN = h_{i,j-1} + \zeta_{i,j-1}^{n} \qquad (v_{i,j-\frac{1}{2}}^{n} > 0) \tag{19b}$$

$$TV1 = h_{i,j+1} + \zeta_{i,j+1}^{n+1} \qquad TV1N = h_{i,j+1} + \zeta_{i,j+1}^{n} \qquad (v_{i,j+\frac{1}{2}}^{n} < 0) \tag{20a}$$

$$TV1 = h_{i,j} + \zeta_{i,j}^{n+1} \qquad TV1N = h_{i,j} + \zeta_{i,j}^{n} \qquad (v_{i,j+\frac{1}{2}}^{n} > 0) \tag{20b}$$

$$u_{i-\frac{1}{2},j}^{n+1} = u_{i-\frac{1}{2},j}^{n} - \Delta t \cdot \vartheta_m \left[\frac{g}{\Delta x} TZU + \frac{1}{\Delta x} u_{i-\frac{1}{2},j}^{n+1} TU1 + \frac{1}{\Delta y} TV \cdot TU2 \right] - \\ - \Delta t (1 - \vartheta_m) \left[\frac{g}{\Delta x} TZUN + \frac{1}{\Delta x} u_{i-\frac{1}{2},j}^{n} TU1N + \frac{1}{\Delta y} TVN \cdot TU2N \right] + \Delta t \cdot CF_j v_{i,j-\frac{1}{2}}^{n} \tag{21}$$

$$v_{i,j-\frac{1}{2}}^{n+1} = v_{i,j-\frac{1}{2}}^{n} - \Delta t \cdot \vartheta_m \left[\frac{g}{\Delta y} TZV + \frac{1}{\Delta x} TU \cdot TV1 + \frac{1}{\Delta y} v_{i,j-\frac{1}{2}}^{n+1} TV2 \right] - \\ - \Delta t \cdot (1 - \vartheta_m) \cdot \left[\frac{g}{\Delta y} TZVN + \frac{1}{\Delta x} TUN \cdot TV1N + \frac{1}{\Delta y} v_{i,j-\frac{1}{2}}^{n} TV2N \right] - \Delta t \cdot CF_j \cdot u_{i-\frac{1}{2},j}^{n} \tag{22}$$

les quantités *TZU, TU* etc. étant définies ci-dessous (éqs. (23)-(31)):

$$TZU = \zeta_{i,j}^{n+1} + \zeta_{i-1,j}^{n+1} \qquad TZUN = \zeta_{i,j}^{n} + \zeta_{i-1,j}^{n} \tag{23}$$

$$TU1 = u_{i+\frac{1}{2},j}^{n+1} - u_{i-\frac{1}{2},j}^{n+1} \qquad TU1N = u_{i+\frac{1}{2},j}^{n} - u_{i-\frac{1}{2},j}^{n} \qquad (u_{i-\frac{1}{2},j}^{n} < 0) \tag{24a}$$

$$TU1 = u_{i-\frac{1}{2},j}^{n+1} - u_{i-\frac{3}{2},j}^{n+1} \qquad TU1N = u_{i-\frac{1}{2},j}^{n} - u_{i-\frac{3}{2},j}^{n} \qquad (u_{i-\frac{1}{2},j}^{n} > 0) \tag{24b}$$

$$TV = \frac{1}{4}\left(v_{i,j-\frac{1}{2}}^{n+1} + v_{i,j+\frac{1}{2}}^{n+1} + v_{i-1,j+\frac{1}{2}}^{n+1} + v_{i-1,j-\frac{1}{2}}^{n+1} \right) \qquad TVN = \frac{1}{4}\left(v_{i,j-\frac{1}{2}}^{n} + v_{i,j+\frac{1}{2}}^{n} + v_{i-1,j+\frac{1}{2}}^{n} + v_{i-1,j-\frac{1}{2}}^{n} \right) \tag{25}$$

$$TU2 = u_{i-\frac{1}{2},j+1}^{n+1} - u_{i-\frac{1}{2},j}^{n+1} \qquad TU2N = u_{i-\frac{1}{2},j+1}^{n} - u_{i-\frac{1}{2},j}^{n} \qquad (TVN < 0) \tag{26a}$$

$$TU2 = u_{i-\frac{1}{2},j}^{n+1} - u_{i-\frac{1}{2},j-1}^{n+1} \qquad TU2N = u_{i-\frac{1}{2},j}^{n} - u_{i-\frac{1}{2},j-1}^{n} \qquad (TVN > 0) \tag{26b}$$

$$TZV = \zeta_{i,j}^{n+1} + \zeta_{i,j-1}^{n+1} \qquad TZUN = \zeta_{i,j}^{n} + \zeta_{i,j-1}^{n} \tag{27}$$

$$TU = \frac{1}{4}\left(u^{n+1}_{i-\frac{1}{2},j} + u^{n+1}_{i+\frac{1}{2},j} + u^{n+1}_{i-\frac{1}{2},j-1} + u^{n+1}_{i+\frac{1}{2},j-1}\right) \qquad TUN = \frac{1}{4}\left(u^{n}_{i-\frac{1}{2},j} + u^{n}_{i+\frac{1}{2},j} + u^{n}_{i-\frac{1}{2},j-1} + u^{n}_{i+\frac{1}{2},j-1}\right) \tag{28}$$

$$TV1 = v^{n+1}_{i+1,j-\frac{1}{2}} - v^{n+1}_{i,j-\frac{1}{2}} \qquad TV1N = v^{n}_{i+1,j-\frac{1}{2}} - v^{n}_{i,j-\frac{1}{2}} \qquad (TU < 0) \tag{29a}$$

$$TV1 = v^{n+1}_{i,j-\frac{1}{2}} - v^{n+1}_{i-1,j-\frac{1}{2}} \qquad TV1N = v^{n}_{i,j-\frac{1}{2}} - v^{n}_{i-1,j-\frac{1}{2}} \qquad (TU > 0) \tag{29b}$$

$$TV2 = v^{n+1}_{i,j+\frac{1}{2}} - v^{n+1}_{i,j-\frac{1}{2}} \qquad TV1N = v^{n+1}_{i,j+\frac{1}{2}} - v^{n+1}_{i,j-\frac{1}{2}} \qquad (v^{n}_{i,j-\frac{1}{2}} < 0) \tag{30a}$$

$$TV2 = v^{n+1}_{i,j+\frac{1}{2}} - v^{n+1}_{i,j-\frac{3}{2}} \qquad TV1N = v^{n+1}_{i,j+\frac{1}{2}} - v^{n+1}_{i,j-\frac{3}{2}} \qquad (v^{n}_{i,j-\frac{1}{2}} > 0) \tag{30b}$$

$$CF_j = 2\omega \sin y_j \tag{31}$$

Dans chacune des équations. (16), (21) et (22) on peut distinguer deux parties: la première contient seulement des quantités calculées au temps n, et qui représentent la partie explicite; la deuxième contient des quantités se référant au temps n+1 et représentent la partie implicite. Lorsque ϑ_c=0 et ϑ_m=0, le schéma est explicite, lorsque ϑ_c=1 et ϑ_m=1 le schéma est complètement implicite. Dans les calculs présentés dans cette thèse, on utilise le schéma de Crank-Nicolson (ϑ_c=1/2 et ϑ_m=1/2), où les contributions des quantités au temps n et n+1 ont le même poids. Le système d'équations est résolu dans le modèle à l'aide d'une procédure itérative, pour un pas de temps donné. En utilisant une notation compacte, on peut schématiser la (k+1)ème itération de la façon suivante:

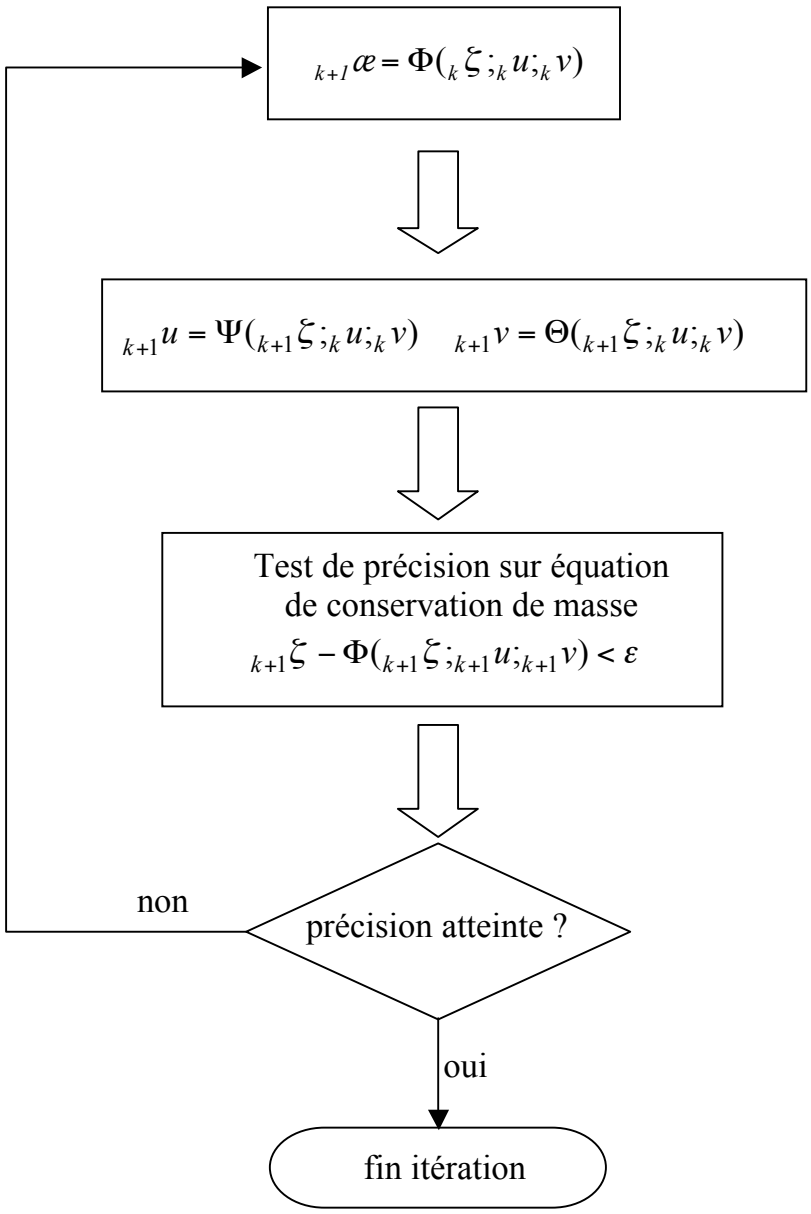

Ici, les fonctions Φ, Ψ et Θ ne sont pas détaillées; elles font intérvenir les quantités discrétisées des fonctions ζ, u et v de la façon indiquée par (16), (21) et (22). On calcule d'abord $_{k+1}\zeta$ à partir des quantités calculées dans l'itération précédente, puis on utilise la valeur courante de $_{k+1}\zeta$ pour calculer $_{k+1}u$ et $_{k+1}v$. A ce stade, on fait un test de précision sur l'équation de continuité, en prenant en compte les dernières valeurs calculées des vitesses et de l'élévation. Si l'équation est satisfaite avec une précision suffisante, on stoppe l'itération, sinon on continue à itérer jusqu'à ce que la précision souhaitée soit atteinte.

3.4.1 Calcul du run-up

Dans le code aux différences finies développé au LDG, le calcul du run-up est prévu, ce qui rend possible de simuler l'inondation de la côte touchée par le tsunami. Le problème est abordé d'une façon très similaire à celle de *Kowalik and Murty* (1993), en extrapolant dans les mailles sèches les quantités calculées dans les mailles voisines mouillées. Les directions *x* et *y* sont traitées séparément. Pour chacune d'entre elles, il y a deux configurations à considérer, numérotées I et II pour la direction *x*, sur la figure 15.

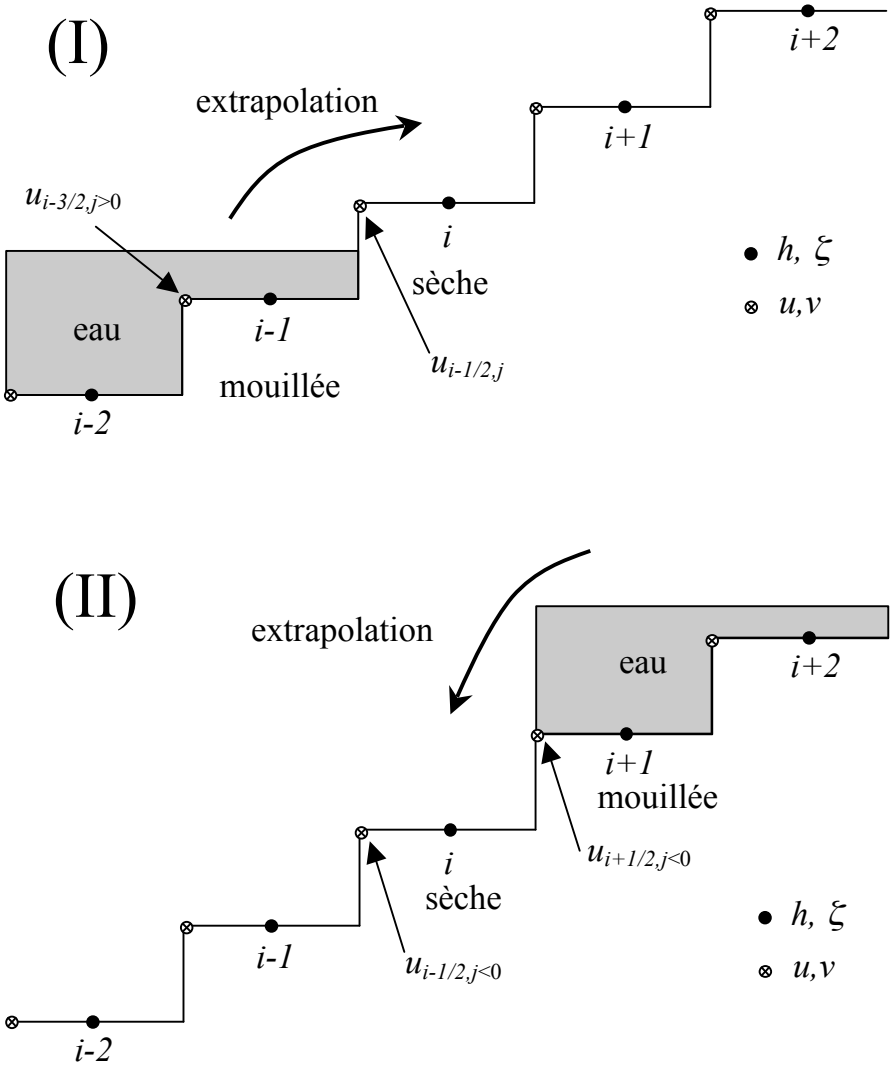

Figure 15. Schéma de la méthode utilisée dans le modèle aux différences finies pour le calcul du run-up.

Dans le cas I, une maille mouillée *i-1*, avec une vitesse $u_{i-3/2,j}>0$, est située à gauche d'une maille sèche *i*. Dans le cas II, une maille mouillée *i+1*, avec une vitesse $u_{i+1/2,j}<0$, est située à droite d'une maille sèche *i*. Seuls les cas I et II donnent lieu au calcul de run-up. Dans les cas où les vitesses ont un signe opposé, les vitesses $u_{i-1/2,j}$ (cas I) et $u_{I+1/2,j}$ (cas II) sont annulées. Dans les cas I et II, on calcule, à partir des mailles mouillées voisines, un flux extrapolé Q_{ex} qui est ensuite utilisé pour le calcul des nouvelles élévations de l'eau, dans la maille sèche comme dans la maille voisine mouillée. Les calculs se déroulent ainsi de la façon suivante:

(I)
$$Q_{ex} = 2u^{n+1}_{i-\frac{3}{2},j}\left(h_{i-1,j} + \zeta^{n+1}_{i-1,j}\right) - u^{n+1}_{i-\frac{5}{2},j}\left(h_{i-2,j} + \zeta^{n+1}_{i-2,j}\right)$$

$$\zeta^{n+1}_{i,j} = \zeta^{n}_{i,j} + \frac{\Delta t}{\Delta x} Q_{ex}$$

$$u^{n+1}_{i-\frac{1}{2},j} = u^{n+1}_{i-\frac{3}{2},j}$$

$$\zeta^{n+1}_{i-1,j} = \zeta^{n+1}_{i-1,j} - \frac{\Delta t}{\Delta x} Q_{ex}$$

(II)
$$Q_{ex} = 2u^{n+1}_{i+\frac{3}{2},j}\left(h_{i+1,j} + \zeta^{n+1}_{i+1,j}\right) - u^{n+1}_{i+\frac{5}{2},j}\left(h_{i+2,j} + \zeta^{n+1}_{i+2,j}\right)$$

$$\zeta^{n+1}_{i,j} = \zeta^{n}_{i,j} + \frac{\Delta t}{\Delta x} Q_{ex}$$

$$u^{n+1}_{i-\frac{1}{2},j} = u^{n+1}_{i+\frac{1}{2},j}$$

$$\zeta^{n+1}_{i+1,j} = \zeta^{n+1}_{i+1,j} - \frac{\Delta t}{\Delta x} Q_{ex}$$

PARTIE II

CARACTERISATION DES SOURCES SISMIQUES PAR LES DONNEES DE TSUNAMI

Considérations préliminaires

La détermination des hypocentres et des mécanismes au foyer des séismes est aujourd'hui un problème routinier en sismologie: plusieurs organismes et laboratoires de géophysique localisent le séisme et donnent les premières estimations des paramètres de la source dans un délai de l'ordre de quelques heures après l'événement. Les inversions des ondes sismiques, à l'aide de techniques plus sophistiquées, permettent en suite de raffiner les estimations et de déterminer certains détails du mécanisme: direction de la rupture, analyse des répliques, distribution du glissement et du moment relâché etc. (voir par exemple *Ihmlé and Ruegg*, 1997; *Cotton and Campillo*, 1995; *Zobin*, 1997). De plus, les données géodésiques GPS et, plus récemment, les données des altimètres satellitaires ERS1 et ERS2 permettent de mesurer, grâce aux techniques d'interférométrie radar (SAR), le champ de la déformation en surface dûe au séisme et de déterminer ainsi la géométrie et la distribution du glissement le long de la faille sismogénique (voir par exemple *Massonnet et al.*, 1993; *Meyer et al.,* 1996; *Michel et al.,* 1999). Mais ces techniques ne sont pas applicables avec la même efficacité à tous les séismes. D'une part les estimations calculées à partir des inversions des ondes sismiques dépendent beaucoup du nombre de stations qui ont enregistré le séisme, de la couverture azimutale du réseau par rapport à la source et de la qualité des enregistrements. D'autre part, les données géodésiques (GPS et SAR) fournissent des contraintes importantes sur le mécanisme à la source à condition que le séisme engendre une déformation permanente de la croûte continentale au dessus du niveau de la mer; d'où la limitation à l'application de ces techniques aux événements dont l'épicentre est localisé à terre ou à proximité de la côte. Les modèles de source issus des mèsures sismologiques fournissent généralement une bonne approximation des déformations de surface (lorsque l'ambiguïté sur les deux plans auxiliaires peut être levée).

Les données de tsunami peuvent permettre d'accéder à la déformation statique au fond de l'océan, qui représente la condition initiale du tsunami. Les données de

tsunami sont donc complémentaires et parfois essentielles pour l'étude des sources sismiques dont une partie de la déformation co-sismique est immergée, en particulier dans les zones de subduction. La sensibilité d'un tsunami à cette déformation permet d'étudier la distribution du glissement sur la faille, aspect très important pour la compréhension de la mécanique des zones des subduction et la validation de modèles tels que celui dit « à aspérités », proposé par *Lay and Kanamori* (1981).

Pour comprendre le fonctionnement d'une zone sismique et en évaluer le potentiel sismique (et aussi tsunamigénique) il faut s'appuyer sur l'étude de la sismicité récente mais aussi historique. Les événements historiques sont répertoriés sur des catalogues ou des bases de données, qui en général ne fournissent d'informations ni sur l'épicentre précis du séisme, ni sur la géométrie de la faille, alors qu'il peut s'agir de séismes majeurs. Les séismes qui se sont produits avant et jusqu'au début de la période instrumentale sont étudiés à partir de l'observation des dégâts et des effets en surface provoqués par le séisme. Les cartes d'intensité tracées à partir de ces observations, jointes aux études géomorphologiques récentes sur le terrain, ont permis d'avancer des hypothèses sur la géométrie des failles responsables de ces séismes, en compatibilité avec le contexte tectonique. Mais, pour un grand nombre de ces événements, la détermination de la faille source reste un problème ouvert. Lorsque ceux-ci ont été tsunamigéniques, les informations disponibles sur le tsunami, qu'il s'agisse de données quantitatives ou seulement d'observations qualitatives, peuvent contraindre l'épicentre et la géométrie de la faille.

Les outils numériques développés dans le Chap. 3 nous permettent maintenant d'aborder le problème qui constitue le cœur de cette thèse, qui est d'utiliser les données de tsunami pour extraire le maximum d'informations sur la source tsunamigénique. Pour répondre à cette question, on se placera dans des cas réels, pour lesquels la source (ou certains de ses paramètres) n'est pas déterminée.

Chapitre 4

Epicentre et orientation du plan de faille

Dans ce chapitre, nous montrons que les données de run-up et la polarité de la première vague peuvent permettre de contraindre la position de l'épicentre et l'orientation du plan de faille, en complément des données macrosismiques.

Dans les sections suivantes on analyse quatre séismes tsunamigéniques en Italie du Sud: le séisme de Gargano en 1627, de Sicile en 1693, de Calabre en 1783 et de Messine en 1908. Les trois premiers événements sont antérieurs à la période instrumentale et seules des données qualitatives sont disponibles. Les données dont on dispose sur les 4 tsunamis sont la polarité de la première vague observée (inondation ou retrait de la mer) en plusieurs localités le long de la côte concernée ainsi que des informations sur les dégâts engendrés par le tsunami, ce qui permet d'estimer l'intensité relative du tsunami dans une localité par rapport à une autre. L'évènement de Messine en 1908 est le dernier tsunami catastrophique survenu en Italie: pour ce dernier on dispose des hauteurs de run-up sur une vingtaine de points le long des deux côtés du détroit de Messine.

Le plan de travail, commun à ces quatre cas, est simple: sur la base des hypothèses déjà avancées dans la littérature, on considère un certain nombre de failles sources et pour chacune d'entre elles on modélise le tsunami théorique correspondant. La comparaison des effets calculés avec les observations permet de connaître la ou les failles les plus probables comme l'origine du tsunami.

4.1 Numerical simulation of the 1627 Gargano tsunami (Southern Italy) to locate the earthquake

NUMERICAL SIMULATIONS OF THE 1627 GARGANO TSUNAMI (SOUTHERN ITALY) TO LOCATE THE EARTHQUAKE SOURCE

S. TINTI AND A. PIATANESI
Dipartimento di Fisica, Settore di Geofisica, Universita di Bologna, Italy
and
A. MARAMAI
Istituto Nazionale di Geofisica, Roma, Italy

Abstract

The historical tsunami that occurred on July 30, 1627 in Gargano (Apulia, Southern Italy) was generated by a very large earthquake (I=XI MCS scale) that produced severe damage in the whole promontory. In spite of the large number of macroseismic observations, it is not possible to determine the epicenter and the generative fault position unambiguously. Though the historical sources concerning the tsunami are not extremely detailed, yet they allow us to locate and to evaluate the most important wave effects on the coasts. A prior tsunami study, conducted by performing numerical simulations based on integrating shallow-water equations via a finite-element technique, assumed a genetic dip-slip focal mechanism on faults that were temptingly placed in different positions both on land and offshore (Tinti and Piatanesi, 1996). The present work, which represents a natural continuation of that investigation, aims mostly at constraining the location of the tsunamigenic fault on physical grounds; this is accomplished by means of tsunami simulations on a new finer finite-element grid and by using the earthquake sources described in the previous paper as well as new inland faults striking N-S. It is shown that mesh refinement leads to better solutions, especially as far as the computation of the maximum elevation along the coast is concerned. Determining the position of the causative fault was one of the main motivations of this research. It has been found that compatibility with the available tsunami data requires that the fault be located inland in the coastal area embracing the Lesina Lake and the mouth of the Fortore River: the strike, however, is not too well constrained, though E-W striking seems preferable to N-S.

115

G. Hebenstreit (ed.), Perspectives on Tsunami Hazard Reduction, 115–131.

1. Introduction

The promontory of Gargano in the southern Adriatic Sea represents one of the most interesting Italian coastal zones subjected to tsunami hazard. Figure 1a gives the geographical map of Italy; with a box embracing the region of Gargano; details of that region are in turn sketched in Figure 1b. Because of the incompleteness of the earthquake and tsunami catalogues, no reports on tsunamis in this area are available prior to 1600 AD. The Gargano events have been recently revised in order to establish their reliability and to attain the phenomenological reconstruction of the tsunamis (Guidoboni and Tinti, 1987 and 1988; Tinti et. al., 1995). This work fits the general purpose of assessing tsunami hazard along the Italian coasts and represents a continuation of a previous study, where the first quantitative description of the 1627 tsunami from a numerical modeling viewpoint was performed (Tinti and Piatanesi, 1996).

The earthquake took place on 30 July 1627 about mid-day and was followed by four large aftershocks. It claimed more than 5,000 victims and destroyed completely numerous villages in the northern Gargano area, with the most severe damage located between S. Severo and Lesina. The earthquake excited a tsunami with the most impressive effects in proximity of the Lesina Lake where the most reliable contemporary chronicles report about an initial sea water withdrawal of about 2 miles and a subsequent penetration inland. Smaller effects were reported also in Termoli and Peschici. Figure 1b shows a geographic sketch of the region involved by the earthquake with an isoseismal map from which we can observe that only the isoseismal line corresponding to Intensity XI is closed, the others being open and suggestive of a continuation in the open sea.

2. Numerical Model

To compute a near-field, numerical simulation of the tsunami we adopted the nonlinear shallow-water approximation of the Navier-Stokes equations. That is adequate when the typical wavelength is much greater than the sea depth. Denoting by ζ, u, and v respectively the water elevation above the mean sea level and the horizontal components of the fluid velocity, the system of equations governing the wave motion can be written in this way:

$$\begin{cases} \partial_t \zeta = -\partial_x (Du) - \partial_y (Dv) \\ \partial_t u = -g\partial_x \zeta - u\partial_x u - v\partial_y u \\ \partial_t v = -g\partial_y \zeta - u\partial_x v - v\partial_y v \end{cases} \quad (1)$$

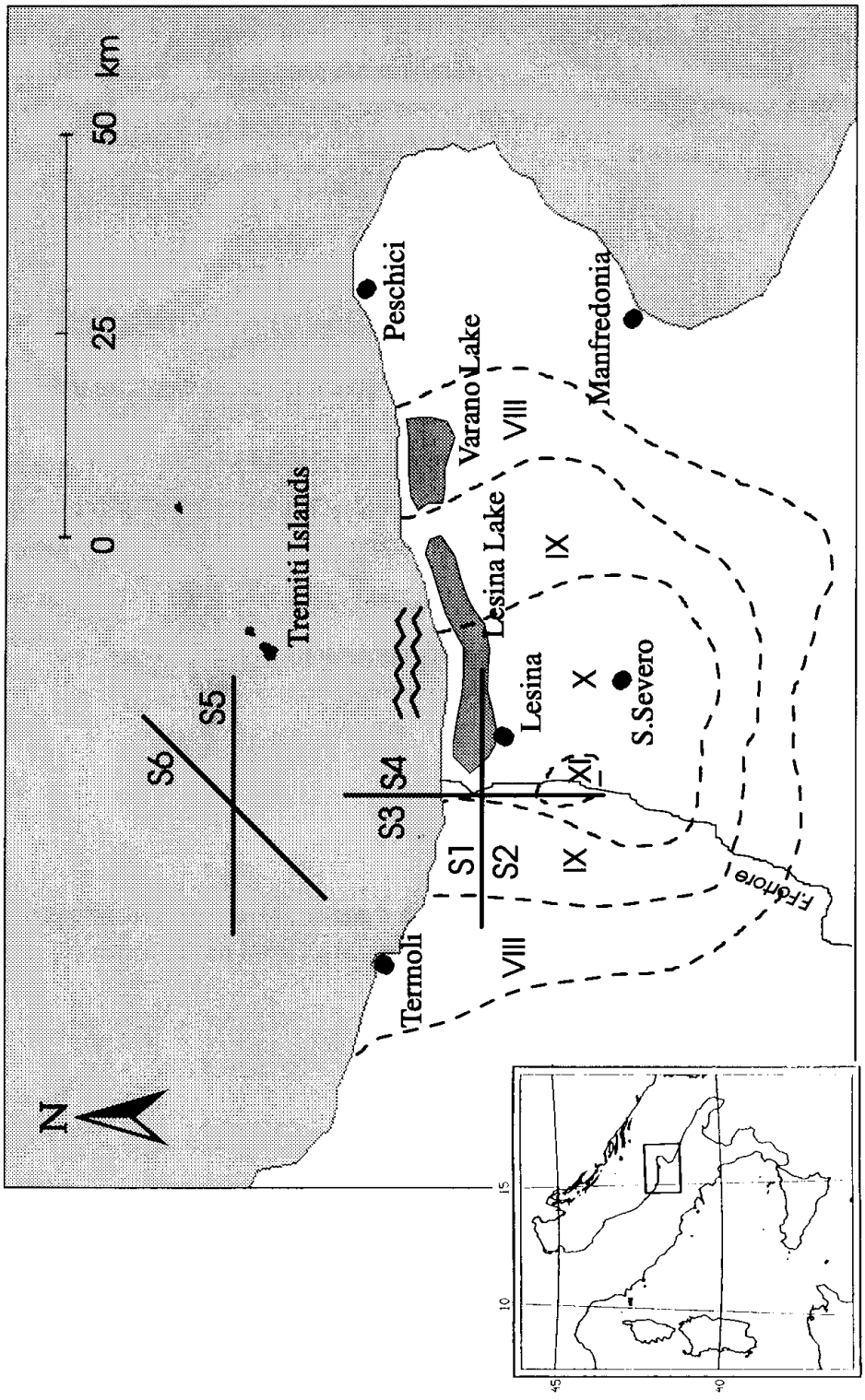

Figure 1. Geographic sketch of the region involved in the 1627 earthquake. Segments represent the fault positions taken into account for simulations. Faults are distinguished by codes S1-S6. Dashed lines are isoseismals after Guidoboni and Tinti (1987). Inset shows map of Italy.

In the above equations, h is the basin depth, g is the gravity acceleration, and D (= h + ζ) is the instantaneous water depth. System (1) is completed by suitable boundary conditions, namely complete wave transmission across the open-sea boundary elements and pure reflection along the coasts:

$$\vec{v} \bullet \vec{n} = 2(c_1 - c_0) \text{ on the open boundary} \quad (2a)$$

$$\vec{v} \bullet \vec{n} = 0 \text{ on the solid boundary} \quad (2b)$$

Here $\vec{v}$ is the horizontal velocity vector, $\vec{n}$ is a unit vector normal to the boundary and outwardly oriented, $c_1 = \left(g\{h+\zeta\}\right)^{\frac{1}{2}}$ represents the local phase velocity and $c_0 = (gh)^{\frac{1}{2}}$ is the phase velocity of the linear wave. The system (1) together with the conditions (2a) and 2b) has been solved numerically by means of a finite-element method making use of a grid consisting of M triangular elements and N nodes. If we denote by $\tilde{\zeta}$, $\tilde{u}$, and $\tilde{v}$ the N-component vectors representing the unknown fields ζ, u and v on the grid nodes, then $\tilde{\xi}$, a 3N-component vector, is defined as:

$$\tilde{\xi} = \begin{pmatrix} \tilde{\zeta} \\ \tilde{u} \\ \tilde{v} \end{pmatrix} \quad (3)$$

and, making use of the Galerkin procedure, the system (1) is reduced to a set of 3N ordinary differential equations in time (see Tinti, et. al., 1994) of the form:

$$A\dot{\tilde{\xi}}(t) = B\left(\tilde{\xi}\right)\tilde{\xi}(t) \quad (4)$$

In this equation A is a matrix that is formed by three N by N diagonal blocks K and is constant in time:

$$A = \begin{pmatrix} K & 0 & 0 \\ 0 & K & 0 \\ 0 & 0 & K \end{pmatrix} \quad (5)$$

while the matrix B depends on the unknown vector $\tilde{\xi}$ itself, because of the nonlinearity of the fundamental system (1). The time integration of the system (4) has been performed by means of an iterative algorithm that computes the solution at regular time steps Δt; the algorithm is accurate up to the second order in Δt. The integration scheme is represented by the following equations:

$$\begin{cases} \tilde{X}_{n+\frac{1}{2}} = \tilde{\xi}_n + \frac{1}{2}\Delta t A^{-1} B\left(\tilde{\xi}_n\right)\tilde{\xi}_n \\ \tilde{\xi}_{n+\frac{1}{2}} = C_{\tilde{X}_{n+\frac{1}{2}}} \\ \tilde{X}_{n+1} = \tilde{\xi}_n + \Delta t A^{-1} B\left(\tilde{\xi}_{n+\frac{1}{2}}\right)\tilde{\xi}_{n+\frac{1}{2}} \\ \tilde{\xi}_{n+1} = C_{\tilde{X}_{n+1}} \end{cases} \tag{6}$$

Here $\tilde{\xi}_n = \tilde{\xi}\left(t_0 + n\Delta t\right)$ is the value of the vector after n loops. The boundary conditions are introduced in the second step of the loop by means of the constraint matrix C which has the property of transforming the auxiliary vector $\tilde{X}_n$ in a vector $\tilde{\xi}_n$ satisfying the boundary conditions. The time integration step Δt plays an important role in the accuracy of the solution; the larger the time step, the larger the errors and the instabilities. On the other hand, the smaller the time step, the larger the computation time. Let c_e be the local propagation velocity of the wave and l_e the typical length of a given element of the grid. Then let $\Delta t_e = l_e/c_e$ be the time taken by the wave to cross the element and let ΔT denote the smallest Δt_e. It was found that in order to avoid unstable solutions a time step about 25% of ΔT is recommended (see Tinti, et. al., 1994). Accordingly, if we perform a mesh refinement to attain a finer resolution, the computation time increases 1) because of the larger number of nodes on which the unknown fields have to be computed, and 2) because of the smaller integration time step required by the stability condition. In our numerical simulations we have used the integration scheme (Equation 6), but in a version that is slightly modified in order to mitigate the numerical short-wavelength noise. In this version we incorporate an appropriate and efficient algorithm of smoothing (see Tinti and Gavagni, 1995 for a detailed description).

3. Numerical Simulations

The basin involved by the near-source tsunami propagation is very shallow, with a maximum depth of 150 meters (see Figure 2) and includes the Tremiti Islands about 25 km away from the coast. To cover the basin a mesh was used with triangular-shaped elements so that even very irregular boundaries could be easily fitted. In fact, even with the coarse grid, consisting of only 1248 elements and 678 nodes, that was used for the preliminary simulations (see Figure 3a, and Tinti and Piatanesi, 1996), it was possible to include the small-scale Tremiti Islands in the model and to delineate the main effects they induced on the propagating tsunami fronts. In this work we made use of a refined mesh (Figure 3b) consisting of 7002 elements and 3646 nodes. All the results and figures shown in this paper refer to this refined grid. In order to show the improvement of this higher resolution model over the coarser one, an illustrative comparison test will be discussed in the next section.

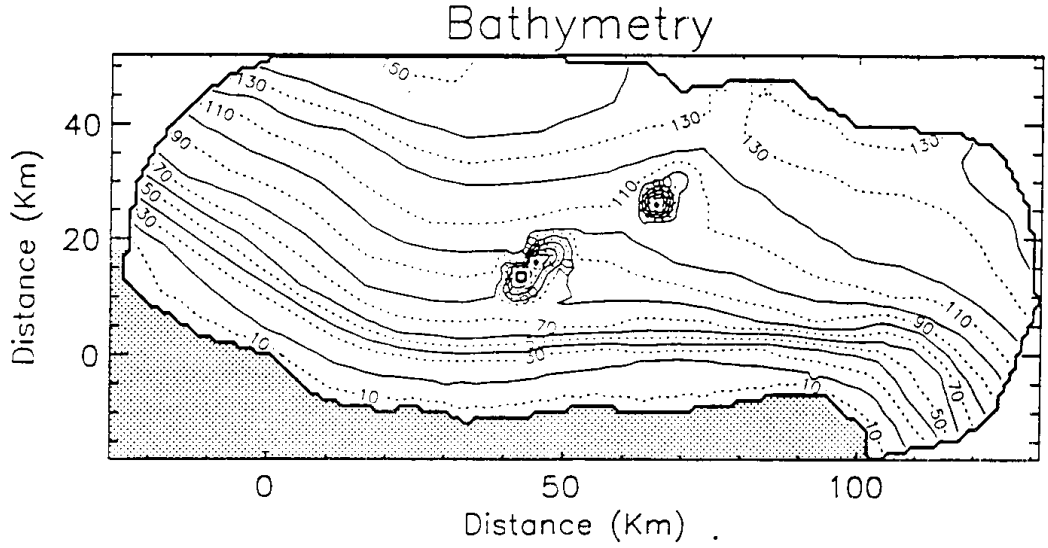

Figure 2. The bathymetry of the basin chosen for the simulations. The shaded area represents the northern promontory of Gargano.

We have assumed here the same kind of faults and of fault positions (two inland and two offshore) as in our previous work (Tinti and Piatanesi, 1996), as well as two additional sources, both with a N-S strike, that are located predominantly inland and approximately along the Fortore River (see Figure 1b). In all experiments the hypothesized earthquake focal mechanism was dip-slip and shallow, with 1.3 m uniform slip over a fault surface 35 km long and 20 km wide, corresponding approximately to a 6.9 earthquake magnitude. Sources are distinguished by the code Si (i=1,2,...,6) both in the main text and in the figures.

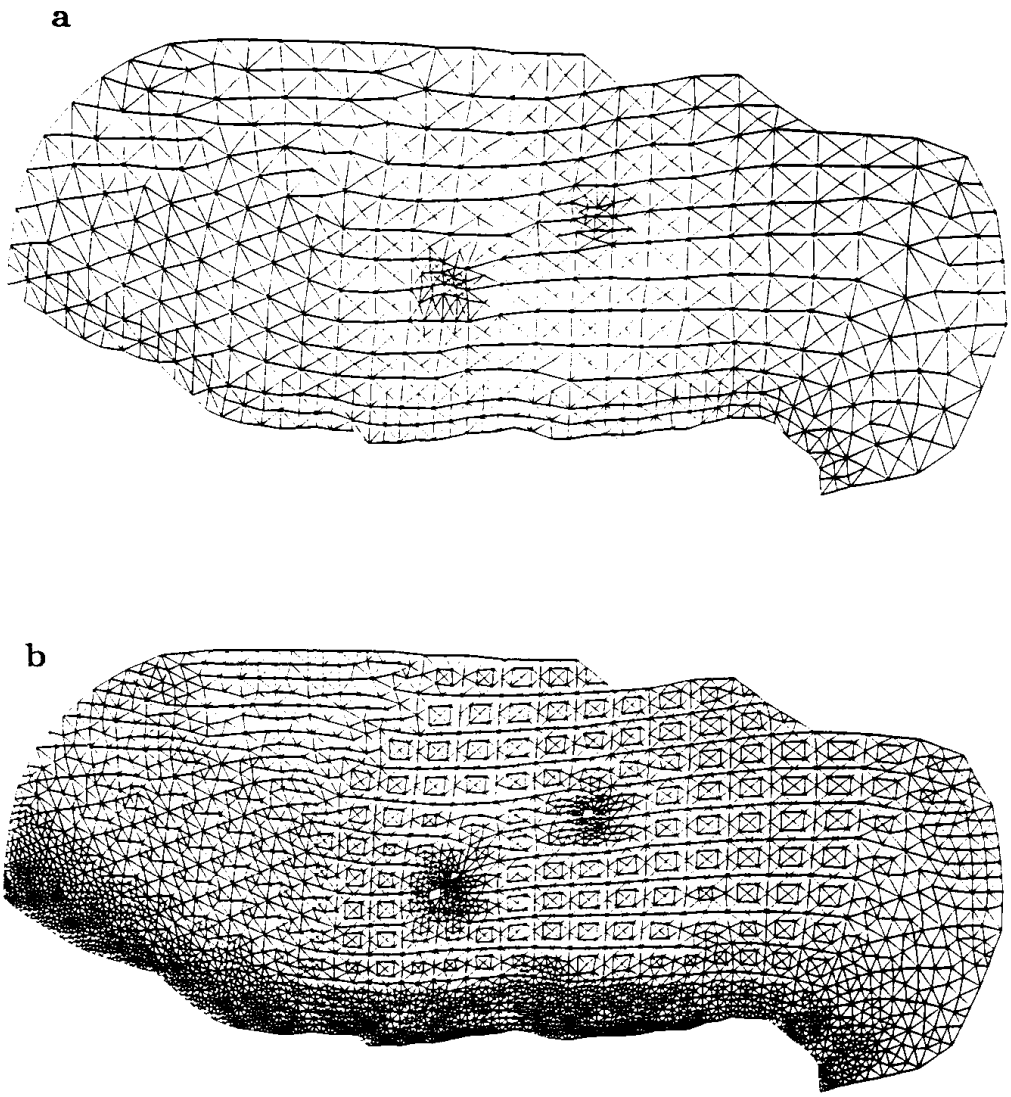

Figure 3. Grids used for the finite-element numerical computation: a) coarse grid used for the preliminary simulations; b) refined grid.

Figure 4 gives the initial water elevation and a further sequence of 9 computed elevation fields, every 600 seconds (i.e., until 5400 s), for the case of the E-W inland source with sea bottom uplift, that is the source S1. The Tremiti Islands represented a small-scale obstacle for the propagating waves, which were not visibly distorted. About one hour after the earthquake the main positive wave had already left the basin, while edge waves were seen to propagate slowly along the coast.

The second inland-fault case used the same fault but with uplift and subsidence interchanged (we call this source S2), producing an initial excitation field that was

identical to the previous case but with changed sign. The mareograms we computed for these two cases by means of the nonlinear system (Equation 1) showed no differences apart from the sign. Since producing inverted outputs in correspondence with inverted excitation inputs is a specific feature of linear systems, our results indirectly demonstrate that nonlinear terms in Equations. (1)-(2) had negligible effects in these tsunami simulations, even with a higher resolution mesh.

The two new sources we employed in the present work correspond to a fault with a N-S strike; the only difference between the two sources was the polarity of the fault. The reason for assuming such a fault position resides in the major earthquake damage pattern. It was observed along the Fortore River valley that this pattern ran approximately N-S in the neighborhood of the mouth. We called S3 the fault causing uplift of the western block, and S4 the other fault. Figure 5 shows the initial water elevation together with a sequence of snapshots for the case with westward uplift (S3). The main remark is that this source excited edge waves propagating along the northern coast of the Gargano peninsula that were stronger than those produced by the E-W inland sources examined above. Observe that even in this case, the S4 fault, where uplift and subsidence were interchanged, generated inverted fields, exactly as expected from a linear system.

The last two numerical experiments focused on the offshore sources, the fault position being assumed to be in correspondence with the fault system marking the margin between Gargano peninsula and the Adriatic microplate. The fault surface was respectively directed E-W and NE-SW; for both cases the downlifting block faced the northern coast of Gargano. Figure 6 shows the initial excitation field and a sequence of snapshots, every 600 seconds, for the E-W fault (source S5). We can note that the initial dipole wave (crest and trough) split completely after 600s. At 1200s one dipole had already left the basin while the second was attacking the coast. This second dipole was then partly backreflected and partly propagated along the coast in form of edge waves (for example, see the field sequence at 2400s, 3000s, and 3600s, where a dipole propagating seaward, with the trough preceding the crest can be, though not easily, delineated.) In this case, because of the shorter wavelength of the incident wave, there was a generation of a small reflected wave on the Tremiti Islands (distinguishable at the 1200s snapshot).

Figure 7 gives the evolution of the last tsunami we simulated, that is related to the NE-SW fault called S6. In this case it is interesting to observe the role of refraction: the two dipoles forming from the initial dipole (clearly visible after 600s) were both deviated towards shallower waters, one westward and the other southward (see the elevation field at 1200s), and as a consequence the coast was attacked by both systems of waves. Also in this case, the main wave interacted noticeably with the Tremiti Islands, leading to the production of a well-formed reflected front (see fields at 1200s and 1800s).

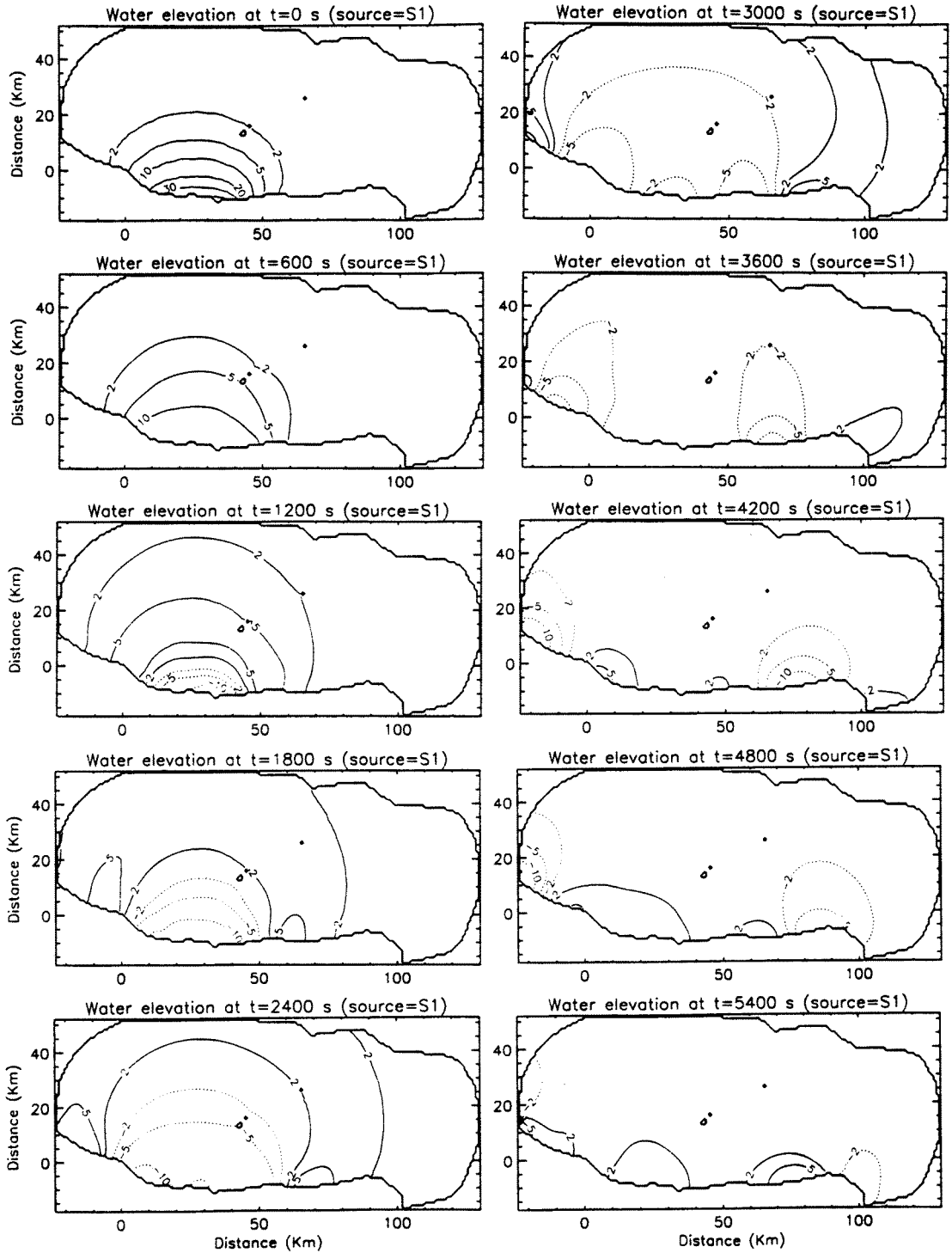

Figure 4. Contour plots of the water elevation fields at t=0s, 600s, 1200s, etc. for the E-W inshore fault with submarine uplift (source S1).

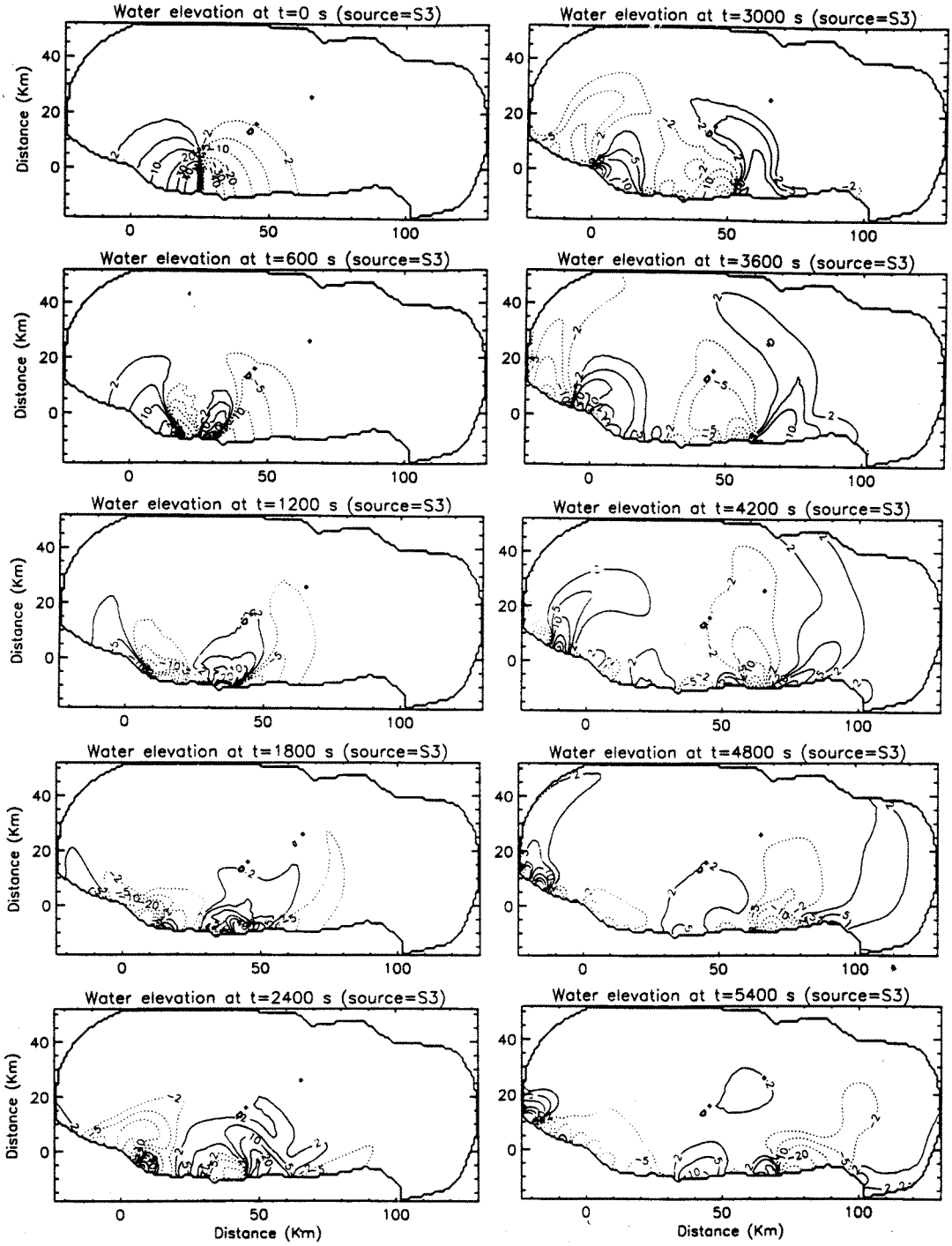

Figure 5. Contour plots of the water elevation field at t=0s, 600s, 1200s, etc. for the N-S inshore fault with westward uplift (source S3).

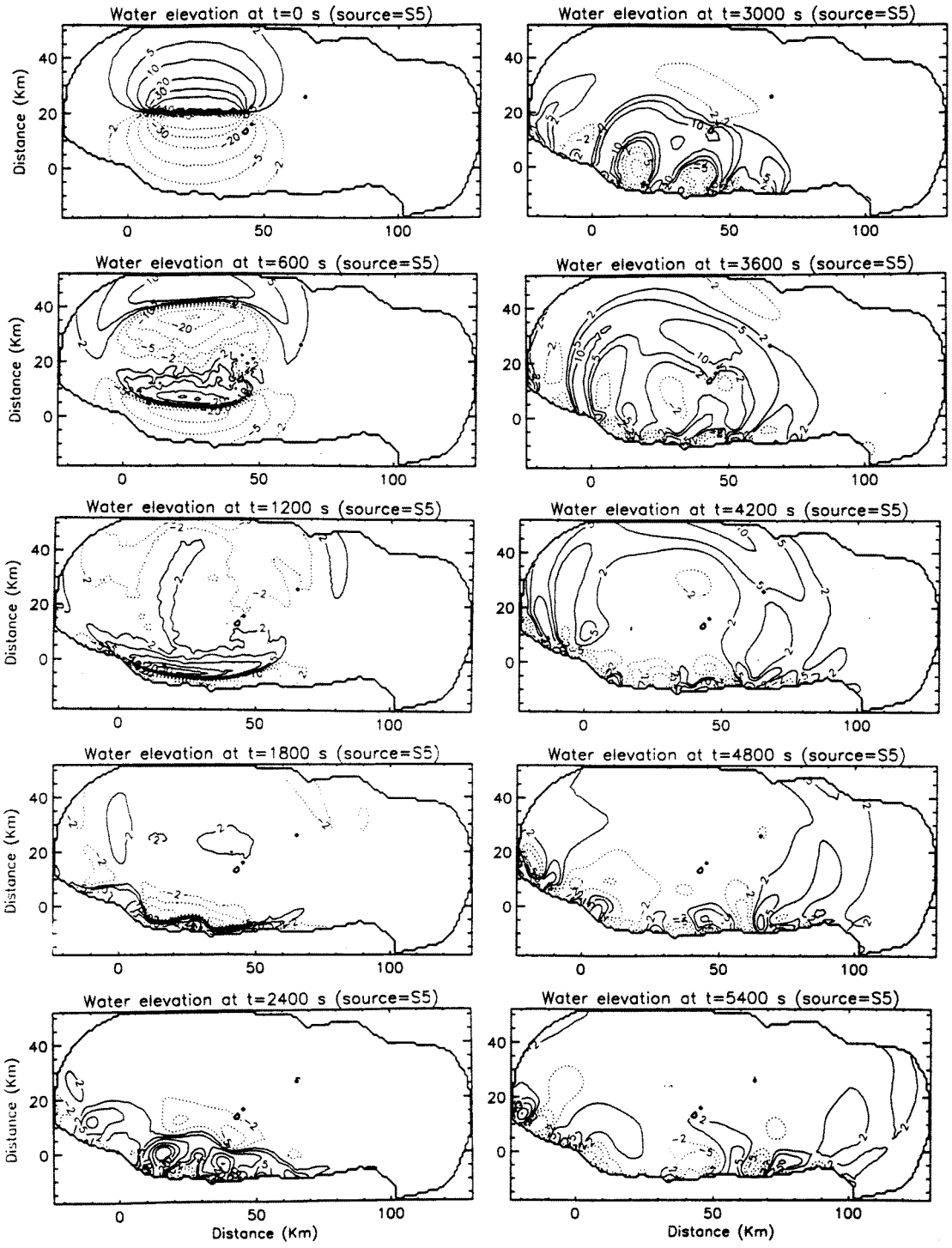

Figure 6. Contour plots of the water elevation field at t=0s, 600s, 1200s, etc. for the E-W offshore fault (source S5).

4. Discussion and Conclusions

Let us first consider the comparison between the results obtained by using the coarse and fine grid; these are depicted in Figures 3a and 3b respectively. Figure 8 shows the tide-gauge records computed at the Lesina Lake with both meshes in the case of the NE-SW offshore source. By simple inspection it can be verified that the coarser grid had the effect of filtering the tsunami signal, which appears remarkably smoothed down, though both arrival time and wave polarity are well computed. The lessons we learn are that a too coarse grid may lead to a sensible underestimation of the wave elevation, especially along the coast, and that consequently the mean grid-triangles size is a parameter to be carefully selected in all the studies where coastal wave amplitudes are of great importance. It should be stressed that the largest wave amplitudes we computed in our simulations, even with the finer grid, were largely smaller than the reported inundation heights. This underestimation is not surprising, since both the governing equations (1)-(2) and the numerical finite-element model with fixed domain boundaries (6) we used cannot account for accurate run-up calculations. This aspect, however, is not critical for the purpose of our present work.

The discussion on tsunami simulations can be carried out with the aid of Figure 9, which shows the mareograms computed at three coastal stations (Lesina, Peschici and Tremiti Islands) for all six sources described in the previous section. The most interesting observations that can be made are summarized in the following. With the offshore source S5 Peschici was marginally invested by the dipole attacking the coast, the maximum, though small, elevations being produced by edge waves which reached this station about 60 minutes after the earthquake. As for the source S6, the dipole moving SE-ward took about 30 minutes to reach the Peschici tide-gauge, while the higher amplitude signal was still due to the later arrival of edge waves. At the Tremiti Islands, mareograms for both source S5 and source S6 showed first a sharp negative-positive peak due to the main radiating wave front and then a second, smaller and smoothed pulse after 50-60 minutes due to the wave backreflected by the Gargano coast.

Although the Tremiti Islands are very close to the offshore sources, the maximum elevations at this station were smaller than those at Lesina. This is not surprising since the wave traveling toward the coast of Gargano experienced a steepening effect that reduced the wavelength and increased the amplitude. We want to stress that this nearshore wave amplification effect can be calculated well only with a grid sufficiently fine to prevent numerical smoothing (see the discussion of Figure 8 above).

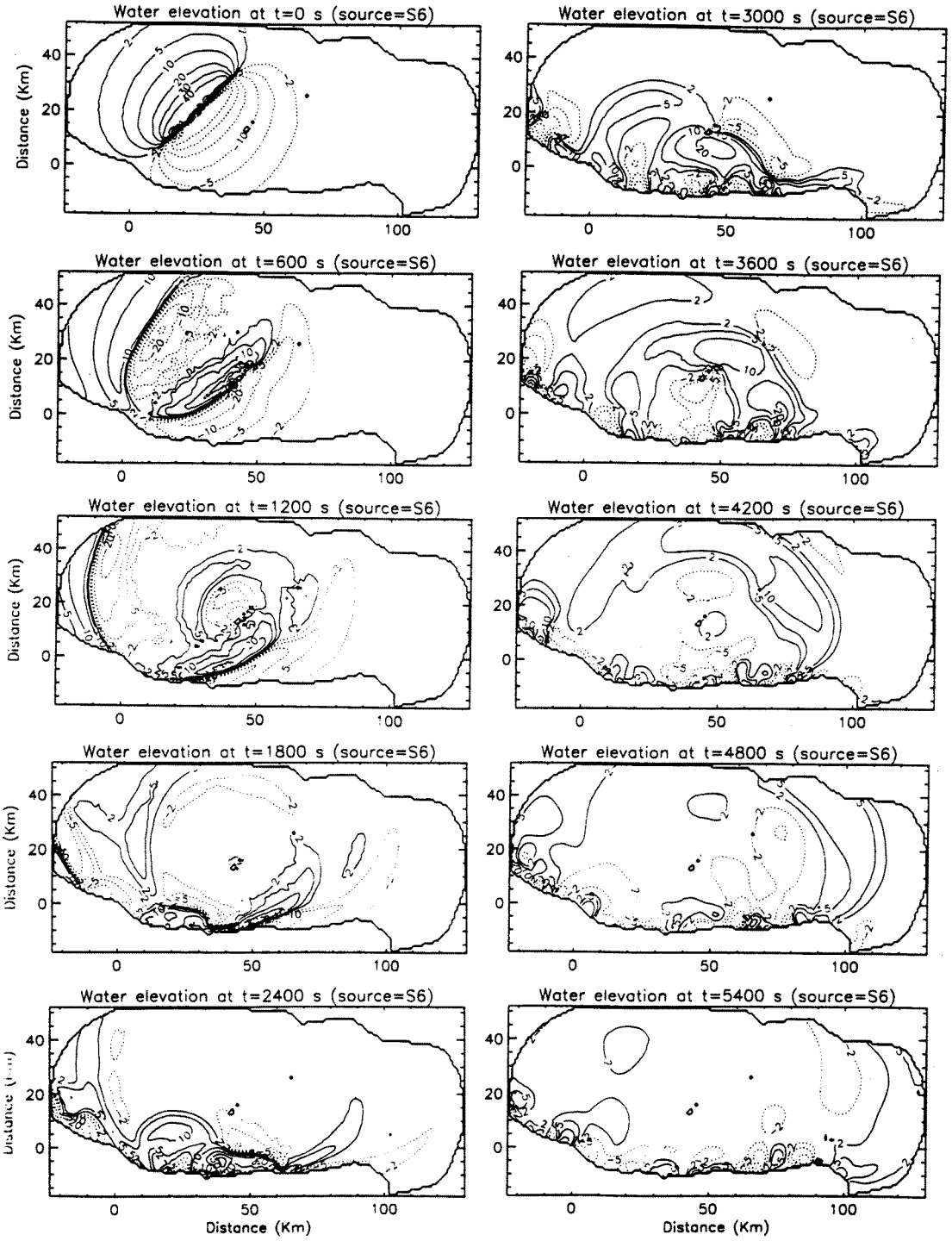

Figure 7. Contour plots of the water elevation field at t=0s, 600s, 1200s, etc. for the NE-SW offshore fault (source S6).

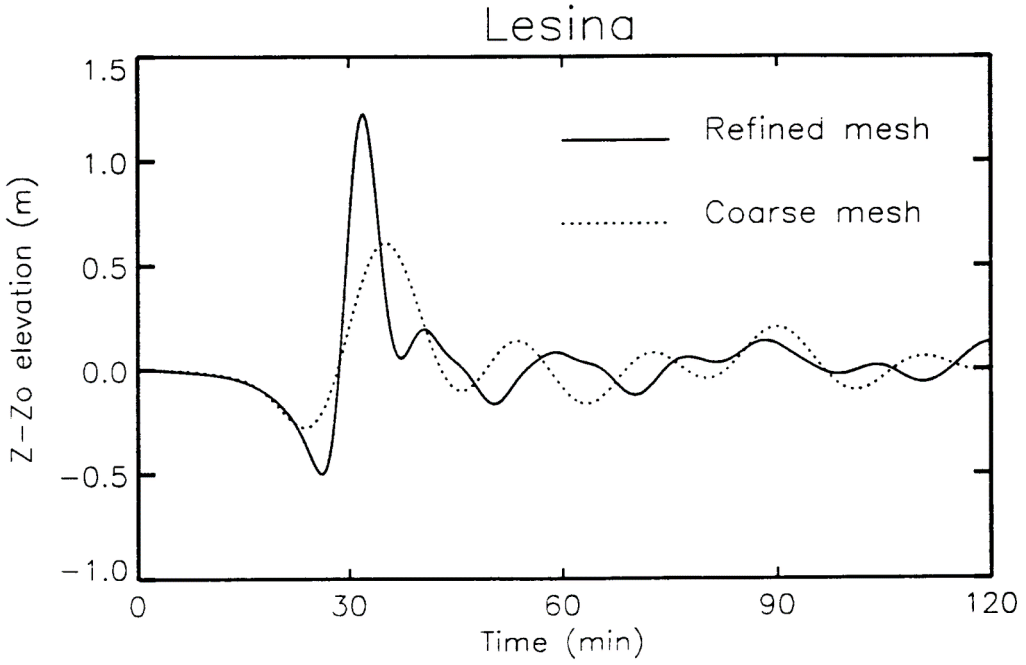

Figure 8. Computed mareograms at Lesina relative to the NE-SW offshore source (S6) obtained by using the coarse and refined meshes.

One of the main objectives of the present research was the determination of the position of the tsunamigenic fault consistent with the known earthquake and tsunami observations. Unfortunately, owing to the scarcity and the qualitative nature of data, a full inversion procedure to infer the earthquake source could not be implemented successfully (very recent, good examples of how inverting tide-gauge and run-up tsunami data can be found in the literature (Johnson, et al., 1996 and Piatanesi, et al., 1996).) Our investigation method was simply based on performing a series of six numerical experiments characterized by reasonable, but different, fault locations Si and correlating the simulated waves against the observations. Comparison with the historical reports (see for example, Ballerani, 1627; Cerqua, 1627) induces us to take some fault mechanisms as implausible; in fact, since in Lesina Lake the first observed water movement was a retreat, we have to reject the cases of the inshore E-W fault with submarine subsidence (S2) and of the N-S fault with westward uplift (S3), because both produce a positive first arrival. Let us then examine the remaining four sources. With only the tsunami data in hand, we would have no strong reasons against the offshore sources S5 and S6; but, if we also take into account seismic data, we are lead to conclude that they should be tendentially rejected, because these sources would produce more severe seismic damage in the Tremiti Islands (very close to the

epicentral area) than in Gargano, and this seems to be in contrast with previous macroseismic studies (see e.g., Molin and Margottini, 1985).

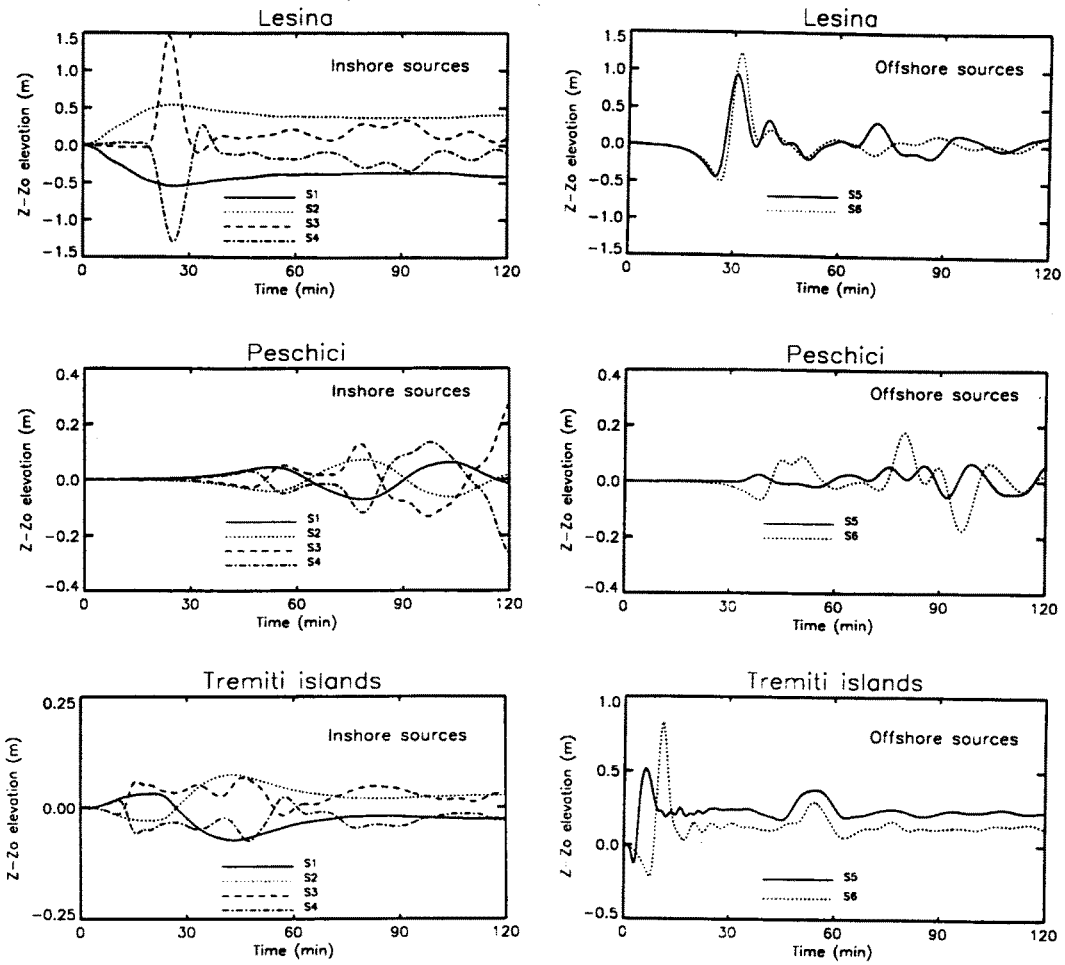

Figure 9. Computed mareograms at Lesina, Peschici and Tremiti Islands for all sources S1-S6 considered in the paper: namely, S1 is the E-W inshore fault with submarine uplift, S2 is the E-W inshore fault with submarine downlift, S3 is the N-S inshore fault with eastward subsidence, S4 is the N-S inshore fault with eastward uplift, S5 is the E-W offshore fault and S6 is the NE-SW offshore fault.

As regards the remaining two cases, it is observed that both determined a first water withdrawal at the Lesina Lake. If we now take into account the water inundation, we see that S1 produced no invasion, while S4 did. This argument would in principle suggest to us that S1 should be ruled out, hence making S4 the only source compatible with data. But, at this point, we have to bear in mind that our model is not able to compute inundation and run-up properly, given the assumed boundary condition of pure reflection on coastal segments (Equations 2a and 2b), where a constant water depth (5m) has been taken, implying vertical boundary walls. This consideration weakens our argument against S1, based on water invasion and does not allow us to discard it completely. We can further observe that the inland E-W fault with the

marine block uplifting (S1) caused large-amplitude and long-period wave systems, whereas the N-S fault S4 produced smaller amplitude and shorter period near-shore waves (see field sequences of Figure 4 for S1, and of Figure 5 for S4, remembering that Figure 5 is technically computed for S3, but it applies also to S4, with signs changed). The latter source has more potential for efficient edge wave generation rather than for the production of a remarkable tsunami wavefront.

From the foregoing, we can state that on the basis of the simulations we have carried out, we are not able to discriminate between the sources S1 and S4 and to decide which one is the best candidate for the 1627 tsunami generation. Furthermore, based on the same reasoning, we have no strong argument to exclude any one of the inland fault positions with intermediate strike, since these can be reasonably expected to produce coastal perturbation with characteristics mid-way between the E-W and the N-S striking faults. Our present results modify slightly the conclusions of our previous work, where we did not take into account the inland N-S faults and where we coherently concluded that the inland E-W fault S1 was our best choice.

It is worthwhile mentioning here the study by Panza, et. al., (1991), in which the 1627 earthquake fault was determined to be located approximately NE-SW at the Fortore River mouth as a result of comparing synthetic against experimental isoseismals. In light of the above considerations, this fault position does not contradict our present results. We believe that a better insight can be gained by using numerical models suitable to compute coastal run-ups, but we also feel that the investigations based only on tsunami simulations and tsunami data cannot lead sensibly further for the 1627 Gargano tsunami and cannot uniquely identify the earthquake source. Further investigations aiming at locating better the causative fault are justified only if new geological, seismological and historical data can be made available.

5. Acknowledgments

The present research has been partially financed by the Commission of the European Communities under the contract EV5V-CT92-0175 as part of the international project GITEC and partially funded by the Italian Ministry of the University and of Technological Research.

6. References

Ballerani, M., 1627. *Caso grandissimo occorso nel presente anno 1627 dove si sentono terremoti, e ruvine di migliara di persone, che pareva proprio giuditio universale, essendosi sommerse in Puglia da 9 lochi principali*, Lanciano-Iesi (in Italian).

Cerqua, G.J., 1627. *Lettera di Giovan Jacopo Cerqua, Lucera 8 Agosto 1627*, in Mercalli, G. (1897) *Ragguaglio del terremoto successo in Puglia a' 30 luglio 1627*, Archivio storico per le Province Napoletane 22, 120-123 (in Italian).

Guidoboni, E., and S. Tinti, S., 1987. I maremoti garganici del seicento. *Atti VI Conv.Naz. GNGTS*, Roma, 491-504 (in Italian).

Guidoboni, E., and S. Tinti, 1988. A review of the historical 1627 tsunami in the Southern Adriatic. *Science of Tsunami Hazard*, **1**, 11-16.

Johnson, J.M., K. Satake, S.R. Holdahl, and J. Sauber, 1996., The 1964 Prince William Sound earthquake: joint inversion of tsunami and geodetic data, in *J. Geophys. Res.*, **101**, 523-532.

Molin, D., and C. Margottini, 1985. The earthquake of July 1627 in the northern Capitanata, in *Atlas of isoseismal maps of Italian earthquakes*, CNR-PFG, Quaderni de "La Ricerca Scientifica", n. 114, vol. 2A, (ed. Pospischl D.), Bologna, 36-37.

Panza, G.F., A. Craglietto, and P. Suhadolc, 1991. Source geometry of historical events retrieved by synthetic isoseismals. *Tectonophysics*, **193**, 173-184.

Piatanesi, A., S. Tinti, and I. Gavagni, 1996. The slip distribution of the 1992 Nicaragua earthquake from tsunami run-up data. *Geophys. Res. Lett.*, **23**, 37-40.

Satake, K., 1989. Inversion of tsunami waveforms for the estimation of heterogeneous fault motion of large submarine earthquakes: the 1968 Tokachi-oki and the 1983 Japan sea earthquakes, *J. Geophys. Res.*, **94**, 5627-5636.

Tinti, S., and I. Gavagni, 1995. A smoothing algorithm to enhance finite-element tsunami modeling: an application to the 5 February 1783 Calabrian case, Italy. *Natural Hazards*, **12**, 161-197.

Tinti, S., and A. Piatanesi, 1996. Numerical simulations of the tsunami induced by the 1627 earthquake affecting Gargano, southern Italy, *J. Geodynamics*, **21**, 141-160.

Tinti, S., I. Gavagni, and A. Piatanesi, 1994. A finite-element numerical approach for modeling tsunamis, *Annali di Geofisica*, **37**, 1009-1026.

Tinti, S., A. Maramai, and P. Favali, 1995. The Gargano promontory: an important Italian seismogenic-tsunamigenic area. *Marine Geology*, **122**, 227-241.

4.2 A revision of the 1693 eastern Sicily earthquake and tsunami

JOURNAL OF GEOPHYSICAL RESEARCH, VOL. 103, NO. B2, PAGES 2749-2758, FEBRUARY 10, 1998

A revision of the 1693 eastern Sicily earthquake and tsunami

Alessio Piatanesi and Stefano Tinti
Dipartimento di Fisica, Settore di Geofisica, Università di Bologna, Italy

Abstract. The 1693 earthquake was a disastrous event affecting eastern Sicily, southern Italy, where it caused over 60,000 victims and total destruction of several villages and towns in the districts of Siracusa, Ragusa, and Catania. The earthquake was followed by a tsunami that struck the Ionian coasts of Sicily and the Messina Strait and was probably observed even in the Aeolian Islands. Historical documents on sea waves and flooding, though not abundant, allow us to form a picture of the tsunami first attack and inundation. The first water movement all along the Sicilian coastline was a strong sea withdrawal, followed by a violent sea return and coastal flooding. The main purpose of this research is to put constraints on the focal mechanism of this earthquake on the basis of the available documents on the tsunami (1) by simulating tsunami from different possible sources via numerical modeling based on finite element technique and shallow water approximation and (2) by choosing the source best fitting the tsunami data as the most plausible cause for this tsunami. The relevance of this study should also be evaluated in light of the circumstance that no certain indication on the earthquake fault can be deduced from the available macroseismic data alone. Solving the source problem for this event, one of the largest occurring in southeastern Sicily in historical times, is a significant contribution to understanding the seismotectonic regime of the region and to assessing the related earthquake and tsunami hazard/risk with implications on mitigation policies.

1. Introduction

Eastern Sicily, together with southern Calabria and the Messina Strait, represents the Italian region most affected by earthquakes. Here extremely violent events have been recorded several times: if we restrict our attention to the earthquakes with a Mercalli-Cancani-Sieberg (MCS) epicentral intensity exceeding X in the period after 1000 A.D., we can mention the February 1169, the December 1542, the October 1624, the January 1693, and the December 1908 events. The seismic activity in this area occurs mostly through strong releases of energy, spaced out by long periods of quiescence or quasi-quiescence, so long that some authors supposed the existence of a seismic gap [*Purcaru and Berckhemer*, 1982; *Mulargia et al.*, 1985]. An outstanding feature of the main events of the region is that in several cases they are preceded by foreshocks, though this was not the case for the last significant earthquake, which occurred here on December 13, 1990 (duration magnitude evaluated by the Istituto Nazionale di Geofisica, Rome: M_d=5.1), for which no previous relevant activity has been recorded [*De Rubeis et al.*, 1993]. The earthquake considered in this work struck eastern Sicily on January 11, 1693, and was preceded by a foreshock on January 9. The damage was striking, with more than 60,000 victims and a completely destroyed area as large as about 5600 km^2 [*Barbano*, 1985]. From this point of view this event may be compared only with the 1908 Messina earthquake. The earthquake generated a large tsunami whose effect was observed along the whole eastern coast of Sicily, the southern coast of Calabria, and possibly, according to *Campis* [1694], at the Aeolian Islands. All the historical sources report an initial withdrawal of the sea in Taormina, Mascali, Catania, Augusta, and Siracusa (see Figure 1) and the subsequent flooding of the coast [*Burgos*, 1693; *Campis*, 1694; *Bottone*, 1718; *Bonaiuti*, 1793] (see also the synthetic description by *Baratta* [1901]). The available accounts do not permit us to draw a detailed map of the observed drawdown and run-up or of the maximum wave amplitude, but it can be certainly assumed that the tsunami was much more violent in the south than in the north of Sicily. A quite detailed description of the tsunami effects is available only for the town of Augusta, which was the most affected by the waves. Here the initial water withdrawal drained the harbour completely, causing severe damage to the ships, especially to two large vessels coming from Malta, which violently touched the sea bottom, as is reported by *Acquaviva*, [1693] and by an anonymous writer, whose report may be presently found at the *Archivo General de Simancas*, [1693]. During

Paper number 97JB03403.
0148-0227/98/97JB-03403$09.00

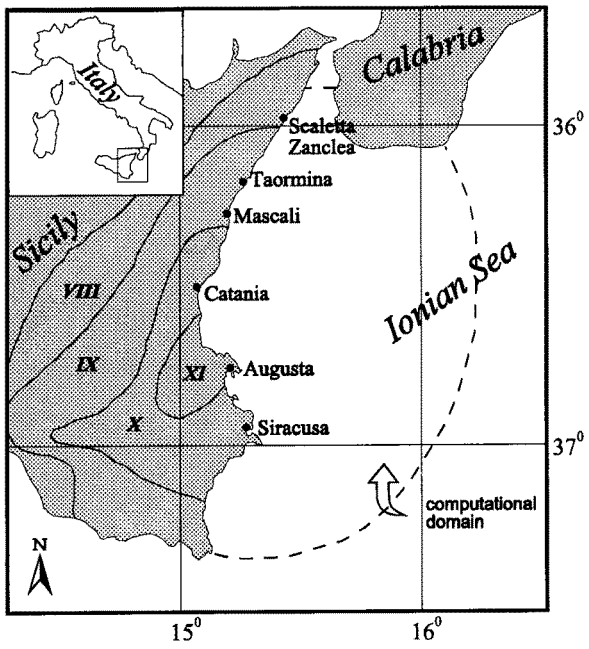

Figure 1. Geographic sketch of the region involved by the 1693 earthquake and tsunami, with superimposed corresponding isoseismal map [from *Barbano,* 1985]. The dashed line marks the boundary in the sea of the computational domain.

the following inundation, the sea submerged the district close to the port as far as the convent of Saint Dominic [*Burgos,* 1693; *Muglielgini,* 1695; *Bottone,* 1718; *Mongitore,* 1743] and killed many of those people, especially women and children, who, alerted by the big foreshock of 2 days before, were camping near the pier (see the account given in the newspaper *La Gazzetta di Bologna,* March 3, 1693).

The tectonic setting of eastern Sicily is quite complex, though the related general frame is explained by the collision between the African plate margin and the crustal unit of the Calabrian arc, which genetically belongs to the Eurasian plate. A schematic description of the main regional structures is given by *Reuther et al.* [1993], who concentrate on the segmentation of the collisional zone taking place in Sicily and on the special features that it implies, consisting of different kinds of faulting styles (see Figure 2). Southeastern Sicily is recognized to be the northern part of the Hyblaean-Malta plateau, which is the leading edge of the African plate, exhibiting a Moho depth of about 23 km [*Finetti,* 1982], significantly larger than the oceanic Moho depth of the next Ionian sea [*Ferrucci et al.,* 1991]. Its western margin is a well-pronounced dextral-shear transform fault extending from the Pantelleria rift in the middle of the Sicily channel up to the Sicily mainland, where it is known as the Scicli-Ragusa fault [*Ghisetti and Vezzani,* 1980]. Its eastern limit is marked by a paramount

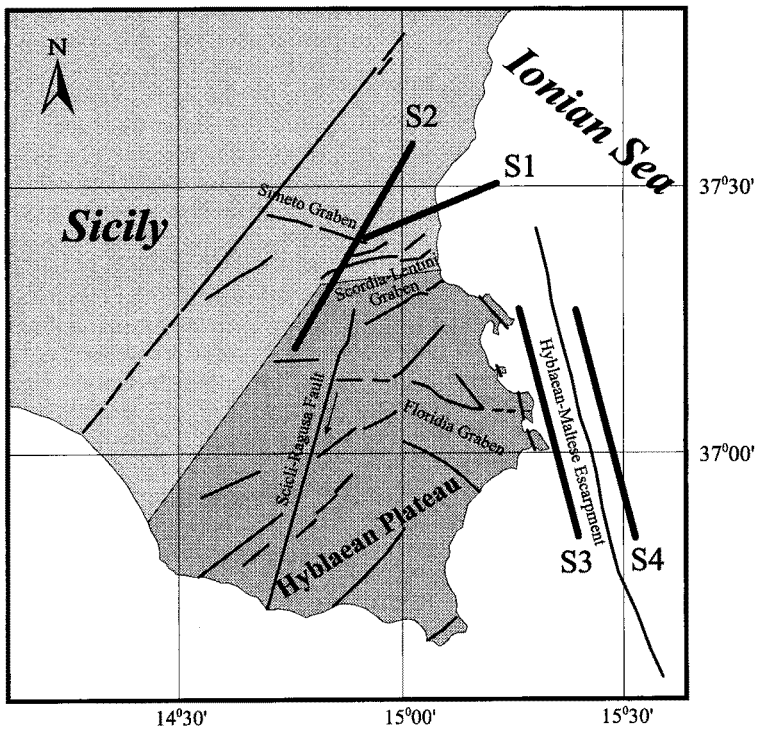

Figure 2. Simplified tectonic sketch of the Hyblaean plateau [from *Ghisetti and Vezzani,* 1980]. Also shown are the position and strike of the four seismic faults, represented by solid segments numbered from S1 to S4, considered in this work.

morphological feature, the Hyblaean-Malta escarpment, about 300 km long, trending NNW-SSE almost parallel to the eastern Sicilian coasts, separating shallow coastal waters from the Ionian abyssal plain, about 4 km deep. There is no doubt that this escarpment is characterised by normal faulting with minor sinistral strike-slip component [*Grasso et al.*, 1985; *Reuther et al.*, 1993] and a remarkable offset exceeding 3 km in some places. The tectonic province to the east of the escarpment is formed by oceanic crust involved in the Calabrian arc subduction zone. In the northern part of this province the Calabrian wedge overthrusts over the Ionian foreland [*Del Ben*, 1993; *Mantovani et al.*, 1997], while the lithospheric slab, identified by deep and intermediate earthquake foci distribution and tomographic studies, is subducted beneath the Calabrian arc and extends to the north underneath the southern Tyrrhenian Sea [*Spakman*, 1990; *Amato et al.*, 1993]. The mainland part of the Hyblaean plateau is crossed by a complex net of faults, some of which are subparallel to the escarpment, but some important pull-apart grabens are almost orthogonal to it, trending SW-NE or W-E (see, for instance, the Scordia-Lentini graben and the Simeto graben to the north and the Floridia graben). The relationship between the tectonic processes going on in the area and the seismic activity is not well understood and is still a subject of intense study. The most relevant earthquake that affected the region is the January 11, 1693, event, for which the basic question on which fault was its source fault is still unsolved, despite the existence of much literature, ranging from coeval reports to recent studies with critical revision of macroseismic data and related production of isoseismal maps [*Barbano*, 1985; *De Rubeis et al.*, 1992]. What seems clear today is that the epicenter originally attributed to this earthquake, which was placed in Val di Noto rather far from the coast, is not very plausible. The fact that all isoseismal lines are open (see Figure 1), with an ideal continuation in the sea, is suggestive of an epicenter close to the coast, which, however might be placed equally well both onshore and offshore. The main hypotheses on the possible fault can be summarized in two prevailing ideas: 1) the source is to be placed in correspondence with the Scordia-Lentini graben depression between Catania and Augusta according mainly to morphogeological considerations [*D'Addezio and Valensise*, 1993], and 2) the source position is associated with a segment of the Hyblaean-Malta escarpment offshore Augusta, according to tectonic data and seismic prospecting data interpretations (P. Scandone, personal communication, 1997). A way to solve the contrast between the two above contradictory points of view is to use the supplementary data available for this tsunamigenic earthquake, that is, the data concerning the tsunami waves impacting the coast. The working scheme of the present paper consists in performing numerical simulations of tsunamis generated by the two assumed source faults. Comparing the computed waves with the tsunami observed along the coasts will allow us to express some motivated judgment on which one of the hypthesized generating faults should be regarded as the probable earthquake origin. Indeed, to test the sensitivity of our approach, we have extended tsunami simulations to two more fault cases that will be adequately illustrated later.

2. Numerical Tsunami Model

For our purposes we have to perform near-field numerical simulations of the tsunami, whose evolution is computed by adopting the nonlinear nondispersive shallow water approximation of the Navier-Stokes equations, known to be adequate when typical wavelengths ($\sim 10^4$-10^5 m) are much larger than water depth ($\sim 10^3$ m). Denoting by ζ the water elevation above the mean sea level, by $\mathbf{v}$ the horizontal velocity vector, averaged over the water column, by h the basin depth, and by g the gravity acceleration, we can write the set of equations governing the wave motion as follows:

$$\begin{cases} \partial_t \zeta = -\nabla \cdot [(h+\zeta)\mathbf{v}] \\ \partial_t \mathbf{v} = -g\nabla\zeta - (\mathbf{v}\cdot\nabla)\mathbf{v} \end{cases} \quad (1)$$

Fields are computed in a finite domain (see Figures 1 and 3) delimited by a boundary on which they satisfy suitable conditions, namely pure wave reflection on the solid boundary (coastline) and full wave transmis-

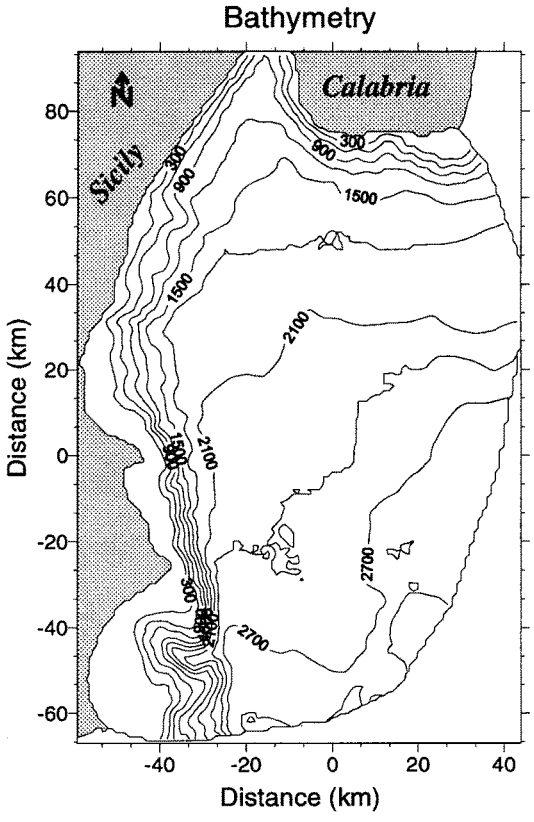

Figure 3. Bathymetry of the basin chosen for the tsunami simulations; line labels are in meters.

sion on the open boundary (open sea). They can be mathematically expressed by the following equations:

$$\mathbf{v}\cdot\mathbf{n} = 2(c_1 - c_0) \quad \text{on the open boundary} \quad (2a)$$

$$\mathbf{v}\cdot\mathbf{n} = 0 \quad \text{on the solid boundary} \quad (2b)$$

Here $\mathbf{n}$ is a unit vector normal to the boundary and outwardly oriented, $c_1 = \sqrt{g(h+\zeta)}$ represents the local phase velocity and $c_0 = \sqrt{gh}$ is the phase velocity of the linear wave. System (1) together with conditions (2a)-(2b) has been solved numerically by means of a finite element method, making use of a Galerkin procedure and linear shape functions [*Tinti et al.,* 1994]. The bathymetry of the basin, shown in Figure 3, is characterized by steep slopes in correspondence with the abrupt Hyblaean-Malta escarpment. To perform stable and reliable simulations, we used a computational grid consisting of 14,400 triangular elements and 7397 nodes, with higher resolution along the coast and in proximity to the escarpment (see Figure 4). In all simulations the initial seawater elevation is assumed to be equal to the coseismic vertical displacement of the sea bottom, which is computed through the analytical Mansinha-Smylie model [*Mansinha and Smylie,* 1971], while the initial field velocity is assumed to be identically null. This assumption is adequate because fault rupture times (~10 s) are much smaller than the typical tsunami period (~100-1000 s),allowing us to consider a static coseismic deformation.

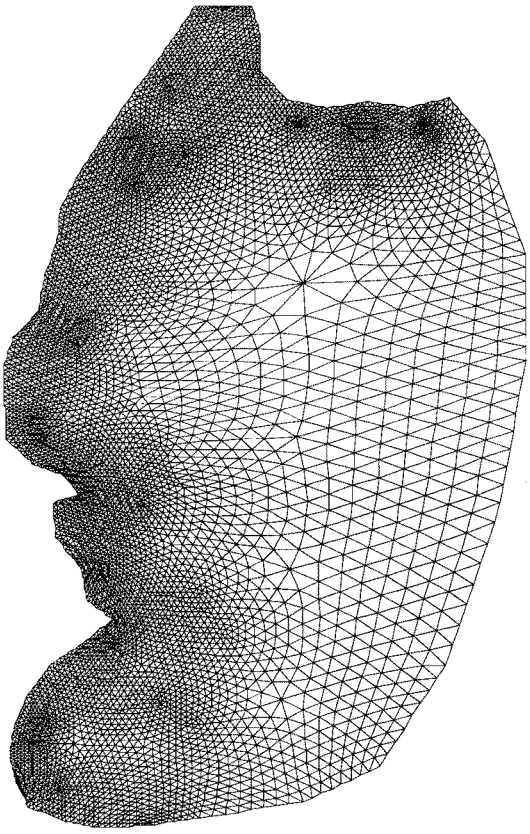

Figure 4. Mesh used for the finite element numerical computation consisting of 14,400 triangular elements and 7397 nodes.

3. Numerical Simulations

The two basic faults taken into account for the numerical simulations are designated by the codes S1 and S3 (see Figure 1). The former is located in the Scordia-Lentini graben and has the following focal parameters: depth of the upper fault border 3 km; width, 15 km; length, 30 km; dip angle, 30°; slip, 8 m, with the southern block uplifting. Fault dimensions and slip orientation are taken from *D'Addezio and Valensise* [1993], whereas the slip is accommodated so as to obtain a value of the seismic moment of the order of $M_0=10^{20}$ Nm, corresponding to an earthquake local magnitude in the range 7-7.5. The block on the northern side of the fault is downgoing, producing a remarkable subsidence of the sea floor together with a slight positive readjustment to the north of the subsiding region. The southern block is associated with an uplift, whose magnitude is substantially smaller than the northern downward displacement. Fault S3 is a pure dip-slip on a vertical plane placed in the Hyblaean-Malta escarpment, with the onshore block uplifting. Its upper border is at a depth of 2 km, its width is 15 km, its length is 50 km and its slip is 6.2 m, corresponding to a magnitude slightly larger than, but basically equivalent to, the previous case. Figure 5 displays the cross section of the faults, together with the associated initial elevation fields of the seawater. Fault S3 produces an initial symmetric dipole configuration with a water depression and a water uplift, while fault S1 determines a more complex disturbance, characterized by an asymmetric dipole surrounded by a small external positive front. In addition to the prior faults that have sound tectonic justification, we have considered two more genetic faults, which, though they are supported by weaker foundation, nevertheless give rise to interesting hydrodynamical experiments and serve to better appreciate the resolution power of our study. Source S2 (see Figures 2 and 5) is a vertical fault with the same geometry and slip magnitude as those of source S3, causing the offshore block to downlift. It has been taken into account here, since it is an onshore fault producing a first initial movement in the sea that differs sensibly from the previous cases by being unipolar: it is a single water depression. Instead, source S4 is chosen to be very similar to S3, the only difference being that it is slightly displaced eastward (see Figures 2 and Figure 5). The distance between the two faults is less than 20 km and for the present discussion can be taken as representative of an acceptable uncertainty in the location of the fault. Interestingly, however, we will see that tsunamis generated by these two sources are different enough to be distinguishable from one another on the basis of the computed mareograms.

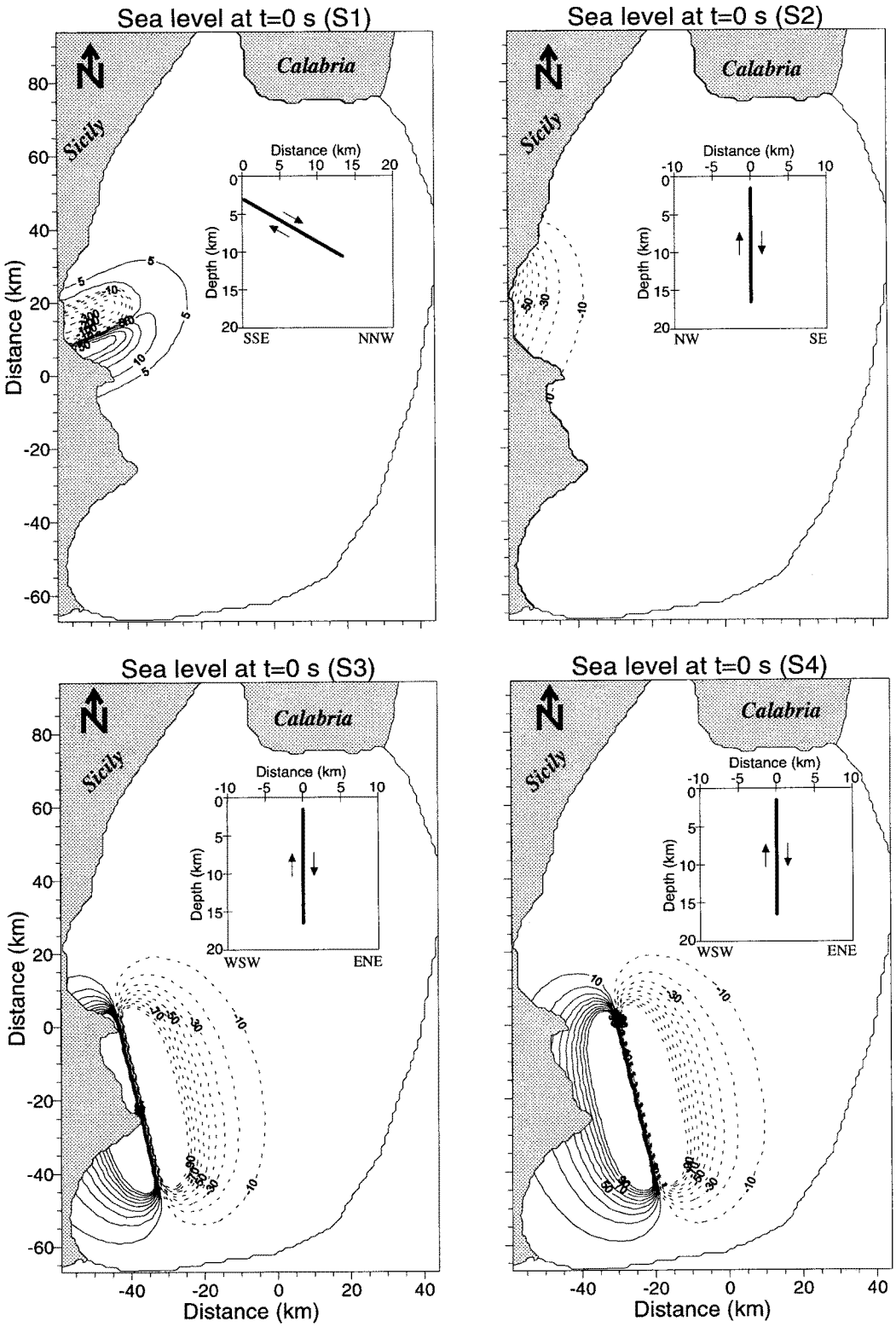

Figure 5. Contour plots of the coseismic vertical displacement of the sea bottom, produced by the source faults depicted in Figure 2. The fields are computed through the *Mansinha and Smylie* [1971] analytical formula. Solid and dotted lines represent positive and negative elevations, respectively; contour labels are in centimeters. Also given are the respective vertical cross sections of the faults, taken on planes orthogonal to the fault strike.

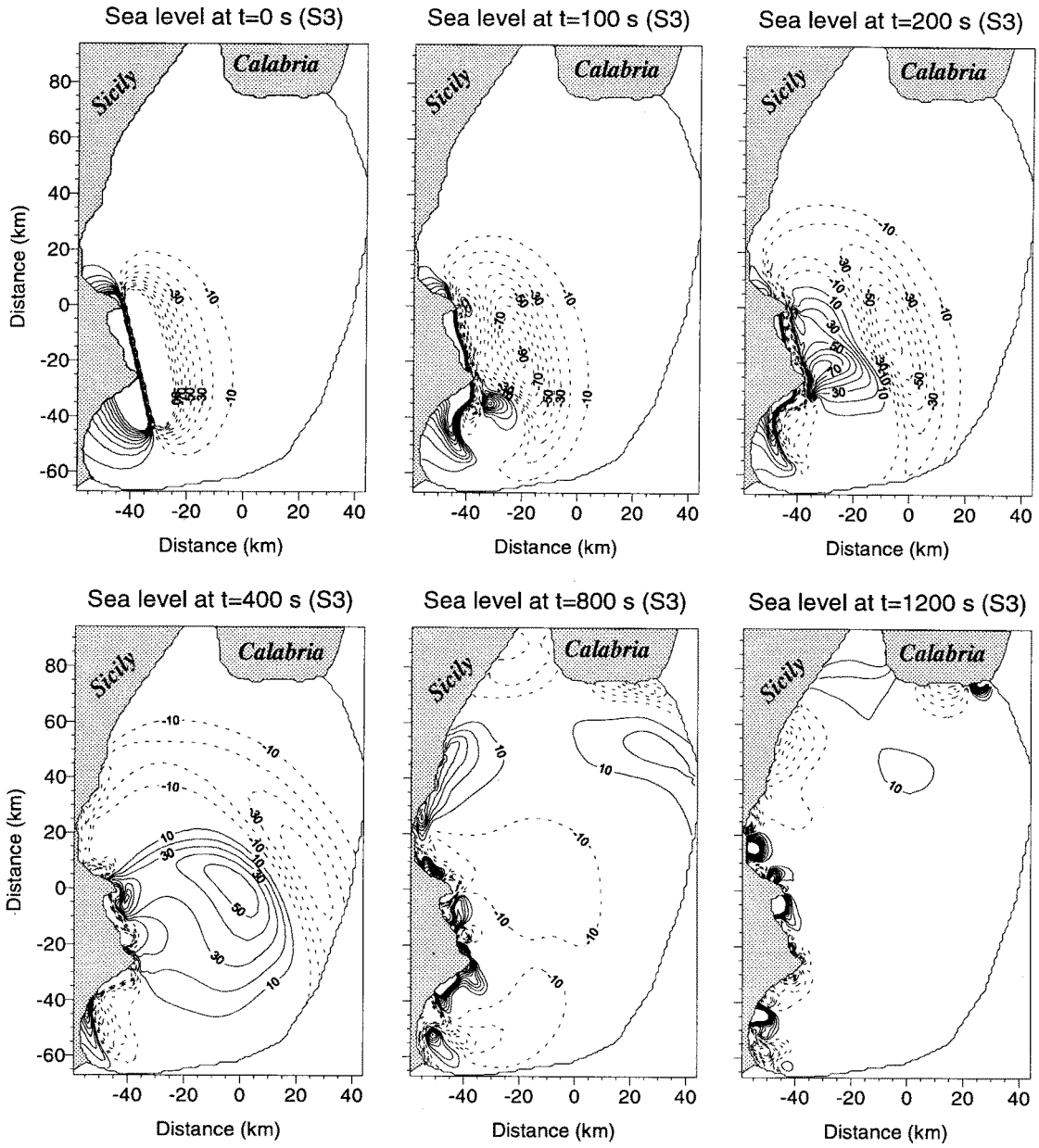

Figure 6. Contour plots of the seawater elevation field computed at t=0, 100, 200, 400, 800, and 1200 s for the source S3. Solid and dotted lines represent positive and negative elevations, respectively; contour labels are in centimeters.

3.1. Water Elevation Fields

The propagation pattern of the tsunami excited by the considered faults has been computed by means of the finite element numerical model based on the equations given in section 2 within the grid domain depicted in Figure 4. To illustrate the main features of the wave propagation, case S3 can be taken as a useful example. Elevation fields are portrayed in Figure 6 at different delays after the origin time. They can be explained by bearing in mind that long waves travel much faster in deep than in shallower waters and that the steep escarpment functions as a shelf that traps wave energy in the shallow coastal zone and favors edge wave formation. After 100 s, the initial wave pattern is only slightly deformed: the offshore depression tends to become larger as it travels fast, while the onshore crest tends to squeeze, for it moves slowly in shallow nearshore waters. After 200 s, two interesting characteristics of the offshore perturbation can be remarked: first, it tends to assume a dipolar character with a

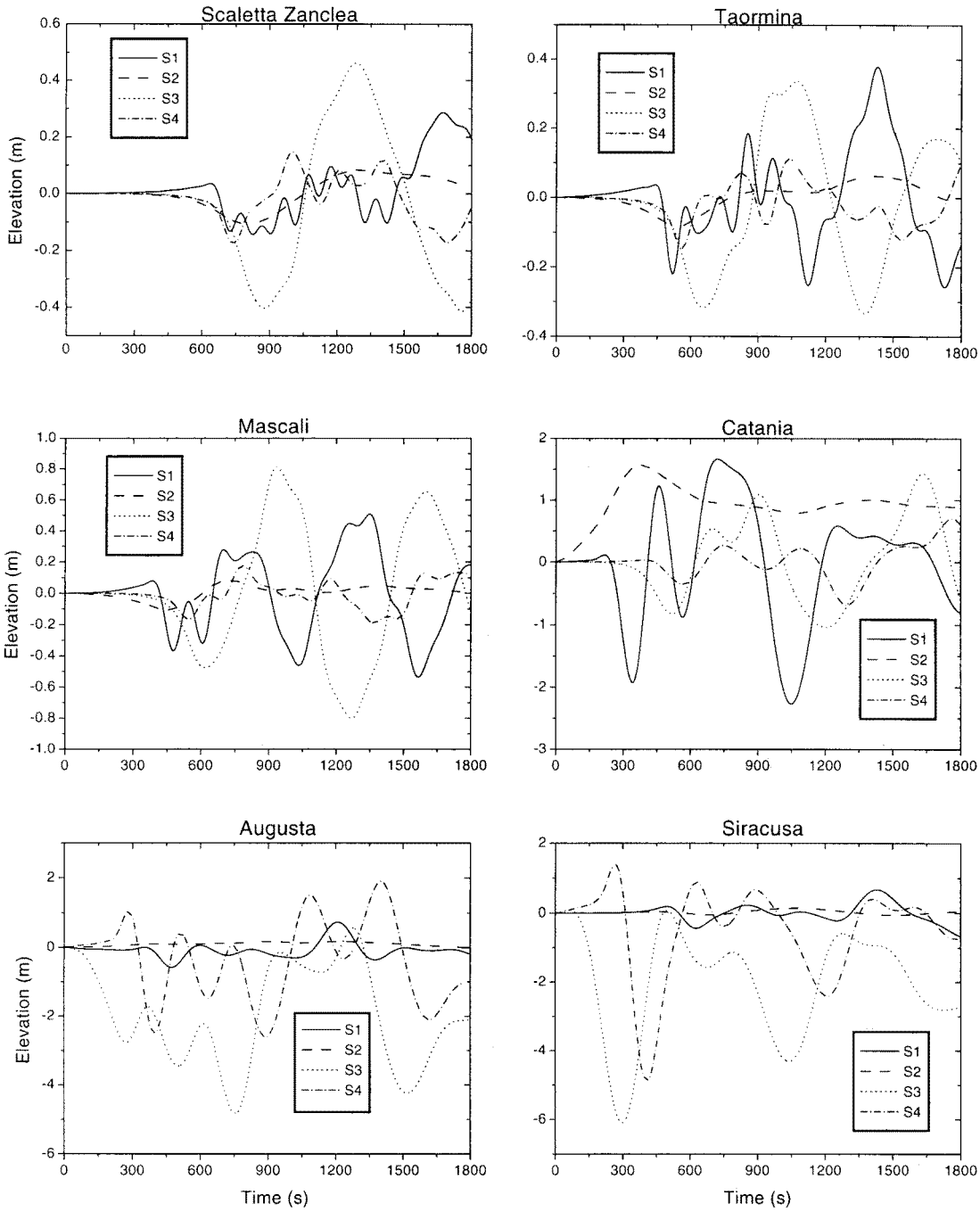

Figure 7. Computed mareograms in the representative coastal sites shown in Figure 1. Each panel includes four curves, labeled S1-S4, relative to the corresponding source faults. All curves start from a zero-level because coastal tide gauges experience exactly the same coseismic displacement as does the water surface.

leading depression followed by a positive wave; second, it tends to progressively travel northward toward the Messina Strait, as the effect of the refraction caused by the deep-sea bathymetry. The internal perturbation remains confined in coastal waters and propagates southward and northward along the eastern Sicily coast in the form of edge waves. In the snapshots taken at later times the offshore system is seen to approach quickly the strait and southern Calabria, where it is the first tsunami arrival, producing a first water retreat along

the coast. Notice that after 20 min most of this wave has abandoned the computational domain where only edge waves continue their slow coastal travel.

3.2. Mareograms

Water elevation fields, such as those shown in Figure 6, give only large-scale information and are certainly useful to delineate the main features of the tsunami propagation. However, the available historical data refer to local effects that were observed on specific locations along the coast, and to carry out our discussion on the tsunami simulations, mareograms have been computed at six coastal stations (Scaletta Zanclea, Taormina, Mascali, Catania, Augusta, and Siracusa) for all four sources considered in the previous section. Notice that mareograms, shown in Figure 7, are as usual computed as the difference between the water elevation at a given time and the initial seawater displacement, meaning that all time histories start from a zero level at the initial time, irrespective of the ground displacement caused by the earthquake. The final computation time is 30 min, sufficiently long to take into account the main waves in all the coastal places selected in the simulations.

Before starting the discussion the preliminary consideration regards the different importance of the sources S1-S4. Our main goal is to discriminate between faults S1 and S3, both of which have been indicated as the source of the 1693 earthquake, sources S2 and S4 having been added in the analysis for completeness. With this fact in mind a first insight into the mareograms suggests that a general distinction can be made between fully inland (S2) and fully or partially offshore sources (the others): any vertical onshore fault gives rise to a unipolar sea level disturbance with a small content of small-scale features and results in mareograms characterized by longer-period oscillations that have considerable amplitude only in the source area. This finding can be ascertained by comparing the mareogram at Catania (within the S2 source region) with the ones computed in the other ports.

The decisive key observation, on which the selection of the earthquake source can be mostly based, happens to be the tsunami wave polarity. All historical sources agree on the point that the first tsunami manifestation was an initial withdrawal of the sea in all the coastal places mentioned above. This constraint results in being highly discriminant, since only source S3 can meet this criterium. In particular, source S2 causes a significant positive first arrival in Catania, while source S4 generates large positive first arrivals in Augusta and in Siracusa, with the result that both sources must be accordingly ruled out. It is worth observing that though sources S3 and S4 are so similar, both being associated with the Hyblaean-Malta escarpment, the corresponding resulting mareograms differ remarkably because of the special bathymetric feature of the involved basin. Consequently, we can discriminate quite easily between S3 and S4, accepting the former and rejecting the latter. Most of the attention of course must be devoted to examining source S1, which gives rise to a larger proportion of edge waves and produces small positive first arrivals in all stations except Augusta; according to our criterion therefore it should be rejected. However, somebody could consider this rejection too unfair and argue instead that the computed positive arrivals are very weak and could have been easily missed by witnesses. If this argument is true, the consequence is that the historical accounts describe as the first sea retreat what was indeed the second tsunami arrival. This objection could be answered by considering that there exist several accounts by seamen and fishermen who were on boats and vessels at the time of tsunami attack [*Campis,* 1694], whose experience should be a guarantee of their capability of perceiving the direction even of small water movements. However, let us accept this objection as a sound argument and hence refrain from ruling out source S1 on the basis of the tsunami polarity.

The second aspect that can be further examined is the comparative tsunami amplitude. For fault S1 the amplitude is rather small everywhere except in Catania, which is inside the source region and is affected much more than Augusta and Siracusa. Conversely, for source S3 it is quite large, especially in Augusta and in Siracusa, which are in the near field and relatively weaker in Catania, at the margin of the source region. This approach seems to agree much better with the tsunami accounts than the previous case, since Augusta is known to be the city where the tsunami produced the largest effects [*Acquaviva,* 1693; *Burgos,* 1693] (see also the recent revisions contained in the Italian earthquake catalogue by *Boschi et al.* [1995], and in the Italian tsunami catalogue by *Tinti and Maramai* [1996]). Therefore the only reasonable conclusion that can be drawn is that the hypothesis that the seismic fault responsible for the 1693 earthquake and tsunami is located in correspondence to the Hyblaean-Malta escarpment is supported by much more evidence, as regards tsunami data, than the alternative view that it is placed in the Scordia-Lentini graben.

3.3. Conclusions

One of the main objectives of the present research was the determination of the position of the tsunamigenic fault consistent with the known earthquake and tsunami observations. The qualitative nature of the available data did not allow us to implement a full inversion procedure to infer the earthquake source (examples of inversion of tide gauge records and tsunami data are available in the literature: see, for example, *Johnson et al.* [1996] and *Piatanesi et al.* [1996]). Our investigation method, already applied to other historical tsunamigenic earthquakes [*Tinti and Piatanesi,* 1996], was simply based on performing a series of numerical experiments relative to different source locations and comparing the simulations against the historical observations. This method enabled us to regard all fault locations except one as implausible and to indicate S3 as the only one satisfying the constraints imposed by the data. Remarkably, we could discriminate between

sources S1 and S3, concluding that the former, placed in the Scordia-Lentini graben, is scarcely consistent with tsunami observations and must be discarded. Our analysis has therefore the merit to have shown that tsunami data support the view that the offshore fault system located on the megastructure known as the Hyblaean-Maltese escarpment generated the earthquake. And noticeably, we stress that this important conclusion could not have been drawn on the basis of the macroseismic data alone, especially because the macroseismic field of the January 11 earthquake was significantly corrupted by the damage produced by the strong foreshock that occurred only 2 days earlier [*Barbano,* 1985]. This finding shows the value of tsunami historical observations and the potential of our method that can be applied to other important cases of tsunamigenic earthquakes in Italy as well as in other regions of the world. Eventually, we emphasize the significance of our results for the outgoing studies aimed at assessing seismic and tsunami hazard and risk in eastern Sicily and at identifying characteristic catastrophe scenarios on which to calibrate appropriate response for disaster prevention and mitigation.

Acknowledgments. This research was financed partly by the European Union, DGXII, under contract ENV4-CT96-0297 (project GITEC-TWO) and partly by the Italian Ministry of the University and of Scientific and Technological Research. The authors wish to thank A. Maramai (ING, Rome) for her cooperation in examining historical sources.

References

Acquaviva, F., Relazione dell'Inquisitore di Malta F. Acquaviva al Segretario di Stato Cardinale Spada sui danni causati a Malta e in Sicilia dal terremoto dell'11 gennaio 1693, Malta 18 gennaio 1693, *Arch. Segreto Vaticano, Segreteria di Stato, Inquisizione Malta, 44,* 11-16, 1693.

Amato, A., B. Alessandrini, G.B. Cimini, A. Frepoli, and G. Selvaggi, Active and remnant subducted slabs beneath Italy: evidence from seismic tomography and seismicity, *Ann. Geofis., 36,* 2104-214, 1993.

Archivo General de Simancas, Relazione dei luoghi che hanno sofferto in Sicilia nei Terremoti dal nove di gennaio fino al cinque di febbraio del 1693 che si sono sentite ventuno scosse, le primi tre grandi e le altre piú lievi, *Secretería de Estado, Negociación de Sicilia, Consultas decretos y notas, legajo 3507-11,* Palermo, Feb 1697.

Baratta, M., *I Terremoti d'Italia: Saggio di Storia, Geografia e Bibliografia Sismica Italiana,* Forni, Torino, 1901.

Barbano, M. S., The Val di Noto earthquake of January 11, 1693, in *Atlas of Isoseismal Maps of Italian Earthquakes,* CNR-PFG, *Quad. Ric. Sci.,* vol. 2A, pp. 48-49, Bologna, 1985.

Bonaiuti, V., Continuazione dello stesso soggetto [Particolarità intorno al tremuoto che ruinò la Sicilia nel 1693], in *Compendio delle Transazioni Filosofiche della Società Reale di Londra,* part I, *Storia naturale,* vol. 1, *Vulcani e Terremoti,* pp. 34-43, Venezia, 1793.

Boschi, E., G. Ferrari, P. Gasperini, E. Guidoboni, G. Smriglio, and G. Valensise, *Catalogo dei Forti Terremoti in Italia dal 461 a.C. al 1980,* Ist. Naz. di Geofis. and SGA, Storia Geofis. e Ambiente, 973 pp., Bologna, 1995.

Bottone, D., De immani Trinacriae terraemotu: Idea historico-physica, in qua non solum telluris concussiones transactae recensetur, sed novissimae Anni 1717, Messina, 1718.

Burgos, A., Distinta relazione avuta per lettera del P. Alessandro Burgos scritta ad un suo amico, che contiene notizie fin'ora avute de danni cagionati in Sicilia da tremuoti a 9 e 11 gennaio 1693, Palermo-Roma, 1693.

Campis, P., *Disegno Historico o Siano l'Abbozzate Historie della Nobile e Fidelissima Città di Lipari,* Edited by G. Iacolino, Lipari, 1991, 1694.

Del Ben, A., Calabrian arc tectonics from seismic exploration, *Boll. Geof. Teor. Appl., 35,* 339-347, 1993.

D'Addezio, G., and G. Valensise, Metodologie per l'individuazione della struttura sismogenetica responsabile del terremoto del 13 dicembre 1990, in *Contributi allo studio del terremoto della Sicilia Orientale del 13 dicembre 1990,* Edited by E. Boschi and A. Basili, *Int. Rep. 537,* pp. 115-125, Ist. Naz. di Geofis., Rome, 1993.

De Rubeis, V., C. Gasparini, A. Maramai, M. Murru, and A. Tertulliani, The uncertainty and ambiguity of isoseismal maps, *Earthquake Eng. Struct. Dyn., 21,* 509-523, 1992.

De Rubeis, V., C. Gasparini, A. Maramai, and M. Anzidei, Il terremoto siciliano del 13 dicembre 1990, in *Contributi allo studio del terremoto della Sicilia Orientale del 13 dicembre 1990,* Edited by E. Boschi and A. Basili, *Int. Rep. 537,* pp. 9-44, Ist. Naz. di Geofis., Rome, 1993.

Ferrucci, F., G. Gaudiosi, A. Hirn and R. Nicolich, Ionian basin and Calabrian arc: Some new elementss from DSS data, *Tectonophysics, 195,* 411-419, 1991.

Finetti, I., Structure, stratigraphy and evolution of central Mediterranean, *Boll. Geofis. Teor. Appl., 24,* 247-312, 1982.

Ghisetti, A., and L. Vezzani, The structural features of the Iblean plateau and the Mt. Judica area (southeastern Sicily): A microtectonic contribution to the deformational history of the Calabrian Arc, *Boll. Soc. Geol. Ital., 99,* 57-102, 1980.

Grasso, M., H.M. Pedley, and C.D. Reuther, The geology of the Pelagian Islands and their structural setting related to the Pantelleria Rift (Central Mediterranean Sea), *Centro, 1,* 1-19, 1985.

Johnson, J.M., K. Satake, S.R. Holdahl, and J. Sauber, The 1964 Prince Williams Sound earthquake: Joint inversion of tsunami and geodetic data, *J. Geophys. Res., 101,* 523-532, 1996.

Mansinha, L., and D. Smylie, The displacement fields of inclined faults, *Bull. Seismol. Soc. Am., 61,* 1433-1440, 1971.

Mantovani, E., D. Albarello, C. Tamburelli, D. Babbucci, and M. Viti, Plate convergence, crustal delamination, extrusion tectonics and minimization of shortening work as main controlling factors of the recent Mediterranean deformation pattern, *Ann. Geofis., 40,* 611-643, 1997.

Mongitore, A., Istoria cronologica de' terremoti di Sicilia, in *Della Sicilia ricercata nelle cose piú memorabili,* vol. 2, pp. 345-445, Palermo, 1743.

Muglielgini, C. (pseudonym of D. Guglielmini), La Catania destrutta, Palermo, 1695.

Mulargia, F., F. Broccio, V. Achilli, and P. Baldi, Evaluation of a seismic quiescence pattern in southeastern Sicily, *Tectonophysics, 116,* 335-364, 1985.

Piatanesi, A., S. Tinti, and I. Gavagni, The slip distribution of the 1992 Nicaragua earthquake from tsunami run-up data, *Geophys. Res. Lett., 23,* 37-40, 1996.

Purcaru, G., and H. Berkhemer, Regularity patterns and zones of seismic potential for future large earthquakes in the Mediterranean region, *Tectonophysics, 85,* 1-30, 1982.

Reuther, C.D., Z. Ben-Avraham, and M. Grasso, Origin and role of major strike-slip transfers during plate collision in the central Mediterranean, *Terra Nova, 5,* 249-257, 1993.

Spakman, W., Tomographic images of the upper mantle below Central Europe and the Mediterranean, *Terra Nova, 2,* 542-553, 1990.

Tinti, S., and A. Maramai, Catalogue of tsunamis generated in Italy and in Côte d'Azur, France: A step towards a unified catalogue of tsunamis in Europe, *Ann. Geofis., 39,* 1253-1299, 1996. (Corrections, *Ann. Geofis., 40,* 781, 1997.)

Tinti, S., and A. Piatanesi, Numerical simulations of the tsunami induced by the 1627 earthquake affecting Gargano, southern Italy, *J. Geodyn. 21,* 141-160, 1996.

Tinti, S., I. Gavagni, and A. Piatanesi, A finite-element numerical approach for modeling tsunamis, *Ann. Geofis., 37,* 1009-1026, 1994.

A. Piatanesi and S. Tinti, Dipartimento di Fisica, Settore di Geofisica, Università di Bologna, Viale Berti Pichat 8, 40127 Bologna, Italy. (e-mail: alex@ibogfs.df.unibo.it; steve@ibogfs.df.unibo.it)

(Received January 24, 1997; revised November 11, 1997; accepted November 18, 1997.)

4.3 Finite-element simulations of the 5 February 1783 calabrian tsunami

Pergamon

Phys. Chem. Earth, Vol. 21, No. 12, pp. 39–43, 1996

0079-1946/96 $15.00 + 0.00

PII: S0079-1946(97)00007-4

Finite-Element Simulations of the 5 February 1783 Calabrian Tsunami

S. Tinti and A. Piatanesi

Dipartimento di Fisica, Settore Geofisica, Università di Bologna, Bologna, Italy

Received 22 July 1996; accepted 15 December 1996

Abstract. Southern Calabria is one of the Italian coastal regions mostly affected by tsunami hazard. This work is a part of a wider study of the assessment of the tsunami hazard in the southern Calabria and eastern Sicily. The tsunami which we focus our attention on was the first of a series of events that were associated with the 1783 Calabrian seismic crisis that was one of the most catastrophic affecting southern Italy in historical times. The tsunami was generated by an I=XI earthquake: the isoseismal field is elongated in the direction of the Apennine chain and centered in the Gioia Tauro plain where the most relevant damage was reported. Several numerical simulations of the tsunami have been performed by means of a finite-element method based on the shallow-water equations with different sources. The Tyrrhenian sea facing southern Calabria, including the Messina Strait, has been covered by a triangle-based mesh. The numerical results, compared with the available historical observations, such as the polarity of the first arriving wave, the mean wave period, etc. enable us to evaluate the most reliable source mechanisms and locations.

1 Introduction

The Messina Strait together with southern Calabria and eastern Sicily represent the Italian coastal zones mostly affected by tsunami hazard. The strong seismic activity, due to a complex fault system both inland and offshore, caused large destructions in this region. From this point of view, 1783 was a particularly unlucky year, characterized by the most impressive seismic crisis that affected the Calabrian region in historical times. In a period of about two months five destructive earthquakes, with MCS I>IX, occurred in southern Calabria. During this period some tsunamis have been generated: the event on which we are focussing our attention in this work is the first of the series, recently revised by Tinti and Guidoboni (1987 and 1988), while the most disastrous tsunami of the series took place two days later and killed about 1,500 people in the small Calabrian village of Scilla.

With respect to the tsunami considered in our study, the available chronicles report that it was not very damaging and made no victims. The Italian seismic catalog (Postpischl, 1985) reports that the tsunamigenic earthquake occurred on the 5 February 1783, about a quarter past noon, with an estimated MCS I=XI and epicen-

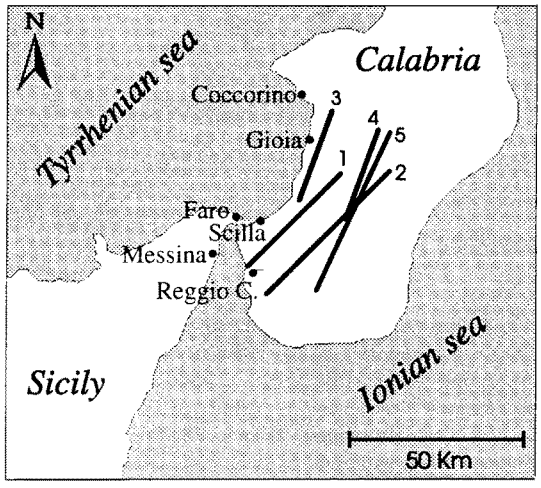

Fig. 1. Geographic sketch of southern Calabria and eastern Sicily, affected by the earthquake. Solid lines, numbered from 1 to 5, represent the faults chosen as tsunamigenic sources in the simulations. Dots show the location of the coastal sites where mareograms are computed.

Correspondence to: S. Tinti

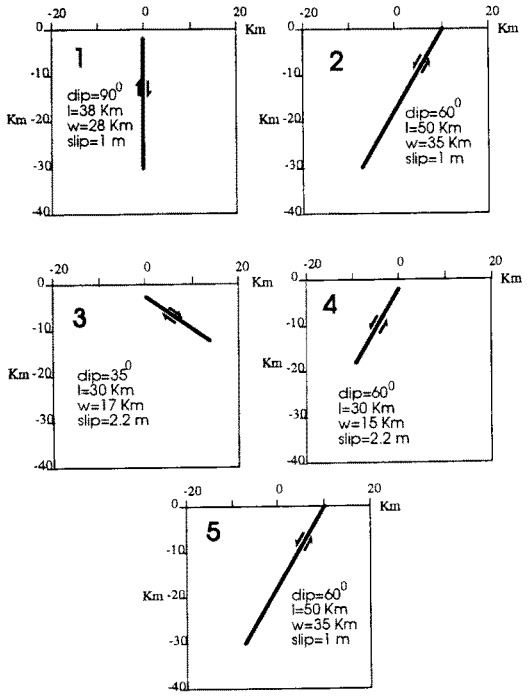

Fig. 2. Cross-section and focal parameters of the faults, numbered from 1 to 5, sketched in Fig. 1.

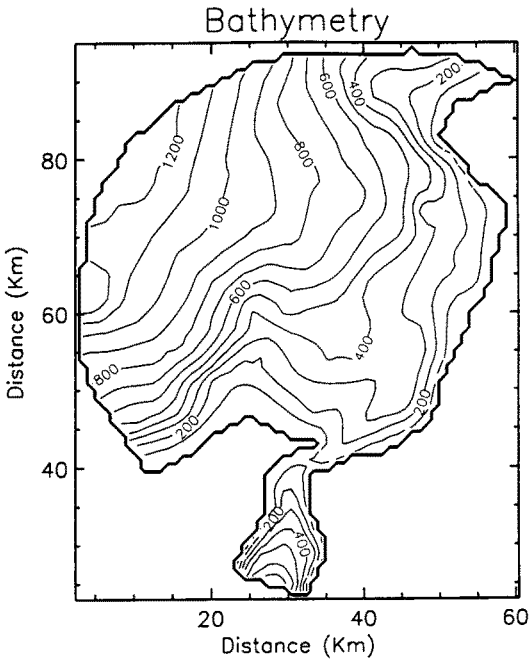

Fig. 3. Bathymetry of the basin chosen for the simulations: contour-line labels are in meters.

tral coordinates 38°20′ N and 16°00′ E. The isoseismal lines are elongated in the NE-SW direction, along the Apennine chain, close to the Gioia Tauro plain, where the largest destruction occurred. Although this event has been widely studied, the identification of the earthquake fault is still open to discussion. From this point of view, the comparison between tsunami simulations and the available tsunami data, such as the first water movement and the period of the waves, is useful to exclude some locations of the fault as well as to constrain the focal mechanism (Piatanesi et al., 1996; Tinti and Piatanesi, 1996). The position and the size of the genetic faults, that we took into account in the present work, are given in Fig. 1, where a geographic sketch of the region affected by the earthquake is also shown.

Furthermore, in Fig. 2 the vertical cross-sections of the above mentioned faults together with the corresponding source parameters are shown. We stress that all fault models do produce subsidence of the Gioia Tauro plain in agreement with geological evidence. In particular, fault number 2 corresponds to the hypothesis advanced by Ogniben (1973) who carried out the first modern geological analysis of this earthquake: this fault was already used to perform a preliminary simulation in a previous work (Tinti and Gavagni, 1995), whose main goal was testing a smoothing algorithm to reduce the numerical noise in the finite-element tsunami modelling. Faults number 3 and 4 have been recently proposed by Valensise and D'Addezio (1994) on the basis of a geomorphological and quantitative geological study of the Gioia Tauro plain. Fault number 5 represents an intermediate hypothesis between faults 2 and 4, while fault 1 is a further tsunamigenic source.

2 Numerical model

In this paper we are focussing our attention on the near-field numerical simulation: to compute the wave evolution we adopt the nonlinear nondispersive shallow-water approximation of the Navier-Stokes equations that is known to be adequate when the typical wavelength is much larger than the water depth. Denoting by ζ the water elevation above the mean sea level, by $\mathbf{v}$ the horizontal velocity vector, averaged over the water column, by h the basin depth and by g the gravity acceleration, the basic dynamic equations can be written as:

$$\begin{cases} \partial_t \zeta = -\nabla \cdot [(h+\zeta)\mathbf{v}] \\ \partial_t \mathbf{v} = -g\nabla\zeta - (\mathbf{v}\cdot\nabla)\mathbf{v} \end{cases} \quad (1)$$

The fields are computed in a finite domain (see Fig. 3) that is delimited by a boundary on which they have to satisfy suitable conditions, that is, pure wave reflection on the solid boundary (coastline) and, ideally, a

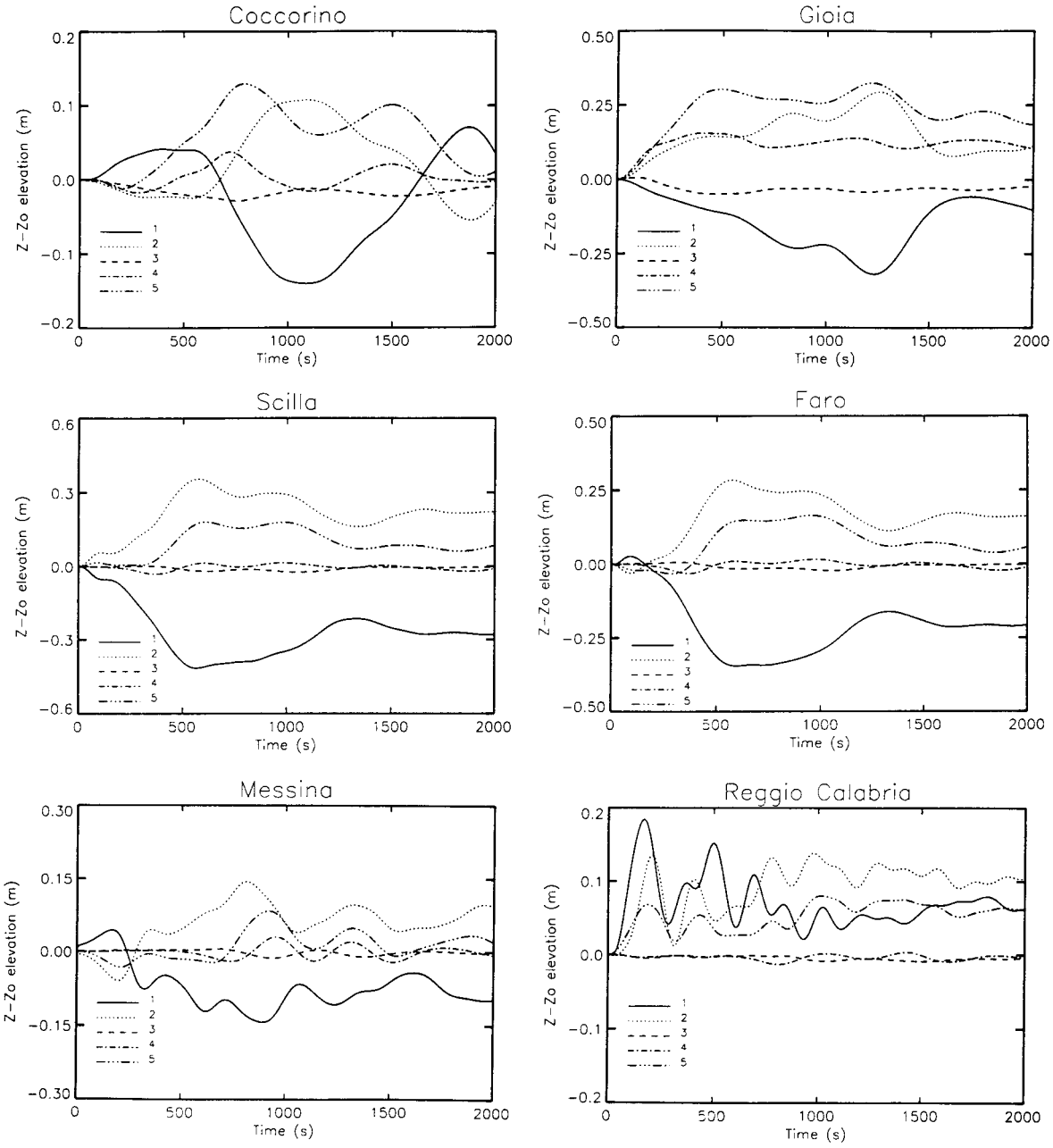

Fig. 4. Computed mareograms in the representative coastal sites shown in Fig. 1. Each panel includes five curves, numbered from 1 to 5, relative to the corresponding source faults. All curves start from a zero-level because coastal tide-gauges experience exactly the same co-seismic displacement as the water surface.

full wave transmission on the open boundary (open sea), mathematically expressed by the following equations:

$$\mathbf{v} \cdot \mathbf{n} = 2(c_1 - c_0) \quad \text{on the open boundary} \tag{2}$$

$$\mathbf{v} \cdot \mathbf{n} = 0 \quad \text{on the solid boundary} \tag{3}$$

Here $c_1 = \sqrt{g(h+\zeta)}$ represents the local phase velocity and $c_0 = \sqrt{gh}$ is the phase velocity of the linear wave. System (1) together with the above conditions has been solved numerically by means of a finite-element method, making use of a Galerkin procedure and linear shape-functions. The basin, shown in Fig. 3, has been covered by a mesh consisting of triangle-shaped elements. In all simulations the initial sea water elevation is assumed to be equal to the coseismic vertical displacement of the sea bottom, that is computed by means of the analytical Manshina-Smylie's model (1971), based on the classic theory of dislocations, which is valid for inclined constant-slip plane faults. This assumption is adequate because the fault's rupture time ($\sim$ 10 s) is much smaller than the typical tsunami period ($\sim$ 1000 s), which allows us to consider a static coseismic deformation. The initial field velocities are considered to be identically null.

3 Discussion and conclusion

We simulated five tsunamis, each relative to a different genetic fault. In order to compare the main features of the simulated tsunamis, six panels are shown in Fig. 4. Each panel is relative to a coastal station (see Fig. 1 for geographic localization) and shows the computed mareograms on this site, corresponding to the five faults numbered from 1 to 5. The final computation time is 2,000 seconds, that is sufficient to take into account the main waves in all the coastal stations considered in the simulations. We want to stress that our basin with reflecting, 10 m deep, vertical walls at the coastal boundaries does not allow to compute the run-up heights and water inundation. Actually, the computed wave amplitudes result to be only a few tens of centimeters, about 5-10 times smaller than what was observed. Specific numerical models dealing with moving boundaries and run-up are believed to reduce this discrepancy, but for the purpose of this research they are not necessary. Coeval sources report that the main effects of the tsunami were observed along the coast of the Messina Strait (see Caputo and Faita, 1984), especially at Scilla and Faro, for which almost all sources describe a small initial withdrawal and a subsequent inundation. In particular, Sarconi (1784) gives us information on the period of the waves observed at Scilla, that was about 10-15 minutes. The tsunami affected also Reggio Calabria, where the sea completely inundated the coastal road. Our analysis leads to the conclusion that faults number 1, 3 and 4 should be rejected as possible tsunami sources. Indeed, from Fig. 4 it can be seen that faults number 3 and 4, that are centered in the Gioia Tauro plain along the Appenine chain, produce wave amplitudes in the Messina Strait that are much smaller than those excited on the Tyrrhenian Calabria (compare for example the time histories at Reggio Calabria and at Gioia): actually the simulated mareograms have a comparatively small amplitude even in the source area, namely at Gioia and at Coccorino. It is therefore clear that these faults, causing indeed a very small displacement of the ocean floor, possess a rather weak capability of generating appreciable tsunami waves, and have to be consequently discarded. As to the fault number 1, we state that even this fault mechanism should be rejected especially because the corresponding tsunami simulation shows an initial inundation in Messina, where a withdrawal was instead observed. In addition, even from a geological point of view, there is no evidence of the existence of this hypothesized fault. It is worth pointing out that all time histories relative to Scilla show that the period of the computed waves is in quite a good accordance with the observed one. The remaining two faults, namely fault number 2 and 5, seem to be the best candidates to the tsunamigenic source of the 5 February 1783 event. In fact, as shown in Fig. 4 and in accordance with the historical reports, they are able to produce an initial withdrawal and a subsequent inundation in Messina. Furthermore, they produce appreciable wave amplitudes both in the town of Scilla, where the main tsunami effects are reported, and in Reggio Calabria, and finally they excite the Strait waters at least as much as the waters in the Calabria Tyrrhenian sea. It is to be remarked that from the available historical tsunami data we are not able to discriminate fault 2 from fault 5 and to establish which one is the most likely tsunami source, but we wish that our research can be followed by further geological and geophysical investigations casting new light in the problem.

Acknowledgements. This research was financed partly by the Commission of the European Communities under the contracts EV5V-CT92-0175 (project GITEC) and ENV4-CT96-0297 (project GITEC-TWO) and partly by the Italian Ministry of the University and of the Scientific and Technological Research.

References

Caputo, M. and Faita, G., Primo catalogo dei maremoti delle coste italiane. *Atti dell' Accademia Nazionale dei Lincei, Mem. Sc. fisiche, matematiche e naturali, Serie VIII, vol. XVII, sez. I,* 7, 213-356, 1984 (in italian).

Manshina, L. and Smylie, D., The displacement fields of inclined faults. *Bull. Seismol. Soc. Amer., 61,* 1433-1440, 1971.

Ogniben, L., Schema geologico della Calabria in base ai dati odierni. *Geol. Romana, 24,* 243-585, 1973 (in Italian).

Piatanesi, A., Tinti, S. and Gavagni, I., The slip distribution of the 1992 Nicaragua earthquake from tsunami run-up data. *Geophys. Res. Lett. ,23,* 37-40, 1996.

Postpischl, D. (ed.), Catalogo dei Terremoti Italiani dall'anno 1000 al 1980, Progetto Finalizzato Geodinamica, CNR, Rome, 1985.

Sarconi, M., Historia de' fenomeni del tremuoto avvenuto nelle Calabrie e nel Valdemone nell'anno 1783 posta in luce dalla Reale Accademia delle Scienze e delle Belle Lettere di Napoli, Napoli, 1784 (in italian).

Tinti, S. and Gavagni, I., A smoothing algorithm to enhance finite-element tsunami modelling: an application to the 5 February Calabrian case, Italy. *Natural Hazards, 12,* 161-197, 1995.

Tinti, S. and Guidoboni, E., Study of the historical tsunamis generated in 1783 off Calabria coasts (Southern Italy). *Proc. Int. Tsunami Symp. 1987,* NOAA/PMEL, 103-108, 1987.

Tinti, S. and Guidoboni, E., Revision of the tsunamis occurred in 1783 in Calabria and Sicily (Italy). *Science of Tsunami Hazards, 6,* 17-22, 1988.

Tinti, S. and Piatanesi, A., Numerical simulations of the tsunami induced by the 1627 earthquake affecting Gargano, Southern Italy. *J. Geodynamics, 21,* 141-160, 1996.

Valensise, G. and D'Addezio, G., Il contributo della geologia di superficie all'identificazione delle strutture sismogenetiche della Piana di Gioia Tauro, ING Internal Report n.559, April 1994, Rome, 1994 (in Italian).

4.4 Finite-element simulations of the 28 December 1908 Messina (Southern Italy) tsunami

Pergamon

Phys. Chem. Earth (A), Vol. 24, No. 2, pp. 145–150, 1999

1464-1895/99/$—see front matter

PII: S1464-1895(99)00010-1

Finite-Element Simulations of the 28 December 1908 Messina Straits (Southern Italy) Tsunami

A. Piatanesi[1,2], S. Tinti[1] and E. Bortolucci[1]

[1]Dipartimento di Fisica, Settore Geofisica, Università di Bologna, Viale Berti Pichat 8, 40127, Bologna, Italy
[2]Present Address: CEA/Laboratoire de Détection et de Geophysique, BP12, 91680 Bruyères-le Châtel, France

Received 15 July 1997; accepted 26 March 1998

Abstract. The earthquake we are dealing with occurred on December 28, 1908: because of the number of victims (about 60,000) and the extension of the destroyed area (6,000 km^2), this earthquake with the epicentral MCS intensity XI may be considered the strongest event ever reported for Italy along with the 1693 eastern Sicily earthquake. The shock produced a large tsunami that caused severe damage and many victims. In all places the first sea movement was a withdrawal for a few minutes, followed by a flooding of the coast with at least three big waves. A post-event survey allowed to estimate flooding and run-up heights (more than 10 m in some places). In this work we perform some numerical simulations of the tsunami generation and propagation, taking into account different source faults: the model is based on the shallow water equations, solved numerically by means of a finite-element method. The computational domain, covered by a mesh consisting of triangular elements, includes the Messina Straits and the sea facing the northeastern coast of Sicily and southern Calabria.

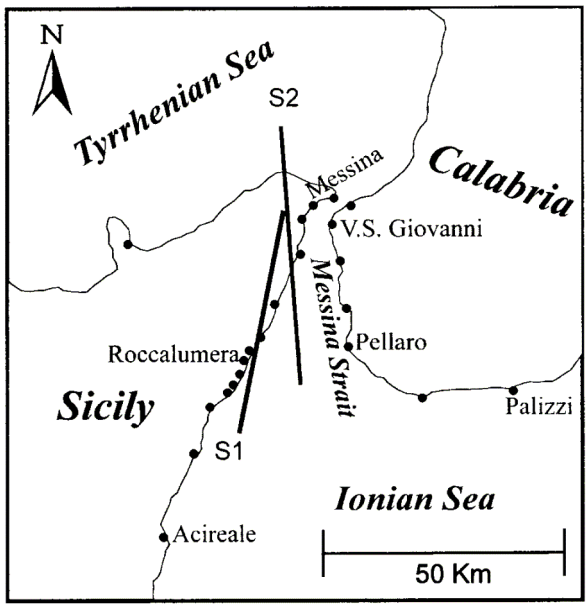

Fig. 1. Geographic sketch of the region involved by the 1908Messina Straits earthquake and tsunami. The solid segments, labeled S1 and S2, are the two faults considered in this work. The dots represent the coastal places for which the polarity of the first impacting wave as well as the run-up heights are available. The six villages where tide-gauge records are computed are also shown.

1 Introduction

The 1908 Messina Straits tsunami is an event of great importance since it was the last catastrophic tsunami that hit the Italian coasts. The generative earthquake was extremely large and destructive, probably the most catastrophic event ever recorded in Italy in our era, causing more than 60,000 victims. The earthquake generated a destructive tsunami that flooded some coastal villages reaching a maximum run-up height exceeding 10 meters. The tsunami started with a large withdrawal along the whole coast of the Messina Straits, followed by a flooding of the coast: three main negative waves and subsequent flooding were reported in many places. Recent studies have tried to estimate the seismic parameters and the focal mechanism of the earthquake source. The magnitude, computed from both body and surface waves, ranges from 7 to 7.2; on the other hand, there is quite a large disagreement on the focal mechanism.

Several source models have been proposed on the basis of seismological observations (Shick, 1977), of levelling observations (Mulargia and Boschi, 1983; Capuano et al., 1988; De Natale and Pingue, 1991; Boschi et al., 1989) and of macroseismic observations (Bottari et al., 1986):

Correspondence to: A. Piatanesi

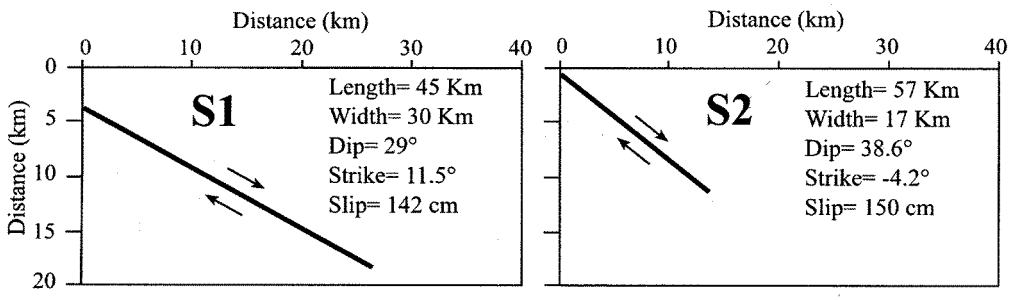

Fig. 2. Vertical cross section of the faults depicted in Fig. 1.

these models are quite different from each other with regard to almost all the fault parameters (length, width, depth, strike and dip angles, etc...).
The aim of this work is to use some fault mechanisms as tsunamigenic source and to simulate the generation, propagation and impact of the tsunami, in such a way to compare the computed effects along the coast with the observed ones.

2 Tsunami modeling

For our simulations we adopt the non-linear shallow water equations:

$$\begin{cases} \partial_t \zeta = -\nabla \cdot [(h+\zeta)\mathbf{v}] \\ \partial_t \mathbf{v} = -g\nabla\zeta - \mathbf{v}\cdot\nabla\mathbf{v} \end{cases} \quad (1)$$

In the above equations ζ represents the water elevation above the mean sea level, $\mathbf{v}$ is the horizontal velocity vector, h the water depth and g the gravity acceleration. This system has been completed by the boundary conditions that are of pure wave reflection on the solid boundary and of full wave transmission on the open boundary, that can be written as:

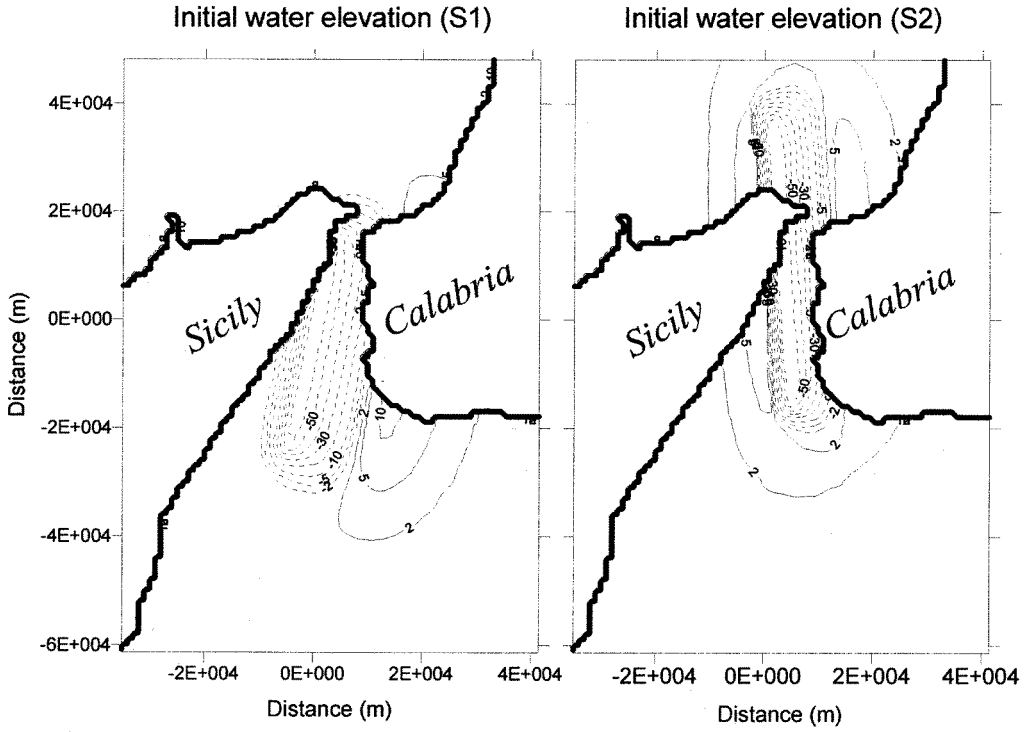

Fig. 3. Contour plots of the initial water elevation induced by the sources S1 (left panel) and S2 (right panel). Solid and dotted lines represent positive and negative elevations respectively: contour labels are in cm.

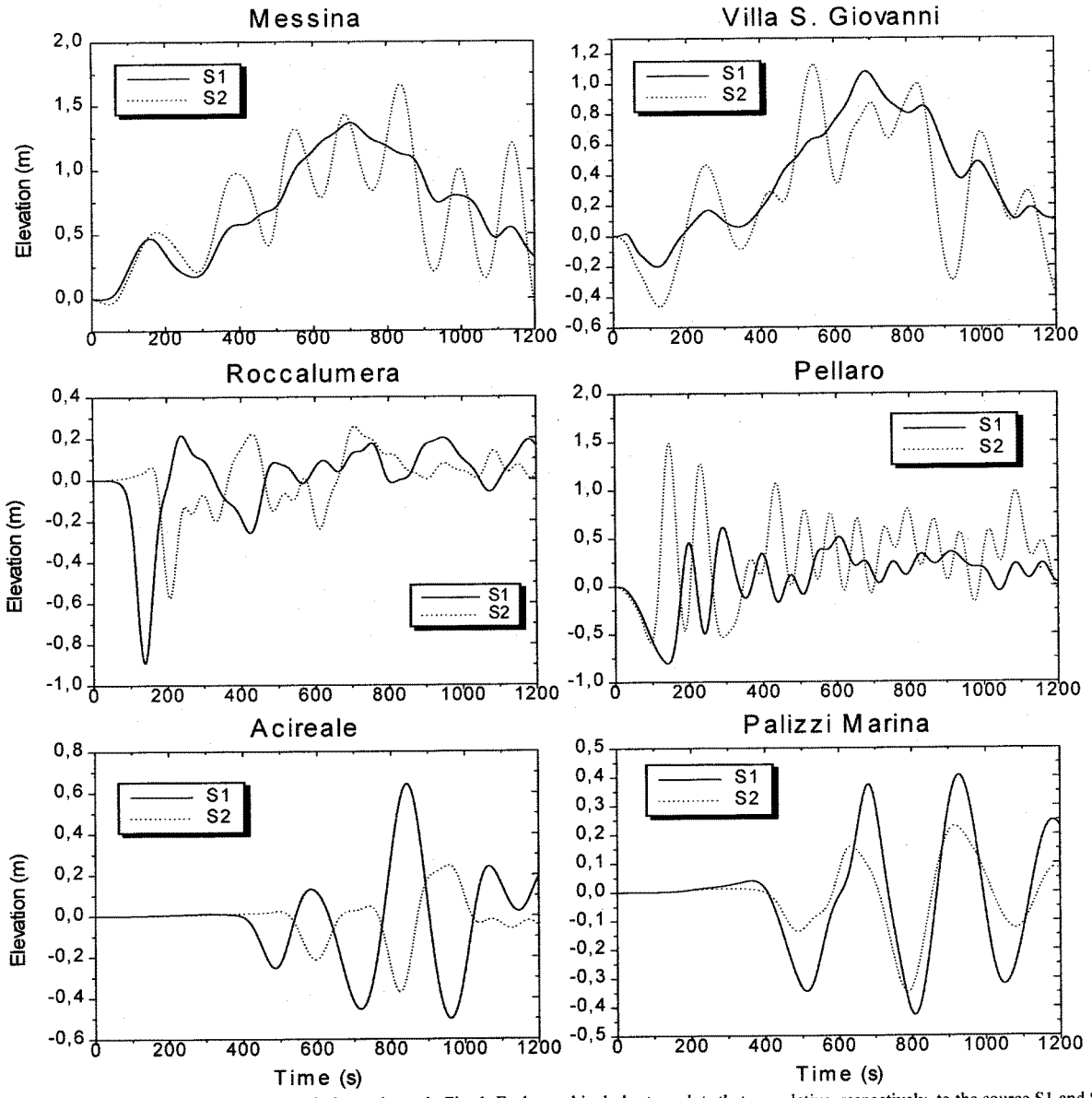

Fig. 4. Computed mareograms in the coastal places shown in Fig. 1. Each panel includes two plots that are relative, respectively, to the source S1 and S2.

$$\mathbf{v}\cdot\mathbf{n} = 2(c_1 - c_0) \quad \text{on the open boundary} \quad (2)$$

$$\mathbf{v}\cdot\mathbf{n} = 0 \quad \text{on the solid boundary} \quad (3)$$

where $c_0=(gh)^{1/2}$ is the phase velocity of the linear wave and $c_1=[g(h+\zeta)]^{1/2}$ is the local phase velocity. In the following simulations the initial sea water elevation is assumed to be equal to the coseismic vertical displacement of the sea bottom, computed through the *Manshina and Smylie* analytical formula (Manshina and Smylie, 1971), while the velocity vector is identically null. Equations (1), (2) and (3) have been solved by means of a finite-element method (Tinti et al., 1994), making use of meshes formed by triangular elements: for the following simulations we used a mesh consisting of about 16,100 elements, that covers the portion of the sea shown in Fig. 1.

3 Numerical simulations

For this event we have information about the polarity of the first impacting wave as well as about run-up heights in some coastal places, that have been measured during a post event field survey (Tinti and Giuliani, 1983; Caputo and

Faita, 1984; Tinti and Maramai, 1996). As tsunamigenic sources we considered two normal faults, labeled S1 and S2, whose locations and source parameters are reported respectively in Fig. 1 and in Fig 2: both faults produce a downlift of the sea bottom along the strait and a smaller uplift in the Calabrian peninsula. Fault S1 has the same strike, dip and mean slip as the fault proposed by Boschi et al. (1989), while fault S2 is similar to that proposed by Capuano et al. (1988), the only difference being that in our case we did not consider a small horizontal slip component. In Fig. 3 the computed initial water elevation fields, produced by the sources S1 and S2, are shown. The initial water elevation induced by fault S1 is a large negative wave involving the whole Messina Straits with a smaller positive wave south of Calabria. Fault S2 produces a similar initial water elevation as in the previous case, the difference being the larger extension of the field north of the straits and the axis orientation.

3.1 Mareograms

To test the tsunami simulations against the available

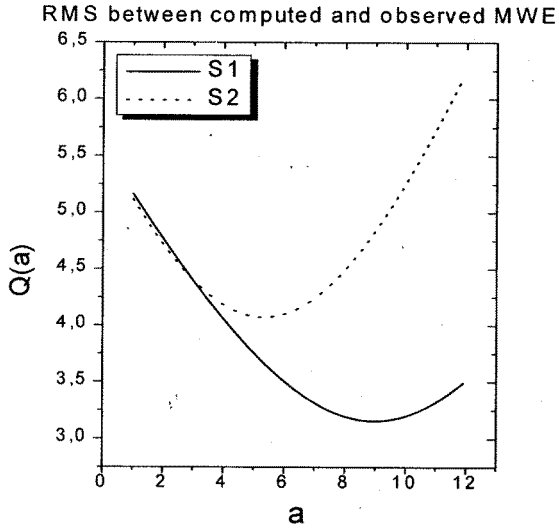

Fig. 5. Root mean square of the residuals versus the amplification factor during the least-squares minimization between the computed maximum water elevations (MWE) and the observed run-up heights.

tsunami data we computed the mareograms in six coastal places for both sources S1 and S2: the geographic sketch of Fig. 1 shows the places we selected for the computation as well as all the localities for which both tsunami polarity and run-up heights are known: in general almost everywhere a first negative wave was seen. The final computation time is 1,200 s, that is sufficient to analyze the main waves for both simulations. From Fig. 4 we can see that in Messina both sources produce a positive first arrival, that is in accordance with the historical reports. At Roccalumera (Sicily coast) we simulated a sharp negative first arrival. In particular, the source S1, that produces a subsequent positive wave about 300 s later, is in good accordance with the observations. Acireale is also in good accordance about wave polarity and arrival time. In Villa S. Giovanni, Pellaro and Palizzi Marina, that can be found along the Calabrian coast from north to south, we simulated a negative first arrival, as reported by local eyewitnesses.

3.2 Maximum water elevations (MWE)

Further important tsunami data available for this event are the run-up heights obtained during a post event field survey. Before showing the comparison between the observed run-up heights and the computed maximum water elevations (MWE) some comments are due about the computed MWE. First of all it is worth stressing that our model, with vertical reflecting, 25 meters deep, walls at the coastal boundaries does not allow to compute the water run-up. Secondly the bathymetry and the finite-element mesh are too coarse to represent the actual coastline and nearshore domain for a reliable local tsunami simulation. Anyway it is useful to compare the shape of the computed and surveyed MWE curves along the coast: to this purpose, we use an amplification factor to adapt the computed elevations to the observed ones. Denoting by Tf the final computation time, the computed MWE w_i at the coastal point i is given simply by:

$$w_i(a) = \max_{t\in[0,T_f]} \{\zeta_i(a,t)\} \tag{4}$$

where the dependence of w_i on the amplification factor a is made explicit. To determine the value of a giving the best fit to the run-up data, a least-squares minimization has been adopted. The root mean square Q:

$$Q(a) = \frac{1}{N}\left(\sum_{i=1}^{N}[w_i(a) - R_i]^2\right)^{1/2} \tag{5}$$

is viewed as a function of a. Here R_i is the observed run-up height at the i-th coastal point and N is the total number of sites (denoted by dots in Fig. 1). The minimum value of Q has been searched for numerically letting the parameter a vary over the range [1,12] at discrete steps of 0.1. Figure 5 shows the results of the minimization applied to the MWE produced by the source S1 and S2. The minimization with the data of source S1 gives the best fit using an amplification factor of 9 while, for source S2 this value is 5.3. Anyway, a better fit with the observed data is obtained

with source S1 than with source S2. The dashed lines in Fig. 6, representing the surveyed run-up heights, shows that the highest water levels are reached in the southern part of the Messina Straits, while the smallest ones are observed northward, in the narrower part of the Straits. The computed MWE, relative to both source S1 and S2, even if multiplied by the respective amplification factors, are different from the surveyed ones. In particular the computed MWE are too large along the northern part of the Calabria coast, while they are rather different along the Sicily coast.

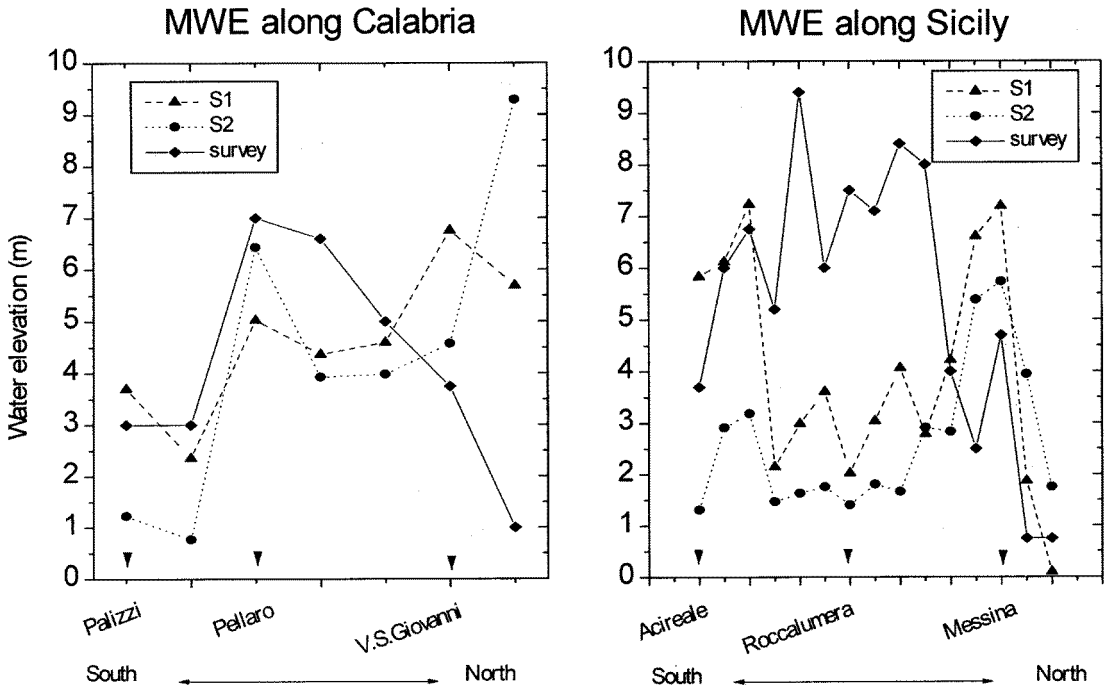

Fig. 6. Comparison between the observed run-up heights and the computed maximum water elevations (MWE) along the coast of Calabria (left panel) and Sicily (right panel). The computed MWE relative to the source S1 and S2, are multiplied, respectively, by an amplification factor equal to 9 and 5.3.

4 Conclusions

The work described in this paper represents a preliminary attempt to simulate the 28 December 1908 Messina Straits tsunami, taking into account the actual bathymetry of the sea and topography of the coast. Two different source mechanisms have been considered. The results of our investigation is that these two sources are compatible with the polarity of the first impacting wave observed in some places along the coast of Sicily and Calabria. Anyway the comparison of the computed maximum water elevations with the observed run-up heights reveals large discrepancies for both sources. One reason is that our model does not allow to compute the water run-up. On the other hand, as recent studies have suggested, a heterogeneous rupture of the fault as well as a horizontal slip component could be reasonable source mechanism. Therefore future developments are needed based on: using finer mesh and more detailed bathymetry data near the coast, using tsunami model especially devoted to run-up calculations and attempting an inversion of the run-up data to infer the slip distribution along the fault, following the method recently used for the Nicaragua 1992 tsunami (see Piatanesi et al., 1996).

Acknowledgements. This research was financed partly by the Commission of the European Communities under the contract ENV4-CT96-0297 (project GITEC-TWO) and partly by the Italian Ministry of the University and of Scientific and Technological Research.

References

Boschi, E., D. Pantosti and G. Valensise, Modello di sorgente per il terremoto di Messina del 1908 ed evoluzione recente dell'area dello Stretto, *Atti VIII Convegno G.N.G.T.S., Roma 1989*, 245-258, 1989 (in Italian).

Bottari, A., E. Carapezza, M. Carapezza, P. Carveni, F. Cefali, E. Lo Giudice and C.Pandolfo, The 1908 Messina Strait earthquake in the regional geostructural framework, *J. Geodynamics, 5*, 275-302, 1986.

Capuano, P., G. De Natale, P. Gasparini, F. Pingue and R. Scarpa, A model for the 1908 Messina Straits (Italy) earthquake by inversion of leveling data, *Bull. Seism. Soc. Am., 78,* 1930-1947, 1988.

Caputo, M. and G. Faita, Primo Catalogo dei Maremoti delle coste italiane, in *Atti dell'Accademia Nazionale dei Lincei, Serie VIII- Volume XVII,* 1984.

De Natale, G. and F. Pingue, A variable slip fault model for the 1908 Messina Straits (Italy) earthquake by inversion of levelling data, *Geophys. J. Int., 104,* 73-84, 1991.

Manshina, L., and D. Smylie, The displacement fields of inclined faults, *Bull. Seismol. Soc. Amer., 61,* 1433-1440, 1971.

Mulargia, F., and E. Boschi, The 1908 Messina earthquake and related seismicity, *Proc. Int. School Phys. E. Fermi,* Earthquakes: observation theory and interpretation, 493-518, 1983.

Piatanesi, A., S. Tinti and I. Gavagni, The slip distribution of the 1992 Nicaragua earthquake from tsunami run-up data, *Geophys. Res. Lett., 23,* 37-40, 1996.

Schick, R., Eine seismotektonische Bearbeitung des Erdbebens von Messina im Jahre 1908, *Geol. Jhrb., 11,* 74, 1977 (in German).

Tinti, S. and D. Giuliani, The Messina Straits Tsunami of December 28, 1908: a critical review of experimental data and observation, *Il Nuovo Cimento, Vol.6,* 429-442, 1983.

Tinti, S.and A. Maramai, Catalogue of tsunamis generated in Italy and in Côte d'Azur, France: a step towards a unified catalogue of tsunamis in Europe, *Annali di Geofisica,* 39,1253-1299, 1996.

Tinti, S., I. Gavagni and A. Piatanesi, A finite-element numerical approach for modeling Tsunamis, *Annali di Geofisica, 37,* 1009-1026, 1994.

Chapitre 5

Distribution du glissement

Le problème de la détermination de la distribution du glissement le long d'une faille sismique tsunamigénique, à l'aide des formes d'onde de tsunamis, a été abordé, pour la première fois, par *Satake* en 1987. Dans ce travail l'utilisation de ce type de donnée est justifiée par l'observation suivante: la bathymétrie des océans, qui détermine la vitesse de propagation des ondes de tsunami, est beaucoup mieux connue que la structure de la Terre déterminant la vitesse des ondes sismiques, si bien que l'effet de la propagation peut être évalué assez précisément à l'aide des calculs numériques. Il présente ensuite une méthode d'inversion des marégrammes, qui permet de déterminer la distribution du glissement sur une faille. *Satake* (1989) applique cette méthode pour étudier la distribution du glissement pour deux séismes tsunamigéniques au Japon: ses résultats montrent que le glissement est distribué, dans les deux cas, d'une façon hétérogène. A la suite de ces travaux, l'inversion des marégrammes devint une méthode assez courant, appliquée avec succès à beaucoup d'autres séismes tsunamigéniques: elle se révèle particulièrement efficace, lorsqu'elle est couplée aux inversions des données géodésiques GPS, qu'elle complète en contraignant la déformation inaccessible au GPS, à savoir celle localisée au fond de l'océan (voir par exemple *Satake*, 1993; *Johnson et al*., 1996; et *Johnson*, 1998 pour une revue).

Toutefois, cette méthode n'est applicable que si on dispose d'un nombre suffisant de formes d'onde de bonne qualité en champ proche. Pour un grand nombre d'événements, celle-ci est difficilement applicable pour les raisons suivantes:

a) on ne dispose pas de marégrammes
b) les marégrammes sont de très mauvaise qualité ou saturés
c) les capteurs qui enregistrent les formes d'onde, sont situés en champ lointain, à plusieurs milliers de kilomètres de la source; dans ce cas, les effets dus aux détails du mécanisme à la source sont généralément effacés par les effets de propagation.

Dans ce chapitre on étudiera la distribution du glissement sur une faille tsunamigénique non pas en s'appuyant sur des formes d'ondes enregistrées, mais sur des hauteurs de run-up en champ proche (se référer à la section 2.3 pour une description de ce type de données), seules données disponibles pour les cas étudiés.

La méthode susdite est ainsi généralisée aux tsunamis qui génèrent des effets locaux, éventuellement dangereux (*Geist and Yoshioka*, 1996; *Geist*, 1998). Cette méthode se base sur l'idée suivante: la forme de la condition initiale et en particulier ses hétérogénéités sont conservées

- au cours de la propagation locale vers la côte et
- au cours de l'inondation des côtes.

Autrement dit, la bathymétrie et la topographie agissent comme une fonction de transfert qui déforme les variations d'amplitude à large échelle de la condition initiale, tout en conservant la distribution gêné des hauteurs des run-up.

On souligne que la méthode proposée, comme d'ailleurs celle de *Satake* (1987) dont elle s'inspire, est valable si la propagation du tsunami est linéaire, ce qui est en général vrai au premier ordre. Pour les deux cas étudiés, les équations de propagation auxquelles on se réfère sont les équations linéaires (2) avec comme conditions limites imposées les équations (3) et (4) (présentées dans le chap.3). L'utilisation de la condition limite (4), qui est une parfaite réflexion de l'onde le long des côtes, ne permet pas le calcul du run-up. De ce fait, on comparera les données de run-up mesurées sur le terrain pendant les inspections post-événements, aux élévations maximales calculées le long de la côte.

Dans la section 4.1, on présentera la méthode d'inversion utilisée et une application au tsunami du Nicaragua de 1992, événement de grand intérêt et très étudié, car il représente un cas typique de « tsunami earthquake » (*Kanamori and*

Kikuchi, 1993). On montre que la distribution du glissement le long de la faille source est très hétérogène, avec deux régions bien délimitées où le glissement est concentré. *Ihmlé* (1996), en utilisant une méthode indépendante d'inversion des ondes de surface longue période, a confirmé ce résultat (voir Figure 16).

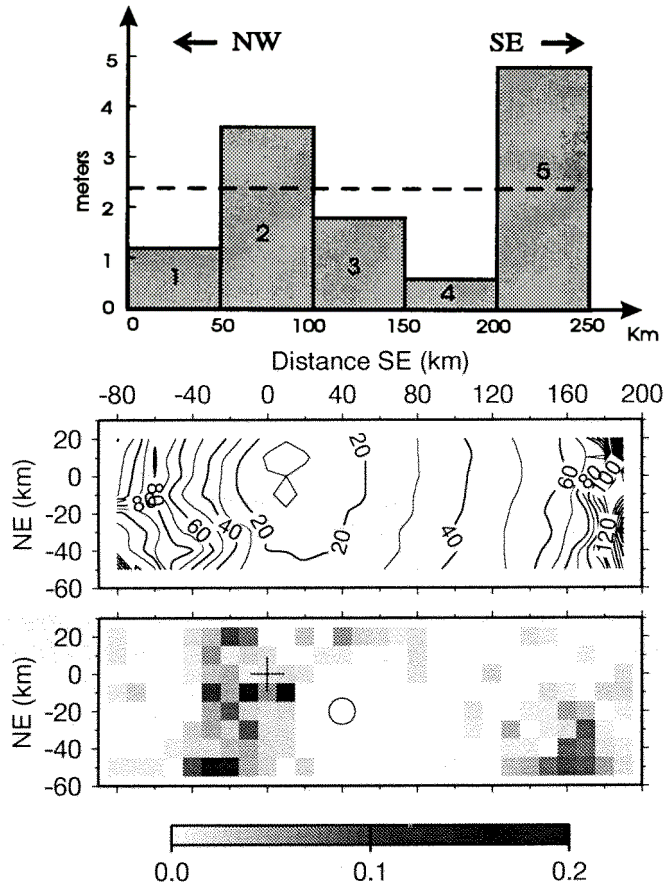

Figure 16. En haut: distribution du glissement le long de la faille du séisme tsunamigénique du Nicaragua 1992, déterminée par les données de run-up (d'après *Piatanesi et al.*, 1996). En bas: distribution de la densité du moment sismique, déterminée par *Ihmlé* (1996) à l'aide d'une technique d'inversion des ondes de surface longue période. Note: l'origine des repères géographiques dans les deux figures est différente, mais l'échelle est la même.

L'article qui constitue la section 4.2 représente la suite de l'étude du tsunami de Messine en 1908, présentée à la section 4.4. On considère ici un nouveau modèle de faille, caractérisé par une distribution hétérogène du glissement qui, par rapport aux modèles à glissement homogène, conduit à des résultats plus proches des données observées de run-up.

5.1 The slip distribution of the 1992 Nicaragua earthquake from tsunami run-up data

GEOPHYSICAL RESEARCH LETTERS, VOL. 23, NO. 1, PAGES 37-40, JANUARY 1, 1996

The slip distribution of the 1992 Nicaragua earthquake from tsunami run-up data

Alessio Piatanesi, Stefano Tinti and Ivan Gavagni
Dipartimento di Fisica, Settore di Geofisica, Università di Bologna

Abstract. The 2 September 1992 Nicaragua tsunami was induced by an $M_S \simeq 7-7.3$ earthquake and caused about 170 victims and significant damage to the coastal areas. The aim of this work is to infer the slip distribution along the causative seismic fault from the available tsunami run-up field data. We have subdivided the fault plane into five slip-independent subfaults and computed the corresponding numerical Green's functions by integrating shallow-water equations via a finite-element technique. The slip distribution on the fault has been determined by applying a least-squares procedure to the differences between the observed run-up values and the computed maximum water levels along the coast. The main result is that the best fit is found for a nonuniform coseismic slip, with the highest displacement taking place in the southernmost part of the fault. The measure of the improvement is given by the global rms residual of the heterogeneous-slip case being circa 25% smaller than that of the uniform case. An ancillary outcome of the analysis is the evaluation of the mean amplification factor of the tsunami wave investing the Nicaraguan coast, that, on assuming a rigidity of 1 x 10^{10} N/m^2, results to be 3.45.

Introduction

On the 2nd September 1992 the Pacific coast of Nicaragua was affected by a large tsunami with wave heights up to 10 meters, causing about 170 victims and damaging numerous villages along the coast. The earthquake epicentre was located in correspondence of the Middle American Trench, off the west coast of Nicaragua. The inversion of both body and surface waves suggested a bilateral rupture and a long source duration time of about 100 sec [*Ide et al.*, 1993; *Kikuchi and Kanamori*, 1995]. Seismological analyses gave a seismic moment of about 3 x 10^{20} Nm, and a fault plane 200 Km long and 100 Km wide [*Ide et al.*, 1993]. The numerical tsunami simulations performed by *Imamura et al.*, [1993], who assumed the above fault size and a standard rigidity $\mu = 3$ x 10^{10} N/m^2, produced results consistent with the observed run-up, but at the cost of taking the seismic moment one order of magnitude greater than that estimated from seismic wave analysis. To reduce this discrepancy *Satake* [1994] suggested a different source model, namely a fault plane 250 Km long and 40 Km wide, a 3 m uniform slip and a rigidity $\mu = 1$ x 10^{10} N/m^2. The result was that the seismic moment was in accordance with that inferred from seismology and the maximum water level, computed along the coast and opportunely multiplied by an amplification factor, fitted generally well the observed data. However, even with Satake's modifications of the source parameters, a substantial discrepancy remains between simulations and observations in the southernmost part of the Nicaraguan coast, south of Casares. In the present work, on renouncing the idea of a uniform-slip source, we will show that a heterogeneous-slip model can be found that reduces noticeably the differences between computations and field data.

Paper number 95GL03606
0094-8534/96/95GL-03606$03.00

Tsunami Simulations

To compute the tsunami evolution we adopted the shallow-water approximation. Denoting by ζ the water elevation above the mean sea level, by $\mathbf{v}$ the horizontal velocity vector, by h the basin depth and by C_f the drag coefficient, the governing set of nonlinear equations can be written as follows:

$$\begin{cases} \partial_t \zeta = -\nabla \cdot [(h+\zeta)\mathbf{v}] \\ \partial_t \mathbf{v} = -g\nabla\zeta - (\mathbf{v}\cdot\nabla)\mathbf{v} - C_f \mathbf{v}|\mathbf{v}|/(h+\zeta) \end{cases} \quad (1a)$$

and further simplified to the following linear form:

$$\begin{cases} \partial_t \zeta = -\nabla \cdot [h\mathbf{v}] \\ \partial_t \mathbf{v} = -g\nabla\zeta \end{cases} \quad (1b)$$

The systems (1) are completed by the conditions of (i) pure wave reflection on the solid boundary (i.e. the coastlines) and (ii) full wave transmission on the open boundary, and have been solved numerically by means of a finite-element method applied over a grid of 13,241 variable-size triangular elements with linear shape functions [see *Tinti et al.*, 1994 for details]. Figure 1 shows the oceanic domain used for the simulations together with the position and the size of the seismic fault. The assumed source parameters, that is fault length of 250 Km, width of 50 Km, strike angle of 312°, dip angle of 16°, rigidity $\mu = 1$ x 10^{10} N/m^2 and an averaged slip of 2.4 m, correspond to a seismic moment that is in accordance with the seismological evidence. The initial water elevation has been taken to be as large as the coseismic vertical displacement of the sea bottom,

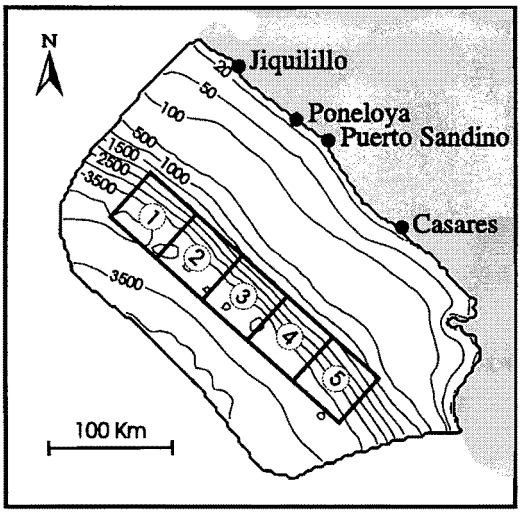

Figure 1. Domain chosen for the simulations. The shaded area is the Pacific coast of Nicaragua. The bathymetric contour-line labels are in meters. The seismic fault (rectangle) is partitioned into slip-independent subfaults numbered 1 to 5 from NW-SE.

while the initial field velocity has been assumed to be identically null. It is worth stressing that our basin with vertical reflecting, 10 m deep, walls at the coastal boundaries does not allow to compute the water run-up: in the following the run-up field data will be therefore compared to the maximum water level, simply denoted by W, calculated along the coast.

Outline of the Method

We have subdivided the fault plane into five slip independent subfaults, each being 50 Km long and 50 Km wide and having a uniform slip. We have then computed the global solution as the superposition of the solutions corresponding to the individual subfaults. The selected dimension of the subfaults is a good compromise between (i) the requirement for their size being remarkably greater than the average grid-element size and (ii) the resolution acceptable for the slip distribution along the seismic fault. *Satake*, [1987], making use of a finite-difference model, inverted tsunami tide-gauge records to infer the slip distribution along a tsunamigenic fault. Unfortunately Satake's method cannot be reliably applied in the present istance since only two tide-gauge records are available for the 2 September 1992 Nicaragua tsunami. The alternative idea is to use the run-up data from the post-event field surveys [*Abe et al.*, 1993; *Baptista et al.*, 1993; *Satake et al.*, 1993], that are available for numerous locations along the coast.

By virtue of the superposition principle applied to the linear system (1b), the water elevation $\zeta_i(t)$ at the coastal point i can be computed as the combination of the time series associated with the elementary sources:

$$\zeta_i(a, \mathbf{c}; t) = a \sum_{j=1}^{N_S} c_j G_{ij}(t) \qquad (2)$$

In this formula G_{ij} is the time history corresponding to the j-th subfault, calculated by means of the finite-element software at the i-th coastal point and may be considered as the numerical Green's function. The parameter vector $\mathbf{c}$ is the vector of the coefficients $c_j (j = 1, 2, ..., N_S)$ related to the slip magnitude of the j-th source ($c_j = 1$ corresponding to the reference slip value of 2.4 m), and N_S is the number of sources (N_S=5 in this case). Furthermore, a is a mean amplification factor, similar to that introduced by Satake in his numerical simulations [1994], that is used to adapt the computed maximum water level to the observations over the whole coastline. It can be interpreted as an estimator of the mean amplification the waves experience in climbing up the beach slope from the model coastal boundary (that is actually slightly offshore, being assumed to be 10 m deep), and therefore it is somehow related to the average run-up along the Nicaraguan coast. Denoting by T_f the final computation time, the computed maximum water level W_i at the coastal point i can be given the following expression:

$$W_i(a, \mathbf{c}) = \max_{t \in [0, T_f]} \left\{ \zeta_i(a, \mathbf{c}; t) \right\} \qquad (3)$$

where the dependence of W_i on both the mean amplification factor and the slip coefficients is made explicit. To determine the slip distribution along the fault giving the best fit to the run-up field data, the least-squares approach has been adopted. The sum Q of the squared residuals:

$$Q(a, \mathbf{c}) = \sum_{i=1}^{N} \left[W_i(a, \mathbf{c}) - R_i \right]^2 \qquad (4)$$

is viewed as a function of the parameters a and $\mathbf{c}$. Here R_i is the mean observed run-up height at the i-th coastal point and N is the total number of sites. The minimum value Q_{min} of the sum Q has been searched for numerically by letting the parameters vary over reasonable ranges at discrete steps. The coefficients c_j have been explored from $c_j = 0.0$ (no slip allowed on the j-th subfault) up to $c_j = N_S$ (all slip concentrated on the j-th subfault) by an increment of 0.25, on imposing the constraint that the average slip value over the

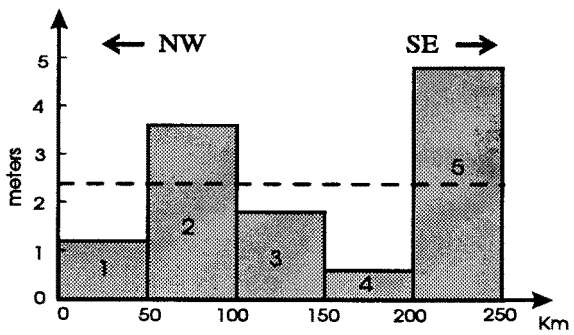

Figure 2. Best estimate of the slip distribution. The numbers inside the rectangles correspond to the subfault numbers shown in Figure 1. The dashed line marks the slip value in the instance of a uniform source.

entire fault be equal to 2.4 m (which implies that their sum be equal to N_S). This resulted in a total of 10,626 possible source configurations. The amplification factor a has been varied in the range [2.5,4.0] by a step of 0.05, which entails the computation of 10,626 × 31 = 329,406 values of the sum Q. The parameters corresponding to Q_{min} give the slip distribution shown in Figure 2. In order to check the stability of the obtained configuration we have considered all the sets of parameters $\{a, \mathbf{c}\}$ associated with the values of Q comprised within the 5% interval around Q_{min}, that is satisfying the inequality $(Q - Q_{min})/Q_{min} < 0.05$, and have then computed the related frequency distribution. They are displayed alltogether in Figure 3, where they are seen to be peaked around the best parameter values we have found, which is especially true for the slip coefficient c_5 that is associated with the southernmost segment of the fault. At this stage, the coseismic sea-floor vertical displacement generated by the found slip distribution and calculated by means of the classical dislocation theory has been assumed as the initial water elevation for the Nicaragua tsunami computation (see Figure 4).

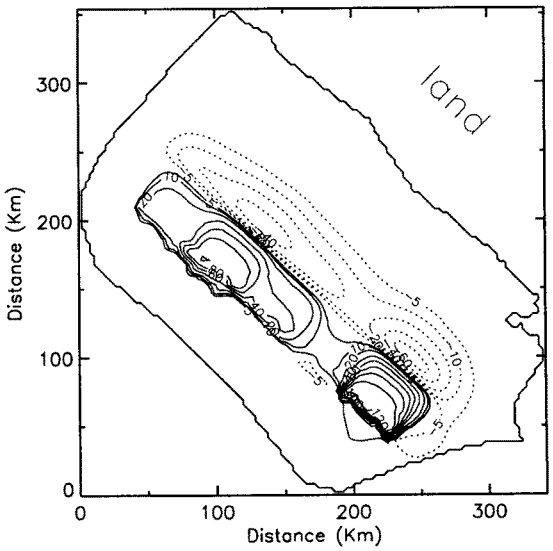

Figure 4. Coseismic sea-bottom vertical displacement generated by the heterogeneous source shown in Figure 2. Line labels are in centimeters, solid and dotted lines being positive and negative elevations respectively.

Discussion and Conclusions

Tsunami simulations have been perfomed by using both the nonlinear and the linear versions of the system (1). Our results show that there is no sensible difference between the two cases: an example is given in Figure 5 where the time history computed at Poneloya is plotted for both models: the first depression as well as the following positive peak are almost equal for the two time series, except for a slight phase displacement, the difference becoming appreciable only for the later oscillations that are however irrelevant for our analysis focussed on the maximum water level. Figure 6 displays the computed maximum water level along the coastal grid nodes corresponding to a uniform- and a heterogeneous-slip source. These can be compared with the run-up heights observed by different international teams in the course of independent field surveys. Though the observed run-up values measured in the same site are rather spread, owing to very local coastal conditions, the curve resulting from the heterogeneous source model exhibits a trend that is visibly better than that corresponding to the uniform-slip, especially in the southernmost part of the coast. To quantify the improvement, we have computed the sum of the root mean square (rms) of all available residuals $W_i - R_i$ (i ranging over all the N sites) for three cases: the uniform-slip (2.4 m) source with linear propagation, and the nonuniform-slip source (given in Figure 2) both with linear and nonlinear propagation. We have found the respective values of 1.89, 1.49 and 1.47 (in meters), the clear conclusion being therefore that the heterogenous source provides about a 25% rms reduction over the uniform-source case, being moreover once again proved that there is no significant difference between linear and nonlinear simu-

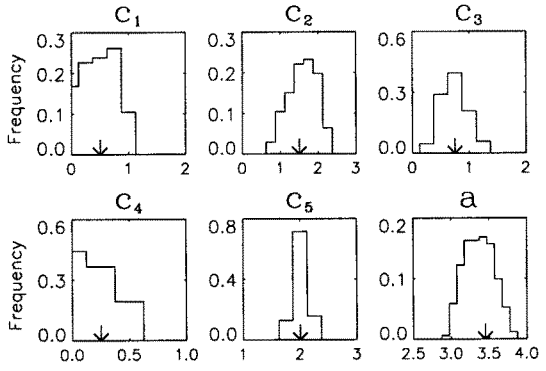

Figure 3. The 5% frequency distributions of the slip coefficients and of the amplification factor: all plots are peaked around the best-fit values (marked by arrows) that are, in the order, 0.5, 1.5, 0.75, 0.25 and 2.0 for the slip coefficients $c_1 \div c_5$ and 3.45 for the amplification factor a.

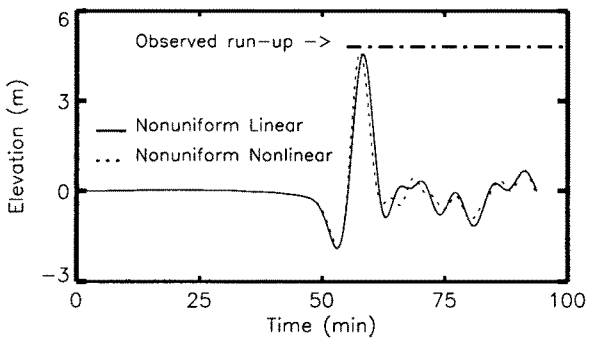

Figure 5. Linear and nonlinear water elevations computed at Poneloya for the final heterogeneous source model. The observed run-up is also given.

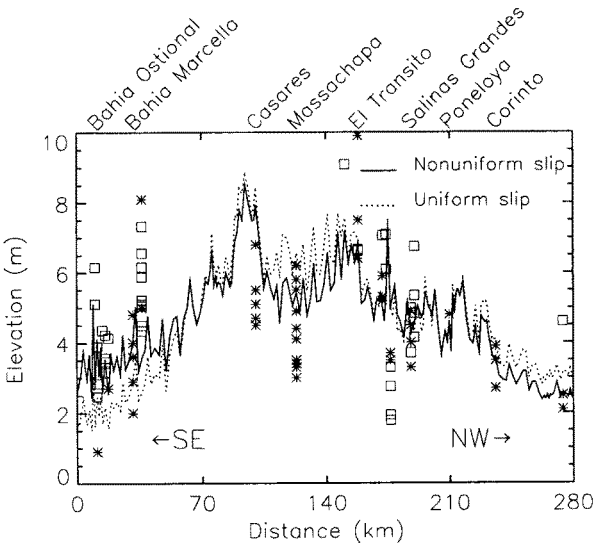

Figure 6. Maximum water levels computed through the nonlinear shallow-water theory for both the uniform (dotted line) and heterogeneous (solid line) source models. Observed run-ups are also given (squares: from *Baptista et al.*, [1993]; stars: from *Abe et al.*, [1993]. Distances are measured along the Nicaragua coastline.

lations. The remaining 75% rms discrepancy cannot be further reduced by our model: it can be easily attributed to run-up variations over very short scale (1 km or less), that could be accounted for only with a much more detailed bathymetry-topography grid and a numerical model explicitly devised for run-up computations (see e.g. *Titov and Synolakis*, [1993]).

The method described in this work has the merit to be applicable even when only run-up observations from post-event field surveys are available. In the case treated here, the inversion of the run-up data has proven to be quite stable, giving parameters distributions satisfactorily peaked around the least-squares best-fit values. The main result is that our analysis is suggestive of a source-slip heterogeneity, the maximum slip value occurring in the southernmost part of the fault. A further outcome of our investigation is the evaluation of the mean amplification of the tsunami waves at the coast ($a = 3.45$). This result can be easily extended to cases with different assumptions of rigidity values, since the mean amplification may be proven to be simply proportional to μ. In fact, in virtue of the seismic moment constraint, the average fault slip and accordingly the coseismic sea bottom displacement are proportional to μ^{-1}. As to the tsunami, this implies that the numerical Green's functions in eq.(2) are proportional to μ^{-1} as well, and hence that assuming a mean amplification $a' = \mu a/\mu_0$ (μ_0 being the reference unitary value) will produce a μ-independent sea-surface elevation ζ, exactly leading to the same least-squares minimization computations and results we found here.

Possible future developments of this study are (i) to use finer grids and more detailed bathymetry data especially near the coast in order to investigate better the local amplification of the waves and (ii) to use tsunami models with dynamically moving boundaries along the coastlines accounting for local inundation.

Acknowledgments. This research was financed partially by the Commission of the European Communities under the contract EV5V-CT92-0175 (project GITEC) and partially by the Italian Ministry of the University and of Scientific and Technological Research. We are indebted to Dr.Satake for providing us files with bathymetric data.

References

Abe, K.,K. Abe, Y. Tsuji, F. Imamura, H. Katao, Y. Iio, K. Satake, J. Bourgeois, E. Noguera, and F. Estrada, Field survey of the Nicaragua earthquake and tsunami of September 2, 1992 (in Japanease), *Bull. Earthq. Res. Inst., Univ. of Tokyo, 68,* 23-70, 1993.

Baptista, A.M., G.R. Priest, and T.S. Murty, Field survey of the 1992 Nicaragua tsunami, *Marine Geodesy, 16,* 169-203, 1993.

Ide, S., F. Imamura, Y. Yoshida, and K. Abe, Source characteristics of the Nicaragua tsunami earthquake of September 2, 1992, *Geophys. Res. Lett., 20,* 863-866, 1993.

Imamura, F., N. Shuto, S. Ide, Y. Yoshida, and K. Abe, Estimate of the tsunami source of the 1992 Nicaragua earthquake from tsunami data, *Geophys. Res. Lett., 20,* 1515-1518, 1993.

Kikuchi, M., and H. Kanamori, Source characteristics of the 1992 Nicaragua tsunami earthquake inferred from teleseismic body waves, *Pure and Applied Geophysics, 144,* 441-453, 1995.

Satake, K., Inversion of tsunami waveforms for the estimation of a fault heterogeneity: method and numerical experiments, *J. Phys. Earth, 35,* 241-254, 1987.

Satake, K., J. Bourgeois, Ku. Abe, Ka. Abe, Y. Tsuji, F. Imamura, Y. Iio, H. Katao, E. Noguera, and F. Estrada, Tsunami field survey of the 1992 Nicaragua earthquake, *Eos, Trans. Am. Geophys. Union, 74, 145,* 156-157, 1993.

Satake, K., Mechanism of the 1992 Nicaragua tsunami earthquake, *Geophys. Res. Lett., 21,* 2519-2522, 1994.

Tinti, S., I. Gavagni, and A. Piatanesi, A finite-element numerical approach for modelling tsunamis, *Annali di Geofisica, 37,* 1009-1026, 1994.

Titov, V.V., and C.E. Synolakis, A numerical study of wave runup of the September 2, 1992 Nicaraguan tsunami, *Proc. of the IUGG/IOC International Tsunami Symposium, Wakayama, Japan,* 627-635, 1993.

Stefano Tinti, Dipartimento di Fisica, Settore di Geofisica, Università di Bologna, Viale Berti Pichat, 8, 40127 Bologna, Italy (e-mail: steve@ibogfs.df.unibo.it).

(received May 17, 1995; revised September 5, 1995; accepted October 20, 1995.)

5.1 The slip distribution of the 1992 Nicaragua earthquake from tsunami run-up data

Pergamon

Phys. Chem. Earth (B), Vol. 24, No. 5, pp. 417–421, 1999

1464-1909/99/$ - see front matter

PII: S1464-1909(99)00022-2

Identification of the Source Fault of the 1908 Messina Earthquake through Tsunami Modelling. Is it a Possible Task?

S. Tinti[1], A. Armigliato[1], E. Bortolucci[1] and A. Piatanesi[2]

[1]Dipartmento di Fisica, Settore di Geofisica, Università di Bologna, Viale Carlo Berti Pichat, 8, 40127, Bologna, Italy
[2]Laboratoire de Detèction et de Geophysique, BP12, 91680 Bruyères-le-Chatel, France

Received 6 August 1998; accepted 9 November 1998

Abstract. The 1908 Messina Straits tsunami is the last catastrophic event that hit the Italian coast. The parent earthquake may be considered one of the strongest shocks reported in Italian seismic catalogues. Several source models have been proposed in the literature that are quite different with regard to almost all the fault parameters. The aim of this work is to evaluate whether tsunami data can add reliable information for the identification of the fault mechanism of this earthquake. Tsunamis generated by two of the faults proposed in the literature were simulated via finite-element modelling in a former work (see Piatanesi et al., 1998): the results were in good agreement with the observations as regards the polarity of the first wave, whereas a relevant disagreement was found as far as run-up data were concerned. In this paper, that may be considered the continuation of the previous work, we focus on a particular fault, the one proposed by Capuano et al. (1988), and simulate the consequent tsunami adding two new features to possibly improve the agreement with run-up observations: i) an algorithm allowing for the effect of the sea bottom bathymetry on the tsunami initial condition, and ii) a heterogeneous slip distribution on the fault.

1 Introduction

The 1908 Messina Straits earthquake is the largest seismic event occurred in Italy in the last century: 60,000 people were killed and extensive damage was produced in Sicily and Calabria. The greatest destruction was suffered by the cities of Messina and Reggio Calabria: in the latter, degree XI of the MSK intensity scale was reached. The estimated magnitude, computed from both body and surface waves, ranges in the interval 7 - 7.2, corresponding to a seismic moment of about 5×10^{19} Nm. Precision levellings had been carried out a few years before the earthquake and some lines were resurveyed just after the event: being the interval between measurements rather short, the observed displacements (see Tinti and Giuliani, 1983) may be reliably interpreted as coseismic movements. All along the Calabrian coast negative values were measured, which implies that this part of Calabria was all downlifted during the rupture process. The amount of available data is smaller as regards Sicily and indicates subsidence also in the area north of Messina, with a large gradient of the displacement that runs from -70 cm to zero in about 12 km of levelling.

The earthquake was followed by a tsunami that started with a large withdrawal along the whole Messina Straits, followed by a flooding of the coast that in some villages produced an observed maximum run-up exceeding 10 m. Three main negative waves and subsequent inundation were reported in many places: locally the water waves entered 200 m inland. By looking at the map of the maximum water heights measured in several places both in Sicily and in Calabria (see Tinti and Giuliani, 1983), we observe that high values were reached not only in the region of the Straits, but also along the southern part of Sicily.

Several source models have been proposed in the last years on the basis of seismological (Shick, 1977), macroseismic (Bottari et al.,1986) or levelling observations (Mulargia and Boschi, 1983; Valensise, 1988; Boschi et al., 1989; Capuano et al., 1988; De Natale and Pingue, 1991). A general agreement on the correct fault has not been achieved yet. The most recent hypotheses on the fault parameters are those proposed on one hand by Valensise (1988) and Boschi et al. (1989), and on the other by Capuano et al. (1988) and De Natale and Pingue (1991). The solid segments depicted in Figure 1a represent the vertical projection of the upper borders of the two faults on the earth's surface (S1 and S2 refer to the sources by Boschi et al. (1989) and by Capuano et al. (1988), respectively). Finite-element (FE) tsunami simulations have been performed for both sources in a previous work by Piatanesi et al. (1998): what they found out in both cases was a good agreement with observations as far as the first wave polarity is concerned, but a large discrepancy between observed run-up values and computed maximum water elevations.

Here we will focus on the Capuano et al. (1988) fault, that is the one for which the most recent studies have been

Correspondence to: S.Tinti

carried out (see De Natale and Pingue, 1991), and try to improve matching between computed and observed run-ups in two ways:

1) by taking into account the effect of bathymetry on the initial water elevation field: we have developed a new algorithm that applies to FE tsunami modelling an idea already introduced by Tanioka and Satake (1996) for finite-difference schemes;
2) by introducing a heterogeneous distribution of the slip along the fault.

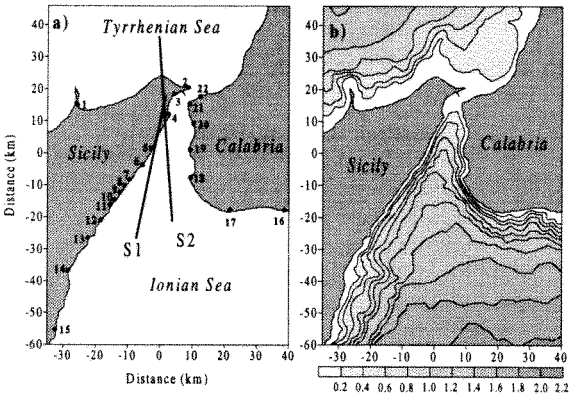

Fig. 1. **(a)** Computational domain used in FE simulations. The domain has been discretised with a grid consisting of 8341 nodes and 16,064 triangular elements. The stations in which time-histories and run-up values have been computed are shown (1. Milazzo, 2. Punta Faro, 3. Pace, 4. Messina, 5. Galati Marina, 6. Scaletta Zanclea, 7. Ali Marina, 8. Nizza Sicula, 9. Roccalumera, 10. Santa Teresa, 11. Sant'Alessio, 12. Letojanni, 13. Giardini Naxos, 14. Riposto, 15. Acireale, 16. Palizzi Marina, 17. Melito di Porto Salvo, 18. Pellaro, 19. Reggio Calabria, 20. Gallico Marina, 21. Villa S.Giovanni, 22. Cannitello). The solid segments represent the vertical projection on the earth's surface of the upper border of the faults proposed by Boschi et al. (1989) and by Capuano et al. (1988), denoted as S1 and S2 respectively. **(b)** Bathymetry adopted in this study. The numbers on the scale are expressed in kilometres.

2 Tsunami modelling

In our simulations we adopt the non-linear shallow water equations:

$$\begin{cases} \partial_t \zeta = -\nabla \cdot [(h+\zeta)\mathbf{v}] \\ \partial_t \mathbf{v} = -g\nabla\zeta - \mathbf{v}\cdot\nabla\mathbf{v} \end{cases} \quad (1)$$

In the above equations ζ represents the water elevation above the mean sea level, h the water depth, $\mathbf{v}$ is the horizontal velocity vector and g the gravity acceleration. System (1) is completed by suitable boundary conditions, that is of pure wave reflection on the solid boundary and of full wave transmission on the open sea:

$$\mathbf{v}\cdot\mathbf{n} = 2(c_l - c_0) \quad \text{on the open sea} \quad (2)$$

$$\mathbf{v}\cdot\mathbf{n} = 0 \quad \text{on the solid boundary} \quad (3)$$

where $c_0 = (gh)^{1/2}$ is the phase velocity of the linear wave and $c_l = [g(h+\zeta)]^{1/2}$ is the local phase velocity. Equations (1)-(3) were solved by means of a FE method (see Tinti et al., 1994). In Figure 1a the computational domain with the places in which time-histories and run-ups have been computed is shown, while the bathymetry is depicted in Figure 1b. The domain was discretised with a FE grid consisting of 8341 nodes and 16,064 triangular elements.

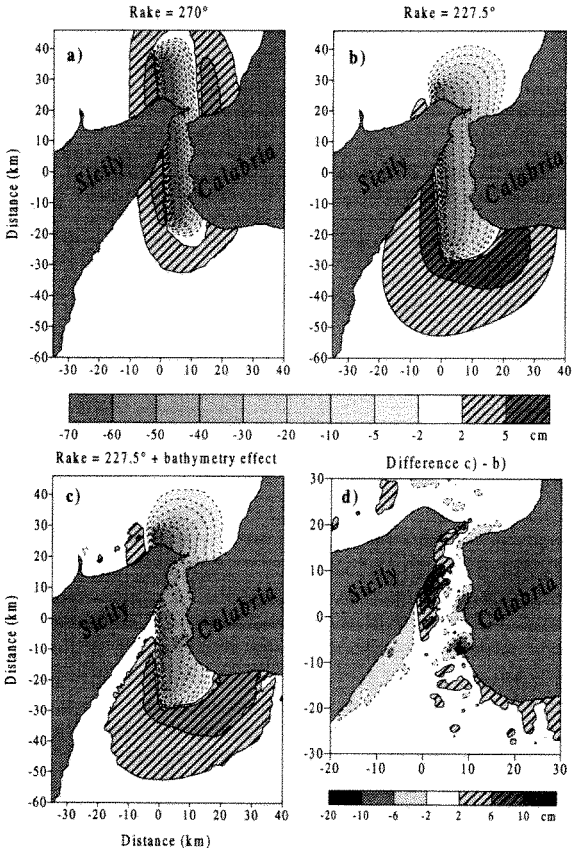

Fig. 2. Coseismic elevation fields induced by the Capuano et al. (1988) fault. Two different mechanisms have been taken into account: **(a)** a pure normal mechanism (see Piatanesi et al., 1998) and **(b)** a normal mechanism with a relevant strike-slip component (Capuano et al., 1988). Panels **(c)** and **(d)** illustrate the total initial sea surface displacement and the correction due to ocean bathymetry, respectively: the major effects are found in correspondence with coastal slopes. Contour lines in all panels are expressed in centimetres: solid lines indicate uplift while dashed lines indicate downlift.

Generally the initial water surface displacement is taken to be identical to the vertical displacement of the sea bottom due to faulting, whereas the horizontal components of the deformation are neglected. But as was already pointed out by Tanioka and Satake (1996), horizontal components of the displacement field generated by an earthquake may play an important role in the tsunami generation process especially if the tsunami source is placed in regions that involve relevant topographic structures and if the slip on the fault has a large horizontal component. A new algorithm, whose details may be found in Tinti and Armigliato (1998),

has been developed and applied to the 1908 tsunami: results will be discussed in the next section.

3 Numerical simulations

The fault proposed by Capuano et al. (1988) is 56.7 km long, 18.5 km wide, and its upper border is 1.1 km deep; the slip on the fault is 1.5 m, while strike and dip angles are respectively 355.8° and 38.6°. Two possible fault mechanisms are considered here: the first is a pure normal mechanism (rake angle 270°) with the hanging wall downlifting (this is the mechanism studied by Piatanesi et al., 1998); the second, that is the one proposed by Capuano et al. (1988), is a normal mechanism with a relevant strike-slip component (rake angle 227.5°). The coseismic vertical displacements generated by the two mechanisms are shown in Figures 2a and 2b respectively: the most evident effect of the strike-slip component is that of extending the deformation field to the south. As for the second mechanism, the total initial water elevation field is shown in Figure 2c. This field is the sum of the vertical coseismic displacement (computed through Okada's (1992) analytical formulas) and of the vertical displacement of the water surface due to horizontal movement of the sea bottom.

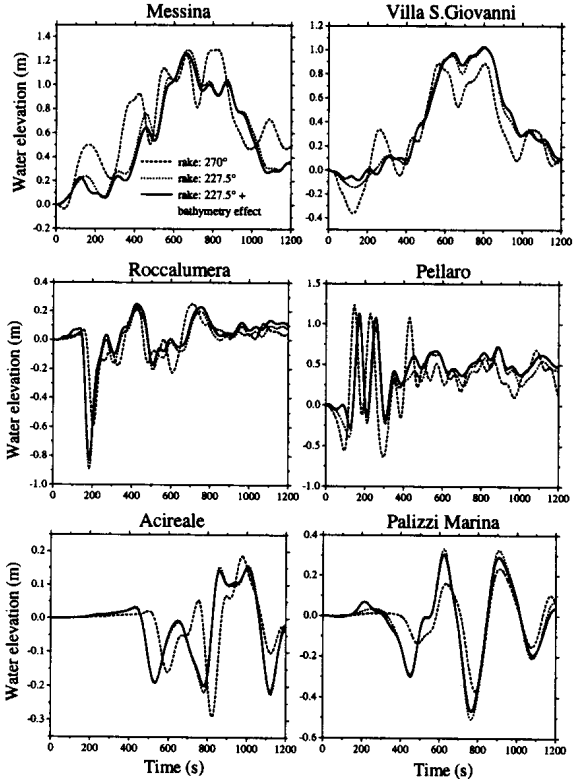

Fig. 3. Tide gauges computed in three stations in Sicily (left panels) and three stations in Calabria (right panels): it may be observed that the sign of the first arrivals is the same for the two different source mechanisms. Moreover, the changes in the initial conditions due to the bathymetry are seen to play only a minor role.

The effect of the bathymetry is depicted in Figure 2d: the correction due to the sea bottom topography does not change significantly the general pattern of the displacement field, but it affects its values by an amount that is in the range of (-22,+14) cm; as expected, the most relevant discrepancies are found in correspondence with coastal slopes.

Time-histories have been computed for three stations along the Sicily coast and for three stations on the Calabria coast: results are illustrated in Figure 3. It may be observed that the two different fault mechanisms produce curves with different shapes, but the polarity of the first arrival is the same in each station. Moreover, bathymetry plays only a minor role in this case, the major effect being that of amplifying or decreasing the maximum water elevations.

Maximum water elevations computed through the least-squares procedure adopted by Piatanesi et al. (1998) are plotted in Figure 4. Along the Calabrian coast the pure normal mechanism seems to lead to better results: the opposite is true for Sicily, in particular for the southern stations. In both cases bathymetry does not improve the situation and again plays only a minor role.

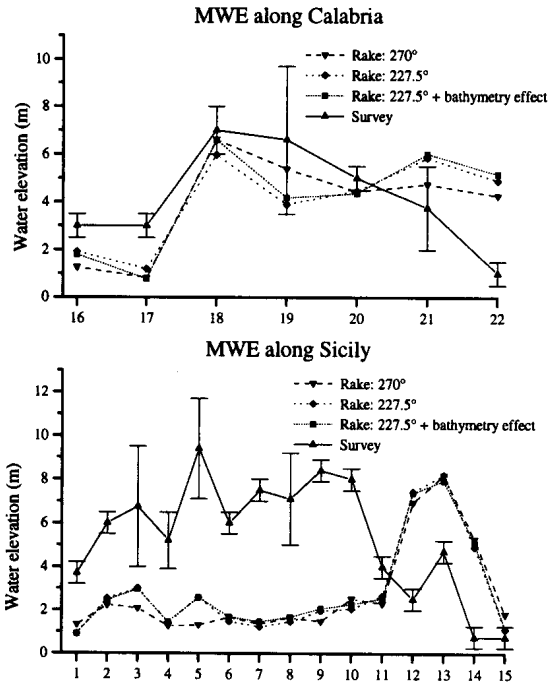

Fig. 4. Maximum water elevations computed for the three cases introduced in Figures 2 and 3, compared with observed run-ups (solid line). Figures on the abscissa correspond to the site numbers shown in Figure 1a. The pure normal mechanism seems to lead to better results along Calabria, while the opposite is true for Sicily. The error bars represent the interval of observed run-up values in those places where several different measurements were performed, the true value identifying with the central value of the interval. A standard error of ±0.5 m has been assigned to all those sites for which only one measure was available.

4 Heterogeneous slip along the fault plane

The second direction towards which we moved was the introduction of a possible heterogeneous slip distribution on the fault plane. A similar study has been carried out by De Natale and Pingue (1991) on the fault proposed by Capuano et al. (1988): they performed an inversion of levelling data and obtained a very good fit with a distribution having the major slip release in the mid part of the fault.

On the basis of tsunami run-up data we would expect something different: in particular the major part of the slip would be expected to be on the southern part of the fault. To compute the slip distribution by inversion of tsunami data we adopted the least-squares scheme introduced by Piatanesi et al. (1996) for the simulation of the 1992 Nicaragua tsunamigenic earthquake. We divided our fault into three subfaults, 18.9 km long and 18.5 km wide each, with slip of 1.5 m, corresponding to the value of the homogeneous case. We then computed the solutions corresponding to each subfault and obtained the global solution by superposition. The water elevation $\zeta_{it}(t)$ at the coastal station i may be computed as the combination of the tide-gauge records associated with each subfault:

$$\zeta_i(A,\mathbf{c};t) = A\sum_{j=1}^{N_s} c_j G_{ij}(t) \qquad (4)$$

where G_{ij} is the time-history corresponding to the j-th subfault computed at the station i, $\mathbf{c}$ is the vector of the coefficients c_j (j=1,2,...,N_s) related to the slip-magnitude on the j-th subfault, N_s is the number of sources. Moreover, A is a mean amplification factor that can be interpreted as an estimator of the mean amplification of the waves climbing up the coastal slope: it is used to match the computed maximum water elevations with the observed run-up values. The slip distribution giving the best fit to the observed data has been determined via a least-squares procedure, i.e. we searched for the minimum of the sum Q of the squared residuals:

$$Q(A,\mathbf{c}) = \sum_{i=1}^{N}\left[W_i(A,\mathbf{c}) - R_i\right]^2 \qquad (5)$$

where N is the total number of stations, R_i and W_i the observed run-up values and the computed maximum water levels at the coastal station i respectively, with:

$$W_i(A,\mathbf{c}) = \max_{t\in[0,T_f]}\left\{\zeta_i(A,\mathbf{c};t)\right\} \qquad (6)$$

In (6) T_f is the final computation time. We let the coefficients c_j vary in the range between c_j=0 (no slip allowed on the j-th subfault) and c_j=N_s=3 (all slip on the j-th subfault) with a discrete increment of 0.1; similarly, the amplification factor A has been varied in the range [1,15] with steps of 0.05. In order to check the stability of the obtained configuration we considered all the sets of parameters (A, $\mathbf{c}$) associated with the values of Q falling within a 15% interval around Q_{min} and then computed the related frequency distribution. The result, depicted in Figure 5, is that nearly all the slip is concentrated on the southern sub-fault. Taking the mean values of each distribution (c_1 = 0.2, c_2 = 0.6, c_3 = 2.2, A = 5.1), we obtained the results shown in Figure 6. Along the Calabria coast the situation seems not to have been improved very much. The opposite is true for the Sicily coast: the fit is better than in the homogeneous case, though some refinements are still needed. An important remark is that in passing from the homogeneous case to the obtained heterogeneous distribution the average residual, defined as $Q^{1/2}/N$, is greatly reduced from 3.8 m down to 2.8 m. Notice further that the former value 3.8 m is largely exceeding the 15% limit (≅3.2 m), which shows that a homogeneous source is rather unlikely.

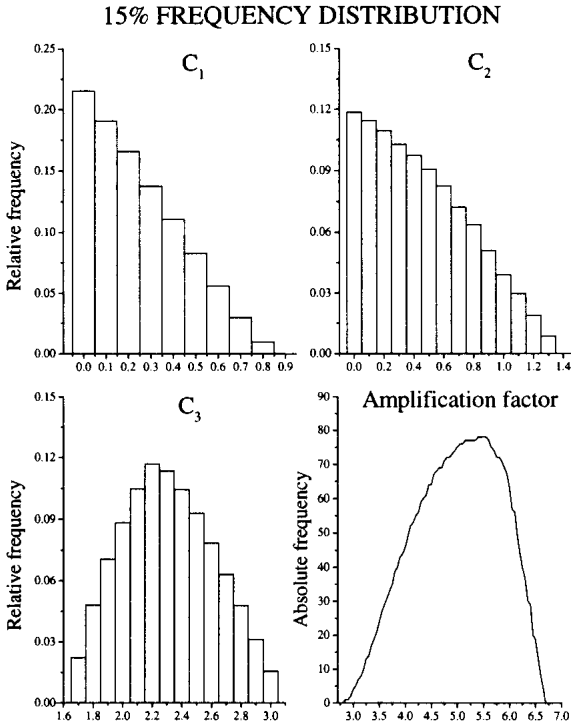

Fig. 5. 15% frequency distributions of the slip coefficients c_j and of the amplification factor A: the greatest part of the slip is concentrated on the southern subfault (c_3).

5 Conclusions

The problem of which fault was responsible for the 1908 Messina earthquake is still open: in this paper, that may be considered the continuation of the study by Piatanesi et al. (1998), we tried to understand if numerical modelling of the consequent tsunami helps to impose more constraints on the fault parameters. In particular, we tried to improve the matching between observed run-up values and computed maximum water elevations by choosing one particular fault proposed in the literature (Capuano et al., 1988) and by adding two new features to the tsunami simulation: i) a new algorithm was applied that enables to compute, in the frame of FE modelling, the effect of the sea bottom topography on the tsunami initial condition; ii) a heterogeneous slip distribution was allowed on the fault plane. The results are:

a) the bathymetry plays only a minor role in this particular case and its effect does not improve significantly the computation of maximum water elevations; b) the inversion of observed run-up data leads to a relevant heterogeneity of the slip distribution on the fault-plane, with most of the slip being released on its southern part.

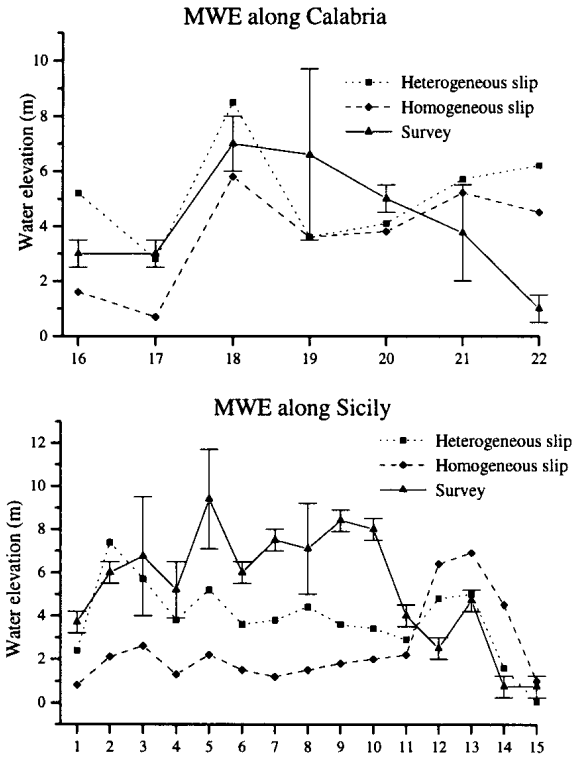

Fig. 6. Computed maximum water elevations for a homogeneous and a heterogeneous distribution (computed taking the mean values of the distributions of Figure 5) of the slip along the Capuano et al. (1988) fault. The comparison with the observed run-ups shows that the fit is significantly improved by the introduction of the heterogeneity, especially along Sicily. Figures on the abscissa correspond to the site numbers shown in Figure 1a.

The result is a clear improvement of the fitting between observed and computed run-up values especially as regards Sicily. This encourages us to further develop our research in the next future by applying this type of study also to other faults. The discrepancies that are still observed, in particular along Calabria coast, may be determined by the fact that our numerical model involves vertical reflecting walls at the coastal boundaries (the minimum depth used in the numerical simulations is 50 m); moreover, a finer grid and a more detailed bathymetry near the coast are needed.

Acknowledgments. The present paper is the result of a work that has been carried out in the framework of the project GITEC-TWO financed by the European Communities by means of the contract ENV4-CT96-0297. It has also been partially financed by the Italian Ministry of the University and of the Scientific and Technological Research.

References

Boschi, E., Pantosti, D., and Valensise, G., Modello di sorgente per il terremoto di Messina del 1908 ed evoluzione recente dell'area dello Stretto, *Atti VIII Convegno G.N.G.T.S., Roma 1989,* 245-258, 1989 (in Italian).

Bottari, A., Carapezza, E., Carapezza, M., Carveni, P., Cefali, F., Lo Giudice, E., and Pandolfo, C., The 1908 Messina Strait earthquake in the regional geostructural framework, *J. Geodynamics, 5,* 275-302, 1986.

Capuano, P., De Natale, G., Gasparini, P., Pingue, F., and Scarpa, R., A model for the 1908 Messina Straits (Italy) earthquake by inversion of levelling data, *Bull. Seism. Soc. Am., 78,* 1930-1947, 1988.

De Natale, G., and Pingue,, F., A variable slip fault model for the 1908 Messina Straits (Italy) earthquake by inversion of levelling data, *Geophys. J. Int., 104, n.1,* 73-84, 1991.

Mulargia, F., and Boschi, E., The 1908 Messina earthquake and related seismicity, *Proc. Int. Shool Phys. E. Fermi,* Earthquakes: observation, theory and interpretation, 493-518, 1983.

Okada, Y., Internal deformation due to shear and tensile faults in a half-space, *Bull. Seism. Soc. Am., 82,* 1018-1040, 1992.

Piatanesi, A., Tinti, S., and Bortolucci, E., Finite-element simulations of the 28 December 1908 Messina Straits (southern Italy) tsunami, *Physics and Chemistry of the Earth* (in press).

Piatanesi, A., Tinti, S., and Gavagni, I., The slip distribution of the 1992 Nicaragua earthquake from tsunami run-up data, *Geophys. Res. Lett., 23, n.1,* 37-40, 1996.

Shick, R., Eine Seismotektonische Bearbeitung des Erdbebens von Messina im Jahre 1908, *Geol. Jhrb., 11,* 74, 1977 (in German).

Tanioka, Y., and Satake, K., Tsunami generation by horizontal displacement of ocean bottom, *Geophys. Res. Lett., 23, 8,* 861-864, 1996.

Tinti, S., and Armigliato, A., Seismic displacements of non-flat sea floor in tsunami generation: application to the 1693 case in SE Sicily, Italy, *Proceedings of the International Conference on Tsunamis,* Paris, 26-28 May 1998 (submitted).

Tinti, S., and Giuliani, D., The Messina Straits Tsunami of December 28, 1908: a critical review of experimental data and observations, *Il Nuovo Cimento, Vol. 6,* 429-442, 1983.

Tinti, S., Gavagni, I., and Piatanesi, A., A finite-element numerical approach for modelling tsunamis, *Annali di Geofisica, 37,* 1009-1026, 1994.

Valensise, G., Low angle normal faulting during the 1908, Messina, earthquake revealed by geodetic data analysis, *EOS Trans. A.G.U., 69,* 1433, 1988 (abstract).

Chapitre 6

Un cas limite pour la résolution du modèle

Au cours de cette thèse, motivés par l'idée d'utiliser les données de tsunami pour déterminer un ou plusieurs paramètres du mécanisme à la source, nous avons abordé l'étude d'un événement récent particulièrement délicat: le séisme tsunamigénique de Shikotan, au large des îles Kouriles le 4 octobre 1994. Ce séisme, bien que localisé dans une zone de subduction, ne représente pas un événement interplaque classique: il a été reconnu comme un séisme lithosphérique, ayant fracturé l'interieur de la plaque en subduction (*Kikuchi and Kanamori*, 1995). Les problèmes concernant cet événement sont la détermination du plan de faille ayant réellement rompu (ambiguïté entre les deux plans nodaux du mécanisme au foyer), l'estimation des dimensions de cette faille, de l'amplitude du glissement et de sa distribution sur le plan de faille (uniforme ou non). Plusieurs études ont été publiées sur ce séisme, avec des conclusions parfois contradictoires. En particulier, *Tanioka et al.* (1995), utilisant les formes d'onde sismiques, la distribution des répliques, les mesures géodésiques et les formes d'onde de tsunami, ont proposé un modèle de faille orientée NW-SE (perpendiculaire à l'axe de la fosse) caractérisée par un faible angle de pendage et une distribution du glissement fortement hétérogène (concentré dans la partie supérieure de la faille). Un an plus tard, *Ozawa* (1996), à l'aide d'une méthode d'inversion des données géodésiques et en utilisant toutes les données GPS disponibles, critique ce résultat et propose un modèle de faille orientée NE-SW (parallèle à l'axe de la fosse) caractérisée par un très fort angle de pendage. La difficulté majeure pour la

détermination du plan de faille vient de ce que les deux modèles de source indiqués ci-dessus engendrent une déformation de la croûte très semblable, dans la zone où les données géodésiques existent, alors que les modèles sont très différents dans leur géométrie. Ce séisme représente donc, vis-à-vis de la caractérisation de la source sismique, un cas particulièrement difficile que nous avons choisi pour étudier la limite de résolution de nos modélisations de tsunami.

L'article qui suit, publié dans un volume thématique de *Pure and Applied Geophysics* dédié aux processus sismogéniques et tsunamigéniques des zones de subduction superficielles, pose le problème de la capacité des données de tsunami à contraindre les paramètres des séismes. Les résultats de nos études montrent que, dans le cas de Shikotan 1994, la résolution des modélisations de tsunami est insuffisante pour distinguer les modèles de source considérés. Afin de le montrer, dans cet article, nous avons estimé une source d'incertitude dans les simulations de tsunami, représentée par un bruit gaussien qui perturbe les données bathymétriques.

6.1 The october 4, 1994 Shikotan (Kurile Islands) tsunamigenic earthquake: an open problem on the source mechanism

Pure appl. geophys. 154 (1999) 555–574
0033–4553/99/040555–20 $ 1.50 + 0.20/0

Pure and Applied Geophysics

The October 4, 1994 Shikotan (Kurile Islands) Tsunamigenic Earthquake: An Open Problem on the Source Mechanism

ALESSIO PIATANESI,[1] PHILIPPE HEINRICH[1] and STEFANO TINTI[2]

Abstract—On October 4, 1994, an earthquake of magnitude $M_w = 8.2$ occurred in the western part of the Kurile Islands, generating a tsunami that has been well recorded along the entire coast of Japan. Previous works have shown that this earthquake does not represent a low angle thrust event, normally expected in a subduction zone, rather an intra-plate event rupturing through the slab. On the basis of the accepted mechanism, two fault models, representative of the nodal plane ambiguity, have been suggested. The goal of this work is to verify whether the tsunami simulations are able to rule out one of the two proposed fault models. Taking into account both fault models together with a heterogeneous slip along the fault, we have performed numerical simulations of the tsunami. All source models produce tide-gauge records in agreement with the observed ones. The limit of resolution of the performed simulations, estimated by means of a perturbed bathymetry, does not allow us to distinguish the best source model.

Key words: Simulation, slip, source mechanism, subduction, tectonics, tsunami.

Introduction

A large earthquake ($M_w = 8.2$) occurred on October 4, 1994 off Shikotan Island, one of the Kurile Islands (see Fig. 1). This event is also referred to as "1994 Hokkaido Toho-Oki earthquake" by the Japan Meteorological Agency. In this paper we will refer to this event as the Shikotan earthquake. The epicenter, located by the National Earthquake Information Service (NEIS), was 43.668°N and 147.336°E, remarkably close to the 1969 event. The latter was a large subduction earthquake, characterized by $M_0 = 2.2 \times 10^{21}$ Nm, dip = 16°, strike = 40° and a source area of 85×180 km^2 (FUKAO and FURUMOTO, 1979). Since the recurrence interval of large/great subduction events in this region is estimated to be of about 100 years (KANAMORI, 1977; SHIMAZAKI, 1978), the Shikotan earthquake has been considered as an unusual event from inception. It was quickly recognized that this earthquake was not a common low-angle thrust event, normally expected in

[1] Laboratoire de Détection et de Géophysique/CEA, BP 12, 91680 Bruyères-le-Châtel, France.
[2] Dip. di Fisica, Università di Bologna, Bologna, Italy.

subduction zones, but a lithospheric earthquake, that is an intra-plate event rupturing through a part of the subducting oceanic lithosphere (KIKUCHI and KANAMORI, 1995).

The earthquake generated a large tsunami that was well recorded by the tide gauge network of Japan and by the tide gauges of the Pacific coast of the U.S., of the Hawaiian Islands and of Tahiti. The strongest effects due to both earthquake and tsunami have been observed in Shikotan Island, located just arcward of the epicentral area, where a subsidence of 50–60 cm of the whole island has been measured by a tide gauge located at Malokurilsk (YEH *et al.*, 1995). A Russian post-event GPS field survey confirmed the subsidence of Shikotan Island (GUSEVA *et al.*, 1994). A tsunami survey conducted from October 16 to 30, 1994 measured the run-up heights in Shikotan, Iturup, Kunashiri, as well as in other smaller islands and detected the maximum run-up height of about 10 m at Dimitrova Bay, in the southeastern coast of Shikotan Island (YEH *et al.*, 1995) (see Fig. 1 for locations).

During the three years following this earthquake, considerable scientific work has been carried out in order to identify the source mechanism and to correctly collocate it inside the tectonic frame of the Kurile trench system. Even though all

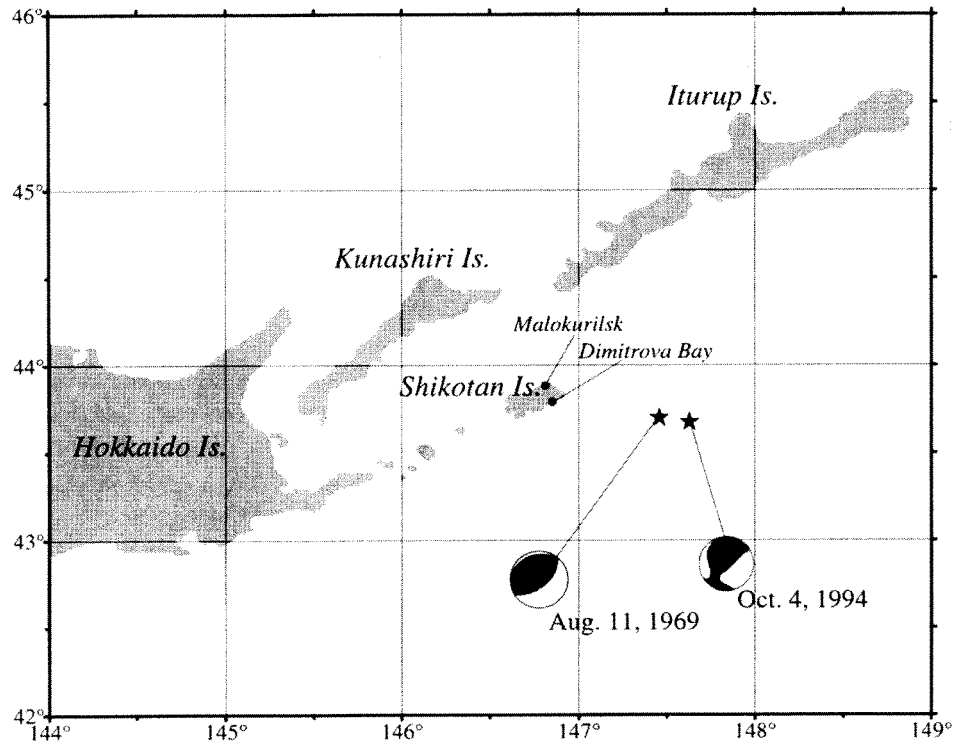

Figure 1
Source region and focal mechanism of the 1994 and 1969 Shikotan earthquakes.

the studies showed that the Shikotan earthquake was an intraplate event, there is no common agreement on which of the two nodal fault planes broke during the earthquake. On the other hand this aspect is essential to understand the mechanism of the Kurile subduction zone. The main results concerning the source mechanism, published in literature, will be briefly summarized in the next section. Thereafter, in order to investigate the capability of the tsunami data to constrain the source parameters of the Shikotan tsunamigenic earthquake, we will illustrate representative numerical simulations considering two different source faults as well as heterogeneous slip. Finally, the effect on the simulations of a Gaussian random noise affecting the bathymetric data will be also investigated.

Source Mechanism and Fault Planes

The published studies regarding the Shikotan earthquake, aimed at determining the source mechanism and the fault plane, can be roughly grouped into four main approaches: inversion of body and surface waves, distribution and relocation of the aftershocks, geodetic measurements and inversion of crustal deformation, tsunami simulation and tide gauge records inversion.

KIKUCHI and KANAMORI (1995) performed an inversion of both body and surface waves. By inverting 32 body-wave records they obtained the following source parameters: location of initial rupture = (43.48°N, 147.40°E), centroid depth = 56 km (strike, dip, rake) = (49°, 75°, 125°), seismic moment $M_0 = 2.6 \times 10^{21}$ Nm ($M_w = 8.2$), source time duration $T = 42$ s, average rupture velocity $v = 2.5$ km/s. Through the inversion of the surface waves they found: (strike, dip, rake) = (54°, 76°, 129°) and $M_0 = 2.3 \times 10^{21}$ Nm. They pointed out that the moment estimates reported by different investigators are very different, ranging from 1.1×10^{21} Nm (ERI, University of Tokyo, body waves) to 3.0×10^{21} Nm (DZIEWONSKI *et al.*, 1995, surface waves), and suggested that this scatter may be partly due to the large vertical extent of the source. They estimated the fault length and width to be respectively 120 and 60 km, with an average slip of 5.6 m and found that a steep-dip fault model fits the body-wave data better than a shallow-dip one, even if the shallow-dip model cannot be completely ruled out (KIKUCHI and KANAMORI, 1995).

KATSUMATA *et al.* (1995) and HURUKAWA (1995) demonstrated that the aftershocks of the Shikotan earthquake occurred on a plane with strike parallel to the trench axis and a near vertical dip angle. They identify the steep fault plane of the Harvard CMT solution (strike, dip, rake) = (50°, 74°, 128°) (DZIEWONSKI *et al.*, 1995) as the fault plane of the mainshock.

TSUJI *et al.* (1995), using a new nationwide continuous GPS array, presented the coseismic deformation field of Hokkaido Island. They compared the GPS result with the displacements calculated from the two source models, assuming fault

planes parallel or perpendicular to the Kurile trench, that in turn represent the nodal planes of the above-mentioned source mechanism. Their conclusion is that both models give satisfactory fits and that, consequently, more geodetic data are necessary to distinguish the two models.

TANIOKA *et al.* (1995) used seismic wave forms, aftershock distribution, geodetic measurements and tsunami wave forms to estimate the fault geometry, depth and slip distribution of the Shikotan earthquake. They found that crustal deformation and tsunami wave forms, computed using both possible nodal planes of the focal mechanism, can explain the observations. Furthermore, choosing the NW–SE striking plane with shallow dip, they performed a joint inversion of geodetic and tsunami data taking into account a 4-subfault model. They showed that the slip distribution along the fault is strongly heterogeneous, with the largest slip, about 17 m, concentrated in the upper end of the fault. OZAWA (1996) has in some ways criticized this result. He performed a geodetic inversion, utilizing all available GPS measurements (TSUJI *et al.*, 1995; GUSEVA *et al.*, 1994) and found that a steep dip fault, with a 2-subfault model, provides the best fit with the observations: thereafter he tested his best model against the TANIOKA *et al.*'s (1995) model showing that the former supplies the best fit. From the literature, briefly reported above, it is quite clear that, in spite of considerable scientific effort made to understand the Shikotan earthquake, the quandry of which fault plane actually ruptured is still open.

Tsunami Simulations

For some ten years it has been recognized that tsunami data, such as tide gauge records and run-up heights, are useful to constrain some parameters of the generative seismic source. SATAKE (1987) illustrated a method to invert the tide gauge records and applied it to determine the slip distribution along the fault of the 1983 Japan Sea tsunamigenic earthquake. Following these experiments, joint inversions of both tsunami and geodetic data have been successfully performed (SATAKE, 1993; WALD and SOMMERVILLE, 1995; JOHNSON *et al.*, 1996). PIATANESI *et al.* (1996) inverted run-up data, measured during post-event field surveys, to determine the slip distribution of the 1992 Nicaragua tsunami earthquake. In this paper we investigate the capability and the limits of resolution of tsunami numerical simulations to constrain the source parameters of the 1994 Shikotan earthquake. The working scheme is very simple: we consider the coseismic vertical displacement fields produced by two seismic sources as initial conditions to perform a near-field simulation of the tsunamis. In particular we compute the tide gauge records on 14 stations, placed along the coast of Japan and on two Russian islands. Then we compare the results of the simulations with the recorded tide gauges to judge which source provides the best fit.

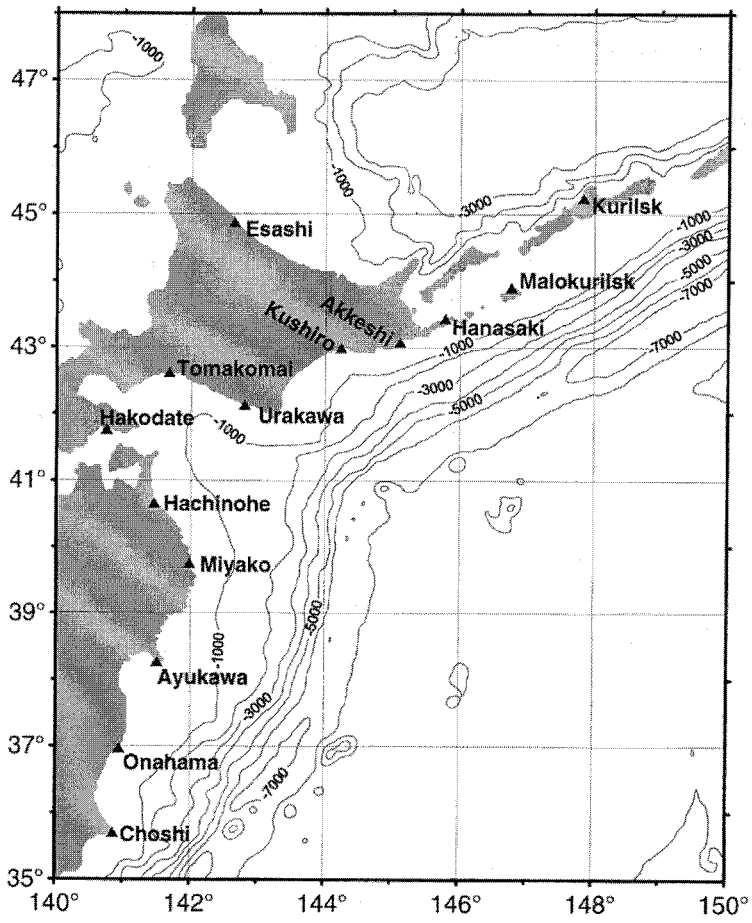

Figure 2
Bathymetry of the portion of ocean chosen for the near-field tsunami simulations; the 14 stations for which tide-gauge records are available are also shown.

Figure 2 shows the bathymetry of the portion of ocean we have chosen for tsunami simulation together with the location of the 14 coastal sites where tide-gauge records are available. Since the distribution of our stations covers only one side of the tsunami propagation area, we also perform a far-field simulation in a larger domain (see Fig. 3), aimed toward checking whether the limited azimuthal coverage of the stations affect our insight into the source process.

The model for tsunami propagation is based on the following shallow-water equations:

$$\begin{cases} \partial_t \zeta = -\nabla \cdot [(h+\zeta)\mathbf{v}] \\ \partial_t \mathbf{v} = -g\nabla\zeta - \mathbf{v}\cdot\nabla\mathbf{v} \end{cases} \tag{1}$$

where ζ is the water elevation above mean sea level, $\mathbf{v}$ the horizontal velocity vector, h the sea depth and g the gravity acceleration. This system has been completed by the boundary conditions of pure wave reflection on the solid boundary (coastlines) and of full wave transmission on the open boundary (open ocean). In the following simulations the initial sea-water elevation is assumed to be equal to the coseismic vertical displacement of the sea bottom, computed through Okada's analytical formulas (OKADA, 1985), while the velocity vector field is identically null. Equations (1) have been solved by means of a finite-difference method, using a mesh with a cell size of 1 and 5 arcmin respectively for the near-field and far-field simulations.

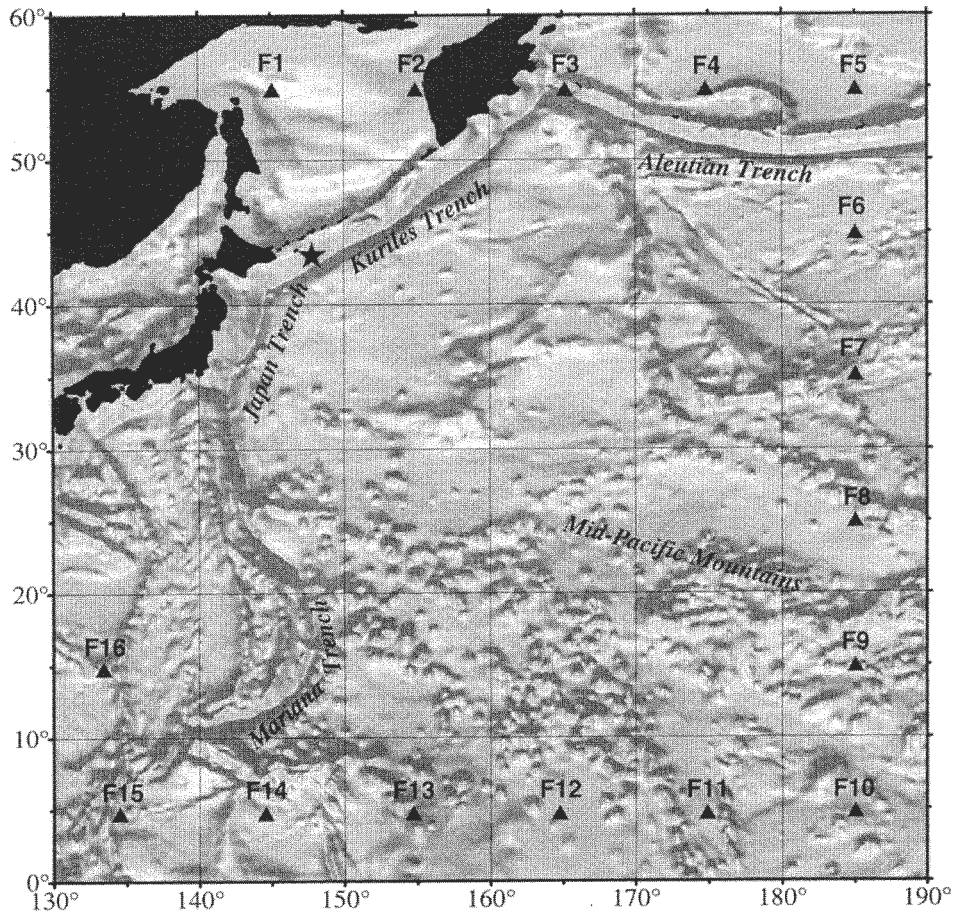

Figure 3
Computational domain used for the far-field tsunami simulations; the 16 virtual tide gauges, labeled from F1 to F16, where wave forms are computed, are also shown.

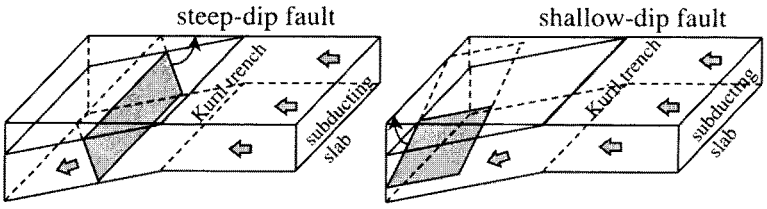

Figure 4
Sketch of the geometry of the two faults considered in this work.

We have considered two fault geometries, schematically shown in Figure 4 and labeled *steep-dip* and *shallow-dip*, that basically represent the two nodal planes of the focal mechanism. The set of parameters that completely defines the geometry of both faults is reported in Table 1. The *steep-dip* model has a similar mechanism to the best OZAWA's (1996) model, the main difference being a smaller dimension of the fault plane and a uniform slip. The *shallow-dip* model mimics the best TANIOKA *et al.*'s (1995) fault model: even in this case the length and width are slightly smaller and the slip is uniform along the fault. Figure 5 displays the coseismic vertical displacement field, computed through Okada's model, produced by the shallow-dip and steep-dip faults: in spite of the substantial difference in the fault geometry, the vertical displacement fields are very similar to each other.

Near-field Simulations

Figure 6 shows the observed and computed tide-gauge records in the 14 stations considered in this work. We have found generally good agreement between the computed and the observed wave forms. The arrival times as well as the amplitudes of the first oscillations are comparatively well reproduced. We observe that in some stations, such as Akkeshi, Kushiro and, to a lesser extent, Esashi, Hachinohe, Miyako and Choshi, there is a gap of a few minutes in the arrival times between the computed and the observed records. This can be due to several reasons: an imperfect localization of the stations in the computational mesh, possible errors in the bathymetry and a time delay in the tide gauge response. The wave amplitudes are comparatively well reproduced, especially if we view the first oscillation: the

Table 1

Fault parameters of the two source models considered in this work

	Lat.	Lon.	Depth	Strike	Dip	Rake	Length	Width	Slip
Steep	43.7°	147.6°	50 km	50°	70°	125°	120 km	45 km	10.8 m
Shallow	43.7°	147.5°	50 km	160°	40°	30°	60 km	70 km	13.9 m

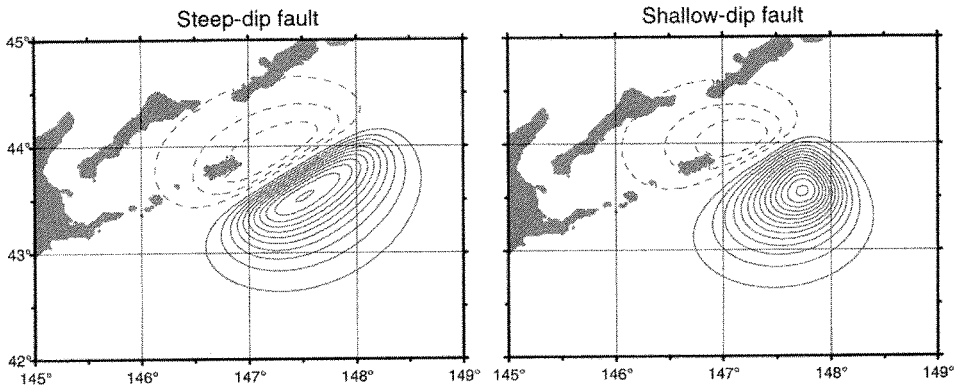

Figure 5
Coseismic vertical displacement fields produced by the steep-dip and shallow-dip source faults; solid curves for uplift and dashed for subsidence are shown with a 20-cm interval.

small discrepancies may be due to both imprecise bathymetry around the tide gauges and an imperfect localization of the stations in the computational grid.

In Malokurilsk, which is the station nearest the epicenter, we observe a minor difference in the arrival time (the computed waves arrive 2 minutes earlier), this is due to the fact that the tide gauge is placed in the inner part of a circular bay, of about 1 km of radius, that is not fully modeled in our simulations. The wave periods are well reproduced, even for the later phases, the main discrepancy between the computed and observed wave forms is the amplitude of the first oscillation. The recorded wave form registers a peak to peak amplitude of about 2.5 m, while the computations exhibit an amplitude of 2.8 and 3.8 m for the steep-dip and shallow-dip fault models, respectively.

It is important to point out that the tsunami simulations are a powerful tool to constrain both the epicenter of the source and the slip amount along the fault. Once the fault geometry is fixed, the maximum displacement depends only on the slip along the fault. We have found that to correctly calculate the wave amplitudes, a slip of about 11–13 m is needed (see Table 1), about two times larger than that estimated by KIKUCHI and KANAMORI (1995).

Figure 6 also shows that, with the exception of Malokurilsk, the computed records are very similar to each other, that is both seismic sources produce resembling tsunami: hence it is very difficult to judge which source gives the best fit with the observations. It is obvious that a choice can always be made on the basis of a goodness estimator, a RMS value between the computed and the observed records, for instance. However, it is also known that in this kind of approach, an error estimate for the model simulations is needed, in order to avoid arbitrary conclusions. Owing to this, we have tried to estimate the resolution of our model, taking into account a major source of uncertainty in tsunami simulations; that is an

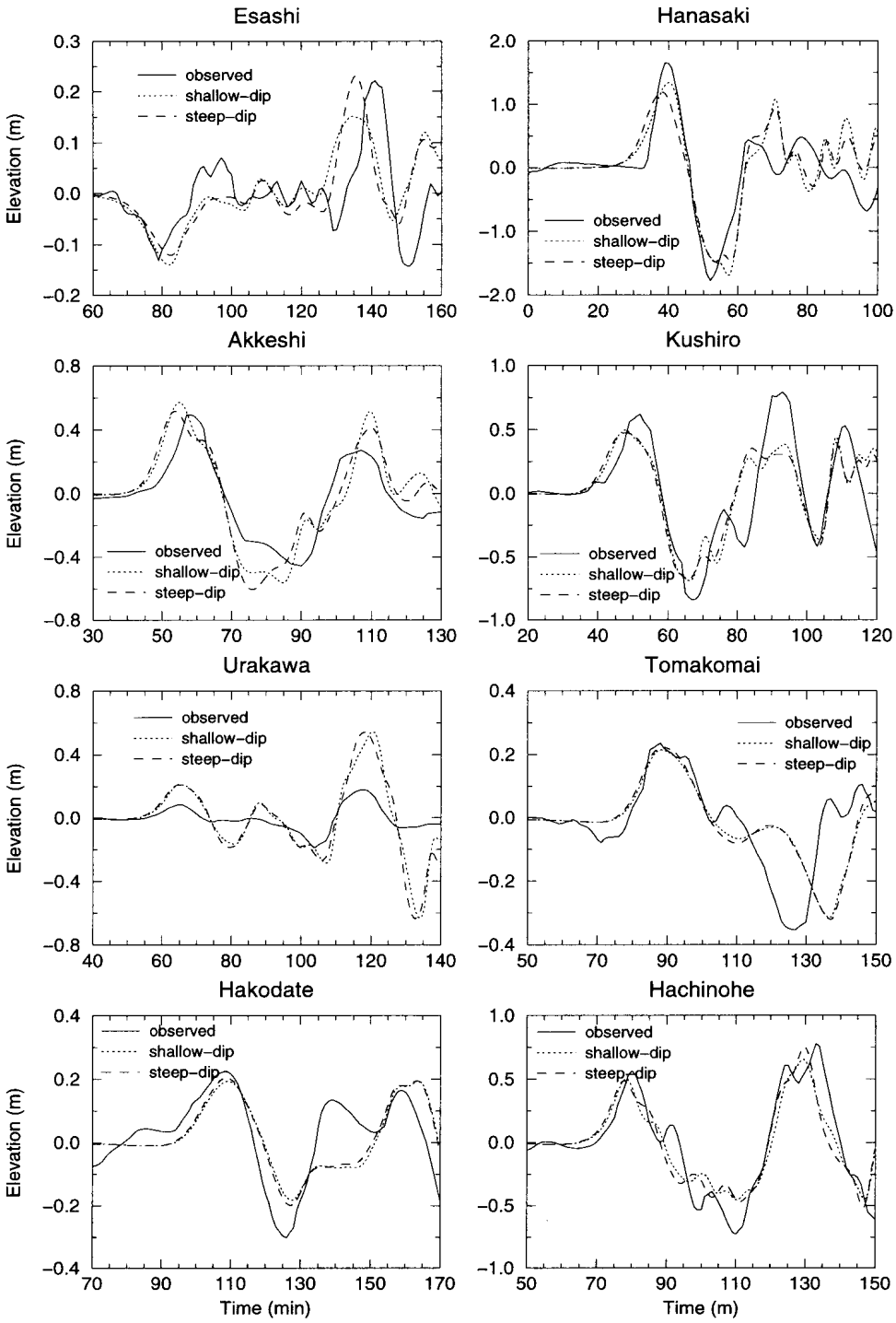
Esashi
Hanasaki
Akkeshi
Kushiro
Urakawa
Tomakomai
Hakodate
Hachinohe
observed
shallow-dip
steep-dip
Elevation (m)
Time (min)
Time (m)

Figure 6

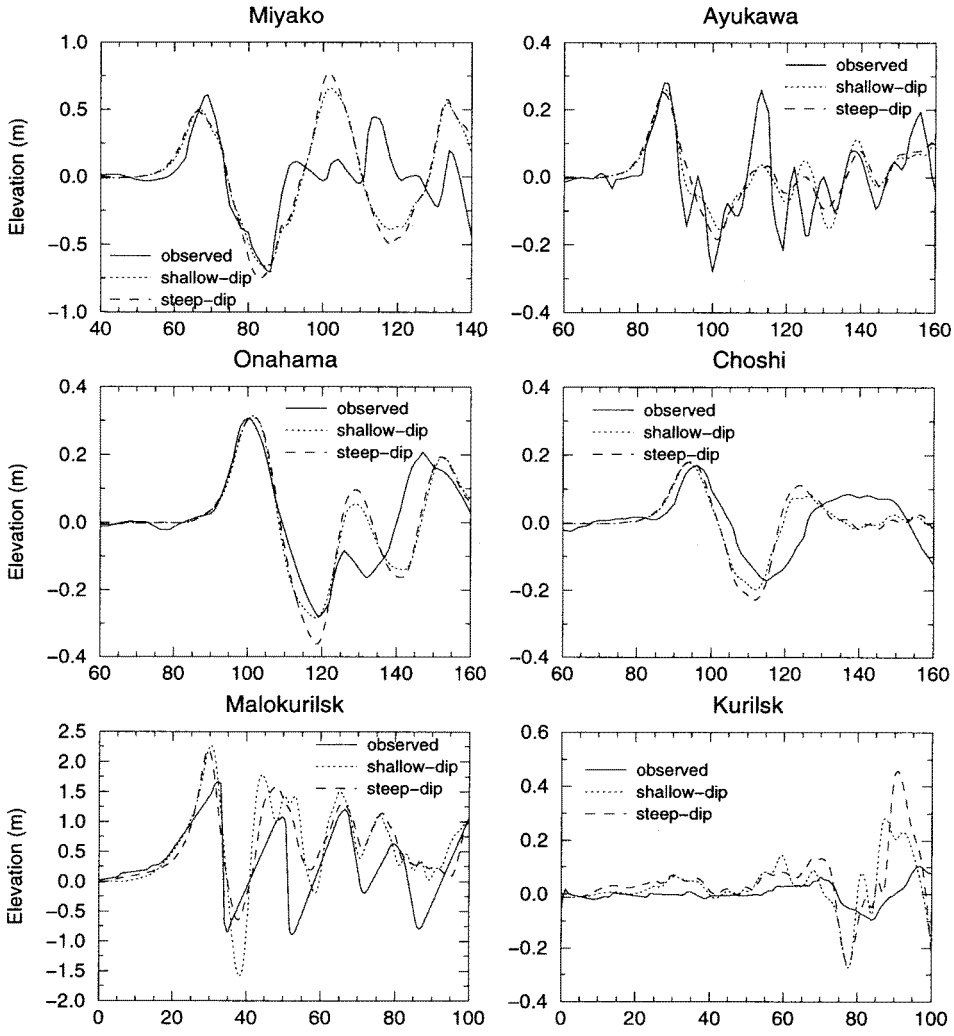

Figure 6
Observed and computed tide-gauge records on the 14 stations shown in Figure 2: the time in the abscissa is in minutes after the origin time of the event.

error in the bathymetric data. To estimate the uncertainty induced on the computed tide-gauge records by an error in the bathymetry, we proceed as follows: we inject a Gaussian random noise with a standard deviation of 10% and a characteristic wavelength of 2 arcmin into the bathymetry matrix. This noise may be interpreted as an error band associated with the bathymetry measurements and/or to the gridding procedure used to obtain regularly spaced bathymetry from raw data (SMITH, 1993; SICHOIX *et al.*, 1998). Then, choosing as a case study the shallow-dip

source model, we perform a new simulation utilizing the perturbed bathymetry. For each station we consider the differences in the records computed using the original bathymetry and the noised one as a band of error. In Figure 7 we represent, for all the stations, the bands of error as a gray region. In each station we overplot the computed tide-gauge record relative to the other seismic source (the steep-dip one), finding that, often, the latter falls into the gray region of uncertainty. This means that the differences in the computed records between the two sources are of the same order of magnitude of the uncertainties due to bathymetric errors. This result, in turn, demonstrates that it is not possible to distinguish between the two seismic sources we have considered. Only in Malokurilsk the two sources still produce quite different wave forms, with a difference of about 80 cm in the negative part of the first oscillation.

Effects of Heterogeneous Slip

As reported above, some authors suggest that high heterogeneous slip may occur along the fault of the Shikotan earthquake (TANIOKA *et al.*, 1995; OZAWA, 1996; CUMMINS *et al.*, 1998). Following the scheme of the previous section, we now consider a simple case of strongly heterogeneous slip. We simulate the tsunami generated by such a source and compare the results with the equivalent homogeneous case computed using the noised bathymetry. We consider the steep-dip fault, already discussed, as the reference case of homogeneous slip. Then we subdivide the steep-dip fault into two equal parts in the direction of the dip, assuming that 75% of the total seismic moment is to be released in the upper part and the remaining 25% in the lower one: so that the slip in the upper segment is three times larger than in the lower one. The computed wave forms relative to the heterogeneous source are shown in Figure 8, together with those relative to the perturbed homogeneous source. The differences between the computed wave forms are very small in all the stations, especially if we look at the first oscillations of the records. Even in this case, the broadest differences between computations are observed in Malokurilsk, which is the closest station to the source. Unlike TANIOKA *et al.* (1995), we conclude that there is no clear indication that the slip must be heterogeneous; the discrepancies in the computed wave forms between competing models correspondent to the uncertainty induced by the bathymetric noise.

Far-field Simulations

The results shown in the previous section seem to indicate that small differences in the fault mechanisms are reflected only on the tide-gauge records situated very close to the source. Hence, the stations we use in this work, that are the closest to the source area, are the best candidates to infer information regarding the source

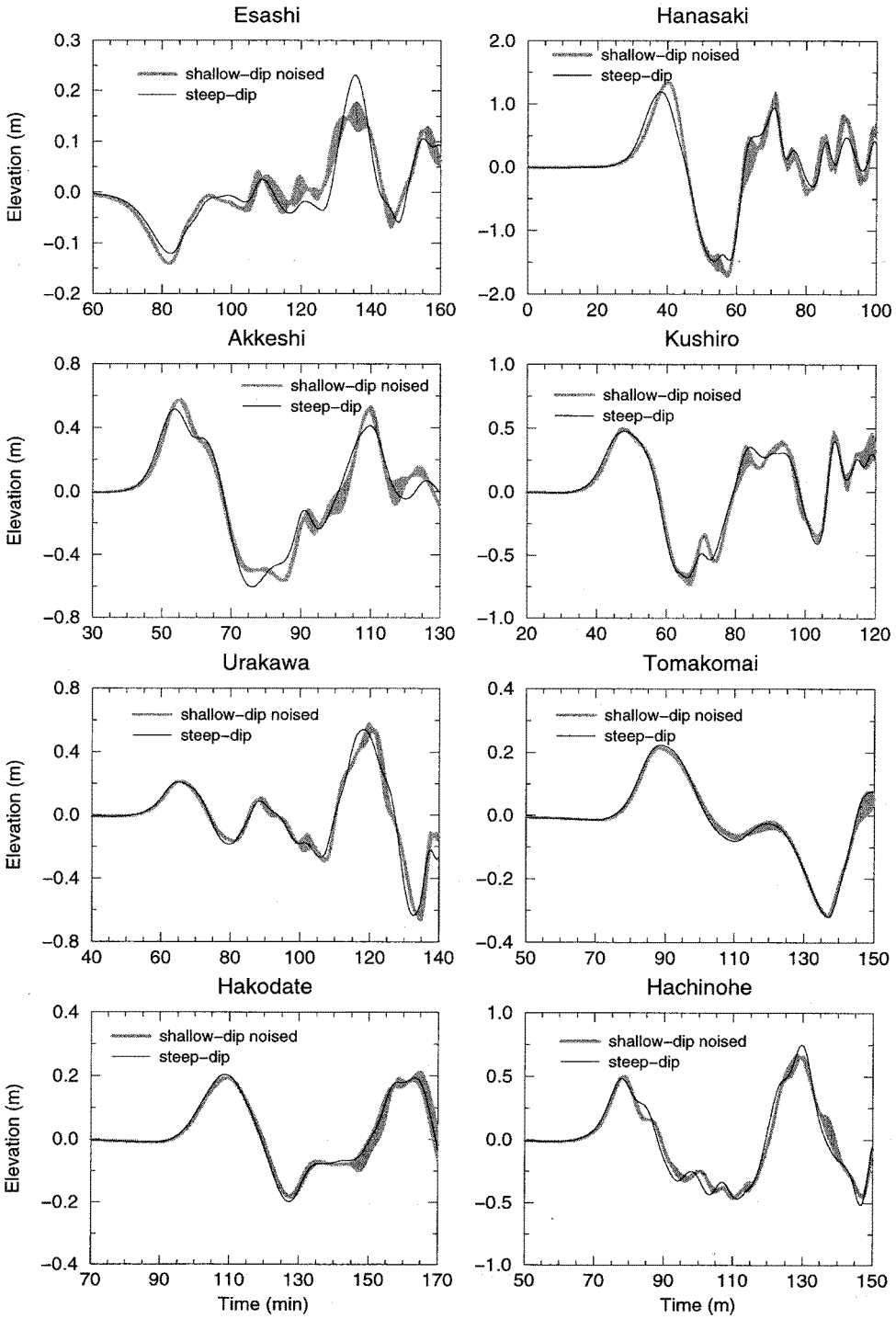
Esashi
Hanasaki
Akkeshi
Kushiro
Urakawa
Tomakomai
Hakodate
Hachinohe
shallow–dip noised
steep–dip
Elevation (m)
Time (min)
Time (m)

Figure 7

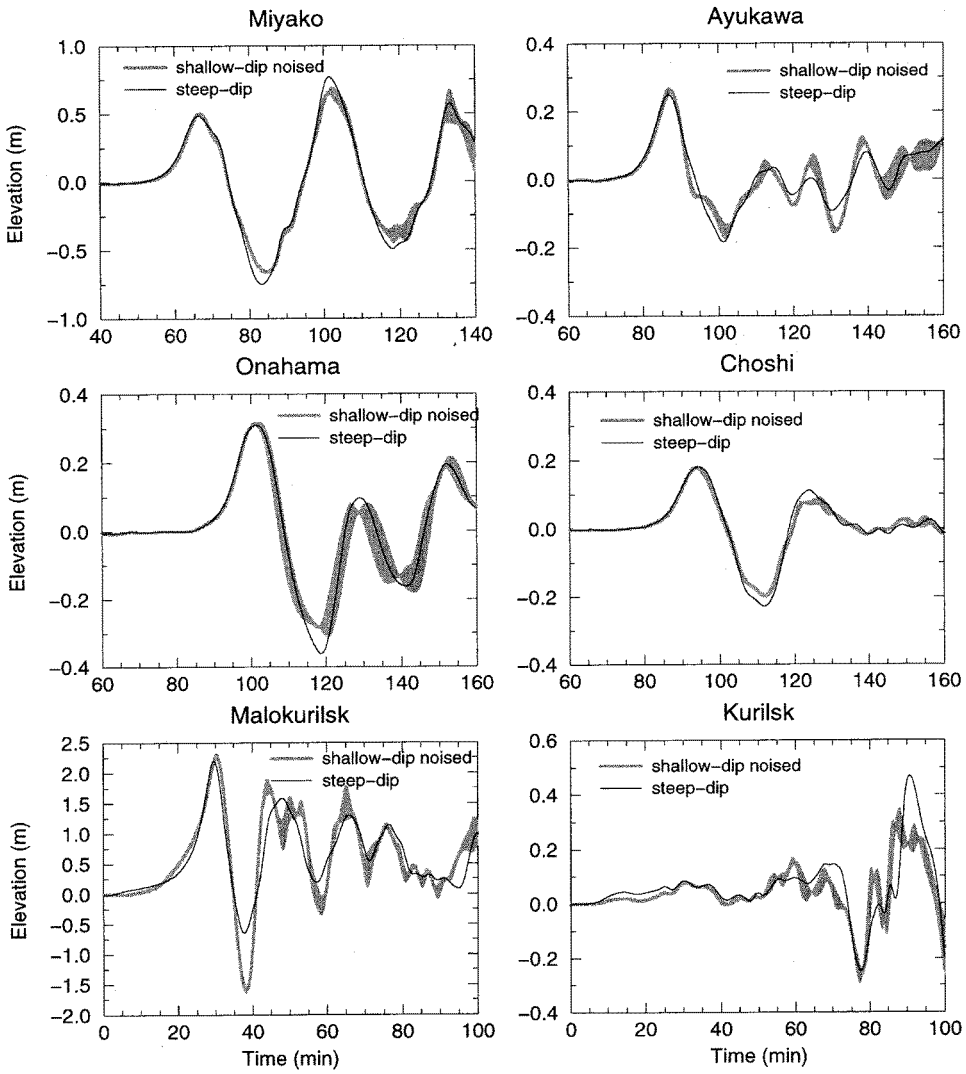

Figure 7
Effects of a Gaussian random error injected in the bathymetry on the computed wave forms. The gray regions represent the band of uncertainty computed for the shallow-dip fault model using the perturbed bathymetry. The solid lines are the computed records relative to the steep-dip fault model shown in Figure 6.

mechanism. In any case, one can argue that we are unable to distinguish between different sources because of a too small azimuthal coverage of the used stations, in fact, as shown in Figure 2, all the stations are placed in one side of the propagation area. To investigate this possibility we perform a far-field tsunami simulation, using a larger computational domain which is shown in Figure 3. In this domain we

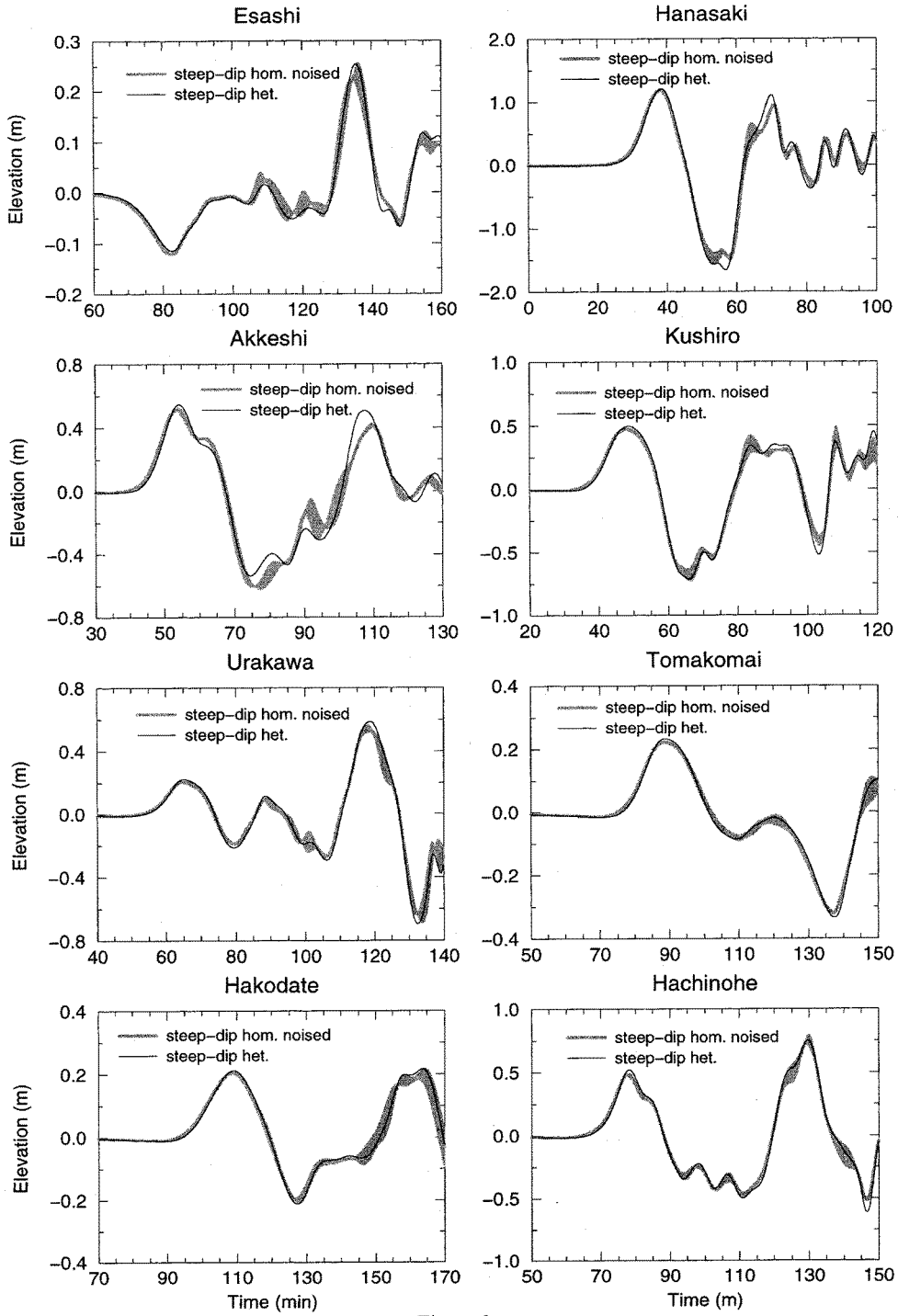
Esashi
Hanasaki
Akkeshi
Kushiro
Urakawa
Tomakomai
Hakodate
Hachinohe
steep–dip hom. noised
steep–dip het.
Elevation (m)
Time (min)
Time (m)

Figure 8

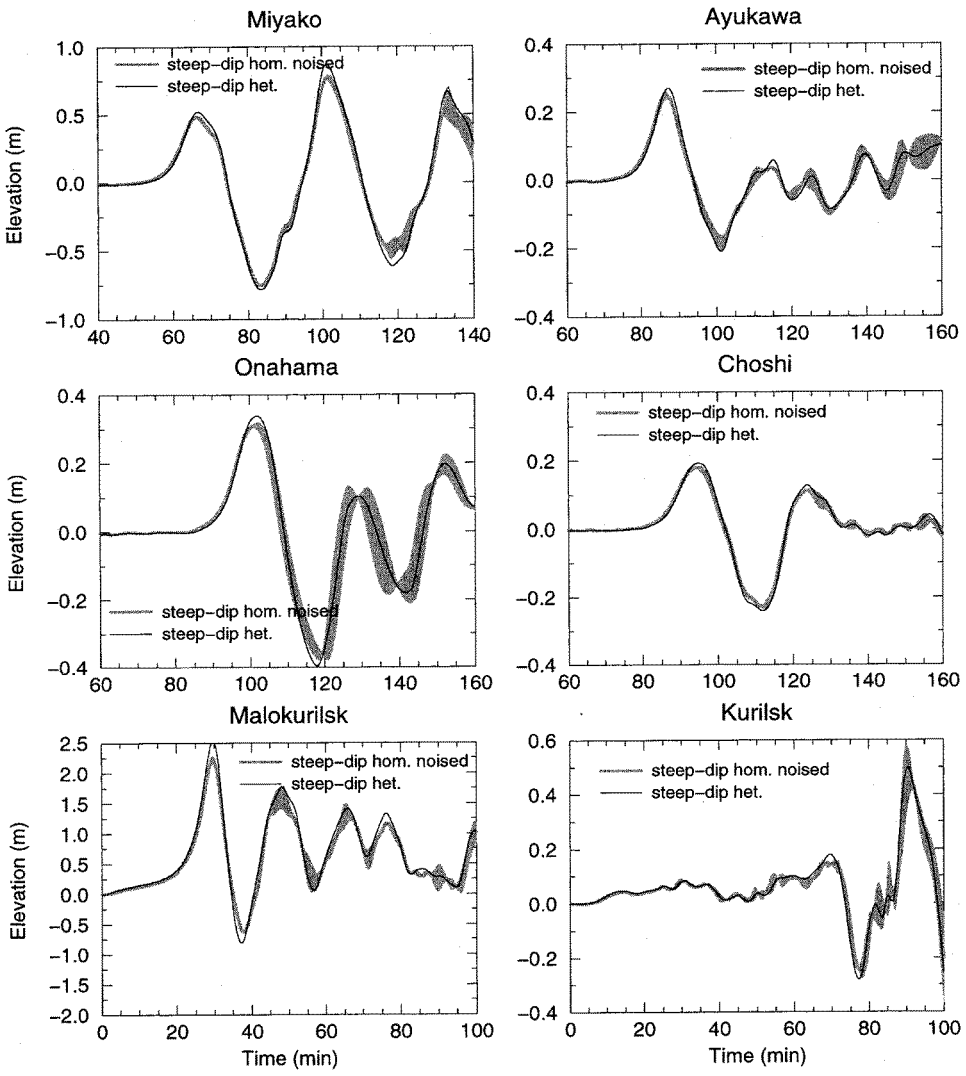

Figure 8
Effects of heterogeneous slip. The gray regions represent the band of uncertainty computed for the homogeneous steep-dip fault model using the perturbed bathymetry. The solid lines are the computed records relative to the heterogeneous steep-dip fault model.

consider 16 virtual tide gauges, labeled from F1 to F16 and which cover a large part of the propagation area, on which we calculate synthetic wave forms. The working scheme is the same as in the previous section: we perturb the bathymetry, injecting a Gaussian random noise with a standard deviation of 10% and a characteristic wavelength of 5 arcmin. Choosing the shallow-dip fault as the reference case, we compute the wave forms using the noised bathymetry. Thereafter we compare these

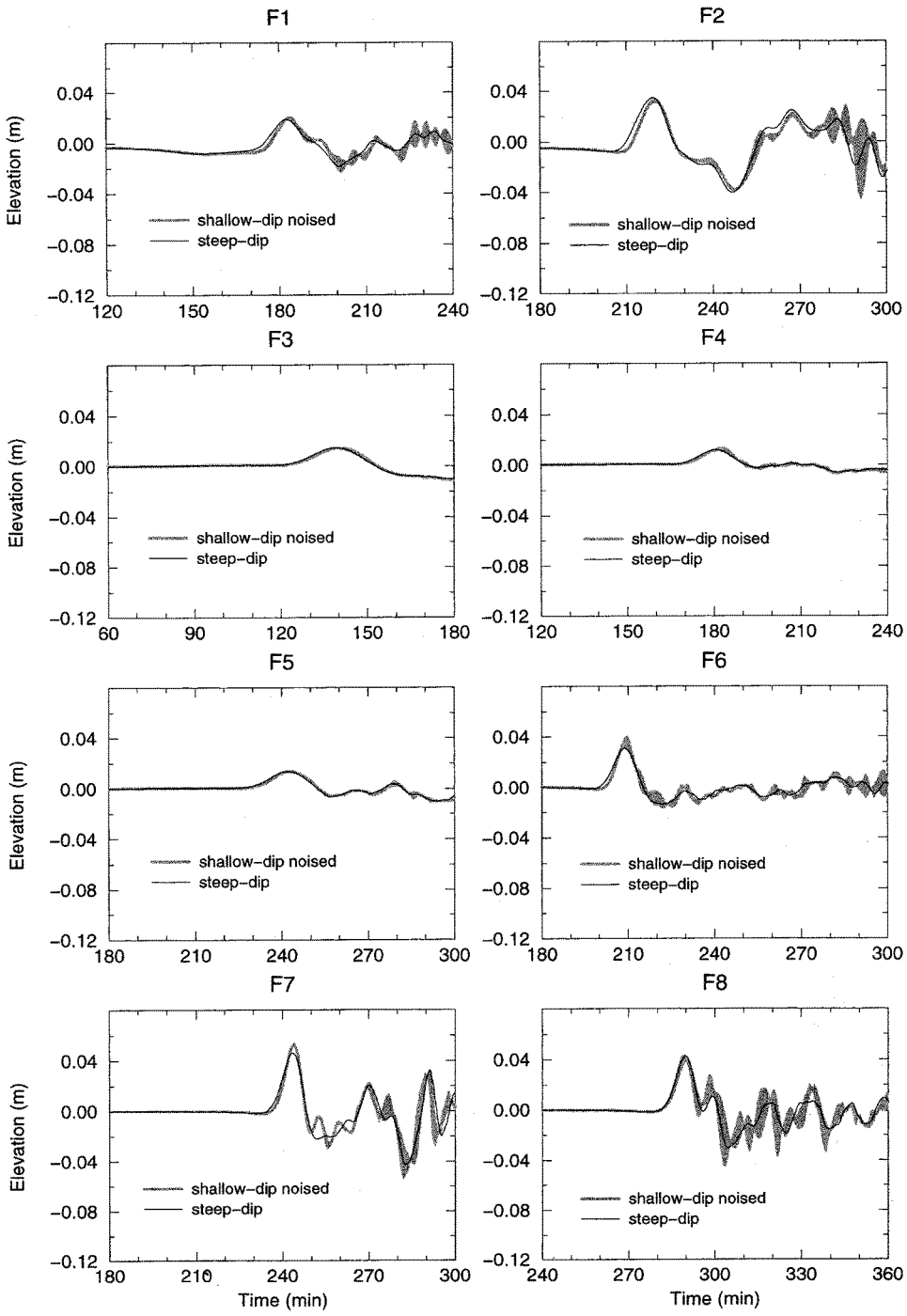

Figure 9
Computed wave forms relative to the far-field simulation. The gray regions represent the band of

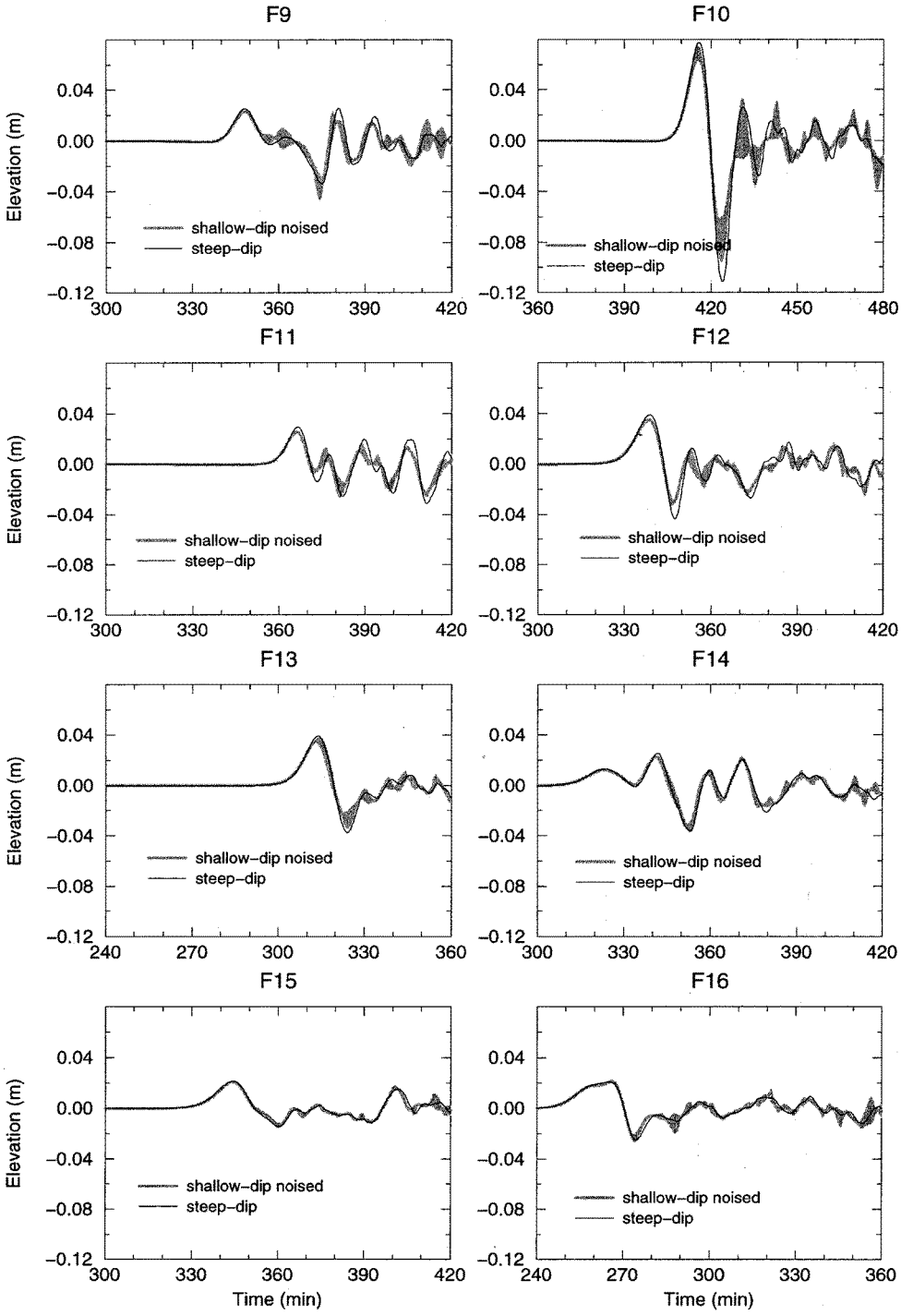

uncertainty computed for the shallow-dip fault model using the perturbed bathymetry. The solid lines are the computed records relative to the steep-dip fault model.

wave forms with those relative to the steep-dip fault, computed using the unperturbed bathymetry: the results are presented in Figure 9. Even though the propagation is not isotropic, the wave forms reflecting differently according to the azimuth of the stations, the two sources produce comparable tsunami. The differences between the computed wave forms, in each station, are always less than, or of the same order of, the uncertainties induced by the noise in the bathymetry. This result confirms that the closest stations to the source area are the most important to retrieve information pertaining to the tsunamigenic mechanism.

Conclusions

In this work we critically investigate the capability of tsunami data to constrain some parameters of the Shikotan earthquake. Even though tsunami data are usually useful to constrain some parameters of the seismic source, this is not actually applicable to this particular earthquake. We verify that the synthetic wave forms, computed for different source mechanisms, are very similar to each other. This forces us to estimate the uncertainty associated with our simulations, by considering a lack of precision in the bathymetric data as a major source of error in wave-forms computations. We illustrate that the differences in the computed wave forms, due to differences in the source mechanism, are of the same order as the uncertainties induced by the error in the bathymetry. Only the wave forms computed in Malokurilsk, which is the closest station to the source area, show important differences: the comparison with the observed record providing a better fit using the steep-dip fault model. In any case we judge that only one record is not sufficient to clearly indicate the steep-dip fault as the best model and to rule out the shallow-dip fault. Choosing the steep-dip fault as a case study, the effect of a heterogeneous slip along the source is also investigated: again, we found that the uncertainties due to a noised bathymetry are of the same order of magnitude as the differences due to heterogeneous slip. From a geophysical point of view our conclusion is that the resolution of the tsunami simulations is insufficient to distinguish between the source models we considered. On the other hand, for the first time, we point out that, if we are dealing with the problem to distinguish between closely competing models, it is necessary to estimate the uncertainties of tsunami simulations. In this paper we introduce a method to take into account a source of uncertainty in tsunami simulation, represented by a noise in the bathymetric data. Nonetheless other errors should be considered, such as imprecise location of the tide gauges. Our feeling is that, to discriminate between sources so similar, additional and more accurate data are needed: the bathymetries, especially close to the tide gauges; the wave forms which should be recorded by tide gauges conceived for tsunami waves; and, finally, data from offshore ocean bottom pressure gauges that may record tsunami waves without contamination of near-shore effects (GONZALEZ and KULIKOV, 1993).

Acknowledgments

We thank R. Dmowska (Harvard University, USA) for helpful comments. We also thank Dr. Y. Tanioka (Japan Meteorological Agency, Tsukuba, Japan) for kindly providing us the bathymetric data and the tide-gauge records of Japan, Dr. H. Yeh (University of Washington, USA) for providing us the record at Malokurilsk, Prof. E. Pelinovsky (Institute of Applied Physics, Nizhny Novogorod, Russia) and G. Shevchenko (Institute of Marine Geology and Geophysics, Yuzhno-Sakhalinsk, Russia) for providing us the record of Kurilsk. This work was partly financed by the European Commission under the TMR project (application n. ENV4-CT96-5044).

REFERENCES

CUMMINS, P. R., HIRANO, S., and KANEDA, Y. (1998), *Refined Coseismic Displacement Modeling for the 1994 Shikotan and Sanriku-oki Earthquakes*, Geophys. Res. Lett. *25*(17), 3219–3222.

DZIEWONSKI, A. M., EKSTRÖM, G., and SALGANIK, M. P. (1995), *Centroid-moment Tensor Solutions for October–December 1994*, Phys. Earth Planet. Inter. *91*, 187–201.

FUKAO, Y., and FURUMOTO, M. (1979), *Stress Drops, Wave Spectra and Recurrence Intervals of Great Earthquakes—Implications of the Etorofu Earthquake of 1958, November 6*, Geophys. J. R. Astr. Soc. *57*, 23–40.

GONZALEZ, F. I., and KULIKOV, YE. A., *Tsunami dispersion observed in deep ocean.* In *Tsunami in the World* (ed. S. Tinti) (Kluwer, Dordrecht 1993) pp. 7–16.

GUSEVA, T., GALAGANOV, O., YAKOVLEV, F., MISHIN, A., KOZHURIN, A., PHILIPOV, M., YANKUSH, A., and VASILENKO, N. (1994), *Results of the Geological Survey and Satellite Geodesic Measurements at Shikotan Island, 18–30 October of 1994*, Special Report 23–31 (in Russian).

JOHNSON, J. M., SATAKE, K., HOLDAHL, S. R., and SAUBER, J. (1996), *The 1964 Prince Williams Sound Earthquake; Joint Inversion of Tsunami and Geodetic Data*, J. Geophys. Res. *101*, 523–532.

HURUKAWA, N. (1995), *Quick Aftershock Relocation of the 1994 Shikotan Earthquake and its Fault Planes*, Geophys. Res. Lett. *22*(23), 3159–3162.

KATSUMATA, K., ICHIYANAGI, M., MIWA, M., KASAHARA, M., and MIYAMACHI, H. (1995), *Aftershock Distribution of the October 4, 1994 M_w 8.3 Kurile Islands Earthquake Determined by a Local Seismic Network in Hokkaido, Japan*, Geophys. Res. Lett. *22*(11), 1321–1324.

KANAMORI, H. (1977), *The Energy Release in Great Earthquakes*, J. Geophys. Res. *82*, 2981–2987.

KIKUCHI, M., and KANAMORI, H. (1995), *The Shikotan Earthquake of October 4, 1994: Lithospheric Earthquake*, Geophys. Res. Lett. *22*(9), 1025–1028.

OKADA, Y. (1985), *Surface Deformation due to Shear and Tensile Faults in a Half Space*, Bull. Seismol. Soc. Am. *75*, 1135–1154.

OZAWA, S. (1996), *Geodetic Inversion for the Fault Model of the 1994 Shikotan Earthquake*, Geophys. Res. Lett. *23*(16), 2009–2112.

PIATANESI, A., TINTI, S., and GAVAGNI, I. (1996), *The Slip Distribution of the 1992 Nicaragua Earthquake from Tsunami Run-up Data*, Geophys. Res. Lett. *23*, 37–40.

SATAKE, K. (1987), *Inversion of Tsunami Wave Forms for the Estimation of a Fault Heterogeneity: Method and Numerical Experiments*, J. Phys. Earth *35*, 241–254.

SATAKE, K. (1993), *Depth Distribution of Coseismic Slip along the Nankai Trough, Japan, from Joint Inversion of Geodetic and Tsunami Data*, J. Geophys. Res. *98*, 4553–4565.

SHIMAZAKI, K. (1978), *Correlation between Intraplate Seismicity and Interplate Earthquake in Tohoku, Northeast Japan*, Bull. Seismol. Soc. Am. *68*, 181–192.

SICHOIX, L., BONNEVILLE, A., and MCNUTT, M. K. (1998), *The Sea-floor Swell and Superswell in French Polynesia*, J. Geophys. Res. *103*, 27,123–27,133.

SMITH, H. F. (1993), *On the Accuracy of Digital Bathymetric Data*, J. Geophys. Res. *98*, 9591–9603.

TANIOKA, Y., RUFF, L., and SATAKE, K. (1995), *The Great Kurile Earthquake of October 4, 1994 Tore the Slab*, Geophys. Res. Lett. *22*(13), 1661–1664.

TSUJI, H., HATANAKA, Y., SAGIYA, T., and HASHIMOTO, M. (1995), *Coseismic Crustal Deformation from the 1994 Hokkaido–Toho–Oki Earthquake Monitored by a Nationwide Continuous GPS Array in Japan*, Geophys. Res. Lett. *22*(13), 1669–1672.

YEH, H., TITOV, V., GUSIAKOV, V., PELINOVSKY, E., KHRAMUSHIN, V., and KAISTRENKO, V. (1995), *The 1994 Shikotan Earthquake Tsunamis*, Pure appl. geophys. *144*, 855–874.

WALD, D. J., and SOMMERVILLE, P. J. (1995), *Variable-slip Rupture Model of the Great 1923 Kanto, Japan, Earthquake: Geodetic and Body-wave Form Analysis*, Bull. Seismol. Soc. Am. *85*, 159–177.

(Received May 13, 1998, revised December 30, 1998, accepted January 5, 1999)

Chapitre 7

Caractéristiques de la source du tsunami de Papouasie Nouvelle-Guinée 1998, déterminées par les données de run-up

Dans ce chapitre, nous étudions le tsunami catastrophique du 17 juillet 1998 en Papouasie Nouvelle-Guinée. Pour étudier ce tsunami, très meurtrier localement, nous disposons seulement des données de run-up mesurées pendent une campagne d'inspection post-événement. Les outils mis en place au cours de cette thèse permettront de préciser certains caractères de la source.

Ce tsunami a provoqué la destruction complète de plusieurs villages et la mort de 2200 personnes, ce qui fait de ce tsunami l'événement le plus meurtrier des 60 dernières années. La magnitude assez modéré (M_S=7.0) du séisme associé et les très importantes hauteurs de run-up (jusqu'à 15 m), mesurées pendant une campagne d'inspection post-événement, ont ouvert une querelle sur le mécanisme de la source tsunamigénique. Le but de ce travail est de déterminer les caracteristiques de la source à l'aide des données de run-up, qui sont les seules observations quantitatives disponibles en champ proche. On montre dans une première étape que la modélisation numerique du tsunami généré par une source sismique, dont les paramètres sont issus des estimations sismologiques, ne reproduit ni la distribution le long de la côte, ni la hauteur maximale des run-ups observés. A l'aide d'une procédure de recherche, nous déterminons d'abord la position de la source, puis nous

extrayons un profil bathymétrique le long d'une trace entre la région de la source et le point côtier où le run-up maximal est observé. En utilisant ce profil bathymetrique, nous conduisons une série de simulations à une dimension, qui nous permet d'estimer l'amplitude minimale nécessaire pour produire le run-up maximal observé. Enfin, à l'aide des simulations aà deux dimensions, qui prennent en compte une source finie et les effets de propagation 2D, nous estimons la longueur maximale de la source, que nous trouvons proche de 30 km. Nous établissons également une relation entre la longueur et l'amplitude des sources qui produisent des distributions de run-up compatibles avec les observations.

Source characteristics of the July 17, 1998 Papua New Guinea tsunami inferred from run-up data

Alessio Piatanesi and Philippe Heinrich

Laboratoire de Detection et de Geophysique/CEA
BP 12, 91680 Bruyères-le-Châtel, France
Email: piatanes@ldg.bruyeres.cea.fr

Submitted to
Journal of Geophysical Research

Abstract

On July 17, 1998 a powerful and local tsunami struck the coast of the Sandaun province of Papua New Guinea (PNG), causing the complete distruction of several villages and the loss of 2200 lives. The moderate magnitude M_S=7.0 of the parent earthquake and the large run-up heights during inundation (up to 15 m), measured during a post-event field survey, opened a problem about the tsunamigenic source mechanism. The aim of this work is to infer the source characteristics of the PNG tsunami from the run-up data, that are the only quantitative observations available in the near-field. Through numerical modeling of the tsunami, we show that a seismic source, whose parameters are in accordance with the seismological estimations, is not able to reproduce the distribution along the coast, nor the maximum heigth, of the observed run-up. Using a test source, we apply a searching procedure and we determine the source location. Then, we extract a bathymetric profile along a track that intersects both the source area and the coastal point where maximum run-up is observed. Using this bathymetric profile, we perform a series of 1D simulations, that unables us to estimate the minimum amplitude necessary to produce the observed maximum run-up. Finally, by means of 2D modeling, where both finiteness of the source and 2D propagation effects are taken into account, we estimate the maximum lengt for the source, that is of 30 km. Furthermore, we establish a relation between the length and the amplitude of the sources that produce run-up distributions that are compatible with the observations.

1. Introduction

On July 17, 1998 an earthquake of magnitude M_S=7.0 took place at 08.49 GMT an epicenter located at (-2.932^0; 141.797^0), near the coast of the Sandaun province of Papua New Guinea (PNG) (Fig. 1). About 20 minutes after the shock, a powerful tsunami struck the coast of PNG, devastating a 25 km long segment of coast, causing the complete distruction of several villages and the loss of 2200 lives, making this event the deadliest tsunami of the last 60 years. Two weeks later, an international team of scientists surveyed the region, with the aim of collecting all useful data to map the inundation (*Kawata et al.*, 1999). They measured 80 inundation heights along a 40 km stretch of coastline, that are presented in Fig. 2. In the Sissano Lagoon and the surrounding areas, they measured a mean of 10 m for run-up heights, with a maximum of 15 m in Arop; then the run-up heights decrease rapidly, both eastward and westward from Sissano Lagoon, to a value of 3-4 m. At Wutung, 100 km east, and at Vanimo, 190 km west from Sissano, 2 to 3 m of wave height was observed. Over both sandspits, closing Sissano Lagoon from the ocean, the team inferred that the water current during tsunami inundation should have been of at least 10 m/s (with a probable peak of 20 m/s). At far-field distances, a few cm of amplitude has been recorded by tide-gauges in the islands of Yap (lat,lon) et Malakal (lat,lon) and 10-20 cm by few stations of the Japanese network.

The large measured maximum inundation depth, together with the shape of the run-up distribution (that is peaked around Sissano Lagoon and decreases rapidly on both sides) and with the relatively small size of the parent earthquake, make this tsunami an intriguing event, opening questions about its source. The aim of this paper is to determine the source characteristics of the PNG tsunami: our method makes use of the run-up heights, measured during the first post-event field survey, as the observational data set (Fig. 2) and of numerical modeling of tsunami to reproduce these data. As we will show in the following sections, our method allow us to determine the precise location, as well as the size and the amplitude, of the tsunamigenic source.

2. Tsunami modeling

The propagation of tsunami waves is usually computed through 2D approximations, both shallow-water (non-dispersive) and Boussinesq (dispersive), of the Navier-Stokes hydrodynamic equations. Since we are dealing with a local tsunami, for which the wave propagation path is only a few wavelengths long, dispersion plays a minor role and the non-dispersive non-linear shallow-water equations represent a good approximation. Denoting by ζ the water elevation above the mean sea level, by **v** the horizontal velocity vector, by *h* the ocean depth and by *g* the gravity acceleration, the governing set of equations can be written as follow:

$$\begin{cases} \partial_t \zeta = -\nabla \cdot [(h+\zeta)\mathbf{v}] \\ \partial_t \mathbf{v} = -g\nabla\zeta - \mathbf{v}\cdot\nabla\mathbf{v} \end{cases} \qquad (1)$$

These equations are solved numerically by means of a finite-differences method based on a Van Leer numerical scheme, that is as accurate as 2^{nd}-order in both time and space (*Van Leer*, 197; *Mangenay et al*, 1999). For 2D simulations we consider a domain whose bottom left and upper right corners are respectively at (-3.25^0;141.5^0) and at (-2.25^0,142.5^0), over a grid consisting of 640,000 cells. Regarding bathymetry, we made a data assimilation (integration), using data from the 2-minute Sandwell-Smith bathymetry for depths greater than 1000 m and data from local nautical charts for shallower depths.

As is well known, in order to perform reliable run-up calculations, accurate and densely sampled topography data are needed. For this reason, even though our numerical model enables us to simulate the tsunami inundation and to calculate run-up heights, we decided not to proceed with these calculations because of a lack in accuracy of the topographic data. Instead, we decided to use 5 m of minimum depth, as a threshold in the bathymetry data, and to consider the boundary conditions of pure

wave reflection along the coastline and of full wave transmission on the boundary in the open ocean. Hence, throughout this paper, we will compare the observed run-up heights to the maximum water elevations computed along the coast.

All simulations presented in the next sections make use of seismic faults, as tsunamigenic sources. For this kind of sources, the coseismic vertical displacement field induced by fault rupture, calculated through Okada's analytical model (*Okada*, 1985), is usually assumed as the initial condition for tsunami calculations.

3. Testing the earthquake source

In a early stage of this study, we first considered a seismic source, whose CMT focal mechanism was computed by Harvard University (*Dziewonski et al.*, 1999), using the epicenter determined by PDE and the projection at the surface of the Harvard centroid. Even though a slight discrepancy between body and surface wave magnitudes suggested that the earthquake could be a "tsunami earthquake" (e.g. *Kanamori*, 1972; *Kanamori and Kikuchi,* 1993), and then particularly efficient as tsunamigenic source, this hypothesis has been ruled out (*Newman and Okal*, 1998; *Okal*, 1999). According to the estimated seismic moment M_0=5.4x10^{19} Nm, we considered a fault with a length of 30 km, a width of 15 km, an average slip of 3.3 m and a rigidity μ=3.5x10^{10} N/m^2, the upper border of the fault being at 3 km of depth: in our frame of reference, the epicenters represent the projection at the surface of the center of the upper border of the fault. The vertical displacement fields, corresponding to both auxiliary planes, are shown in Fig. 3. The fault plane solution FP1 represents a rupture on a shallow dipping fault, that, in the tectonic frame of PNG, may be interpreted as an underthrust (subduction) event. Alternatively, the fault plane solution FP2 represents a dipping rupture on a steep fault plane, with little horizontal component, that may be interpreted as an outer-rise compressional event.

Using these sources, we computed the run-up distribution along the coast of PNG, and we compared them with the observed one. Fig. 4 shows the observed run-ups,

compared with those calculated using the steep fault mechanism (fault plane 2 in Fig. 3), for both Harvard and PDE epicenter. We observe that the amplitudes of the computed run-ups are largely underestimated for both sources: we found a maximum run-up of 2.66 m and 1.44 m for the Harvard and PDE epicenter respectively. As shown in Fig. 4, the run-up heights distribution is not able to reproduce correctly the observations. The Harvard epicenter gives a run-up distribution peaked at lon 142.4^0 (while the observations are peaked at lon 142.12^0) and a lack of energy in the eastern side. The PDE epicenter works even worst, producing a large relative maximum in the western side of the distribution, where the observations decrease at their minimum. These features suggest that the source should certainly be much more energetic and localized elsewhere. In the next section we are dealing with the problem of the search for the source location.

4. Search for the source location

The method used in this paper is based on the main idea that the run-up distribution, produced in the near-field by a tsunami, is very sensitive to the characteristics of the source, i.e. to its location, size and amplitude. This idea has already been investigated by *Piatanesi et al.* (1996), who used near-field run-up data and tsunami numerical modeling to determine the slip distribution along the seismic fault that generated the 1992 Nicaragua tsunami. More recently *Piatanesi et al.* (1999) and *Tinti et al.* (1999) used a similar approach to study the source characteristics of the 1908 Messina (Southern Italy) tsunamigenic earthquake.

To search for the location of the source we proceed as follows. We consider the source fault characterized by a steep dip angle, already used in the preceding section and shown in Fig. 3, as a test source. Keeping fixed all source parameters except the epicenter coordinates, we explore the portion of ocean facing the inundated coast: Fig. 5 shows all source location, i.e. the projection at the surface of the center of the upper border of the fault, considered in this work and that are numbered from 1 to 22.

For each source location we compute the corresponding run-up distribution that we compare with the observed one. As a goodness estimator for the computed run-up distribution, we calculate the linear correlation coefficient τ as follow:

$$\tau = \frac{\sum_{i=1}^{N} (\xi_i - \bar{\xi})(r_i - \bar{r})}{\left[\sum_{i=1}^{N} (\xi_i - \bar{\xi})^2 \sum_{i=1}^{N} (r_i - \bar{r})^2 \right]^{1/2}} \qquad (2)$$

In the above equation, ξ_i and r_i are, respectively, the computed and measured run-up at the i-th observation point, $\bar{\xi}$ and $\bar{r}$ are the mean of the computed and measured run-ups respectively. This coefficient ranges from 0 (no correlation between sets) to 1 (perfect correlation) and can, eventually, assume a negative value, meaning that we are dealing with anti-correlated sets. Hence, we consider as good a source producing a run-up distribution well positively correlated with the observations, and as bad a source giving a poor (or negatively) correlated distribution.

To show the sensibility of the computed run-up distributions, to modifications in the source location, we illustrate in some details two examples, where both an along shore and a perpendicular to the shore variations of the source epicenter is considered. Fig. 6 shows the computed run-up distribution for three different source locations, in which the source is displaced, in an along shore direction, from west (S11) to east (S15). The run-up distribution corresponding to S11 features too much energy in the western side and a lack in both the center and eastern side. As long as the source is placed more eastward (S13), the run-up distribution fits better the observations. Finally, when the source is located in the easternmost part of the explored area, the distribution shows a lack of energy in the western side and a too large concentration in the eastern one. For the case of a perpendicular to the shore variation of the epicenter, shown in Fig. 7, the differences between the computed distributions are less striking : moving from S3 (near the coast) to S22 (open ocean),

the run-ups reduce in the western side and raise in the eastern side, leaving the central peak almost unchanged.

In Table 1 we give a complete list of our searching procedure: for each source we give the mean and maximum computed run-up, the value of our estimator τ as well as the RMS between computed and observed run-up. Our results show that S13 is the best source location, closely followed by S18 (see also Fig. 5).

5. Search for amplitude and size

In comparing the mean and the maximum of the computed and observed run-ups, we found that the formers are largely underestimated, at least by a factor 2.5. One may think that a simple multiplication by a factor 2.5 is sufficient to obtain a final good fit. Anyway, since it is known that non-linear effects play an important role during tsunami propagation in very shallow waters, the amplification of the source amplitude by a multiplicative factor, doesn't allow for the same amplification in the computed run-up heights.

5.1 1D non-linear effects

To estimate correctly the amplitude of the source, we first investigate the non-linear effects by means of 1D tsunami propagation. We extract a bathymetric profile along the track shown in Fig. 5: this profile samples the 2D bathymetry along a track that intersects both the source area (between S13 and S18) and the inundated coast in correspondence of the eastern sandbar of the Sissano Lagoon, where maximum run-up is observed. Using this bathymetry we perform a series of numerical simulations, considering the same source used in the preceding section and letting the slip amount vary, that in turns allows us to consider different amplitudes of initial condition. As an example of 1D propagation, in Fig. 8 we show the wavefield profiles every 30 s of time interval, for the case of 1 m of slip (amplitude=0.6 m) and 10 m of slip (amplitude=6 m). The initial wave splits into two, the first propagating toward the ocean, the second propagating landward. The wave propagating towards the coast

experiences a growing of amplitude, a shortening of the wavelength and a steepening of the wavefront, as bathymetry shoals. But, as shown in Fig. 8a (top panel), the amplitude almost stops to grow at around lat= -3.02^0, where a back-reflection occurs in correspondence of the abrupt change of the bathymetric slope, subtracting energy to the incoming wave. In addition to that, a non-linear effect, striking for the case of 10 m of slip (see Fig. 8b), occurs in the so-called "region of rapid decay" (*Synolakis and Skjelbreia*, 1993).

We define the amplification factor as the ratio between the computed maximum elevation at the coast and the initial wave amplitude. As shown in Fig. 9, the amplification factor is not constant, as expected in a linear case, but decreasing from a value of 3.33 (for an initial wave amplitude of 0.6 m) to 2.35 (for an initial wave amplitude of 14.4 m). Fig. 9 also shows the maximum water elevation computed at the coast, as a function of the initial wave amplitude: an amplitude of 6 m is necessary to produce a run-up of about 15 m.

5.2 2D propagation effects

The 1D simulations led us to reach a deeper insight into the non-linear dynamics of this tsunami and to estimate the initial wave amplitude necessary to produce the observed maximum run-up. Now, by means of 2D simulations, the effects of both finiteness of the source and 2D propagation are taken into account. We consider 5 sources, with the same focal mechanism as in section 4, but with a varying fault length of, respectively, 50, 30, 25, 20, 15, 10, 5 and 2.5 km. The slip along the fault is arranged in such a way as to produce, for all sources, a maximum amplitude of 6 m in the vertical displacement field. For each source, we compute the corresponding run-up distributions, that are shown in Fig. 10. The effect of the length of the fault is evident: the source with a fault length of 50 km produce the correct maximum run-up of 15 m, as expected from 1D numerical experiments, but it also gives too large heights in both sides of the run-up distribution. A length of 30 km fits the observations well. Then, as the length of the source is shortened, 2D propagation effects become important and strongly damps the central peak of maximum run-up.

These results enable us to fix some limits to the source parameters: to correctly reproduce the observed run-up distribution, the initial amplitude has to be of at least 6 m and the fault no longer than 30 km. Anyway the possibility that a shorter source, with a larger amplitude, can reproduce correctly the observations, are not yet explored. To do this, it is necessary to know the amplitude we have to allow on each of such a source, to produce a maximum run-up of about 15 m. Instead to deal with a CPU expensive trial and error procedure, we proceed as follow. On the basis of the results we obtained for an amplitude of 6 m (Fig. 10), we estimate the 2D propagation effects, acting on a finite source of length L, by means of the coefficient $\gamma(L)$ defined as:

$$\gamma(L) = \frac{R_{2D}(L)}{R_{1D}} \qquad (3)$$

In eq. (3) R_{1D} is the maximum run-up computed in the 1D case and $R_{2D}(L)$ is the maximum run-up computed in the 2D case using a source of length L. In Table 2 we list the values of $\gamma(L)$. Now, making the hypothesis that $\gamma(L)$ is only slightly dependent on the amplitude, we consider R_{2D}=15 m (that is the desired maximum run-up) as fixed and, through eq. (3), we calculate the value R_{1D} for the various fault lengths. Once reported on the plot of Fig. 9, these values give an estimate of the amplitudes one should take for the various fault lengths. This allows us to determine a class of "equivalent seismic sources", that are able to produce the observed run-up distribution: these fault sources have to satisfy a length-amplitude relation and consequently, since the amplitude is proportional to the slip, a length-slip relation, that are shown in Fig. 11. To verify that such a procedure gives a reliable estimation of the amplitudes, we perform a test simulation using a fault length of 2.5 km, the shortest we considered in this work, for which we estimate an amplitude of 14 m (corresponding to 88 m of slip). Using such a source we compute the run-up distribution. The comparison with the observations, presented in Fig. 12, shows that the main features are quite well reproduced as well as the maximum run-up.

6. Discussion and conclusion

The results we reached in the above section show that the source of the tsunami must have minimum vertical amplitude of 6 m (corresponding to ~10 m of slip on the fault), maximum length of 30 km (see Fig. 11) and seismic moment 3 times larger than that estimated by means of seismological data: these numbers are not compatible with any known seismic source of magnitude M_w=7. Several eyewitnesses established that the tsunami struck the coast of PNG about 20 minutes after the earthquake (*Kawata et al.*, 1999). This time constraint is not compatible with a source localized at around (-2.85; 142.20), that starts to propagate immediately after the shock: in fact, the tsunami, generated by such a source, should have reached the coast only 10 minutes later. These arguments lead us to rule out the mainshock, as well as any other seismic source, as the source of the tsunami and to propose a submarine landslide as the source of the PNG tsunami. Preliminary simulations show that the spatial extent and the amplitude of the water elevation field, produced by a submarine slide of 3 km^3 of volume, are in good accordance with our estimations (Heinrich, personal communication).

The idea of a slump is supported by some data obtained during a cruise organized in January 1999. The survey, that explored the continental shelf off the coast of the Sandaun province, revealed a fresh underwater slump centered at (-2.85^0, 142.25^0) (*Tappin et al.*, 1999). These coordinates correspond perfectly with our best estimation of the source location (see Fig. 5).

Both main shock and aftershocks produced T waves, that have been well recorded at the Wake Island seismic station. An examination of the waveforms shows that an event, starting at 09:02 GMT, features a duration of about 50 s, a considerable duration for this small event of m_b=4.4 (*Okal,* 1999). Furthermore the 95%-confidence ellipse of the location of this event intersects the area of the slump. He has tentatively suggested that this event is indeed a slump triggered by the main shock and responsible by the tsunami generation.

On the basis of our results and of that above mentioned, it is likely that the source of the PNG tsunami is a submarine landslide. The next step to complete understand this event will be the modeling of the tsunami, in particular of the run-up distribution, generated by such a source. The constraints on the source characteristics we give in this paper, will be certainly useful for further investigators.

We feel that the method presented in this paper is well adapted to study the source characteristics of the so-called "local tsunamis" (*Geist*, 1998; *Geist and Yoshioka*, 1995), for which the run-ups, measured during post-event field surveys, are often the only available quantitative data to study the source mechanism. The Papua New Guinea tsunami "local tsunami" shows that this kind of events represent a regional hazard that should be re-evaluated.

References

Dziewonski, A.M., G. Ekström and N.N. Maternovskaya, Centroid-moment tensor solutions for July-September, 1998, *Phys. Earth and Planet. Int.*, 114, 99-107, 1999.

Geist, E.L., Local tsunamis and earthquake source parameters, *Adv. Geophys.*, **39**, 117-209, 1998.

Geist, E.L., and S. Yoshioka, Source parameters controlling the generation and propagation of potential local tsunamis along the Cascadian margin, *Natural Hazards*, 13, 151-177, 1995.

Kanamori, H., Mechanism of tsunami earthquakes, *Phys. Earth Planet. Inter.*, 6, 246-259.

Kanamori, H., and M. Kikuchi, The 1992 Nicaragua earthquake: a slow tsunami earthquake assciated with subducted sediments, *Nature*, **361**, 714-716, 1993.

Kawata, Y., B.C. Benson, J.C. Borrero, J.L. Borrero, H.L. Davies, W.P. de Lange, F. Imamura, H. Letz, J. Nott and C.E. Synolakis, Tsunami in Papua New Guinea was as intense as first thought, *Eos Trans. AGU,* **80**, pp. 101 and 104-105, 1999.

Mangenay, A., Ph. Heinrich and R. Roche, Analytical solution for testing debris avalanche numerical models, *Pure App. Geophys., **157** (*in press*).*

Newman, A.V. and Okal E.A., Teleseismic estimates of radiated seismic energy: the E/M_0 discriminant for tsunami earthquakes*, J. Geophys. Res.,* **103**, 26885-26898, 1998.

Okada, Y., Surface deformation due to shear and tensile faults in a half space, *Bull. Seism. Soc. Am.,* **75***,* 1135-1154, 1985.

Okal, E.A., The 1998 Papua New Guinea tsunami: an overview, *Proc. of the International Conference on Tsunamis*, 26-28 may, Paris-France, 1999.

Piatanesi, A., S. Tinti and I. Gavagni, The slip distribution of the 1992 Nicaragua earthquake from tsunami run-up data, *Geophys. Res. Lett.*, **23**, 37-40, 1996.

Piatanesi, A., S. Tinti and E. Bortolucci, Finite-element simulations of the 28 December 1908 Messina Straits (Southern Italy) tsunami, *J. Phys. Chem. Earth*, **24**, 145-150, 1999.

Synolakis, E.C., and J.I. Skjelbreia, Evolution of maximum amplitude of solitary wave on plane beaches, *J. Wtrwy. Harb. Port and Coast. Engrg.*, **119**(3), 323-342, 1993.

Tappin, D. R., M. Takeshi, P. Watts, K. Satake, G.M. McMurty, M. Matsuyama, Y. Lafoy, Y. Tsuji, T. Kanamatsu, W. Lus, Y. Iwabuchi, H. Yeh, Y. Matsumotu, M. Nakamura, M. Mahoi, P. Hill, K. Crook, L. Anton, and J.P. Walsh, Sediment slump likely caused 1998 Papua New Guinea tsunami, *Eos Trans. AGU,* **80**, pp. 329, 334 and 340, 1999.

Tinti, S., A. Armigliato, E. Bortolucci and A. Piatanesi, Identification of the source fault of the 1908 Messina earthquake through tsunami modeling. It is a possible task?, *J. Phys. Chem. Earth*, **24**, 417-421, 1999.

Van Leer, B., Toward the ultimate conservation schemeV. A second order sequel to Godunov's method, *J. Comput. Phys.*, **32**, 106-136, 1979

Figure captions

Figure 1. Map of the Papua New Guinea. The rectangle shows the area affected by the July 17, 1998 tsunami and the beach-ball represents the Harvard CMT of the parent earthquake.

Figure 2. Run-up heights measured during the first post-event field survey along the coast affected by the tsunami.

Figure 3. Co-seismic vertical displacement fields generated by the earthquake, for both auxiliary fault planes of the Harvard CMT.

Figure 4. Computed run-up distribution using the fault plane solutions 2 (see Fig. 3) using PDE epicenter and the position of the Harvard centroid.

Figure 5. Bathymetry of the ocean facing the coast affected by the tsunami. The circles, labelled from S1 to S22, indicate the positions of the sources used in the search for location procedure. Source locations, giving high correlation between the computed and observed run-up, are in dark grey. The solid line represents the track of the 1D bathymetric profile, used to perform 1D simulations.

Figure 6. Computed run-up distributions using the source positions S11, S13 and S15. Each distribution is normalized in dividing the run-up heigths by its mean.

Figure 7. Computed run-up distributions for the source positions S3, S13 and S22. Each distribution is normalized in dividing the run-up heigths by its mean.

Figure 8. a) 1D tsunami propagation along the track depicted in Fig. 5 for a source of small amplitude (top panel) and of large amplitude (middle panel), using the

bathymetry profile shown in the bottom panel. **b)** close-up of the zone of strong amplitude decay.

Figure 9. Non-linear dependence of both maximum water elevation computed at the coast and amplification factor from the initial wave amplitude. The amplification factor is defined as the ratio between the maximum elevation at the coast and the initial wave amplitude.

Figure 10. Computed run-up distributions using differents lengths of the seismic fault and an amplitude of 6 m.

Figure 11. Relation between the length and the amplitude of equivalent seismic sources that give run-up distributions that are compatible with the observations.

Figure 12. Computed run-up distribution using a seismic source with 2.5 km of length and an amplitude of 14 m.

Table 1

	Mean run-up (m)	Max run-up (m)	Correlat.	RMS (m)
Observed	6.87	14.78	1.00	0.00
PDE (fp1)	0.324	0.84	-0.130	7.20
PDE (fp2)	0.275	1.44	-0.290	7.26
HAR (fp1)	0.734	1.51	0.224	6.80
HAR (fp2)	1.34	2.66	0.347	6.21
S1	1.45	4.43	0.022	6.28
S2	1.83	4.69	0.237	5.84
S3	2.16	3.94	0.587	5.34
S4	2.15	3.74	0.497	5.41
S5	1.84	3.43	0.212	5.82
S6	1.70	4.48	0.239	5.95
S7	1.83	4.69	0.237	5.84
S8	2.54	5.30	0.636	4.93
S9	2.75	5.10	0.638	4.75
S10	2.57	4.95	0.251	5.21
S11	1.86	4.20	0.410	5.96
S12	2.21	4.93	0.559	5.29
S13	2.62	5.72	0.697	4.81
S14	2.75	5.35	0.638	4.75
S15	2.54	4.63	0.351	5.15
S16	2.01	4.33	0.531	5.50
S17	2.29	4.96	0.652	5.16
S18	2.50	5.47	0.693	4.93
S19	2.61	5.01	0.556	4.95
S20	2.09	4.28	0.600	5.38
S21	2.35	5.14	0.673	5.09
S22	2.46	4.92	0.639	5.03

Table 2

	L=50 km	L=30 km	L=25 km	L=20 km	L=15 km	L=10 km	L=5 km	L=2.5 km
$\gamma(L)$	0.980	0.930	0.871	0.789	0.692	0.590	0.495	0.458

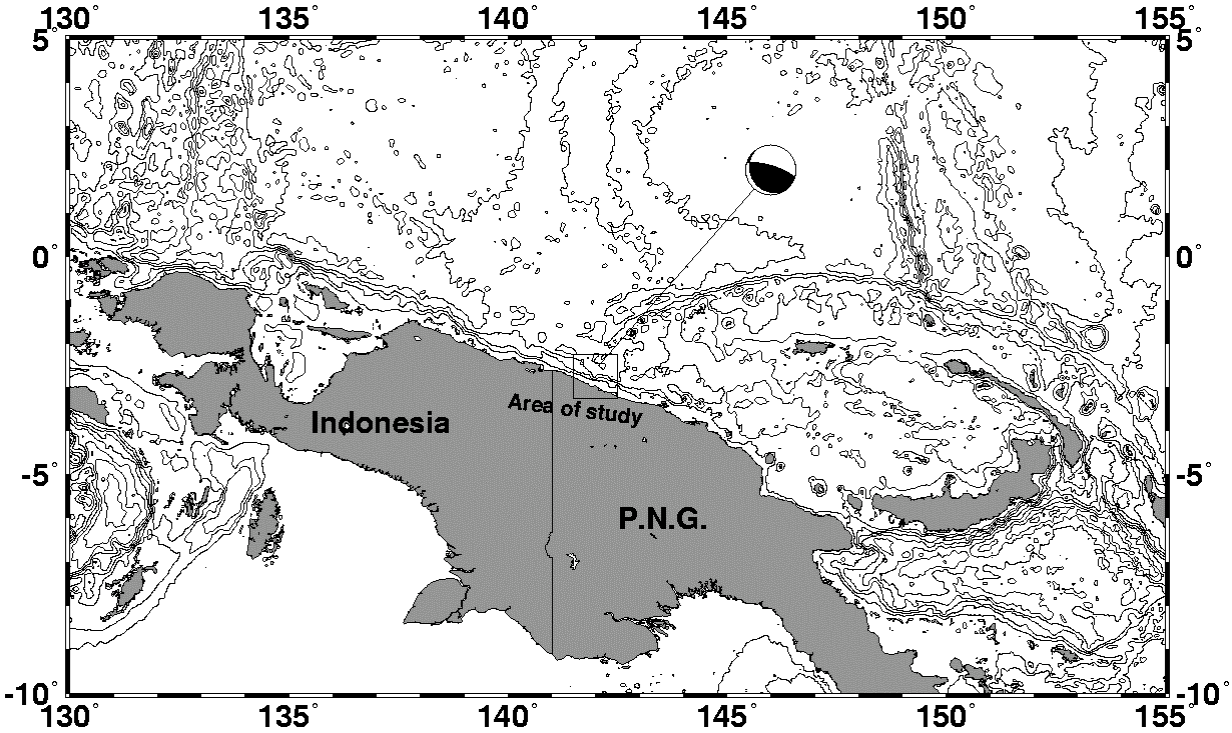

Figure 1

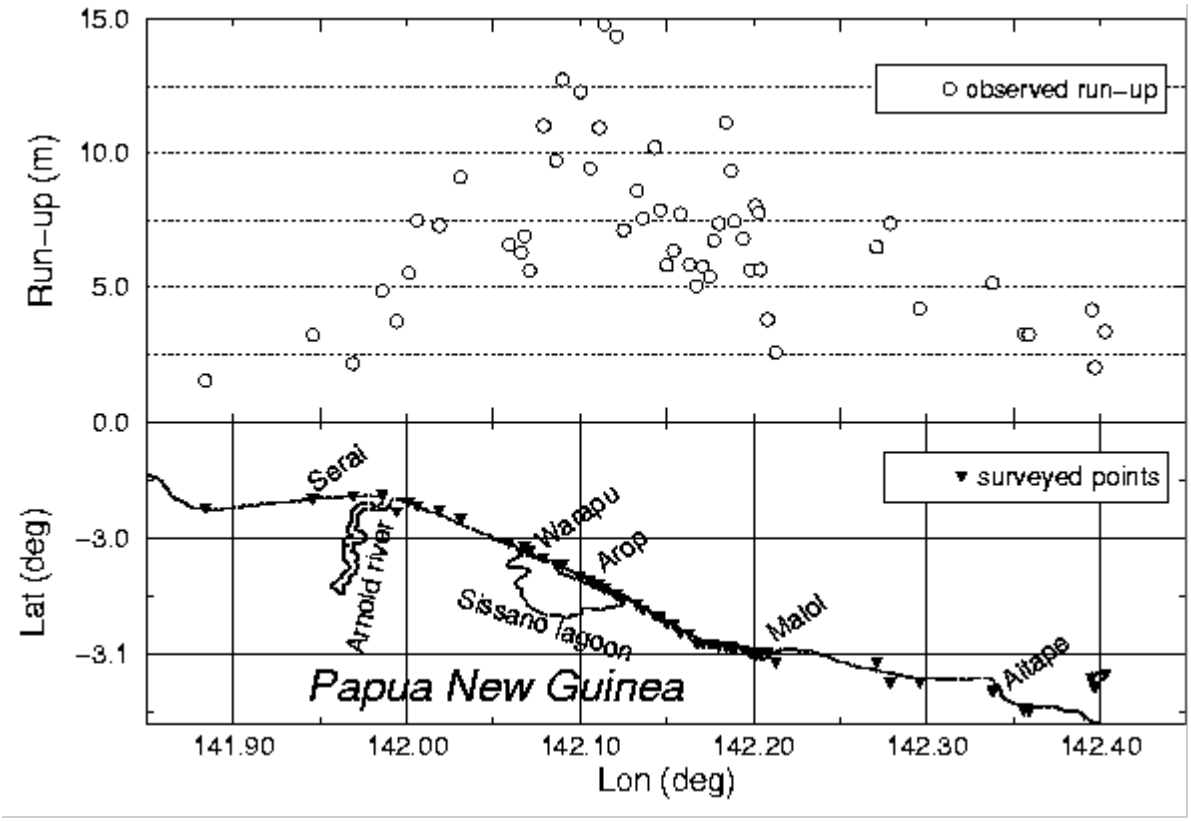
15.0
10.0
5.0
0.0
Run–up (m)
observed run–up
surveyed points
Lat (deg)
−3.0
−3.1
Serai
Arnold river
Warapu
Arop
Sissano lagoon
Malol
Aitape
Papua New Guinea
141.90
142.00
142.10
142.20
142.30
142.40
Lon (deg)

Figure 2

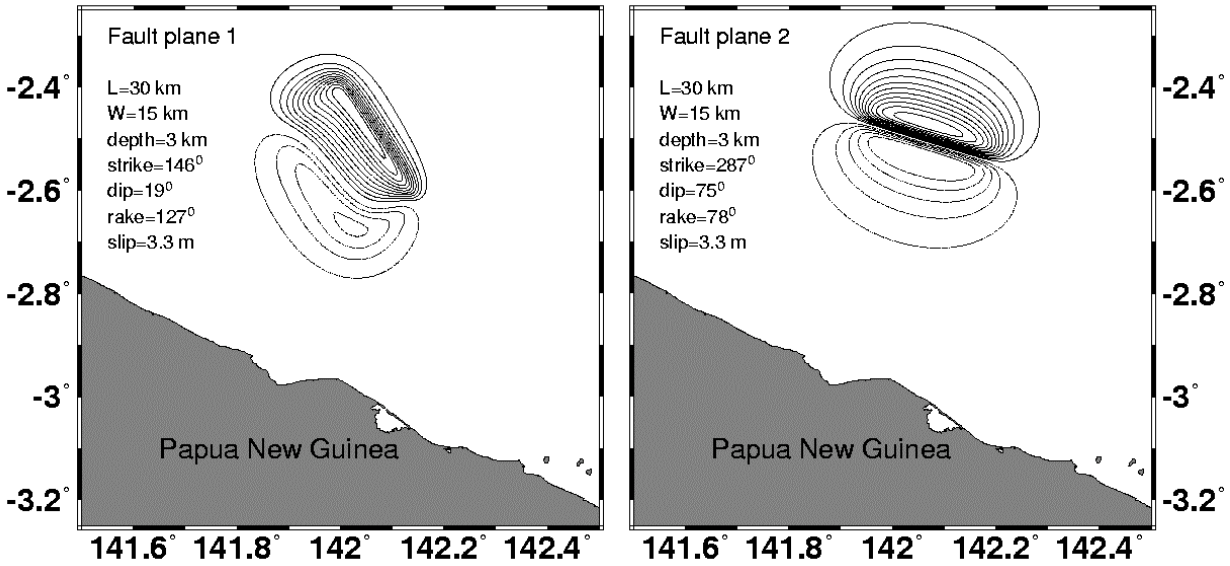
Fault plane 1
L=30 km
W=15 km
depth=3 km
strike=146°
dip=19°
rake=127°
slip=3.3 m
Papua New Guinea
Fault plane 2
L=30 km
W=15 km
depth=3 km
strike=287°
dip=75°
rake=78°
slip=3.3 m
Papua New Guinea
-2.4°
-2.6°
-2.8°
-3°
-3.2°
141.6° 141.8° 142° 142.2° 142.4°

Figure 3

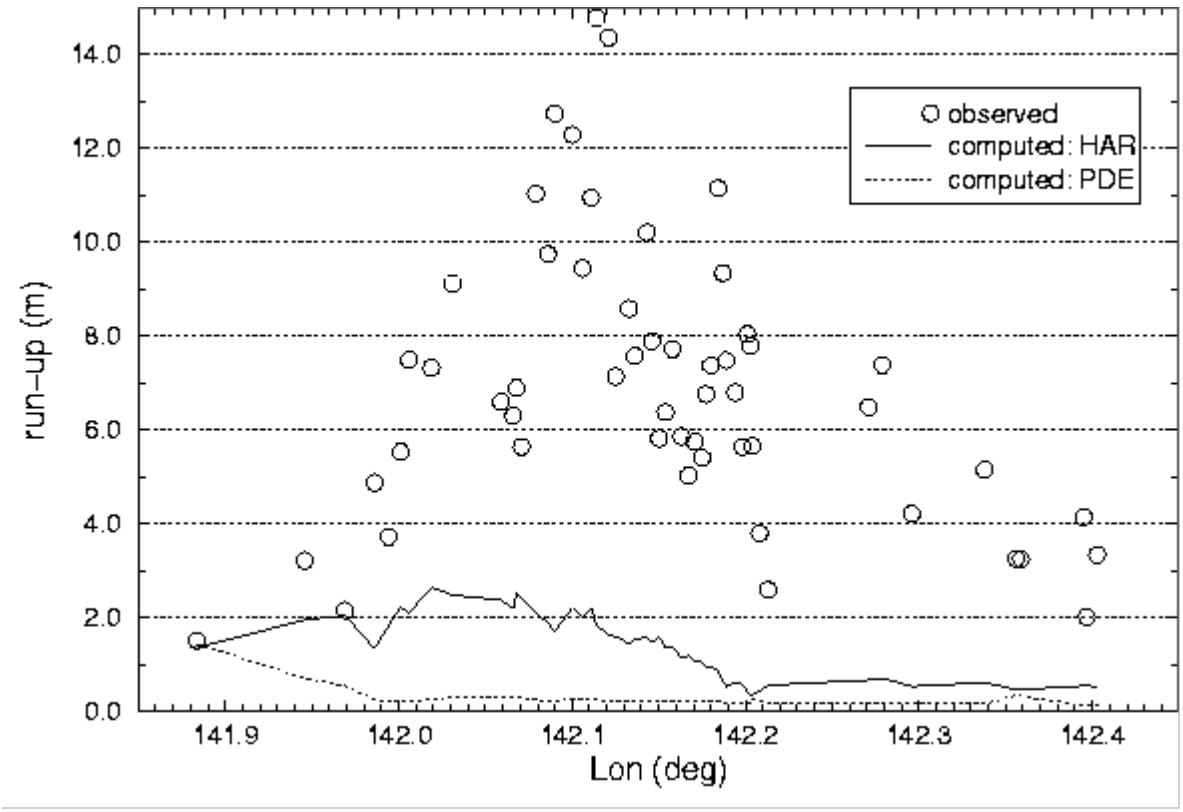
observed
computed: HAR
computed: PDE
run-up (m)
Lon (deg)
0.0
2.0
4.0
6.0
8.0
10.0
12.0
14.0
141.9
142.0
142.1
142.2
142.3
142.4

Figure 4

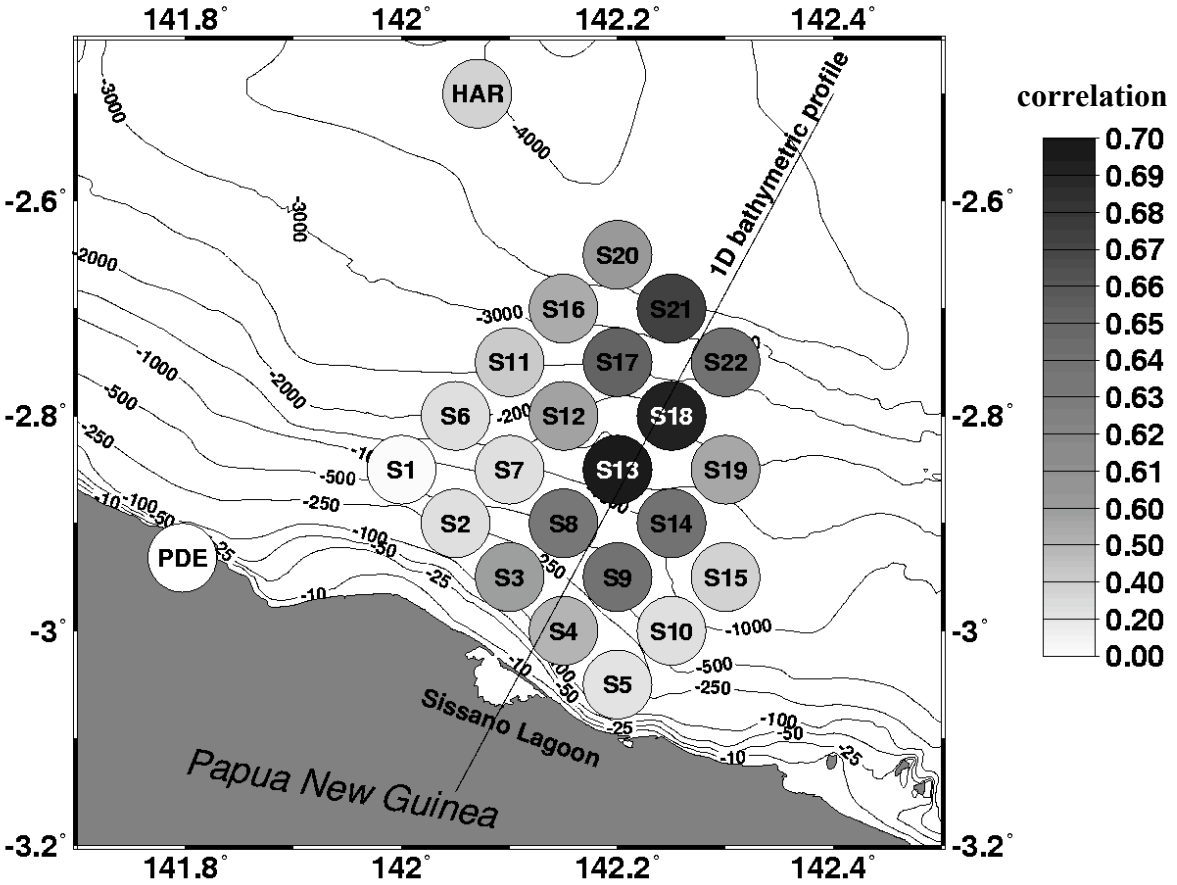
141.8°
142°
142.2°
142.4°
-2.6°
-2.8°
-3°
-3.2°
HAR
PDE
S1
S2
S3
S4
S5
S6
S7
S8
S9
S10
S11
S12
S13
S14
S15
S16
S17
S18
S19
S20
S21
S22
1D bathymetric profile
Sissano Lagoon
Papua New Guinea
correlation
0.70
0.69
0.68
0.67
0.66
0.65
0.64
0.63
0.62
0.61
0.60
0.50
0.40
0.20
0.00

Figure 5

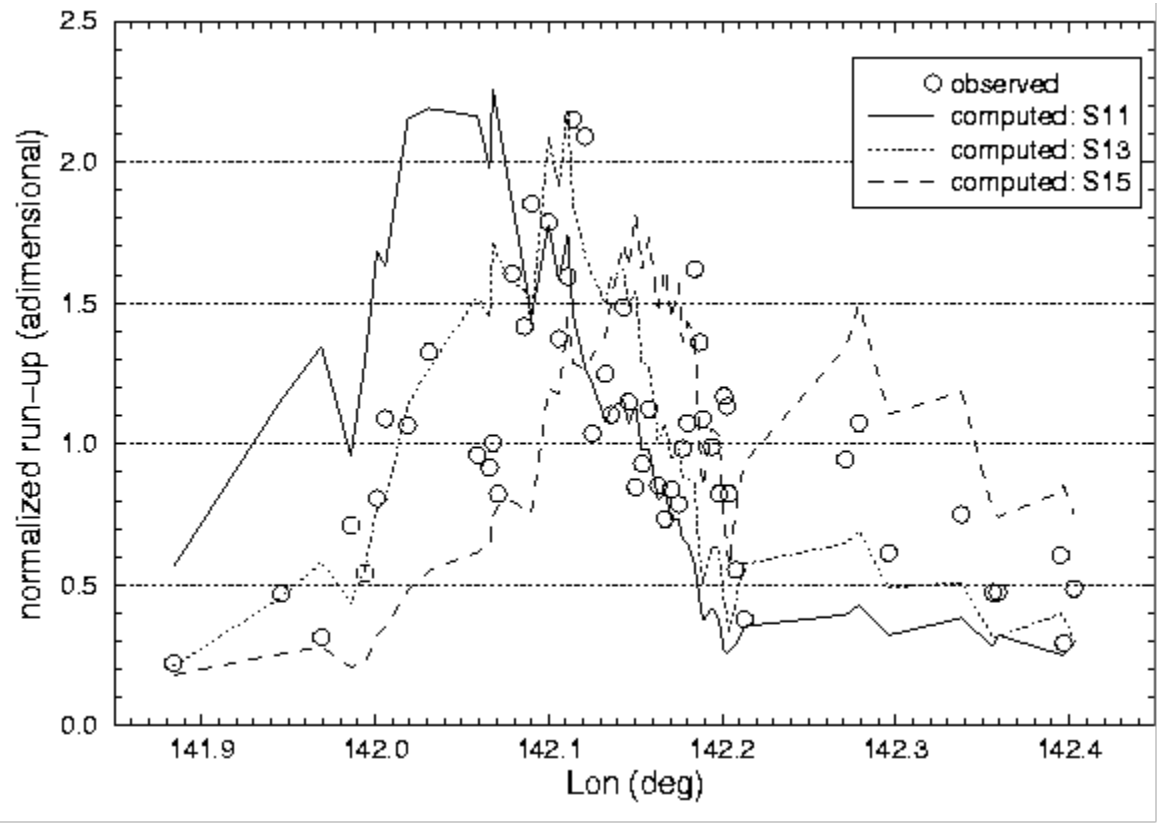
observed
computed: S11
computed: S13
computed: S15
normalized run-up (adimensional)
Lon (deg)
0.0
0.5
1.0
1.5
2.0
2.5
141.9
142.0
142.1
142.2
142.3
142.4

Figure 6

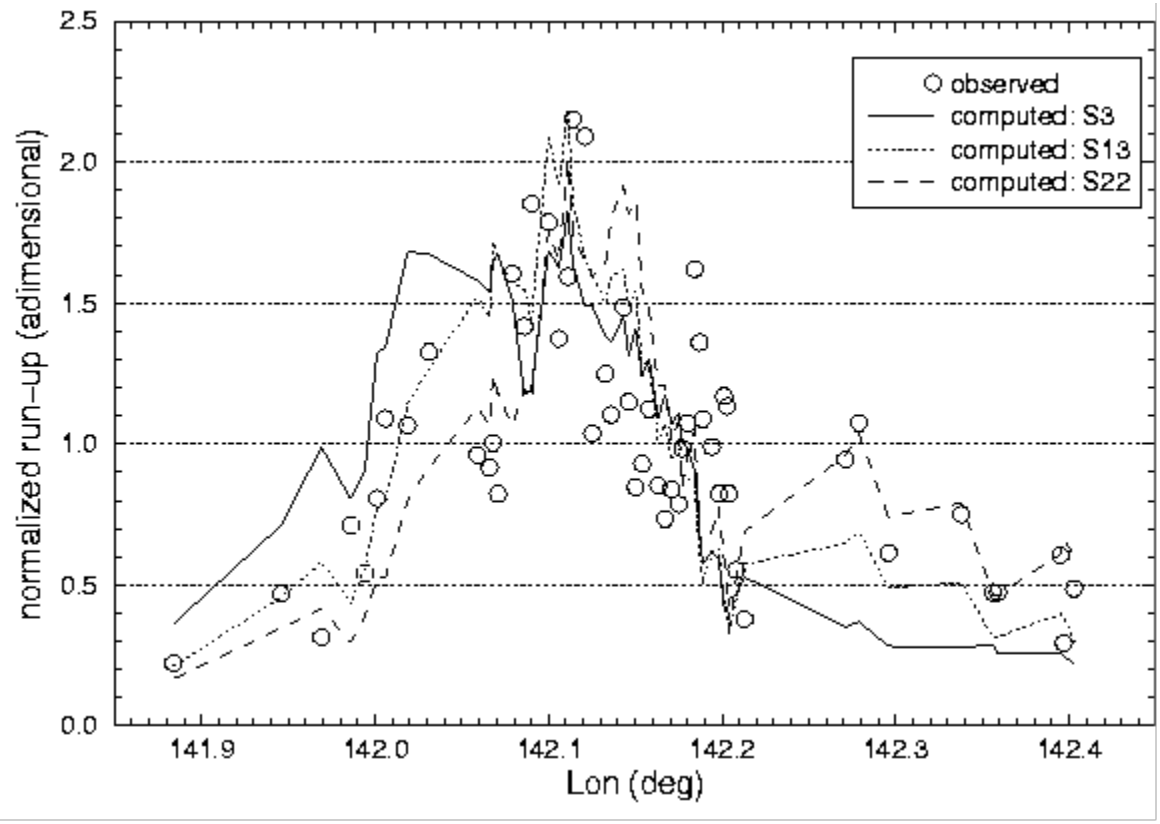
observed
computed: S3
computed: S13
computed: S22
normalized run-up (adimensional)
Lon (deg)
0.0
0.5
1.0
1.5
2.0
2.5
141.9
142.0
142.1
142.2
142.3
142.4

Figure 7

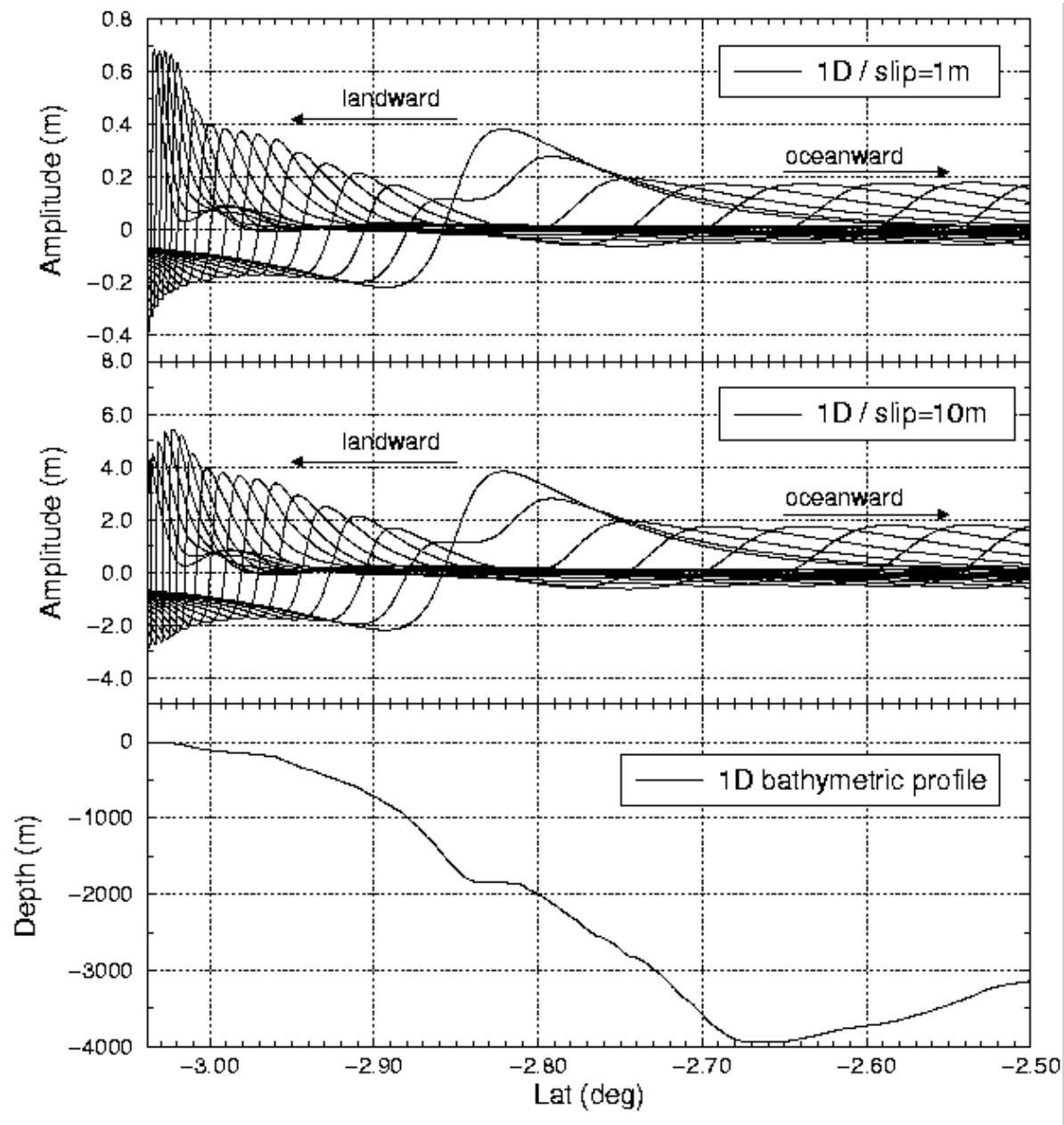
1D / slip=1m
landward
oceanward
Amplitude (m)
1D / slip=10m
landward
oceanward
Amplitude (m)
1D bathymetric profile
Depth (m)
Lat (deg)

Figure 8a

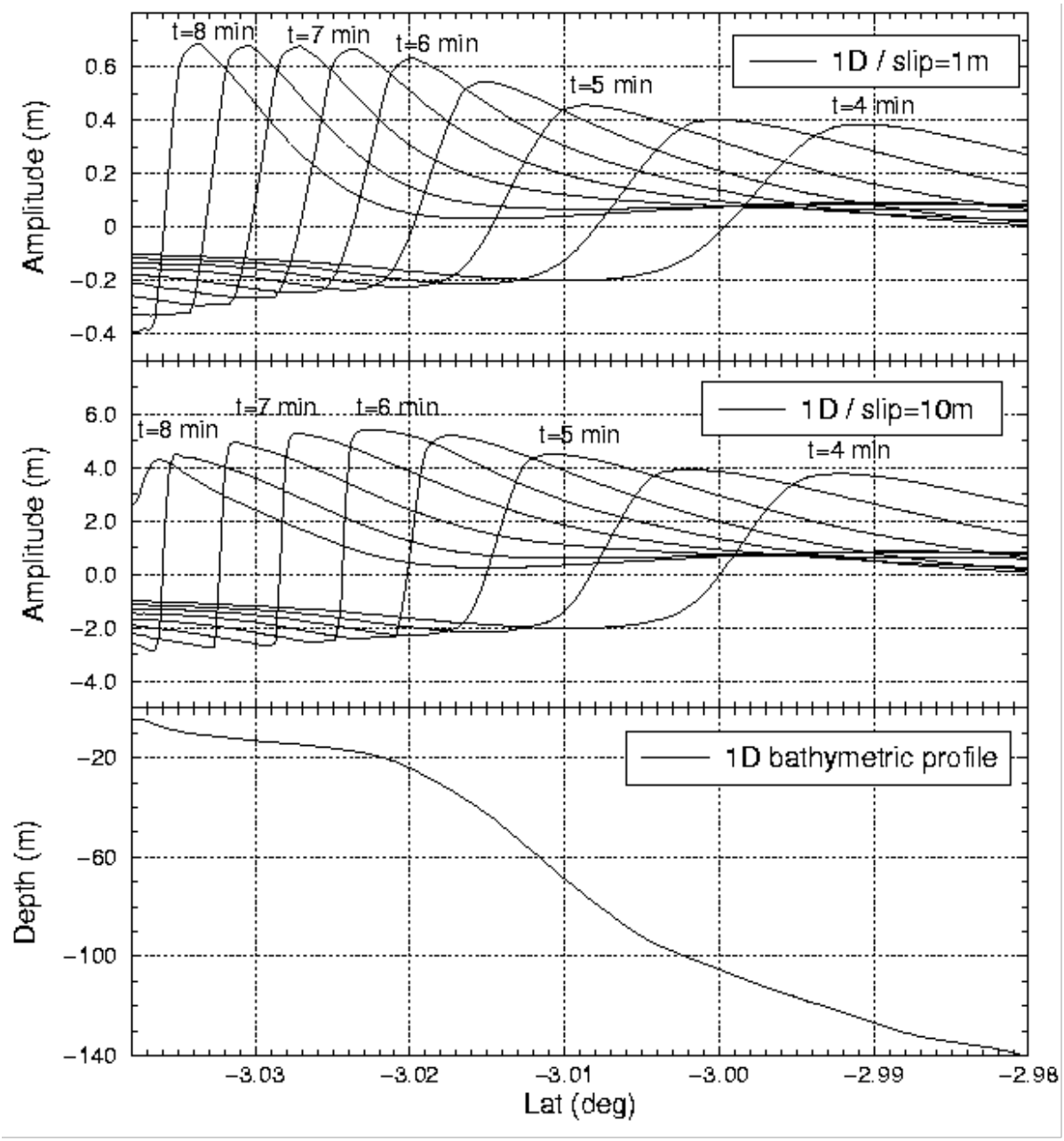
t=8 min
t=7 min
t=6 min
t=5 min
t=4 min
1D / slip=1m
Amplitude (m)
0.6
0.4
0.2
0
−0.2
−0.4
t=8 min
t=7 min
t=6 min
t=5 min
t=4 min
1D / slip=10m
Amplitude (m)
6.0
4.0
2.0
0.0
−2.0
−4.0
1D bathymetric profile
Depth (m)
−20
−60
−100
−140
−3.03
−3.02
−3.01
−3.00
−2.99
−2.98
Lat (deg)

Figure 8b

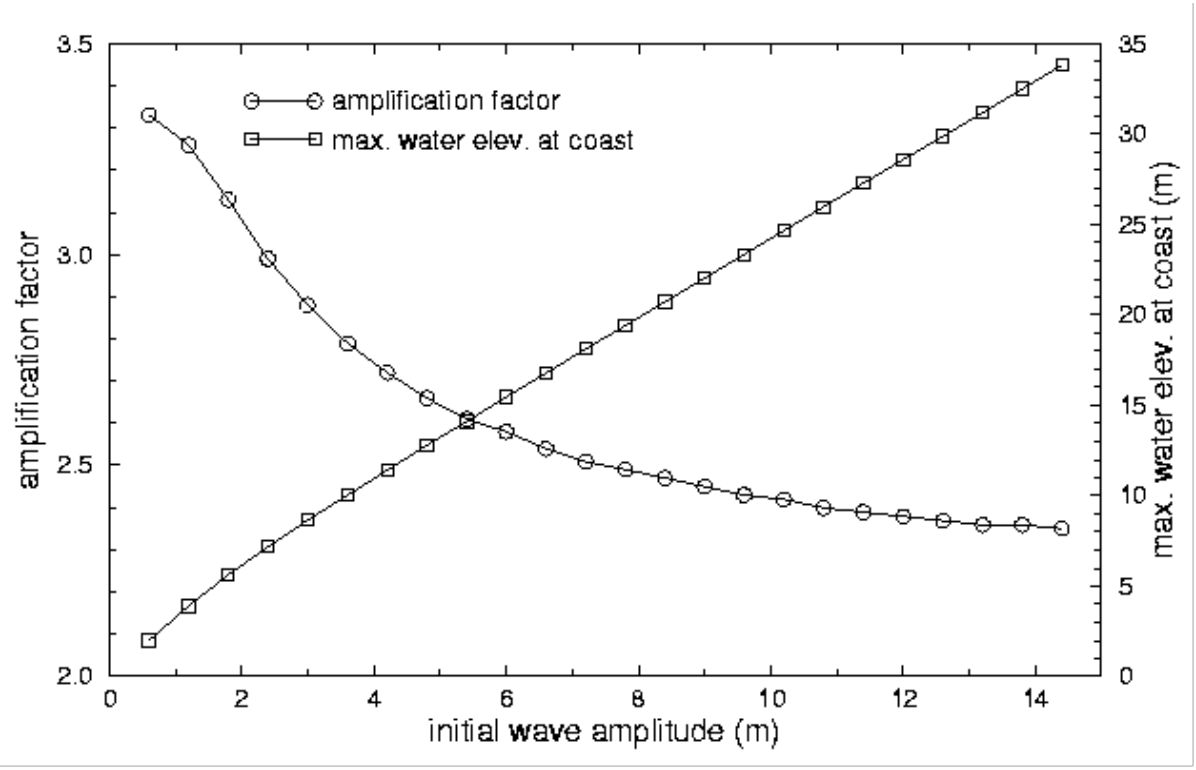
amplification factor
max. water elev. at coast
amplification factor
max. water elev. at coast (m)
initial wave amplitude (m)
3.5
3.0
2.5
2.0
35
30
25
20
15
10
5
0
0
2
4
6
8
10
12
14

Figure 9

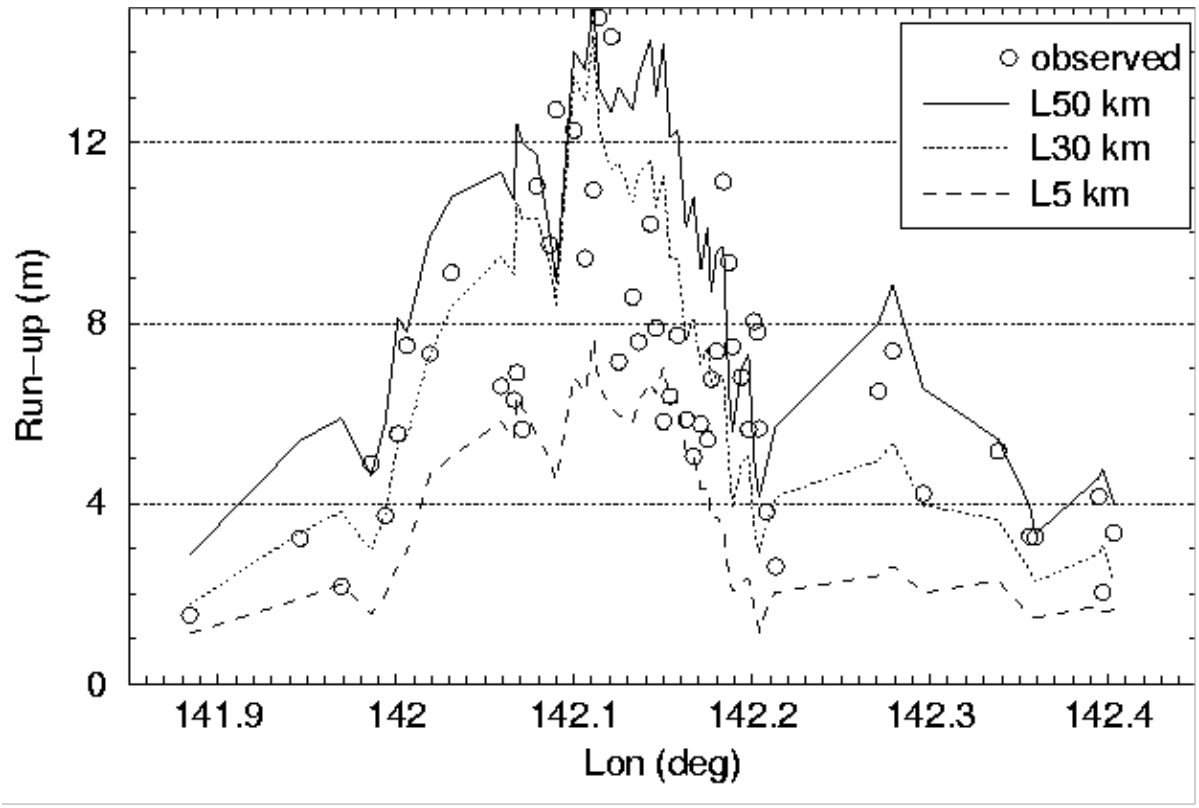
observed
L50 km
L30 km
L5 km
Run-up (m)
0
4
8
12
141.9
142
142.1
142.2
142.3
142.4
Lon (deg)

Figure 10

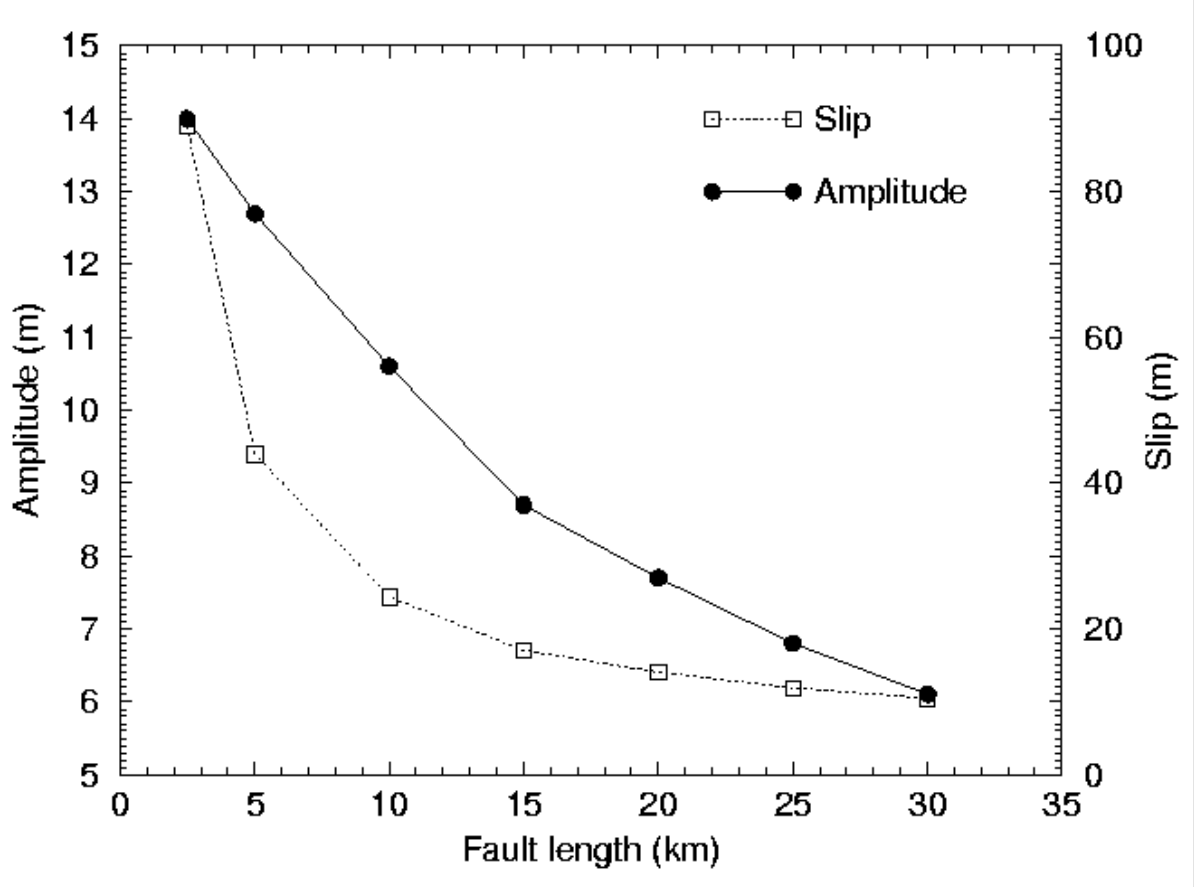
Slip
Amplitude
Amplitude (m)
Slip (m)
Fault length (km)
15
14
13
12
11
10
9
8
7
6
5
100
80
60
40
20
0
0
5
10
15
20
25
30
35

Figure 11

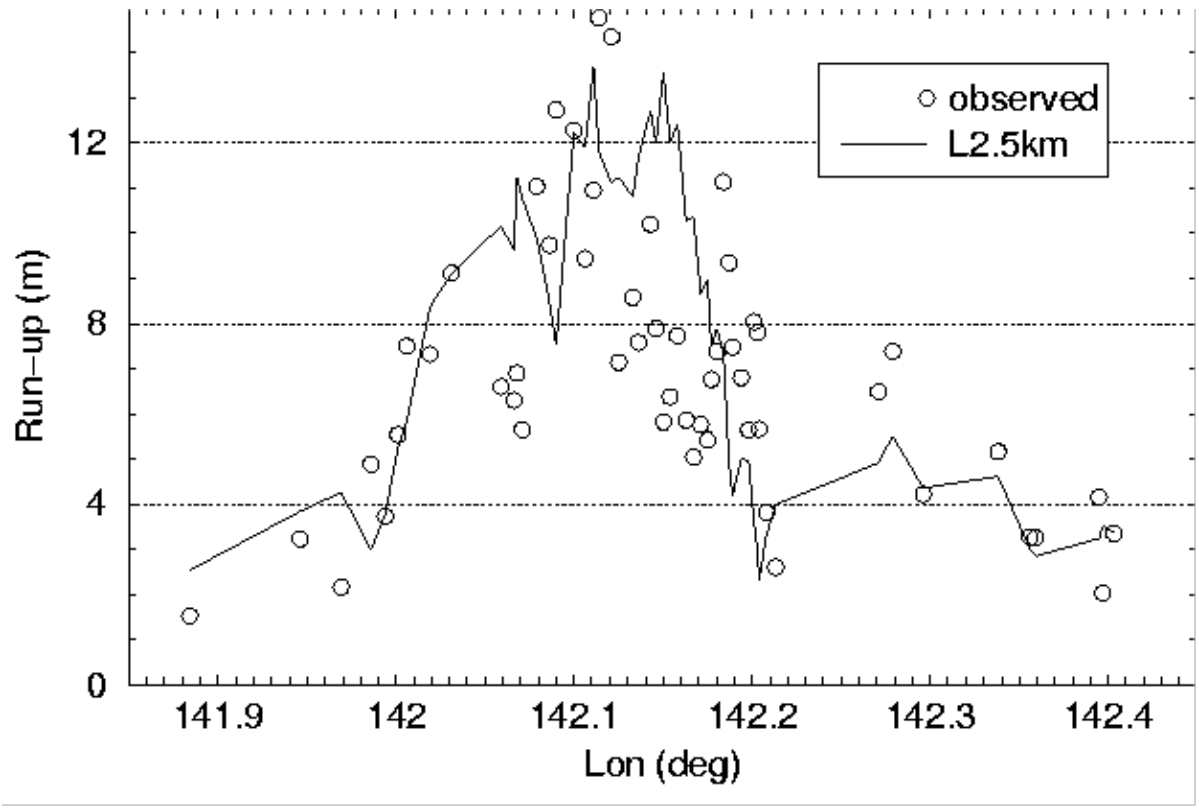
observed
L2.5km
Run–up (m)
0
4
8
12
141.9
142
142.1
142.2
142.3
142.4
Lon (deg)

Figure 12

Conclusion générale

Les outils numériques (méthode aux éléments finis et aux différences finies), dont la description fait l'objet du chapitre 3, ont permis de modéliser la génération, la propagation et l'impact des tsunamis. Grâce à ces outils, nous avons pu aborder l'étude de cas réels et comparer les différentes données disponibles avec les résultats de nos simulations. A travers l'étude de plusieurs tsunamis historiques, dans le chapitre 4, nous avons montré que les modélisations de tsunami permettent de contraindre le mécanisme de la source, même lorsqu'on ne dispose que de données qualitatives. Nos modélisations se sont révélées très sensibles à la localisation de la source sismique et à l'orientation du plan de faille. En particulier, dans le cas du séisme tsunamigénique de la Sicile orientale en 1693, et à la différence d'une étude précédente qui proposait une faille localisée à terre le long du graben de Scordia-Lentini, nous avons montré que la faille source est plus probablement localisée en mer, à proximité de la mégastructure tectonique qui constitue l'escarpement ibleo-maltais. Ainsi, nos modélisations permettent de valider les modèles de faille à la source existants et, d'autre part de proposer des modèles nouveaux.

Dans le chapitre 5, nous avons proposé une méthode d'inversion des hauteurs de run-up pour déterminer la distribution du glissement le long d'une faille tsunamigénique. Nous l'avons appliquée au tsunami du Nicaragua de 1992, et obtenu comme résultats la détermination d'une distribution du glissement très hétérogène: *Ihmlé* (1996), en utilisant une méthode indépendante d'inversion d'ondes de surface longue période, a confirmé ce résultat.

Dans le chapitre 6, en considérant un séisme tsunamigénique récent (Iles Kouriles, 1994) pour lequel on disposait de très bonnes données expérimentales (14 marégrammes en champ proche et moyen), nous avons étudié la limite de résolution des modélisations de tsunami. Nous avons montré que dans ce cas, où il

fallait distinguer parmi des modèles de source très proches, la résolution de nos modélisations, estimée en considérant une incertitude dans les données bathymétriques, était trop faible.

Enfin dans le chapitre 7, nous avons étudié les caractéristiques de la source du dernier tsunami catastrophique, survenu en Papouasie Nouvelle-Guinée en juillet 1998. Ce tsunami fut très meurtrier localement: ainsi, les seules données utilisables pour étudier le mécanisme à la source ont été les hauteurs de run-up, mesurées deux semaines plus tard au cours d'une première inspection post-événement. Néanmoins, les méthodes mises au point dans cette thèse, ont permis de déterminer avec précision la localisation de la source, ses dimensions et l'amplitude nécessaire pour engendrer les effets observés le long de la côte affectée. Nous avons ainsi montré que la déformation co-sismique due au séisme n'est pas à l'origine de ce tsunami; il est vraisemblable que le séisme ait déclenché un effondrement sous-marin, responsable de la génération du tsunami, et détecté par une campagne océanographique récente.

D'une façon générale, nous pouvons affirmer que les données de tsunami et leur modélisation, apportent une contrainte supplémentaire aux données sismologiques classiques pour la détermination des mécanismes tsunamigéniques. Ainsi pour les séismes tsunamigéniques historiques, l'étude des cas pour lesquels on dispose de données, soit de type quantitatif (marégrammes et run-ups) soit de type plus qualitatif (polarité de la première vague, nombre de vagues observées, dégâts etc.…) permet, comme nous l'avons montré dans cette thèse, d'apporter une contrainte sur le mécanisme à la source.

Pour étudier les prochains tsunamis, les marégrammes enregistrés le long des côtes sont et resteront les premières données exploitables; l'installation de nouveaux capteurs de pression océaniques permettra d'obtenir également les formes d'ondes enregistrées au large. Enfin, le développement des technologies satellitaires, permettra dans l'avenir de détecter un tsunami et de suivre sa propagation à la surface de l'océan, d'une façon plus précise et plus simple qu'aujourd'hui, où l'on

peut considérer que l'étude des tsunamis par altimétrie satellitaire est encore au stade expérimental.

L'un des points importants de cette thèse est d'avoir montré la grande utilité des mesures de run-up acquises après l'événement. Pouvoir exploiter cette donnée pour les études de source, s'avère d'une importance fondamentale dans tous les cas où on ne dispose ni d'un nombre suffisant de marégrammes de bonne qualité ni de formes d'ondes enregistrées par les capteurs océaniques: c'est par exemple le cas des tsunamis historiques et des tsunamis locaux. Ces hauteurs de run-up représentent d'ailleurs la donnée principale vis-à-vis du risque tsunami. Le tsunami de Papouasie Nouvelle-Guinée en juillet 1998, nous a ainsi montré, d'une façon dramatique, le danger que les tsunamis locaux représentent pour les populations installées les long des côtes.

Annexe I

Dans cette annexe nous présentons un article, paru récemment dans *Journal of Geophysical Research*, où nous abordons le problème de la détection des tsunamis par altimétrie satellitaire.
En utilisant les données d'altimétrie satellitaire des missions TOPEX/POSEIDON et ERS-1, des techniques de spectrogramme pour l'analyse des signaux et des méthodes numériques pour la synthèse des formes d'onde, dans ce travail nous étudions sept séismes tsunamigéniques récents. Dans le cas du Nicaragua en 1992, nous identifions avec certitude le signal du tsunami en propagation en plein océan, que nous détectons à 15^0S, 106^0W, cinq heures après le temps origine.

Le sujet de ce travail s'écarte peut être un peu du fil conducteur de cette thèse, à savoir l'utilisation des données de tsunami pour contraindre certains paramètres de la source tsunamigénique. Néanmoins, comme il s'agit de la première détection d'un tsunami par altimétrie satellitaire, que la détection positive a été faite pour le tsunami du Nicaragua en 1992 (dont nous avons précédemment étudié la source précédemment dans cette thèse) et que la modélisation du tsunami à été un outil important pour aboutir à ce résultat, nous avons décidé de présenter ce travail sous forme d'annexe, à cette thèse.

JOURNAL OF GEOPHYSICAL RESEARCH, VOL. 104, NO. B1, PAGES 599-615, JANUARY 10, 1999

Tsunami detection by satellite altimetry

Emile A. Okal
Department of Geological Sciences, Northwestern University, Evanston, Illinois

Alessio Piatanesi and Philippe Heinrich
Département Analyse et Surveillance de l'Environnement, Commissariat à l'Energie Atomique
Bruyères-le-Châtel, France

Abstract. We present what is to our knowledge the first direct observation of the deformation of the surface of the ocean upon passage of a tsunami wave, on the high seas, far from the influence of shorelines and continental shelves. We use satellite altimetry data from the ERS-1 and TOPEX/POSEIDON programs, complemented by spectrogram techniques and synthetic maregrams to examine the case of seven recent tsunamigenic earthquakes. We make a positive identification of the tsunami wave field in the case of the 1992 Nicaraguan tsunami, which we detect at 15°S, 106°W, five hours after origin time. We model the observed spectrogram by injecting a synthetic of variable amplitude into the signal of a repetitive cycle of the satellite along the same track, concluding that the Nicaraguan tsunami had a zero-to-peak amplitude of 8 cm in that region. In the case of the 1995 Chilean tsunami, a large scatter in the spectral properties of the reference tracks renders the detection tentative. We fail to detect the tsunamis of five other large events, including the 1996 Biak and 1996 Peru earthquakes, primarily on account of unfavorable source directivity in the geometry of existing satellite tracks, and of the strong and incoherent noise produced by large current systems, such as the Kuroshio in the Northwest Pacific.

1. Introduction and Background

While tsunamis are routinely recorded by tidal gauge stations located at continent or island shorelines, they have never, to our knowledge, been recorded directly on the high seas. This is due to the combination of relatively small wave amplitudes (estimated at less than 1 m even for exceptionally large events) and very large wavelengths ($\Lambda \geq 100$ km), which prevents any direct observation of the deformation of the surface of the ocean. The only reported detections involved ocean-bottom pressure gauges which recorded the Petatlan, Mexico tsunami of March 14, 1979 during a deployment at the mouth of the Gulf of California [*Filloux,* 1982], and similar devices later deployed in the Gulf of Alaska, which detected the tsunamis generated by the intraplate earthquakes of November 30, 1987 and March 6, 1988 [*González et al.,* 1991]. In contrast, records from ocean-bottom seismometers tethered to the shoreline [e.g., *Okada,* 1991; *Imamura and Shuto,* 1993] remain regional in character and do not sample the tsunami field at distances from the coast that are large compared to the wavelength.

This inability to document the amplitude of the tsunami wave on the high seas is unfortunate since the only measurable record of a tsunami then consists of tidal gauge amplitudes at coastal stations, which result from the complex, strongly nonlinear, effects accompanying the interaction of the wave with the coastal structure, on scales of hundreds of meters. In addition, these devices may have complex instrumental responses [*Braddock,* 1980]. Also, the generation of the wave occasionally involves poorly known parameters (such as the precise geometry of rupture) or structures (such as sedimentary layers). Thus it would be of great interest to obtain independent constraints in the form of the direct measurement of the amplitude of a tsunami wave on the high seas, since we would then be in a position to separate the generation of the tsunami (from earthquake source to high-seas amplitude) from its coastal interaction (from high-seas amplitude to run-up amplitude or tidal gauge record); as we stand now, we can study only the product of the two effects.

In the past few years, progress in satellite altimetry, in particular under the TOPEX/POSEIDON (T/P) project, has allowed the characterization of sea surface height variability [e.g., *Wunsch and Stammer,* 1995], the tracking of oceanic currents [*Teague et al.,* 1995], eddies [*Gründlingh,* 1995], Rossby waves [*Chelton and Schlax,* 1996], and the monitoring of the rise and fall of lakes and inland seas [*Birkett,* 1995; *Cazenave et al.,* 1997]. The amplitude of the altimetric signals for many of these phenomena is on the order of a few centimeters; their wavelengths are typically hundreds to thousands of kilometers, and their characteristic times range from weeks to years. Such observations then suggest that it might be possible, at least in principle, to detect a tsunami wave on the high seas by satellite altimetry. Indeed a number of attempts have been reported [e.g., *Callahan and Daffer,* 1994], but to our knowledge all have up to now been unsuccessful.

In this paper, we present a systematic search involving seven recent tsunamis. With the help of synthetic waveforms and spectrogram techniques, we make a positive identification in the case of the 1992 Nicaraguan tsunami, where the amplitude detected is 1.5 times that predicted by our synthetics, and a tentative one in the case of the 1995 Chilean tsunami. We dis-

Paper number 1998JB00018.
0148-0227/99/1998JB00018$09.00

Table 1. Earthquake and Satellite Data Used in This Study

Region	Event							T/P data		
	Date and Time		Epicenter		Depth,	Moment	Focal Geometry	Track	Target	Reference
	Date (DOY), Year	UT	°N	°E	km	10^{27} dyn-cm	ϕ, δ, λ		Cycle	Cycles
Nicaragua	Sep. 2 (246), 1992	0016:01.7	11.2	-87.8	15	3.4	122, 78, 90	523*, 525*	005	004,006
Java	June 2 (153), 1994	1817:36.8	-11.03	113.04	15	5.3	278, 7, 89	77	63	61-65
Japan Sea	July 12 (193), 1993	1317:11.9	42.71	139.28	16	4.7	179, 55, 90	127	30	28, 29, 32
Kuriles	Oct. 4 (277), 1994	1322:55.8	43.6	147.63	68	30	158, 41, 24	201	75	73-77
Chile	July 30 (211), 1995	0511:23.6	-23.34	-70.29	46	12.	354, 22, 87	230	105	103-107
Biak, Indonesia	Feb. 17 (048), 1996	0559:33.7	-0.63	136.59	15	22	114, 11, 91	73, 75	126	124-128
Chimbote, Peru	Feb. 21 (052), 1996	1251:04	-10.06	-80.17	15	2.16	153, 75, 88	180	126	122-132

DOY, (Julian) Day Of Year.
* ERS-1 data.

cuss probable reasons for our failure to detect the other tsunamis.

2. Data Set and Methodology

We concentrate here on seven tsunamigenic earthquakes spanning the years 1992–1996, whose principal parameters are listed in Table 1. These events and their respective tsunamis have been described by *Schindelé et al.* [1995], *Ruegg et al.* [1996], *Tanioka et al.* [1996], *Newman and Okal* [1996], and *Guibourg et al.* [1997]. Smaller tsunamis, such as the Halmahera event of January 21, 1994, or those taking place in small closed seas, such as the Flores Sea event of December 12, 1992, are not included.

The satellite altimetry data sets used in this study consist of T/P corrected sea surface heights. In the case of the 1992 Nicaraguan earthquake, which occurred during the verification phase of the T/P project, we use ERS-1 data.

We seek to detect the tsunami signal where it is expected to be largest, i.e., when the satellite track would cross the initial wavefront, hopefully at a steep azimuthal angle, and in the first few hours following its generation, before geometrical spreading on the spherical Earth and dispersive propagation significantly reduce the amplitude of the wave. Potential hits were identified by comparing the ephemerides of individual satellite tracks with digital travel-time maps computed using a smoothed ocean bathymetry and the algorithm of *Woods and Okal* [1987]. Example of suitable tracks are given on Figure 1.

For each track so identified, we isolated in the sea-surface-height signal a segment of time series varying from 549 to 1367 s in duration (or 3856 to 7931 km in sea surface track), which we call the "target" data series. In the case of the 1993 Japan Sea tsunami, the data series are much shorter since they are limited to that inland sea. We also extracted similar series for repetitive cycles along the same track, which we call "reference" data series. The latter can be regarded as the background noise out of which we seek to extract a signal. The repeat periods of the satellites (35 days for the multidisciplinary phase of ERS-1; 9.916 days for T/P) should allow the elimination of any seasonal effect (and of static components expressing the short-wavelength geoid) in the differential series obtained by subtracting any reference series from the target series.

The altimetry profiles shown in this study are oriented mostly North-South. Some are ascending tracks, i.e., with time increasing Northwards, and others descending. For a uniform presentation of the data, descending series were reversed and all profiles will be presented with latitude increasing from South to North along the profile.

2.1. Spectral Analysis

Ideally, and for a sufficiently large deformation of the ocean surface, one could hope to detect a decimetric tsunami signal by direct visual inspection of the unprocessed target series, or possibly of the differential series. However, in all cases involved (with the marginal exception of Track 525 of the 1992 Nicaraguan tsunami), no such signal prevailed over background noise. For this reason, we proceeded to Fourier-transform the data series and analyze their spectra.

The data series consist of measurements taken at regular time intervals aboard the satellite (occasionally corrected by linear interpolation when a few points were missing). Since the latter orbits at a ground velocity of approximately 6–7 km/s, each point in the series is displaced from the previous one both in time (δt = 0.98 s (ERS-1); 1.17 s (T/P)) and space on the ocean surface (δd = 7.06 km (ERS-1); 6.77 km (T/P)). Because of the large disparity in surface velocity between the spacecraft (7.2 km/s (ERS-1); 5.8 km/s (T/P)) and the expected tsunami wave (typically 210 m/s for an ocean depth of 4500 m), any data series represents more a snapshot of the surface of the ocean at a given time than a maregram at a given point, and it approaches more a "space series" than a "time series". Accordingly, the "frequency" in the Fourier space resulting from the application of a standard transform to the data series is hybrid in nature but approaches a spatial frequency sampling the wavenumber space, which we will conveniently characterize with units of inverse distance (km^{-1}). Spectral amplitudes will then have units of squared length (m^2). Note however that the resulting "wavenumbers" k_t are measured along the satellite track, which is generally oriented at an angle to the local tsunami ray, and thus may not be representative of the true wavenumbers k of the tsunami field at the corresponding space-time combination.

We further use the standard spectrogram technique, originally introduced in geophysics by *Landisman et al.* [1969], and consisting of Fourier-transforming a moving window in the original data set. This identifies the exact portion(s) of the data series contributing energy at a given k_t, in particular in relation to the causality of any window with respect to the expected timing of the tsunami wave field. For all spectrograms shown in this study, the length of the moving windows was 2^6 points (or 452 km for ERS-1 and 433 km for T/P), and the interval between windows was 7 samples (or 49.4 km for ERS-1 and 47.4 km for T/P). The spectrograms were then interpolated and plotted using 50–km pixels.

2.2. Tsunami Synthetics.

We generate synthetic profiles ("synthetics") of tsunami amplitudes expected along the various tracks in the following

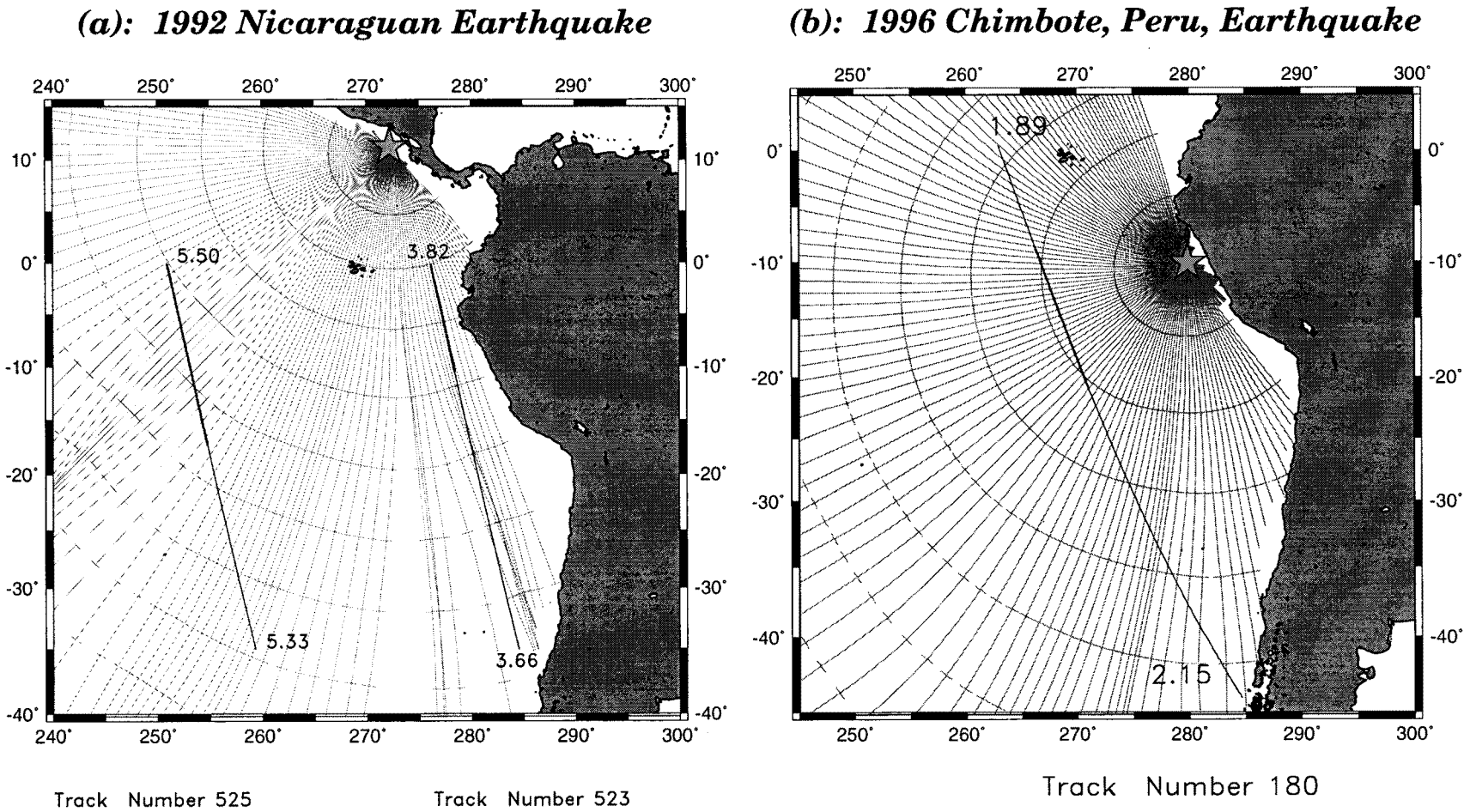

Figure 1. (a) Map of satellite tracks used for the 1992 Nicaraguan tsunami. The half-tone lines are rays traced from the epicenter (star) leaving at intervals of 2° in azimuth and stopped at the coastlines [*Woods and Okal,* 1987]. Tick marks delineate the progress of the wave front in hours after the origin time of the centroid solution (0016:42 UT). The two segments are the trajectories of Tracks 523 and 525 of ERS-1 Cycle 005, between 40°S and 0°S, with the numbers showing the time (in decimal hours) elapsed since origin time at the beginning and end of each track segment. The thicker traces identify those portions inside the wave field, where signals are expected to be causal. (b) Same as Figure 1a for the 1996 Chimbote tsunami. The only available trajectory is Track 180 of T/P Cycle 126. The origin time of the event is 1251:04 UT.

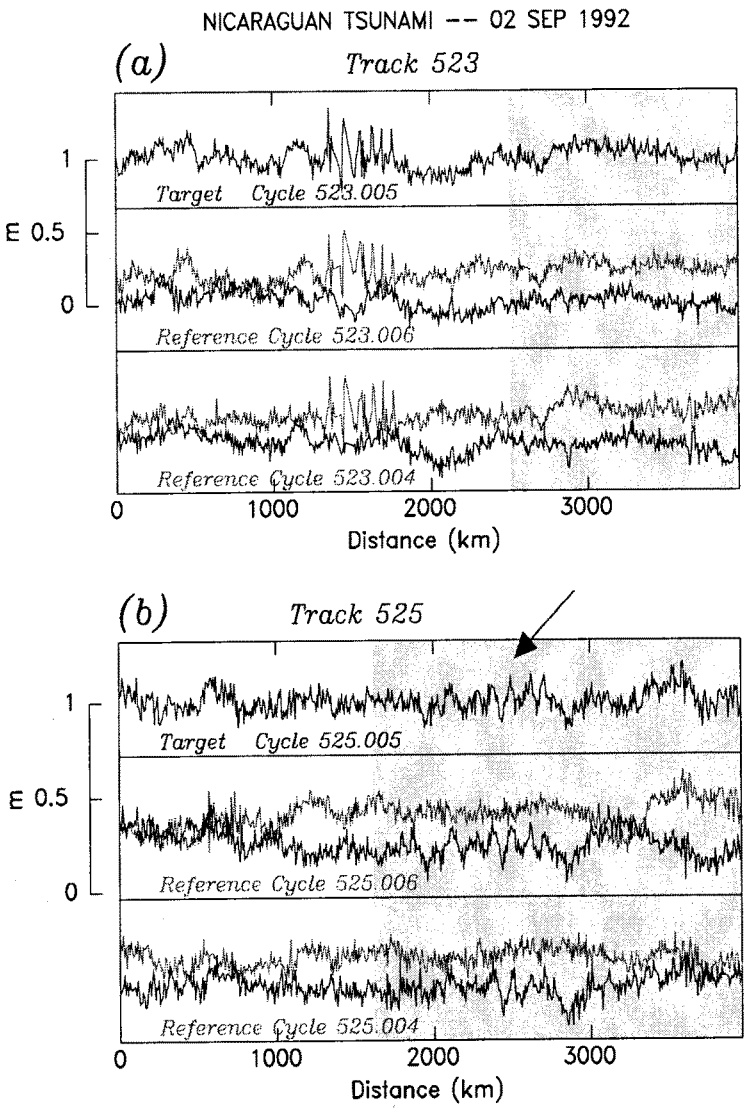

Figure 2. ERS-1 Data series for the 1992 Nicaraguan tsunami: (a) Track 523 and (b) Track 525. In both cases, the top frame shows the target series from Cycle 005, where the tsunami signal is expected. Abscissa is distance along track, starting in the South. In the other frames, the top trace is the reference series for another cycle along the exact same track; the bottom trace is the difference between the target and reference series. The vertical scale is common to all plots for the same track. The shaded bands indicate the portion of the tracks located inside the wave field, where signals are expected to be causal. In Figure 2a, note that the strong signal, ~1600 km into the series, and present in all three cycles, is related to the geoid. In Figure 2b, the arrow identifies the signature of the tsunami signal, as inferred from Plate 1.

way. Starting with a model of the static ocean-bottom displacement derived from the earthquake's moment tensor [*Okada,* 1985], we use a finite difference code [*Mader,* 1988; *Guibourg et al.,* 1997] to create a full three-dimensional space-time grid of the expected wave amplitude, which we then interpolate to recreate a synthetic series with the exact same time and space sampling as the target altimeter data series.

Such synthetics could be inaccurate for several reasons. First, even though the moment of the earthquake is usually well constrained, and the fault length L can be estimated from directivity studies [*Ben-Menahem,* 1961], the traditional trade-off subsists between amplitude of slip, D, and area of rupture $S = L\,W$. Although normal mode theory predicts that the overall amplitude of the tsunami wave at teleseismic distances should be controlled only by the moment tensor of the source [*Ward,* 1980; *Okal,* 1982], its spectral content could be affected by the details of the rupture geometry. Additionally, the involvement of sedimentary structures in the hypocentral area could significantly affect both the spectral content of the wave and its overall amplitude [*Okal,* 1988]. It is in this very general framework that we take our synthetics as representative of the expected signal that we seek in the target data series.

2.3. Injecting the Synthetic into a Reference Signal

In order to determine the feasibility of extracting a signal (represented by our synthetic series) from the background noise

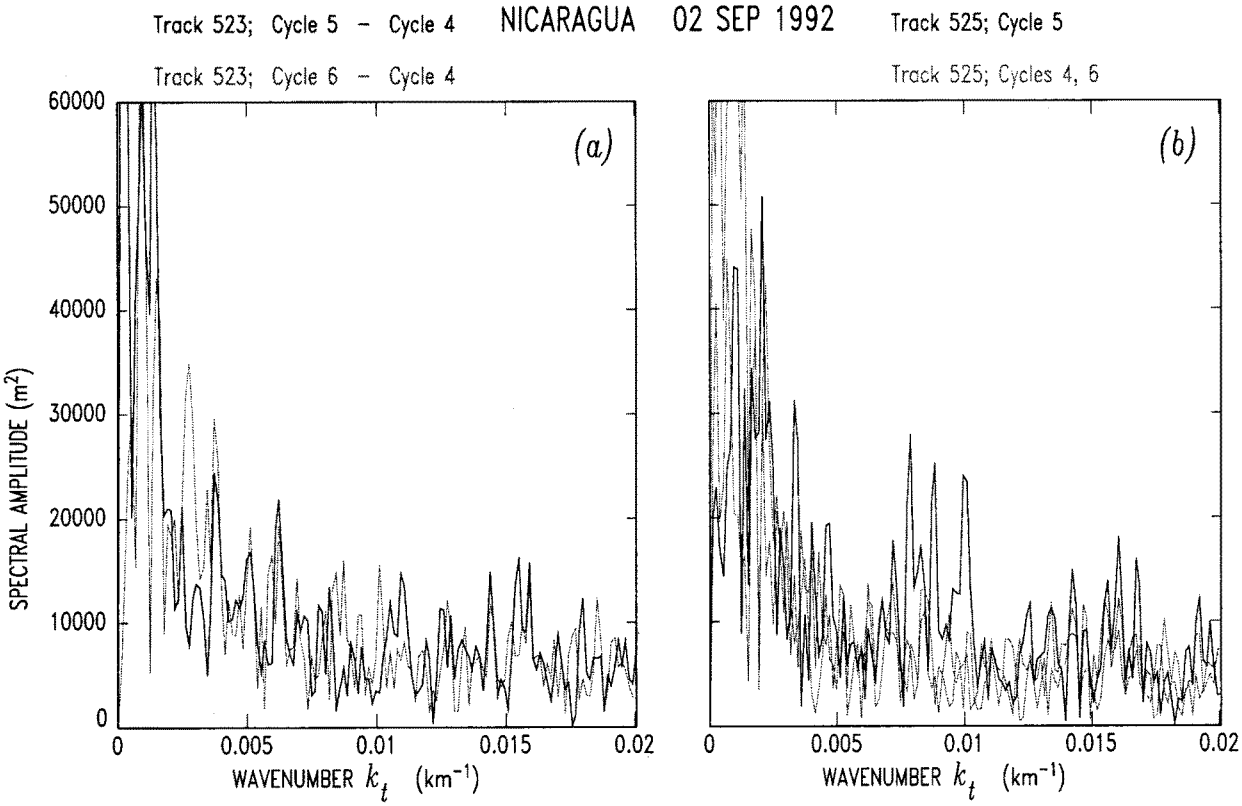

Figure 3. Spectral amplitude of the target series (thick trace) and reference series (thin traces) for the 1992 Nicaraguan tsunami. (a) Track 523. In this instance, the data processed consist of the difference between Cycles 5 and 4 (target series) and between Cycles 6 and 4 (reference series). Note the absence of signal in the target series. (b) Track 525. Note the significant spectral amplitude at 0.007–0.01 km^{-1}.

(represented by the reference series), we conducted the following experiment: we added the synthetic series (multiplied by a variable amplitude factor α) to a reference series for the same track, and analyzed the spectrogram of the resulting series. We varied both the reference cycle (to illustrate the variable level of noise depending on climatic conditions) and the value of α, which ranged between 0.1 and 100. Only a sample of the spectrograms computed will be shown.

This technique can achieve either of two goals: upon positive identification of a tsunami signal, the spectral amplitudes of the target spectrogram can be used to best-fit α, thus providing a measurement of the amplitude of the detected tsunami on the high seas; if on the other hand, we fail to detect the tsunami signal, we can similarly infer a maximum amplitude for its wave.

3. The 1992 Nicaraguan Tsunami: Positive Detection

We recall that this event qualified as a "tsunami earthquake", i.e., that its tsunami was larger than expected from its seismic waves [*Kanamori,* 1972], due to an exceptionally slow rupture [*Kanamori and Kikuchi,* 1993; *Newman and Okal,* 1998].

We use altimetry data from Tracks 523 and 525, Cycle 005 of the ERS-1 mission (Figure 1), with Cycles 004 and 006 as references series. Both tracks are ascending, traveling from South to North, approximately 3.7 and 5.4 hours after the event, respectively. They are expected to penetrate the tsunami wave field around 11°S and 17°S respectively. The corresponding signals are shown on Figure 2, and their spectra on Figure 3.

For Track 523, all cycles are dominated by strong permanent signals reflecting geoid anomalies, in particular in the vicinity of the Nazca Ridge (19°S or 1600 km into the series). For this reason, we take as our target series the difference between Cycles 005 and 004, and as reference series, the difference between Cycles 006 and 004. As shown on Figure 3, the former rises only marginally above the noise level defined by the latter, and we must conclude that no signal can be extracted from the space series of Track 523.

On the other hand, in the case of Track 525, which misses the Nazca Ridge and its accompanying perturbations in the geoid, we find it unnecessary to compute differences between tracks, and instead use the raw track data as target and reference series. Figure 3b shows that Track 525, Cycle 005 exhibits significant spectral amplitudes ($\simeq$ 25,000 m^2) in the band 0.007–0.01 km^{-1}, about twice the amplitude of the corresponding spectra for the reference cycles. Spectrograms for Track 525 are shown on Plate 1. For the target cycle, Plate 1a indicates that the large spectral amplitudes are confined to the wavenumber range $k_t \leq 0.015\,km^{-1}$, in the distance window 2000–2800 km from the beginning of the trace, or from latitudes 17°S to 10°S, i.e., at the expected location of the tsunami wave front. While some energy is present in the noncausal part of the target series (400 to 1300 km into the series), both its amplitude and spectral characteristics are comparable to

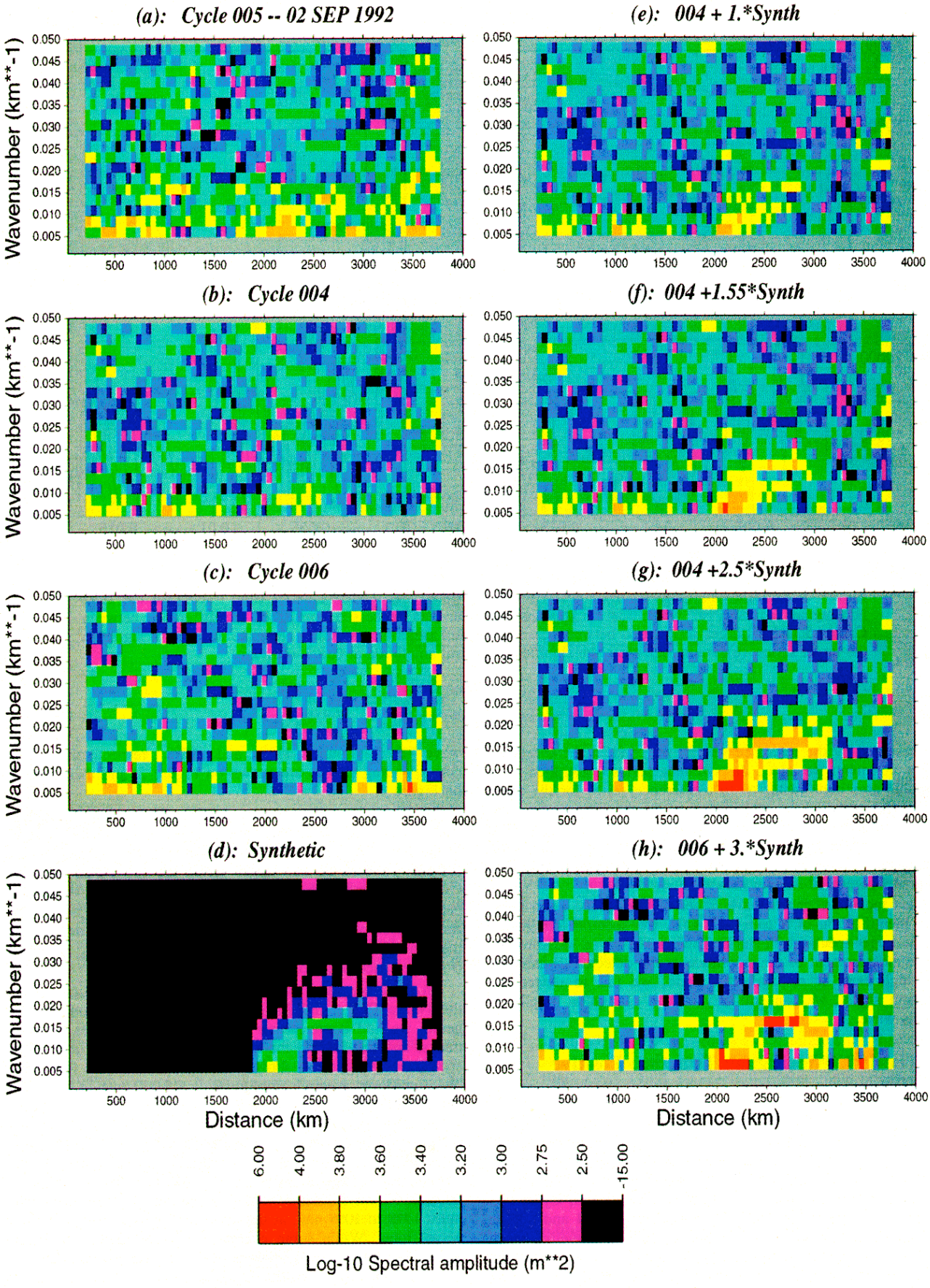
(a): Cycle 005 -- 02 SEP 1992
(b): Cycle 004
(c): Cycle 006
(d): Synthetic
(e): 004 + 1.*Synth
(f): 004 +1.55*Synth
(g): 004 +2.5*Synth
(h): 006 + 3.*Synth
Wavenumber (km**-1)
Distance (km)
6.00
4.00
3.80
3.60
3.40
3.20
3.00
2.75
2.50
-15.00
Log-10 Spectral amplitude (m**2)

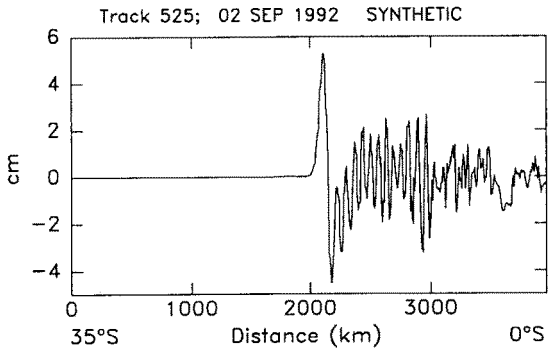

Figure 4. Synthetic maregram computed along Track 525 for the 1992 Nicaraguan tsunami.

those of reference Cycle 006 in the same distance window (Plate 1c). The latter is also significantly noisy at very low wavenumbers at the northern end of the track. By contrast, Reference Cycle 004 (Plate 1b) is much quieter throughout the distance-wavenumber plane.

It is interesting to note that the spectrum of the target cycle between distances of 2000 and 2700 km into the series exhibits some level of "spatial dispersion": the low wavenumbers (0.005 km^{-1}) are sampled at 2050–2400 km, while the higher wavenumbers (0.012 km^{-1}) are sampled around 2750 km, i.e., farther North along the track, or closer to the epicenter. This systematic pattern is absent from the spectrogram of the reference series.

A synthetic maregram was computed for Track 525 using *Piatanesi et al.*'s [1996] source deformation model, and is presented in Figure 4 (space series) and Plate 1d (spectrogram). The latter exhibits a spatial dispersion remarkably similar to that described above: the lower wavenumbers (0.005 km^{-1}) are present between 2000 and 2300 km, and the higher ones (0.015 km^{-1}) between 2500 and 3000 km. The corresponding difference in epicentral distance is 9%, but a direct interpretation of this observed dispersion in terms of the true dispersion of the tsunami wave field is made difficult by the fact that our wavenumbers k_t are measured along track, at an angle θ close to 45° from the tsunami rays, and are thus $\cos\theta = 0.7$ times the true wavenumbers k of the tsunami wave field, the relevant periods sampled being 850 and 350 s, respectively. The suggested 9% dispersion between those periods is slightly larger than the 7.7% measured by *González and Kulikov* [1993] on the ocean-bottom signals from the 1988 Gulf of Alaska earthquake; the difference is however easily explained by the fact that our paths sample shallower seas, where dispersion is expected to be stronger at comparable wavenumbers.

Injection experiments were performed using both Reference Cycles 004 and 006 as noise. In general, the former gave spectrograms more in line with that of the target series; Plates 1e, 1f, and 1g show corresponding spectrograms for $\alpha = 1$, 1.55, and 2.5, respectively. The central value is the estimate optimizing the general pattern of computed and observed spectrograms. The target series, however, retain a significant noise level in their noncausal segment, which would be better modeled by injecting the synthetic into Reference Cycle 006, as documented by the spectrogram in Plate 1h.

The conclusion from Plate 1 is a good correlation between the distance-wavenumber combination of the pulse of energy observed in the target series and that predicted by the synthetic: the pulse is found at the right place at the right time, it has the right wavenumber, and it exhibits the predicted dispersion. On the basis of this evidence, and especially of the latter observation, we propose that the signal detected in the spectrogram of Track 525, Cycle 005 between distances of 2000 and 2800 km is the tsunami wave field of the Nicaraguan earthquake. Note that matching the energy levels of the target series and the synthetic would require a tsunami 1.55 times larger than synthesized, corresponding to a zero-to-peak amplitude of 8 cm, which is also in general agreement with the oscillations identifiable in that distance window in the space series (see arrow on Figure 2b).

Finally, the difference in results between Tracks 523 and 525 (no signal along the former despite a wavefront crossing earlier after the origin time) is easily explained by source directivity. Following *Ben-Menahem* [1961], we compute the directivity coefficient $D(\phi)$ for a surface wave observed in the far field at the azimuth ϕ from a fault of length L rupturing at velocity V_R as

$$D(\phi) = \frac{\sin Y}{Y} \quad \text{with} \quad Y = \frac{k\,L}{2}\left[\frac{c}{V_R} - \cos\phi\right] \qquad (1)$$

where k is the wavenumber of the tsunami and c its phase velocity. For hypersonic rupture velocities ($V_R/c \gg 1$), it is a classical result that D is maximum at right angles from the direction of rupture [*Ben-Menahem and Rosenman,* 1972; *Okal and Talandier,* 1991]. Using published values of the geometry and rupture velocity of the Nicaraguan event [*Kikuchi and Kanamori,* 1995], we find $\phi = 70°$ and $D = 61\%$ for Track 525, but $\phi = 28°$, and only $D = 17\%$ for Track 523. This more than compensates for the amplitude effects of geometrical spreading and dispersion along the different lengths of the two tracks. This is confirmed by the maximum amplitudes of the synthetics computed for the two tracks: 9.8 cm peak-to-peak for Track 525 versus only 4.3 cm for Track 523. This remark illustrates the crucial influence of directivity on tsunami amplitudes; in this respect, it is interesting to note, following *Okal and Talandier* [1991], that directivity lobes for tsunamis are narrower than for conventional seismic waves, further hampering the potential detection of tsunami signals by satellite altimetry.

Plate 1. Spectrograms for the Nicaraguan tsunami along Track 525. Distance is along track from the southern end of the series. (a) Target series. This frame shows that the energy identified at 0.015 km^{-1} on Figure 3 is concentrated around a location 1600-2000 km into the series, and as such, noncausal with respect to the tsunami source. (b, c) Same as Plate 1a for Reference Cycles 004 and 006. (d) Same as Plate 1a for the synthetic maregram. The black bands define the extent of the noncausal segment in the target series. Plates 1e ($\alpha = 1$), 1f ($\alpha = 1.55$), and 1g ($\alpha = 2.5$) are the same as Plate 1b after a fraction α of the synthetic maregram is injected into the reference series for Cycle 004. Note that the energy of the tsunami signal becomes comparable to that in the causal segment of the target series (Plate 1a) for $\alpha = 1.55$ (Plate 1f), suggesting detection of a tsunami with zero-to-peak amplitude 8 cm. (h) Same as Plate 1e, using Cycle 006 as reference, and $\alpha = 3$.

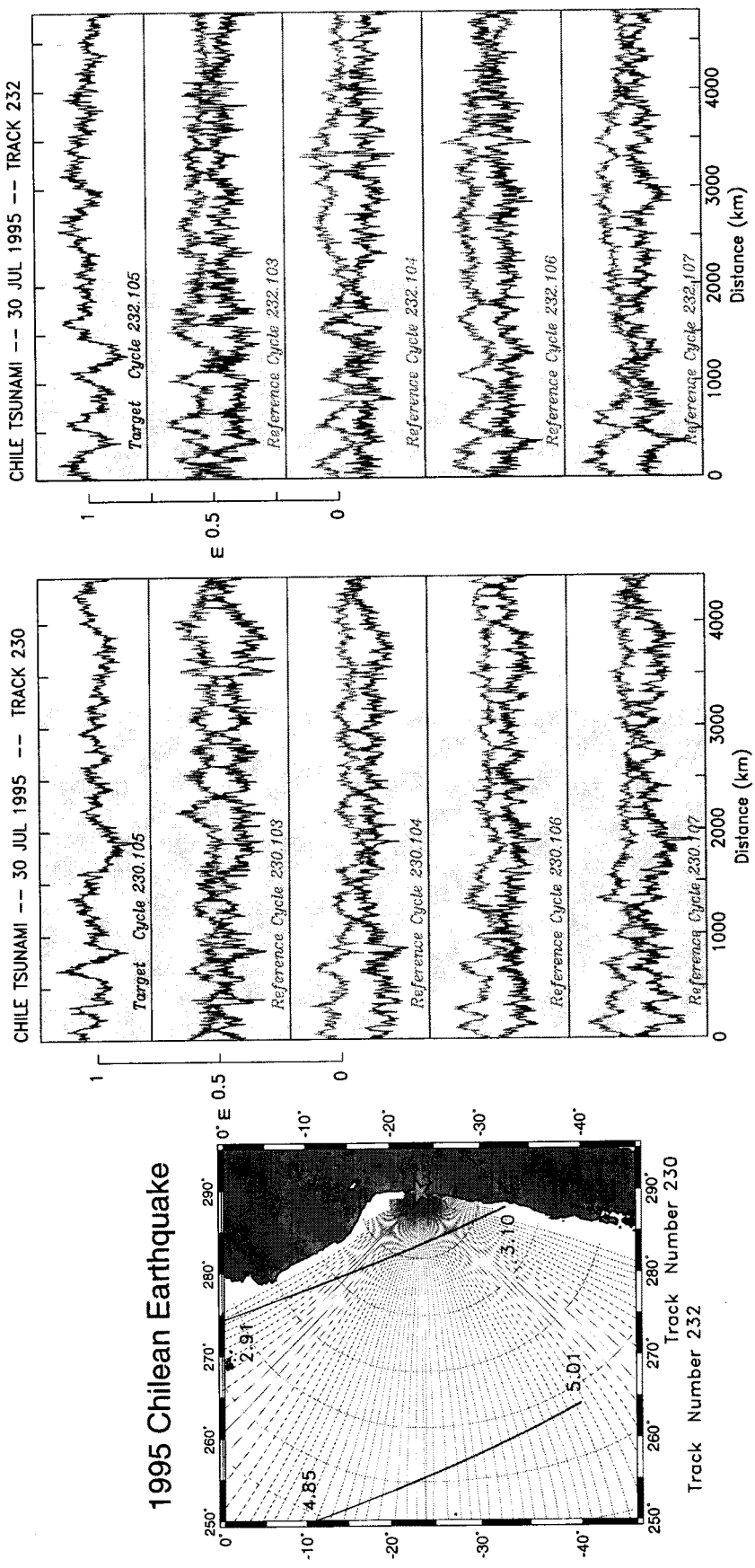

Figure 5: Map and plots of target and reference series for the 1995 Chilean tsunami. (left) Map (similar to Figure 1); (center) Track 230; (right) Track 232 (both similar to Figure 2).

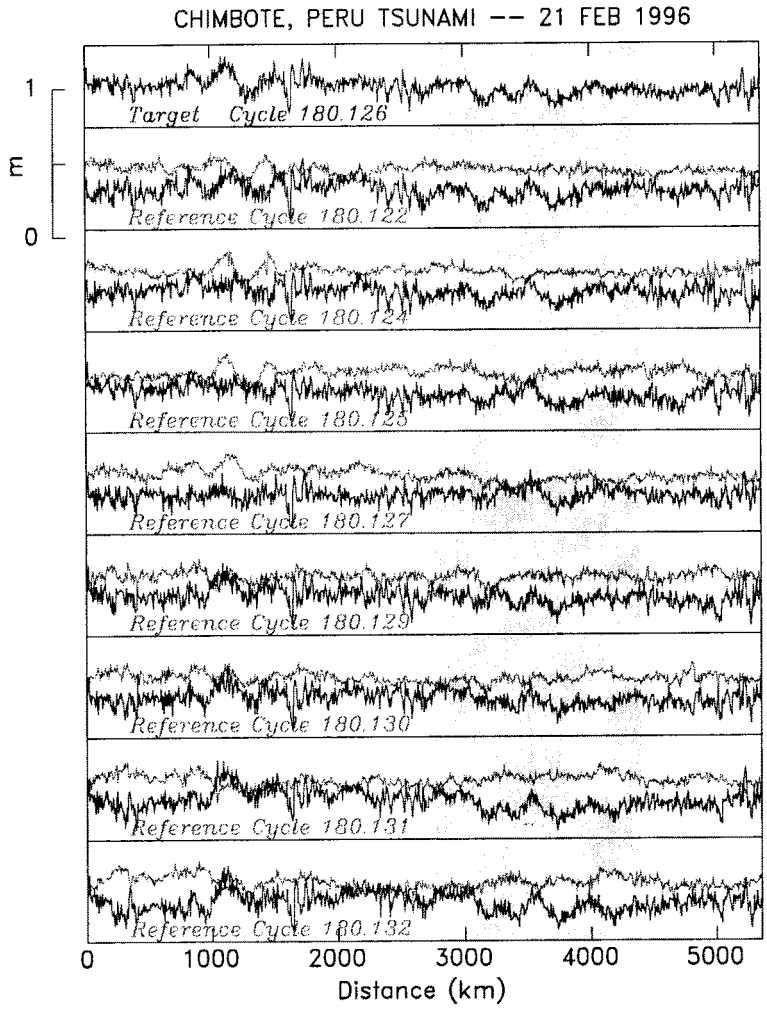

Figure 6. Same as Figure 2 for the 1996 Chimbote, Peru earthquake.

4. The 1995 Antofagasta, Chile Tsunami: Tentative Identification

This relatively large earthquake ($M_0 = 1.2 \times 10^{28}$ dyn-cm) generated a powerful tsunami, which ran up 2 m in the Marquesas Islands, where it sank a boat in a harbor, 7500 km away from the epicenter. Two profiles are available during T/P Cycle 105: Track 230 sampling the wave field 3 hours after origin time, and Track 232 farther out at sea, 5 hours after origin time (Figure 5).

Synthetics computed for the rupture model of *Guibourg et al.* [1997] suggest an amplitude of 10 cm peak-to-peak along Track 230, with the energy concentrated mostly at 0.007 km^{-1}, approximately 1500 km into the series. The spectrogram of Cycle 105 does not match these characteristics, being dominated by energy at lower wavenumbers, and remarkably quiet in the central part of the expected wave field. We conclude that no signal is detected in Track 230. This is probably due to the fact that the section of track intersecting the wave front (its northernmost part) suffers from unfavorable source directivity.

Spectrograms for Track 232 are presented in Plate 2. Synthetics suggest an amplitude of 11 cm peak-to-peak with energy concentrated in two peaks, one 500 km into the series, at 36°S, and the other, stronger one 1700 km into the series, at 25°S, closer to the point where the profile leaves the causal wave field. Wavenumbers are generally low, in the range 0.003 to 0.005 km^{-1}. Examination of the spectrogram of the target profile (Cycle 105) indeed reveals remarkably low amplitudes in its noncausal parts, with a strong burst of energy at 0.003 to 0.006 km^{-1} between 1500 and 1850 km into the series, and sustained energy at 0.003 km^{-1} between 450 and 1100 km. The former signal is absent from most reference cycles, with Cycle 104, however, being relatively noisy. Injection experiments suggest that the northern section of the wave field (from 1500 to 1900 km into the series) is well modeled by superimposing 1.5 times the synthetic onto Cycle 107, considered as "noise", but also possibly by using a lesser synthetic amplitude (0.7) and the noisier reference cycle 104. Given the uncertainty on the amplitude of the synthetic to be injected in order to match the observed spectrogram, we regard the detection of the tsunami signal as tentative.

5. The 1996 Chimbote, Peru, Tsunami: Failure to Detect

With $M_0 = 2 \times 10^{27}$ dyn-cm, this "tsunami earthquake" was only slightly weaker than the Nicaraguan event, and generated a damaging tsunami on the Peruvian coast [*Tanioka et al.*,

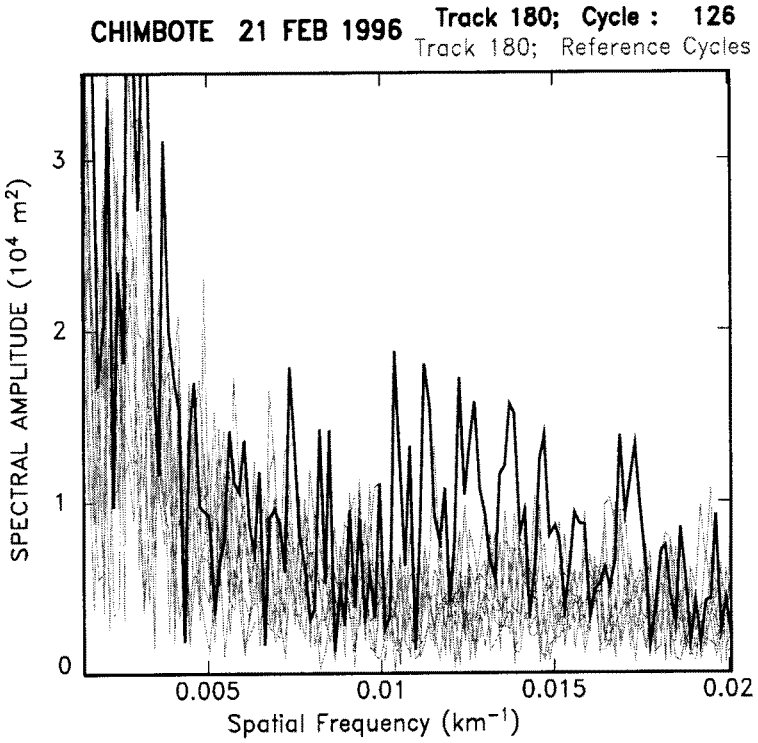

Figure 7. Spectral amplitude of the target series (thick trace) and reference series (thin traces) for the 1996 Chimbote tsunami. Note that the target spectrum has significant energy in the 0.01–0.015 km^{-1} range. The experiment in Plate 3 shows that this signal is, however, non causal.

1996]. A promising altimetric signal turned out to be unrelated to the tsunami.

The tsunami signal is expected on Track 180 of T/P Cycle 126, with reference series from Cycles 122, 124, 125, 127, 129–132. The track is descending and was reversed. As shown on Figure 6, neither direct visual inspection of the target series, nor the subtraction from it of a reference series, results in obvious detection of a tsunami signal in the space domain.

Figure 7 shows the spectrum of the target data series, and compares it with those of the eight reference cycles. Only the target cycle, 126, exhibits a significant rise above noise level in the wavenumber range k_t = 0.01 to 0.015 km^{-1}. While the corresponding wavelengths (70 to 100 km) are shorter than would be expected for a tsunami wave, the possibility that the tsunami had significant short-period energy cannot be dismissed a priori. The spectral amplitude of the possible signal reaches 17,000 to 20,000 m^2.

Spectrograms are shown in Plate 3, comparable to Plate 1. Plate 3a confirms the absence of any detectable signal above noise level and, in particular, indicates that the peak at 0.015 km^{-1} in Cycle 126 takes place 1800 km into the target series, around 30°S, or 1100 km ahead of the tsunami wavefront. This spectral signal is therefore noncausal with respect to the tsunami source and cannot be associated with it, even though the signal was present only in the target series and absent from the reference series. This transient perturbation, whose origin is unknown, is present fortuitously on the day of the tsunami, and its spectrogram analysis underscores the care which must be taken before any association with the tsunami source can be proposed.

The synthetic series for Track 180 is shown on Figure 8. It exhibits two positive peaks of approximately +6 cm amplitude, and a trough of -6 cm amplitude, corresponding to the satellite entering the wave field in the South around 19°S (first peak), crossing the distorted ocean above the wave field, and then exiting the wave field in the North around 12°S (second peak). The spectrogram of the synthetic (Plate 3c) shows most of the energy concentrated in the center of the wave field, at wavenumbers $k_t \leq 0.010$ km^{-1} and with spectral amplitudes reaching about 10,000 m^2. We conclude that the spectrogram of the target trace on Plate 3a does not match the characteristics expected from the synthetic trace.

Paltes 3d, 3e, 3f show results from the injection experiments, using Cycle 132 as reference signal, and $\alpha = 1$, 3, and 10, respectively. The expected amplitude of the tsunami, as modeled by the synthetic ($\alpha = 1$), remains too small to emerge

Plate 2. Same as Plate 1 for the 1995 Antofagasta, Chile tsunami. Shown are spectrograms for (a) the target cycle, (b, c) selected reference cycles (note higher level of noise in Cycle 104), (d) the synthetic maregram, and (e, f, g, h) injection experiments. Note that the target spectrogram is well modeled by injecting 1.5 times the synthetic into Cycle 107 (Plate 2f), but that a good fit would also be obtained with 0.7 times the synthetic superimposed on Cycle 104 (Plate 2h).

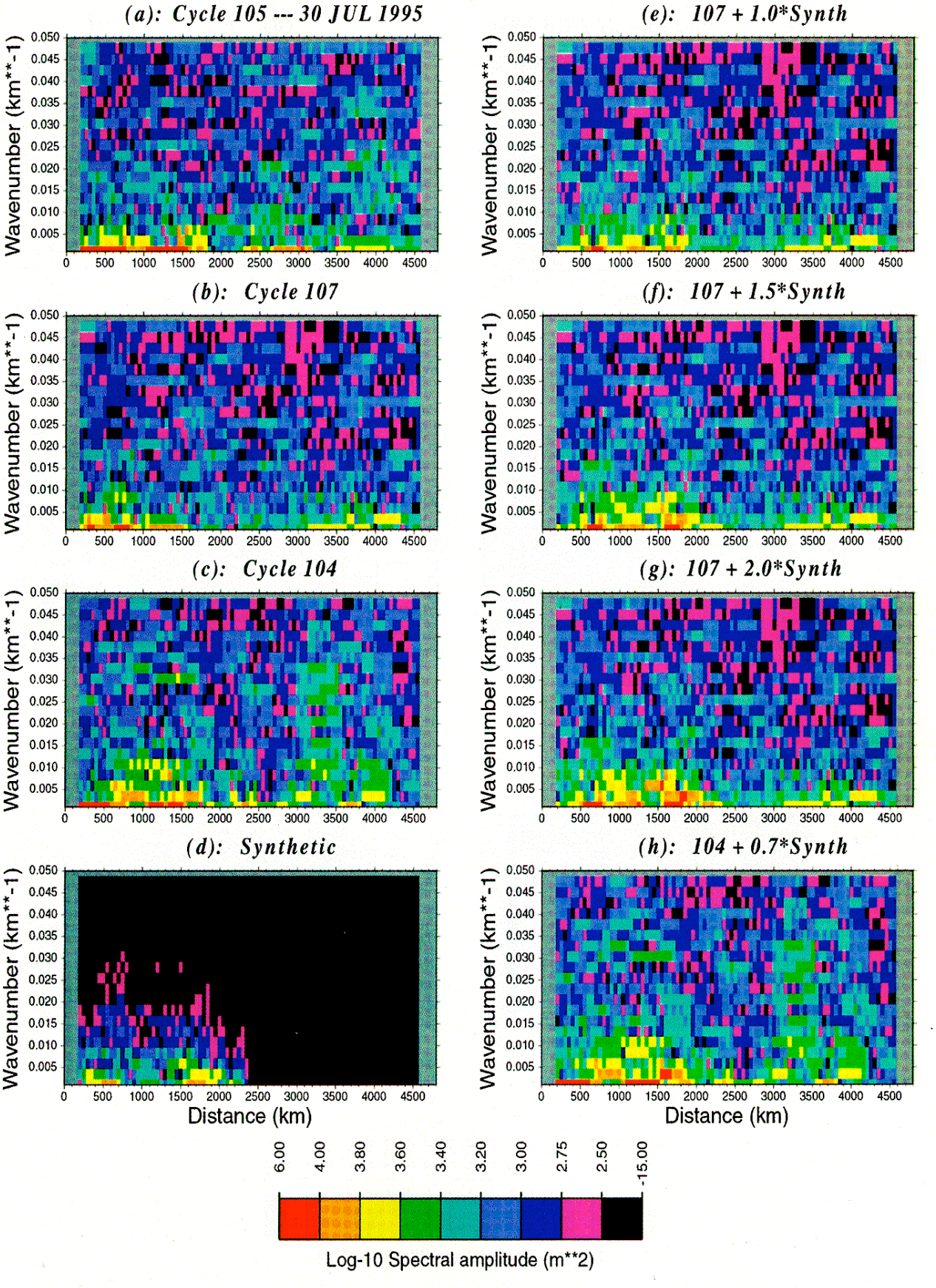
(a): Cycle 105 --- 30 JUL 1995
(b): Cycle 107
(c): Cycle 104
(d): Synthetic
(e): 107 + 1.0*Synth
(f): 107 + 1.5*Synth
(g): 107 + 2.0*Synth
(h): 104 + 0.7*Synth
Wavenumber (km**-1)
Distance (km)
6.00 4.00 3.80 3.60 3.40 3.20 3.00 2.75 2.50 -15.00
Log-10 Spectral amplitude (m**2)

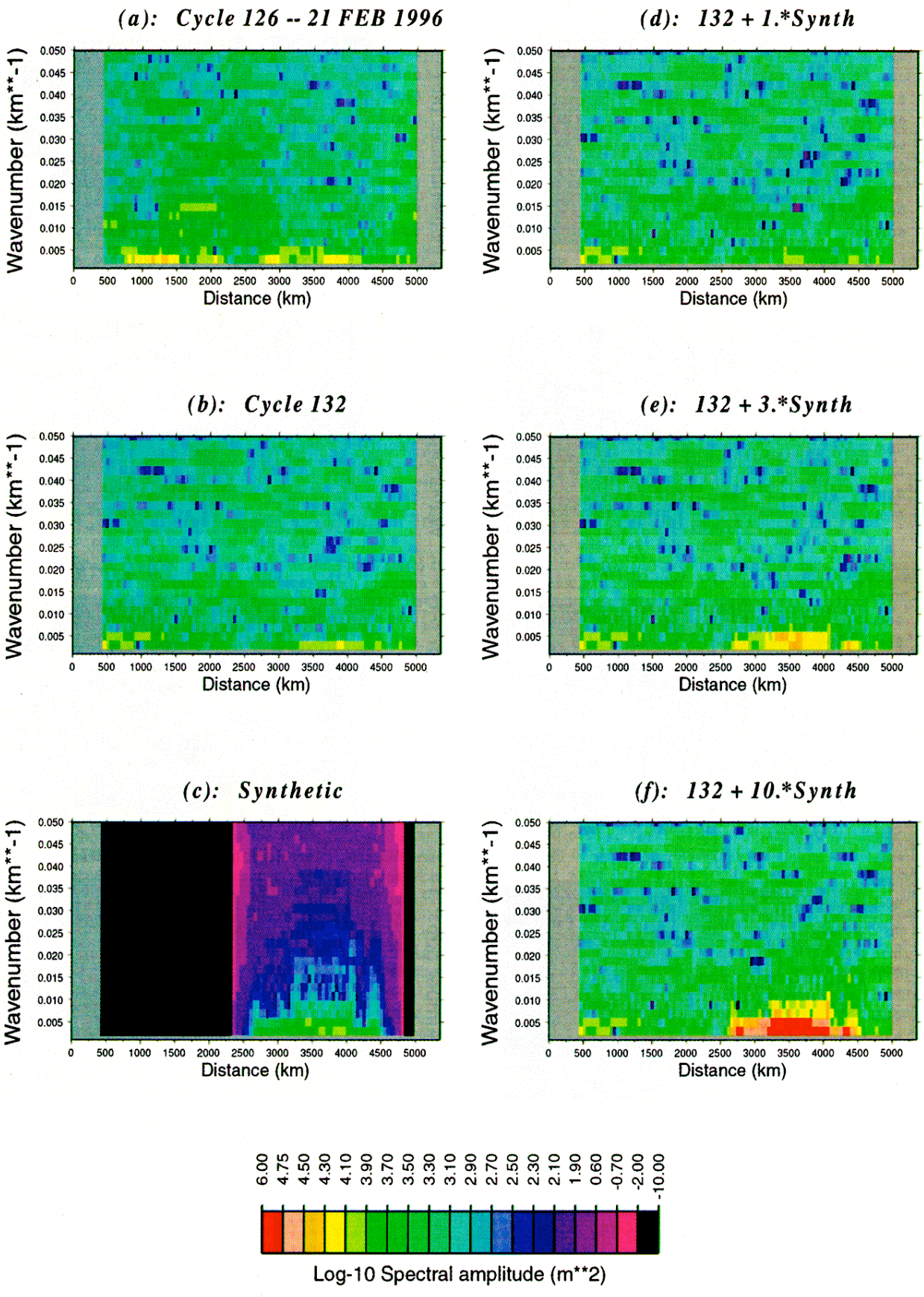
(a): Cycle 126 -- 21 FEB 1996
(d): 132 + 1.*Synth
(b): Cycle 132
(e): 132 + 3.*Synth
(c): Synthetic
(f): 132 + 10.*Synth
Wavenumber (km**-1)
Distance (km)
0.050
0.045
0.040
0.035
0.030
0.025
0.020
0.015
0.010
0.005
0 500 1000 1500 2000 2500 3000 3500 4000 4500 5000
6.00 4.75 4.50 4.30 4.10 3.90 3.70 3.50 3.30 3.10 2.90 2.70 2.50 2.30 2.10 1.90 0.60 -0.70 -2.00 -10.00
Log-10 Spectral amplitude (m**2)

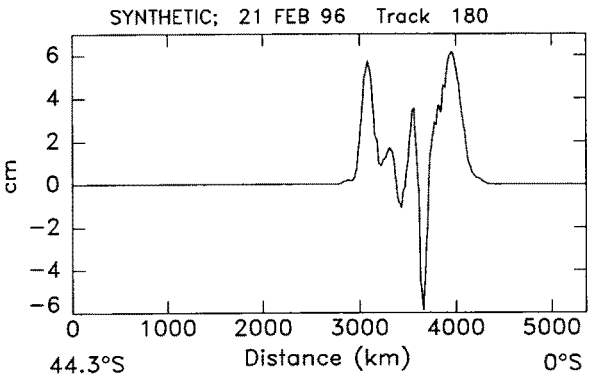

Figure 8. Synthetic maregram computed along Track 180 for the Chimbote, Peru tsunami of February 21, 1996.

from the noise, defined from the reference tracks as being typically 12,000 m^2 at the relevant wavenumber of 0.003 km^{-1}. Cycle 126 does show a slightly higher level of spectral amplitude at the latitudes expected for the tsunami wavefront, which could be interpreted as due to a tsunami with 1.5 to 2 times the amplitude of the synthetic. However, the presence of the noncausal energy in the southern part of the target series (both around 0.003 km^{-1}, 1300 km into the record, and at 0.015 km^{-1}, 1800 km into the record) renders this interpretation unwarranted: we cannot positively identify the tsunami in the target series of Cycle 126, and it would take a tsunami 2.5 to 3 times larger than synthesized (corresponding to amplitudes of 15–20 cm zero-to-peak, or spectral amplitudes of 16,000 m^2) to convincingly emerge from the noise (Plate 3e). This failure to detect the Chimbote tsunami is due to generally higher noise levels (as present in the reference series), rather than a demonstrably smaller tsunami.

6. Other Events

In this section, we discuss the case of the other tsunamis in Table 1, for which we failed to detect an altimetric signal.

6.1. The Biak Tsunami of February 17, 1996

With $M_0 = 2.4 \times 10^{28}$ dyn-cm, and at the time of writing (Oct. 24, 1998), this earthquake is the largest shallow interplate thrust event since the inception of the Centroid Moment Tensor catalog (*Dziewonski et al.*, [1983] and subsequent quarterly updates). It occurred along a segment of the New Guinea trench where no previous seismicity had been documented [*Okal*, 1996]. The associated tsunami was devastating on Biak and neighboring islands, where it reached run-up heights of 7 m; the toll from the combination of the earthquake and tsunami was upward of 100 fatalities. As such, this event was a promising candidate in our study, and our failure to detect a tsunami signal from space deserves some discussion.

Two ascending satellite tracks from T/P Cycle 126 are available immediately following the Biak earthquake (Figure 9): Track 073 crosses the tsunami wave field over the Ontong-Java Plateau to the East; it intersects the wavefront and becomes noncausal over the Marshall Islands, approximately 4.5 hours after origin time. Its orientation is expected to be unfavorable in terms of source directivity, but on the other hand, our ray-tracing experiments suggest focusing over the Caroline Sea and onto the Ontong-Java Plateau; additionally, the shallow depths over the plateau may result in higher surface amplitudes for the wave. Track 075 crosses the tsunami wave field over the West Mariana Basin of the Philippine Sea, the Bonin Islands, and the Northwest Pacific Basin, where it intersects the wavefront approximately 6.6 hours after origin time. This latter track would appear to have a better chance of sampling the tsunami field in the direction of maximum directivity at the source. However, it comes later (6 hours after the event), samples a region significantly disturbed by the Bonin-Marianas island arc, and in its northern part, close to the wavefront, enters a region of very high sea-surface variability [*Wunsch and Stammer*, 1995]. This area is traversed by the Kuroshio current, whose strong signal is expressed consistently (but not coherently between cycles) both in the target series and in the reference tracks (Figure 9), and effectively prevents the detection of a tsunami signal in either the target series or its spectrogram.

We present on Figure 9 a plot of the target and reference series for Track 073 following the Biak earthquake. It is apparent on this figure that the target series exhibits a high-frequency signal clearly identifiable in the space domain, in its southernmost part (between 275 and 900 km from the beginning of the trace), of which no counterpart can be found on the reference tracks, either in this region or farther North. It still appears in the space domain when the target series is subtracted from any reference series. The signal has two well-separated components, one centered 400 km into the series (at 0.9°N, 159.8°E), the other 800 km into the series (at 4.2°N, 161.0°E). Both are approximately 30 cm peak-to-peak. These locations are on the Ontong-Java Plateau, but not in its shallowest regions. The corresponding spectrogram (Plate 4a) has abundant energy in the band 0.004–0.02 km^{-1}. All cycles are noticeably noisy in the northern, noncausal, part of the track.

Tsunami synthetics were computed along Track 073 using the source model of the Biak earthquake derived by Y. Tanioka [*Tanioka et al.*, 1996; Y. Tanioka, personal communication, 1998], and are shown on Figure 10 (space domain) and Plate 4d (spectrogram). The synthetic amplitudes (maximum peak-to-peak 3.2 cm) are much smaller than the signal observed in the target series of Track 073. A multiplicative factor α of at least 20 would be necessary before the amplitude of the observed spectrogram could be matched by our synthetics (Plates 4g and 4h). We believe that such a large error in the geometry of source rupture is highly unlikely, especially since Tanioka's fault parameters were developed in part to successfully model the local tsunami around Biak and Yapen Islands. In addition, a robust characteristic of synthetics computed for a variety of slight alterations to Tanioka's source parameters is that their maximum amplitude takes place in the vicinity of the wavefront, not 1500 km behind it. Finally, the bathymetry in the area of the observed signal is shallow (2500 to 3500 m), but not sufficiently so as to create nonlinear amplifications in the wave field and render our finite-difference synthetics, computed under the shallow water approximations, inadequate. Thus, even though we cannot explain the origin of the signal observed at 0.9°N, 159.8°E, we must conclude against associat-

Plate 3. Spectrograms for the Chimbote tsunami along Track 180. This figure is comparable to Plate 1. Note in Plate 3a that the energy identified at 0.015 km^{-1} on Figure 7 is concentrated around a location 1600-2000 km into the series, and as such, noncausal with respect to the tsunami source. Also, the injection experiments (Plates 3d, 3e, 3f) show that the energy of the tsunami signal becomes detectable convincingly only on Plate 3e, suggesting $\alpha \approx 2.5$ as a threshold of detection.

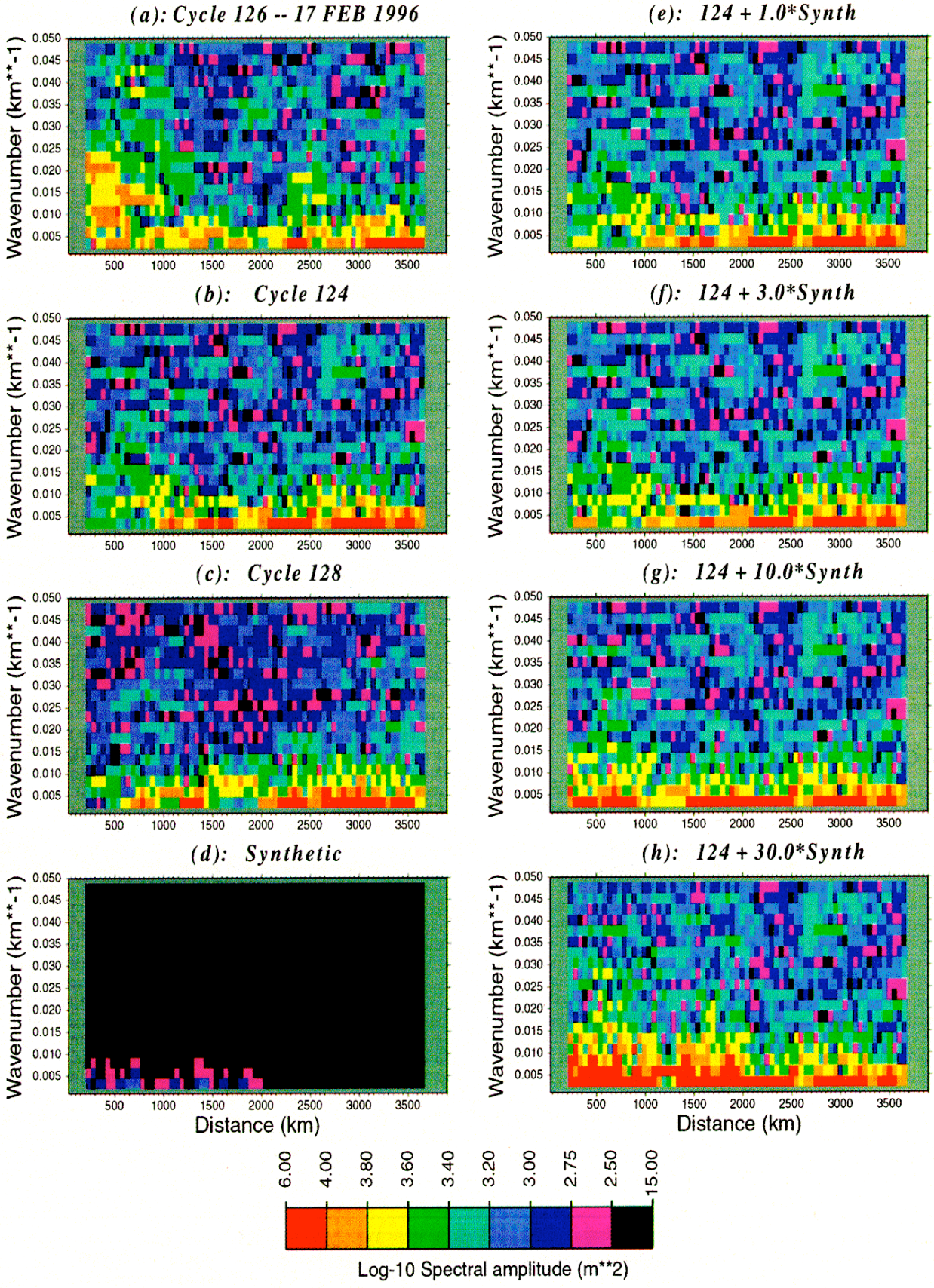

Plate 4. Same as Plate 1 for the 1996 Biak tsunami. See text for details.

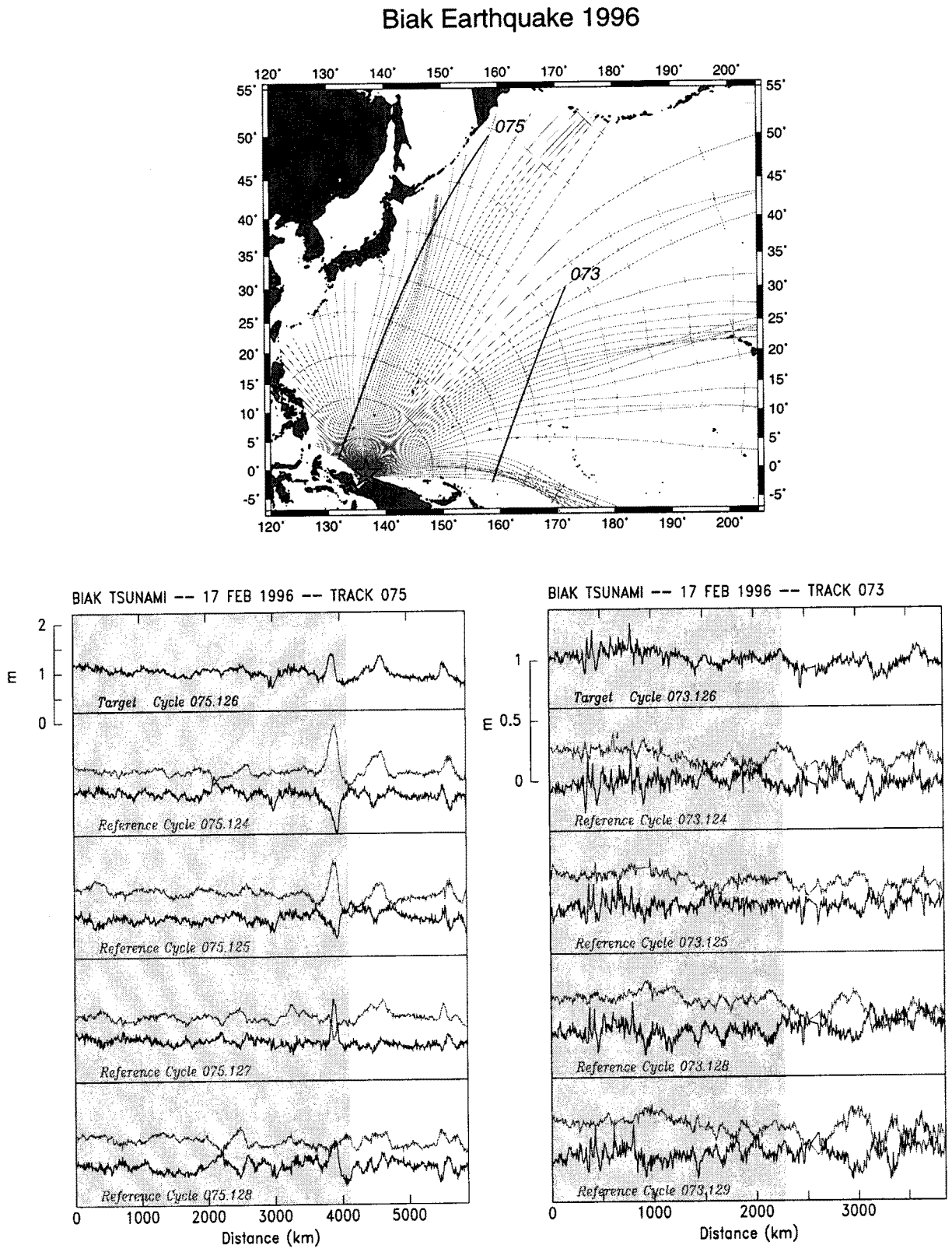

Figure 9. Case of the 1996 Biak tsunami. (top) Identification of the target tracks. The star indicates the epicenter. (bottom) as in Figure 2: (left) Track 075. Note that the signal is dominated by the signature of the Kuroshio current, approximately 4000 km into the series. (right) Track 073. Note the strong high-frequency signal toward the southern extremity of the target series, which, however, cannot be reconciled with acceptable synthetics.

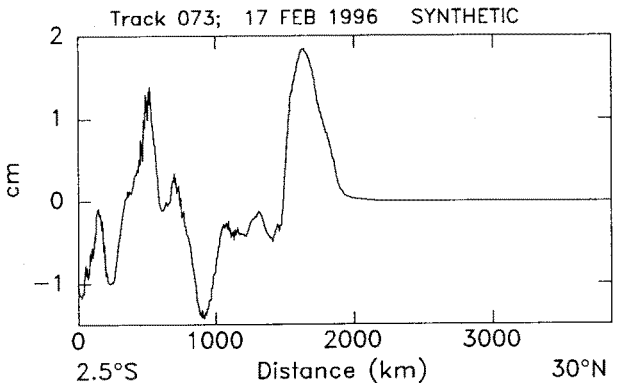

Figure 10. Synthetic maregram computed along Track 073 for Tanioka's fault model of the 1996 Biak earthquake.

ing it with the tsunami wave field. This is upheld by the fact that the signal detected has significant energy at relatively short wavelengths ($\Lambda_t = 50$ km), in a range where the synthetic's contribution is very weak, and by the low amplitude (2 cm peak-to-peak) of the tidal gauge signal at the nearby island of Pohnpei (M. Blackford, personal communication, 1998).

6.2. The Java Tsunami of June 2, 1994

Like the 1992 Nicaraguan event, this earthquake featured a slow rupture, presumably involving a sedimentary structure, and resulted in a significantly larger local tsunami than would have been expected from its seismic waves [*Tanioka and Satake,* 1996; *Newman and Okal,* 1998].

We identified Cycle 063 of T/P Track 077 as a target series, and Cycles 061, 062, 064 and 065 as references. While some energy is present at 0.010 km^{-1} in the target spectrograms, it does not rise above the background noise as expressed by Reference Cycles 061 and 065, and we conclude that the tsunami cannot be detected.

6.3. The Kuriles Tsunami of October 4, 1994

This very large earthquake ($M_0 = 3.0 \times 10^{28}$ dyn-cm) generated a significant tsunami which inflicted considerable damage on the Southern Kurile Islands [*Yeh et al.,* 1995]. However, because the earthquake was an intraplate event with substantial depth (its inverted centroid being at 68 km [*Dziewonski et al.* 1995]), it did not unleash a powerful Pacific-wide tsunami. We nevertheless sought to detect the tsunami signal in altimetry data sets, using Cycles 075 (target) and 073, 074, 076 and 077 (reference) of T/P Track 201. Unfortunately, as in the case of the Biak earthquake, the series are dominated by the signal of the Kuroshio current, and no signal convincingly attributable to the tsunami emerges from the spectrograms.

6.4. The Japan Sea Tsunami of July 12, 1993

This particular tsunami is totally contained in the Sea of Japan. The only target profile (Cycle 030 of T/P Track 127) has a total length over the sea of 600 km and is directed at a low angle to the wave front. The reference series (Cycles 029 and 033) show considerable noise at the low wavenumbers (0.005 to 0.01 km^{-1}) most prominent in the synthetic; the small extent of the profile does not allow an appropriate separation of long wavelengths along track, and we cannot detect this tsunami in the Sea of Japan.

7. Conclusion

The conclusions of this study are in a sense mixed. On the one hand, we have presented in the case of the 1992 Nicaraguan earthquake what constitutes to our knowledge the first direct detection and measurement of the deformation of the surface of the ocean in a tsunami wave field, on the high seas and unaffected by coastal effects. In particular, the similarity in dispersion found in the target series, the synthetics, and *González and Kulikov*'s [1993] Gulf of Alaska records, identifies the tsunami signal in the spectrogram of the target series. Modeling the spectral amplitudes of the detected signal requires a tsunami wave scaled by a factor $\alpha = 1.55$ with respect to the synthetic computed from *Piatanesi et al.*'s [1996] model, developed primarily to match regional run-up and inundation data along the Central American coast. We regard such a value of the ratio α as similar, for example, to the range of the typical scatter in moment values obtained when different investigators use different techniques to model the same large earthquake; in view of the uncertainties in source parameters mentioned above, we would certainly not regard its departure from unity as significantly degrading the detection. The peak-to-peak amplitude of the inferred tsunami wave field, 8 cm, corresponds to oscillations identifiable in the target series, but direct detection in the space domain may not be warranted.

In the case of the 1995 Chilean earthquake, the pulse of energy detected in the target series is most probably due to the tsunami wave field. However, the variability of the spectra of the various reference series lead to a scatter of a factor of 2 in the possible values of the ratio α, depending on which cycle is used as background noise. This prevents us from reaching a robust conclusion regarding the amplitude of the detected signal, and in order to stay on the safe side, we prefer to qualify this signal as a tentative detection.

On the other hand, we fail to detect several significant tsunamis, such as the 1996 Biak, the 1996 Chimbote, or the 1994 Java, tsunamis, the latter two being in many respects comparable to the 1992 Nicaraguan one. Indeed, among the seven events targeted in this study, the only confirmed detection is for the earthquake with the second-smallest seismic moment (Table 1). In this respect, our experience with Java, and with Tracks 523 (Nicaragua) and 230 (Chile), underscores the primary importance of directivity effects: in the latter two cases, the detection is possible (or probable) only on the later passage, i.e., at a greater epicentral distance, for which the wave would be expected to be of smaller amplitude, but along a path sampling tsunami rays that leave the source in the lobes of its directivity pattern. This means that for a detection to be achieved, not only must the satellite cross the wave front in an adequate space-time combination, but the portion of the wave field sampled must be favored in terms of directivity. Because the lobes of directivity functions become narrower as the dimension of the source grows [*Okal and Talandier,* 1991], this problem will not be simply compensated by growth in source size, and the influence of directivity is expected to remain crucial even for the largest tsunamis (as illustrated, for example, by the minimal amplitudes of the 1964 Alaskan tsunami in Hawaii and Polynesia). Directivity is probably the major effect preventing detection of the Biak tsunami in Micronesia, where ray tracing would suggest some positive focusing.

Our experience also indicates that a number of other factors contribute many sources of "noise" to the altimetric signal. Some of it, such as the geoid signature of the Nazca Ridge encountered on Track 523 for Nicaragua, is, of course, static and can be removed by subtracting reference series; some however, like the Kuroshio current, have a level of variability over the satellite's repeat period, which prevents this form of pro-

cessing, resulting in the masking of any potential signal of the Biak tsunami (and probably also of the Kuriles one), even though the geometry of Track 075 would have suggested a favorable directivity effect. Finally, there remain some unexplained transient signals; those occurring at noncausal space-time combinations, as in the case of Track 180 for the 1996 Peruvian tsunami, can be easily dismissed; on the other hand, the signal present in Track 073 of the Biak event had to be eliminated on account of our failure to match it from all reasonable models of the earthquake rupture.

As a final word, we want to stress that considerable insight into the characteristics of a tsunami wave on the high seas could and will certainly be gained from satellite observations of future large tsunamis. However, and given the handful of altimetry satellites presently operational, direct real-time detection of tsunami waves for the purpose of transoceanic tsunami warning is not presently feasible; our experience indicates that finding the satellite at the right place at the right time, i.e., under the right space-time combination of epicentral location, source directivity, and satellite ephemerides, remains the exception rather than the rule.

Acknowledgments. We are grateful to Philippe Gaspar and the Staff of Collecte Localisation Satellites, Toulouse, for providing the satellite altimetry data used in this work. Sandrine Guibourg helped with several synthetics in the early stages of the project. We thank Yuichiro Tanioka for providing his model of source ground motion for the Biak earthquake in advance of publication, Michael Blackford for a copy of the Biak tidal gauge record at Pohnpei, and Carolina Lithgow-Bertelloni for a personalized interlibrary loan. The paper benefited from careful reviews by John Vidale and Kenji Satake. This work was supported by CEA–DASE.

References

Ben-Menahem, A., Radiation of seismic surface waves from finite moving sources, *Bull. Seismol. Soc. Am., 51,* 401-435, 1961.

Ben-Menahem, A., and M. Rosenman, Amplitude patterns of tsunami waves from submarine earthquakes, *J. Geophys. Res., 77,* 3097-3128, 1972.

Birkett, C.M., The contribution of TOPEX/POSEIDON to the global monitoring of climatically sensitive lakes, *J. Geophys. Res., 100,* 25179-25204, 1995.

Braddock, R.D., Response of a conventional tide gauge to a tsunami, *Mar. Geod., 4,* 223-236, 1980.

Callahan, P.S., and W.H. Daffer, Search for earthquake effects in TOPEX/POSEIDON data (abstract), *Eos, Trans. AGU, 75, (44),* Fall Mtg. Supp., 357, 1994.

Cazenave, A., P. Bonnefond, K. Dominh, and P. Schaeffer, Caspian Sea level from TOPEX-POSEIDON altimetry: Level now falling, *Geophys. Res. Lett., 24,* 881-884, 1997.

Chelton, D.B., and M.G. Schlax, Global observation of oceanic Rossby waves, *Science, 272,* 234-238, 1996.

Dziewonski, A.M., A. Friedman, D. Giardini, and J.H. Woodhouse, Global seismicity of 1982: Centroid moment tensor solutions for 308 earthquakes, *Phys. Earth Planet. Inter., 33,* 76-90, 1983.

Dziewonski, A.M., G. Ekström, and M.P. Salganik, Centroid-moment tensor solutions for October-December 1994, *Phys. Earth Planet. Inter., 91,* 187-201, 1995.

Filloux, J.H., Tsunami recorded on the open ocean floor, *Geophys. Res. Lett., 9,* 25-28, 1982.

González, F.I., and Ye.A. Kulikov, Tsunami dispersion observed in the deep ocean, in: *Tsunamis in the World,* edited by S. Tinti, pp. 7-16, Kluwer Acad., Norwell, Mass., 1993.

González, F.I., C.L. Mader, M.C. Eble, and E.N. Bernard, The 1987–88 Alaskan Bight tsunamis: Deep ocean data and model comparisons, *Natural Hazards, 4,* 119-140, 1991.

Gründlingh, M.L., Tracking eddies in the Southeast Atlantic and Southwest Indian Oceans with TOPEX/POSEIDON, *J. Geophys. Res., 100,* 24977-24986, 1995.

Guibourg, S., P. Heinrich, and R. Roche, Numerical modeling of the 1995 Chilean tsunami; impact on French Polynesia, *Geophys. Res. Lett., 24,* 775-778, 1997.

Imamura, F., and N. Shuto, Analysis of OBS data and numerical simulation for the 1990 Mariana earthquake tsunami, in: *Tsunamis in the World,* edited by S. Tinti, pp. 95-106, Kluwer Acad., Norwell, Mass., 1993.

Kanamori, H., Mechanism of tsunami earthquakes, *Phys. Earth Planet. Inter., 6,* 346-359, 1972.

Kanamori, H., and M. Kikuchi, The 1992 Nicaragua earthquake: a slow tsunami earthquake associated with subducted sediments, *Nature, 361,* 714-716, 1993.

Kikuchi, M., and H. Kanamori, Source characteristics of the 1992 Nicaragua tsunami earthquake inferred from teleseismic body waves, *Pure Appl. Geophys., 144,* 441-453, 1995.

Landisman, M., A. Dziewonski, and Y. Satô, Recent improvements in the analysis of surface wave observations, *Geophys. J. Roy. astr. Soc., 17,* 369-403, 1969.

Mader, C.L., *Numerical Modeling of Water Waves,* Univ. of Calif. Press, Berkeley, 1988.

Newman, A.V., and E. A. Okal, Source slowness of the February 21, 1996 Chimbote earthquake studied from teleseismic energy estimates (abstract), *Eos, Trans. AGU, 77, (17),* Spring Mtg. Supp., S184, 1996.

Newman, A.V., and E.A. Okal, Teleseismic estimates of radiated seismic energy: The E/M_0 discriminant for tsunami earthquakes, *J. Geophys. Res., 103,* 26885–26898, 1998.

Okada, M., Ocean-bottom pressure gauge for tsunami warning system in Japan, in: *Proceedings of the 2nd UJNR Tsunami Workshop,* pp. 219–227, NOAA, Boulder, Colo., 1991.

Okada, Y., Surface deformation due to shear and tensile faults in a half-space, *Bull. Seismol. Soc. Am., 75,* 1135-1154, 1985.

Okal, E.A., Mode-wave equivalence and other asymptotic problems in tsunami theory, *Phys. Earth Planet. Inter., 30,* 1-11, 1982.

Okal, E.A., Seismic parameters controlling far-field tsunami amplitudes: A review, *Natural Hazards, 1,* 67-96, 1988.

Okal, E.A., Seismotectonic setting of the February 17, 1996 Biak, Indonesia earthquake (abstract), *Eos, Trans. AGU, 77, (17),* Spring Mtg. Suppl., S184, 1996.

Okal, E.A., and J. Talandier, Single-station estimates of the seismic moment of the 1960 Chilean and 1964 Alaskan earthquakes, using the mantle magnitude M_m, *Pure Appl. Geophys., 136,* 103-126, 1991.

Piatanesi, A., S. Tinti, and I. Gavagni, The slip distribution of the 1992 Nicaragua earthquake from tsunami run-up data, *Geophys. Res. Lett., 23,* 37-40, 1996.

Ruegg, J.-C., et al., The $M_w = 8.1$ Antofagasta (North Chile) earthquake of July 30, 1995: First results from teleseismic and geodetic data, *Geophys. Res. Lett., 23,* 917-920, 1996.

Schindelé, F., D. Reymond, E. Gaucher, and E.A. Okal, Analysis and automatic processing in near-field of the eight 1992-1994 tsunamigenic earthquakes: Improvements in real-time tsunami warning, *Pure Appl. Geophys., 144,* 381–408, 1995.

Tanioka, Y., and K. Satake, Tsunami displacement by horizontal displacement of ocean bottom, *Geophys. Res. Lett., 23,* 861-864, 1996.

Tanioka, Y., L.J. Ruff, and K. Satake, The recent large tsunamigenic earthquakes (abstract), *Eos, Trans. AGU, 77, (17),* Spring Mtg. Suppl., S184, 1996.

Teague, W.J., Z.R. Hallock, G.A. Jacobs, and J.L. Mitchell, Kuroshio sea surface fluctuations observed simultaneously with inverted echo sounders and TOPEX/POSEIDON, *J. Geophys. Res., 100,* 24987-24994, 1995.

Ward, S.N., Relationships of tsunami generation and an earthquake source, *J. Phys. Earth, 28,* 441-474, 1980.

Woods, M.T., and E.A. Okal, Effect of variable bathymetry on the amplitude of teleseismic tsunamis: a ray-tracing experiment, *Geophys. Res. Lett., 14,* 765-768, 1987.

Wunsch, C., and D. Stammer, The global frequency-wavenumber spectrum of oceanic variability estimated from TOPEX/POSEIDON altimetric measurements, *J. Geophys. Res., 100,* 24895–24910, 1995.

Yeh, H., V. Titov, V. Gusiakov, E. Pelinovsky, V. Khramushin, and V. Kaistrenko, The 1994 Shikotan earthquake tsunamis, *Pure Appl. Geophys., 144,* 855-874, 1995.

P. Heinrich and A. Piatanesi, Département Analyse et Surveillance de l'Environnement, Commissariat à l'Energie Atomique, B.P. 12, F-91680 Bruyères-le-Châtel, France.

E. A. Okal, Department of Geological Sciences, Northwestern University, Evanston, IL 60208.

(Received June 9, 1998; revised August 27, 1998; accepted September 19, 1998.)

Références bibliographiques

Abe, K., 1979. Size of great earthquakes of 1837-1974 inferred from tsunami data, *J. Geophys. Res.*, **84**, 1561-1568.

Abe, K., 1995. Estimate of tsunami run-up heights from earthquake magnitudes, *In* "Tsunami: progress in prediction, disaster prevention and warning" (Y. Tsuchiya and N. Shuto, eds.), Kluwer Academic Publishers, Dordrecht, The Netherland, pp. 21-35.

Cotton, F., and Campillo M., 1995. Frequency domain inversion of strong motions: application to the 1992 Landers earthquake, *J. Geophys. Res.*, **100**, 3961-3975.

Dahlen F.A. and Tromp J., 1998. *Theoretical global seismology*, Princeton Univ. Press, 944 pp.

Fukao, Y., 1979. Tsunami earthquakes and subduction processes near deep-sea trenches, *J. Geophys. Res.*, **84**, 2303-2314.

Geist, E.L., 1998. Local tsunamis and earthquake source parameters, *Advances in Geophysics*, **39**, 117-209.

Geist, E.L. and Yoshioka S., 1996. Source parameters controlling the generation and propagation of potential local tsunamis along the Cascadian margin, *Natural Hazards*, **13**, 151-177.

Gonzalez, F.I. and Kulikov Y.A., 1993. Tsunami dispersion observed in the deep-ocean, in *Tsunamis in the world*, S. Tinti (Editor), Kluwer Academic Publishers, Dordrecht, The Netherlands, 7-16.

Gonzalez, F.I., Mader, C.L., Eble M.C. and Bernard E.N., 1991. The 1987-1988 Alaskan Bight tsunamis: deep ocean data and model comparisons, *Natural Hazards*, **4**, 119-139.

Heinrich, Ph., Guibourg S., Mangenay A. and Roche R., 1998a. Numerical modeling of a landslide-generated tsunami following a potential explosion of the Montserrat volcano, *J. Phys. Chem. Earth*, **24**, 163-168.

Heinrich, Ph., Mangenay A., Guibourg S. and Roche R., 1998b. Simulation of water waves generated by a potential debris avalanche in Montserrat, Lesser Antilles, *Geophys. Res. Lett.*, **25**, 3697-3700.

Heinrich, Ph., Mangenay A., Boudon G. and Roche R., 1999. Modéliser un raz de marée crée par un volcan, *La Recherche*, **318**, 66-71.

Hidayat, D., Barker J.S. and Satake K., 1995. Modeling the seismic source and tsunami generation of the December 12, 1992 Flores Island, Indonesia, earthquake, *Pure Appl. Geophys.*, **144**, 537-554.

Ihmlé, P.F., 1996. Monte Carlo slip inversion in the frequency domain: application to the 1992 Nicaragua slow earthquake, *Geophys. Res. Lett.*, **23**, 913-916.

Ihmlé, P. F., and Ruegg J.C., 1997. Source tomography by simulated annealing using broad-band surface waves and geodetic data: application to the M_W=8.1 Chile 1995 event, *Geophys. J. Int.*, **131**, 146-158.

Imamura, F., Gica E., Takahashi T. and Shuto N., 1995. Numerical simulation of the 1992 Flores tsunami: interpretation of tsunami phenomena in northeastern Flores Island and damage at Babi Island, *Pure Appl. Geophys.*, **144**, 555-568.

Johnson, J.M., 1998. Heterogeneous coupling along Alaska-Aleutians as inferred from tsunami, seismic,and geodetic inversions, *Advances in Geophysics*, **39**, 1-116.

Johnson, J.M., Satake K., Holdahl S.R. and Sauber, 1996. The 1964 Prince Williams Sound earthquake: joint inversion of tsunami and geodetic data, *J. Geophys. Res.*, **101**, 523-532.

Kajura, K., 1963. The leading wave of a tsunami, *Bull. Earthquake Res. Inst.*, **41**, 535-571.

Kajura, K., 1981. Tsunami energy in relation to parameters of the earthquake fault model, *Bull. Earthquake Res. Inst.*, **56**, 415-440.

Kanamori, H., 1972. Mechanism of tsunami earthquakes, *Phys. Earth Planet. Inter.*, **6**, 246-259.

Kanamori, H., and Kikuchi M., 1993. The 1992 Nicaragua earthquake: a slow tsunami earthquake associated with subducted sediments, *Nature*, **361**, 714-716.

Kikuchi, M., and Kanamori H., 1995. The Shikotan earthquake of october 4, 1994: lithospheric earthquake, *Geophys. Res. Lett.*, **22**, 1025-1028.

Kowalik, Z., 1997. Landslide Generated Tsunami in Skagway, Alaska, *Science Tsunami Hazard,* **15**, 89-106.

Kowalik, Z., and Murty T.S., 1993. Numerical simulation of two-dimensional tsunami run-up, *Marine Geodesy*,**16**, 87-100.

Lander, James F. and Patricia A. Lockridge, 1989. *United States Tsunamis*. Publication 41-2. U.S. Department of Commerce. August 1989.

Lay, T., and Kanamori, H., 1981. An asperity model of large earthquake sequences, *In* "Earthquake prediction – an international review" (D.W. Simpson, P.G. Richards, eds.). American Geophysical Union, Washington, DC, pp. 579-592.

Lundgren, P.R., and Okal E.A., 1988. Slab Decoupling in the Tonga Arc: The June 22, 1977, Earthquake, *J. Geophys. Res.*, **93**, 13355-

Ma, K.-F., Kanamori, H. and Satake, K.,1999. Mechanism of the 1975 Kalapana, Hawaii, earthquake inferred from tsunami data, *J. Geophys. Res*. **104**, 13153-

Manshina, L. and Smylie D.E., 1971. The displacements fields of inclined faults, *Bull. Seismol. Soc. Am.*, **61**, 1433-1440.

Massonnet, D., Rossi M., Carmona C., Adragna F., Peltzer G., Feigl K. and Rabaute T., 1993. The displacement field of the Landers earthquake mapped by radar interferometry, *Nature*, **364**, 138-142.

Meyer, B., Armijo R., Massonnet D., de Chabalier J.B., Delacourt C., Ruegg J.C., Achache J., Briole P. and Papanastassiou D., 1996. The 1995 Grevena (Northern Greece) earthquake: Fault model constrained with tectonic observation and SAR interferometry, *Geophys. Res. Lett.*, **23**, 2677-2680.

Michel, R., Avouac J.-P.; Taboury J., 1999. Measuring ground displacements from SAR amplitude images: Application to the Landers earthquake, *Geophys. Res. Lett*. **26**, 875-878.

Newman, A.V. and Okal E.A., 1998. Teleseismic estimates of radiated seismic energy: the E/M_0 discriminant for tsunami earthquakes, *J. Geophys. Res.,***103**, 26885- 26898.

Okada Y., 1985. Surface deformation due to shear and tensile faults in a half-space, *Bull. Seismol. Soc. Am.,* **75**, 1135-1154.

Okal, E.A., 1982. Mode-wave equivalence and other asymptotic problems in tsunami theory,*Phys. Earth Planet. Int.,* **30**, 1-11.

Okal E.A., 1988. Seismic parameters controlling far-field tsunami amplitudes: a review, *Natural Hazards,* **1**, 67-96.

Okal, E.A., 1999. The 1998 Papua New Guinea tsunami: an overview, *Proc. of the International Conference on Tsunamis*, 26-28 may, Paris-France.

Okal, E.A. and Talandier J., 1987. M_n: theory of a variable-period mantle magnitude, *Geophys. Res. Lett.*, **14**, 836-839.

Okal, E.A. and Talandier J., 1989. M_n: a variable period mantle magnitude, *J. Geophys. Res.,* **94**, 4169-4193.

Okal, E.A. and Talandier J., 1991. Single station estimate of the seismic moment of the1960 Chilean and 1964 Alaskan earthquakes, using mantle magnitude, *Pure and Appl. Geophys.*, **136**, 103-126.

Okal, E.A., Piatanesi A. and Heinrich Ph., 1999. Tsunami detection by satellite altimetry, *J. Geophys. Res.,* **104**, 599-615.

Pelayo, A.M., and Wiens D.A., 1992. Tsunami earthquakes: slow thrust-faulting events in the accretionary wedge, *J. Geophys. Res.,* **97**, 15321-15337.

Peyret, R., and Taylor T.D., *Computational methods for fluid flow*, Springer-Verlag, New York, 1983.

Piatanesi, A., Tinti S., and Gavagni I., 1996. The slip distribution of the 1992 Nicaragua earthquake from tsunami run-up data, *Gephys. Res. Lett.,***23**, 37-40.

Piatanesi, A., and Tinti S., 1998. A revision of the eastern Sicily earthquake and tsunami, *J. Geophys. Res.,***103**, 2749-2758.

Piatanesi, A., Heinrich Ph. And Tinti S., 1999. The October 4, 1994 Shikotan (Kurile Islands) tsunamigenic earthquake: an open problem on the source mechanism, *Pure App. Geophys.,* **154**, 555-574.

Piatanesi, A., Tinti S. and Bortolucci E., 1999. Finite-element simulations of the 28 December 1908 Messina Strait tsunami, *J. Phys. Chem. Earth (A),***24**, 145-150.

Rabinovich, A., 1997. Spectral analysis of tsunami waves: separation of source and topography effects, *J. Gephys. Res.*, **102**, C6, 12663-12676.

Rzadkiewicz, S. and Heinrich Ph., 1999. Numerical simulation of the 1979 Nice tsunami, *Pure Appl. Geophys.* (submitted).

Reymond, D., Hyvernaud O. and Talandier J., 1991. Automatic detection, location and quantification of earthquakes: application to tsunami warning, *Pure Appl. Geophys.,* **135**, 361-382.

Ritsema, J., Ward S.N. and Gonzalez F.I., 1995. Inversion of deep-ocean tsunami records for 1987 to 1988 gulf of Alaska earthquake parameters, *Bull. Seismol. Soc. Am.*, **85**, 747-754.

Satake, K., 1987. Inversion of tsunami waveforms for the estimation of a fault heterogeneity: method and numerical experiment, *J. Phys. Earth*, **35**, 241-254.

Satake, K., 1989. Inversion of tsunami wave forms for the estimation of Heterogeneous fault motion of large submarine earthquakes: the 1968

Tokachi-oki and the 1983 Japan Sea earthquakes, *J. Geophys. Res.*, **94**, 5627-5636.

Satake, K., 1993. Depth distribution of coseismic slip along the Nankai Trough, Japan, from joint inversion of geodetic and tsunami data, *J. Geophys. Res.*, **98**, 4553-4565.

Satake, K., and Tanioka, Y., 1999. Sources of tsunami and tsunamigenic earthquakes insubduction zones, *Pure Appl. Geophys.*, **154**, 467-483.

Schindele, F., Reymond, D., Gaucher, E., and Okal, E.A., 1995. Analysis and Automatic processing in near-field of eight 1992-1994 tsunamigenic earthquakes: improvements towards real-time tsunami warning, *Pure Appl. Geophys.,* **144**, 381-408.

Talandier, J. and Okal A.E., 1989. An algorithm for automated tsunami warning in French Polynesia, based on mantle magnitudes, *Bull. Seismol. Soc. Am.,* **72**, 1-14.

Talandier, J., Reymond D. and Okal A.E., 1987. M_m: use of a variable-period mantle magnitude for the rapid one-station estimation of teleseismic moments, *Geophys. Res. Lett.*, **14**, 840-843.

Tinti, S. and Gavagni I., 1995. A smoothing algorithm to enhance finite-element tsunami modeling: an application to the 5 February 1783 Calabrian case, Italy, *Natural Hazards,***12**, 161-197.

Tinti S. and Piatanesi A., 1995. The wave-propagator in finite element modeling tsunamis, *Marine Geodesy,* **18**, 273-298.

Tinti, S. and Piatanesi A., 1996a. Numerical simulations of the tsunami induced by the1627 earthquake affecting Gargano, southern Italy, *J. Geodynamics,* **21**, 141-160.

Tinti, S., and Piatanesi A., 1996b. Finite-element simulations of the 5 February 1783 Calabrian tsunami, *J. Phys. Chem. Earth,* **21**, 12, 39-43.

Tinti, S., and Vannini C., 1995. Tsunami trapping near circular islands, *Pure App. Geophys.*, **144**, 595-

Tinti, S., Gavagni I. and Piatanesi A., 1994. A finite-element numerical approach for modeling tsunamis, *Annali di geofisica*, **5**, 1009-1026.

Tinti, S., Piatanesi A. and Maramai A., 1997. Numerical simulations of the 1627 Gargano tsunami (southern Italy) to locate the earthquake source, in Hebenstreit, G. (ed.), *Perspectives on Tsunami Hazard Reduction,* 115-131, Kluwer Academic Publisher, The Netherlands.

Tinti, S., Armigliato A., Bortolucci E. and Piatanesi A., 1999a. Identification of the source fault of the 1908 Messina earthquake through tsunami modelling. Is it a possible task?, *J. Phys. Chem. Earth (B)*, **24**, 417-421.

Tinti,S., Bortolucci E and Armigliato A., 1999b, Numerical simulation of the landslide-induced tsunami of 1988 on Vulcano Island, Italy, *Bull. Volcanol.,* **61**, 121-

Tsuji, Y., Matsutomi H., Imamura F., Takeo M., Kawata Y., Matsuyama M., Takahashi T., Harjadi S. and Harjadi P., 1995. Damage to coastal villages due to the 1992 Flores Island earthquake tsunami, *Pure App. Geophys.*, **144**, 481-524.

Ward, S.N., 1980. Relationships of tsunami generation and an earhquake source, *J. Phys. Earth,* **28**, 441-474.

Ward, S.N., 1981. On tsunami nucleation: I. A point source, *J. Geophys. Res.,***86**, 7895-7900.

Ward, S.N., 1982. On tsunami nucleation: II. An instantaneous modulated line source, *Phys. Earth Planet Inter.*, **27**, 273-285.

Webb, S.C., Zhang X. and Crawford W., 1991. Infragravity waves in the deep ocean, *J. Geophys. Res.*, **96**, C2, 2723-2736.

Zobin, V.M., 1997. The rupture history of the M_W=8.0 Jalisco, Mexico, earthquake of 1995 October 9, *Geophys. J. Int.*, **130**, 220-228.

Résumé

Les tsunamis sont des ondes de gravité qui se propagent à la surface des océans: ils sont caractérisés par des longueurs d'onde qui peuvent varier de 10 à plusieurs centaines de km et par des périodes de 5 à 45 minutes. Les tsunamis sont générés, dans la plupart des cas, par des séismes qui produisent un déplacement vertical important du fond océanique (typiquement dans les zones de subduction) et, moins fréquemment, par des effondrements sous-marins et par des explosions volcaniques. L'objet de cette thèse est de montrer que la modélisation et l'observation des tsunamis peuvent apporter des informations complémentaires sur la source sismique. Les différentes phases de la vie d'un tsunami (génération, propagation et impact sur la côte) sont modélisées à l'aide de méthodes numériques (éléments finis et différences finies) qui résolvent les équations d'ondes longues. Les simulations de plusieurs tsunamis, pour lesquels des observations existent, montrent que les données de tsunami (même de type qualitatives) permettent de contraindre l'épicentre, l'orientation du plan de faille et la distribution du glissement co-sismique. Les simulations par méthode directe nous ont permis de valider des modèles de source pour les tsunamis historiques du Gargano 1627, de Sicile 1693, de Calabre 1783 et de Messine 1908 (Italie du Sud). D'autre part nous avons développé une méthode d'inversion, qui utilise les hauteurs de run-up en champ proche acquises après l'événement, pour déterminer la distribution du glissement co-sismique le long de la faille source: cette méthode a été appliquée au tsunami de Nicaragua 1992 et de Messine (Italie du Sud) 1908. Enfin, en étudiant le dernier tsunami catastrophique, survenu en Papouasie Nouvelle-Guinée le 17 juillet 1998, nous proposons une méthodologie qui, à partir des seules données de run-up, permet de déterminer la position, les dimensions et l'amplitude de la source.

Mots-clefs: modélisation numérique, paramètres de source, risque sismique, risque tsunamique, source sismique, tsunami

Abstract

Tsunamis are gravity waves propagating at the ocean surface: they are characterized by wavelengths that may vary from 10 to several hundred of km and by periods from 5 to 45 minutes. Tsunamis are generated, in most cases, by earthquakes that produce large vertical displacement of the ocean bottom and, less frequently, by submarine landslide and by volcanic explosions. The aim of this thesis is to show that tsunami modeling and observation can give complementary information on the tsunamigenic seismic source. The different phases of a tsunami (i.e. generation, propagation and impact on the coast) are modeled by means of numerical methods (both finite-elements and finite-differences) that solves the shallow water equations. The simulations of several tsunamis, for which observations are available, show that tsunami data (even of qualitative type) are able to constrain the epicenter, the orientation of the fault plane and the co-seismic slip distribution. Direct simulations allow us to validate source models for the Gargano 1627, Sicily 1693, Calabria 1783 and Messina 1908 (southern Italy) historical tsunamis. Furthermore we developed an inversion method, that makes use of near-field run-up heights measured after the event, to determine the co-seismic slip distribution on the source fault: we applied this method to the 1992 Nicaragua and to 1908 Messina (southern Italy) tsunamis. Finally, through the study of the last catastrophic tsunami, occurred in Papua New Guinea on July 17 1998, we propose a methodology that, by means of run-up data solely, allows for the determination of the position, dimensions and amplitude of the source.

Key-words: numerical modeling, source parameters, seismic hazard, seismic source, tsunami, tsunami hazard